PROGRESS IN RESEARCH

April 1, 2019 - March 31, 2020

CYCLOTRON INSTITUTE

Texas A&M University

College Station, Texas

PROGRESS IN RESEARCH

APRIL 1, 2019 - MARCH 31, 2020

Prepared By

The Cyclotron Institute Staff

Texas A&M University

College Station, TX 77843-3366

Phone: (979) 845-1411
Fax: (979) 845-1899

Web: http://cyclotron.tamu.edu

August 2020

TABLE OF CONTENTS

SECTION I: NUCLEAR STRUCTURE, FUNDAMENTAL INTERACTIONS AND ASTROPHYSICS

SECTION II: HEAVY ION REACTIONS

SECTION III: NUCLEAR THEORY

SECTION IV: SUPERCONDUCTING CYCLOTRON, INSTRUMENTATION AND RIB UPGRADE

SECTION V: PUBLICATIONS

SECTION VI: APPENDIX

Introduction
April 1, 2019 – March 31, 2020

Progress in research and operations at the Texas A&M Cyclotron Institute is summarized in this report for the period April 1, 2019 through March 31, 2020. The period covered by this report includes the onset of the COVID-19 pandemic world-wide and here in Texas. On the16 of March we suspended the SEE line running to establish new procedures to ensure that we could run as safe as reasonably achievable. We also instituted new procedures for the discovery science program that limited access to the operations portions of the building and reduced person density throughout the facility. Late in March all but essential research at the University was shut down. The CI continued to run the radiation effects program due to its importance to national security. I am indebted to the dedicated operations staff that kept the facility running during this challenging period.

TexAT has been fully commissioned and is a valuable device for the discovery science program, including a sensitive measurement of the democratic decay of the Hoyle state. AstroBox II is also producing science, including detection of low energy protons from the β-delayed protons of ^{27}P. AGGIE is fully installed and the characterization of this spectrometer is underway. TAMUTRAP is operational and producing some nice mass measurements. TexNUET is beginning construction. Progress is being made on the DAPPER array.

The Cyclotron Institute continued to explore the capability of producing radioisotopes for medicine, in particular the alpha particle emitter ^{211}At. The K150 cyclotron provided a beam of ^{4}He for the ^{209}Bi(α,2n)^{211}At reaction. Typically, the irradiation takes place overnight, the irradiated target being retrieved after approximately 8 to 12 hours. The irradiated bismuth target is chemically processed, and ^{211}At is separated and counted. Several runs were conducted, the highest quantity of ^{211}At produced in one run being approximately 40 mCi. Cooling the bismuth target, minimizing the handling of the irradiated target, and optimizing the ^{4}He beam will be future priorities in this project.

The Light Ion Guide (LIG) project entered a major upgrade phase: two new chambers were fabricated for easier installation and maintenance of the SPIG (SextuPole Ion Guide). In addition, the capability was added of extracting radioactive ions from the target cell in the direction opposite to the original direction in order to serve the TAMUTRAP project. For this project the production of ^{25}Si, ^{24}Si (proton emitting isotopes), and other isotopes (e.g.^{20}Na, $^{25\text{-}24}$Al) using a ^{3}He beam was successfully attempted using a larger gas cell and with a different extraction geometry. In the trial a ^{3}He beam impinged on an isotopically enriched ^{24}Mg target inside the gas cell and provided confirmation that the LIG can produce quantities of ^{25}Si useful to TAMUTRAP. This was the starting point for the future design of a separator that will purify and transport the radioactive products to the TAMUTRAP location.

The K500 provided an impressive 6416 hours of beam for both science and radiation effects testing. The K150 cyclotron provided 4024 hours of beam on target and continues to be used by external users for radiation effects testing with its proton beams. Additionally, efforts to meet the increasing radiation testing demand are underway by developing a series of 15 MeV/u heavy-ion beams from the K150. Significant effort was devoted during annual maintenance to improve the K150 cyclotron vacuum leading to new intensity records for light ions such as $^{4}He^{+}$ and $^{3}He^{+}$.

As in previous reports, I include here some scientific highlights.

- New constrains on the $^{22}Ne(\alpha,\gamma)$ and $^{22}Ne(\alpha,n)$ astrophysical s-factors with significant consequences for the final abundances of the s-process elements were obtained.
- Location of the 2s1/2 shell in ^{9}C has been identified in the $^{8}B+p$ resonance scattering experiment with Texas Active Target.
- First β-delayed charged particle emission measurements were performed with TexAT and the results on Hoyle state branching ratio and half-life were obtained.
- Search for a high-spin (6^{+}) member of the α:2n:α band in ^{10}Be resulted in tight constrains on the partial width for the hypothetical 6^{+} state.
- Determined the shell effect on the nuclear level density within the micro- and macroscopic ensembles method, using the extended Thomas-Fermi approximation, and compared with experimental data.
- State-of-art theory of the surrogate Trojan horse method has been developed, which was applied for the analysis of important resonance astrophysical reactions including carbon-carbon fusion playing a very important role in a wide variety of stellar burning scenarios such as massive stars, type Ia supernovae and superbursts.

Institute scientists remain active in a number of collaborative research efforts around the world. Major programs include: measurements of beta decays with the TRINAT collaboration at TRIUMF; nuclear structure measurements with TexAT at TRIUMF; continued work with the STAR collaboration at RHIC; fusion studies at MSU; and participation in the SAMURAI collaboration at RIBF in Tokyo, Japan.

The format of this report follows that of previous years. Sections I through III contain reports from individual research projects. Operation and technical developments are given in Section IV. Section V lists the publications with Cyclotron Institute authors and outside users and the Appendix gives additional information including talks presented by members of the Institute during the past year. Once again, the full volume of this year's Progress in Research is available only on our web site (http://cyclotron.tamu.edu). *Since most of the contributions presented here are truly reports on progress* *in research, results and conclusions should not be quoted from the report without the consent of the authors.*

I am indebted to Dr. Y.-W. Lui for assembling this report.

S.J. Yennello
August 15, 2020

SECTION I

NUCLEAR STRUCTURE, FUNDAMENTAL INTERACTIONS AND ASTROPHYSICS

Improving the *ft* value of ^{37}K via a precision measurement of the branching ratios

A. Ozmetin, V.E. Iacob, J.C. Hardy, V.S. Kolhinen, D. Melconian, M. Nasser, H.I. Park,
B. Schroeder, and P.D. Shidling

As part of the TRIUMF Neutral Atom Trap (TRINAT) collaboration, our goal is to search for physics beyond the standard model via precision measurements of the polarized angular correlations of the isobaric analogue β^+ decay of ^{37}K. A recent measurement of the β asymmetry parameter, A_β, has reached 0.3% precision [1] which, when combined with the comparative half-life or *ft* value, was used to improve the value of V_{ud} for this decay as well as to search for right-handed currents. Plans are underway to improve the A_β measurement, at which point uncertainties in the ft value will no longer be negligible. Presently, the uncertainty in the ft value is dominated by the 97.99(14)% branch to the ground state following an improved half-life measurement performed at the Cyclotron Institute [2]. The 1997 measurement which dominates the present value of the branching ratio [3] was limited by the absolute efficiency of the HPGe detector. Using the fast-tape-transport system at the Cyclotron Institute and the world's most precisely calibrated HPGe, we measured the decay of ^{37}K to significantly improve the branching ratio and hence the ft value.

We have filtered the data to obtain a clean data set (e.g. vetoing bad cycles where the tape does not stop between the HPGe γ detector and the plastic scintillator β detector) and minimized accidental coincidences via the E_γ vs β-γ timing 2D spectrum. In order to optimize the reduction of backgrounds and random coincidences, we iteratively optimized our cuts in both the γ energy and β-γ timing.

Branches were acquired from fits to the areas of the γ photopeaks that account for the random coincidences and background, and include small effects such as incomplete charge collection. These branches were corrected for dead-time, pile-up, pre-emption, β-singles losses, annihilation and bremsstrahlung summing.

Systematic uncertainties that were quantitatively known (the first block of Table I) was propagated as usual. For the remaining, quantitative values were obtained via a rigorous process of isolating systematics from every relevant steps of the analysis to account for any possible bias introduced (second block in Table I). This process involved making objective variations in a given systematic procedure and analyzing the response in the final result. The final result for the branching ratio is

$$\mathrm{BR} = 97.81(2)\%.$$

We improved the uncertainty in the branching ratio by a factor of 5. This has doubled the precision of the *ft* value which is being used to test the standard model. With our contribution (Fig. 1), uncertainties in the *ft* value will not impact the precision of V_{ud} from ^{37}K even after precision of ρ, the Gamow-Teller to Fermi mixing ratio, is measured to < 0.1%.

Table I. Systematic and statistical uncertainties in the branching ratios for the transitions observed. Blank entries indicate an uncertainty below 0.001% and are therefore negligible.

Source	Uncertainty, σ_{BR} [%]			
	$E_\gamma = 1184$ keV	1611 keV	2796 keV	3601 keV
γ efficiencies	–	–	0.011	–
Internal conversion	–	–	–	–
Peak-to-total	–	–	–	–
$t_\beta - t_\gamma$ cuts	0.001	0.001	0.006	0.001
Pre-emption correction	–	–	0.005	–
β/HI cuts	0.001	–	0.004	–
Fitting range	–	–	–	–
Total systematics	0.001	0.001	0.015	0.001
Statistical	0.003	0.003	0.017	0.002
Total uncertainty	0.004	0.003	0.022	0.003

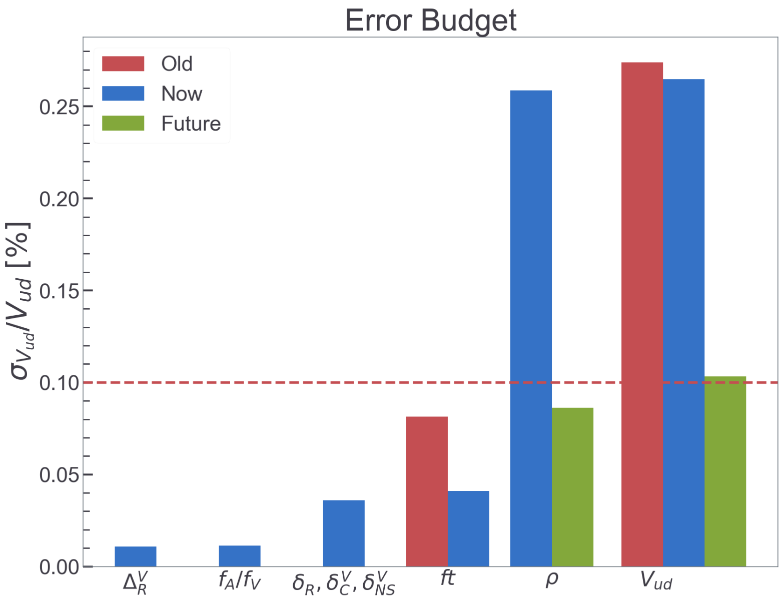

Fig. 1. Final error budget showing the previous, current (our contribution) and expected future uncertainty contributions to V_{ud} in ^{37}K.

[1] B. Fenker *et al.*, Phys. Rev. Lett. **120**, 062502 (2018).
[2] P.D. Shidling *et al.*, Phys. Rev. C **90**, 032501(R) (2014).
[3] E. Hagberg *et al.*, Phys. Rev. C **56**, 135 (1997).

Loss calculations for an ion trap update to ^{6}He CRES experiment

D. McClain, V.E. Iacob, V.S. Kolhinen, D. Melconian, M. Nasser, A. Ozmetin,
B. Schroeder, and P.D. Shidling

In the Standard Model, the weak interaction is described by a *V–A* or vector minus axial-vector Lagrangian in which there are no scalar or tensor currents. This makes the weak interaction purely left-handed. In searching for physics beyond the standard model, we look for non-zero coupling coefficients for chirality-flipping interactions such as scalar or tensor interactions. We are able to see the decay rate is proportional to the following [1].

$$W(E_e)dE_e \propto \frac{F(\pm Z, E_e)}{2\pi^3} p_e E_e (E_0 - E_e)^2 dE_e \xi \left(1 + a_{\beta\nu} \frac{p_e \cdot p_\nu}{E_e E_\nu} + b_{\text{Fierz}} \frac{m_e}{E_e}\right).$$

From here we can see that the β spectrum depends on b_{Fierz} which, for a purely Gamow-Teller decay such as ^{6}He, is given as

$$b_{Fierz} \approx \left(\frac{C_T + C_T{}'}{C_A}\right),$$

where C_T and C'_T are exotic couplings which are set to zero in the standard model. Finding a non-zero b_{Fierz} via a precision measurement of the shape of the β spectrum would point to physics beyond the standard model. The cyclotron radiation emission spectroscopy (CRES) technique developed by the Project-8 collaboration [2] is being utilized to measure the β spectrum of ^{6}He from radiation emitted due to cyclotron radiation as a charged particle precesses in a magnetic field. The cyclotron frequency, *f*, of an electron is dependent on the kinetic energy E_e of the electron according to

$$f = \frac{1}{2\pi} \frac{eB}{m_e + E_e},$$

where *e* is electron charge, *B* is the magnetic field, and m_e is the rest mass of the electron. The incredible sensitivity of the CRES technique is this ability to use a frequency measurement to deduce the energy of the electron [3].

The experiment consists of a rectangular waveguide with a U-shape turn to read frequencies from either end to be able to cancel out the Doppler shift. The rectangular waveguide is split on one side of the U shape to include a circular waveguide that exists as a decay volume for the ^{6}He as shown in Fig. 1.

The current phase of the project involves pumping ^{6}He gas into a decay volume via 25 ʐ≈ 1 mm-diameter holes. The decay volume is ~ 10 cm in length and 1.156 cm in diameter. This radius propagates frequencies between 18-24 GHz well. The magnetic field can be varied from 0.5-7.0 T to shift our 18 - 24 GHz window to different energies and scan the whole β spectrum. The decay volume also has a coil around it creating a magnetic trap. This setup allows ^{6}He atoms to freely move about within the decay volume. The emitted βs of the ^{6}He nuclei that are near the walls are lost, and because of an increasing

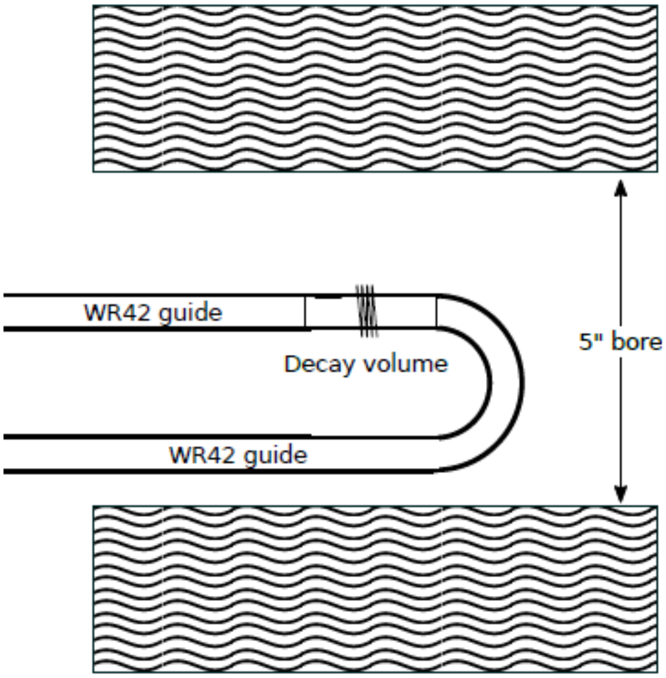

Fig. 1. Drawing of the U-shaped waveguide in the magnet.

cyclotron radius with higher energy; higher energy βs would be more likely to hit the wall, as show in Fig. 2, resulting a bias toward lower energies in our energy spectrum. With this issue it is still expected to get the uncertainty of $b_{\mathrm{Fierz}}<10^{-3}$ [4].

The next phase of the experiment involves the implementation of an ion trap to radially confine the ^{6}He ions and eliminate wall collisions, effectively bringing our expected precision to 10^{-4}. This however requires more modifications to the experimental setup as we would no longer be able to pump in neutral ^{6}He into holes within the trap. The waveguide will need to be modified to have a hole that allows

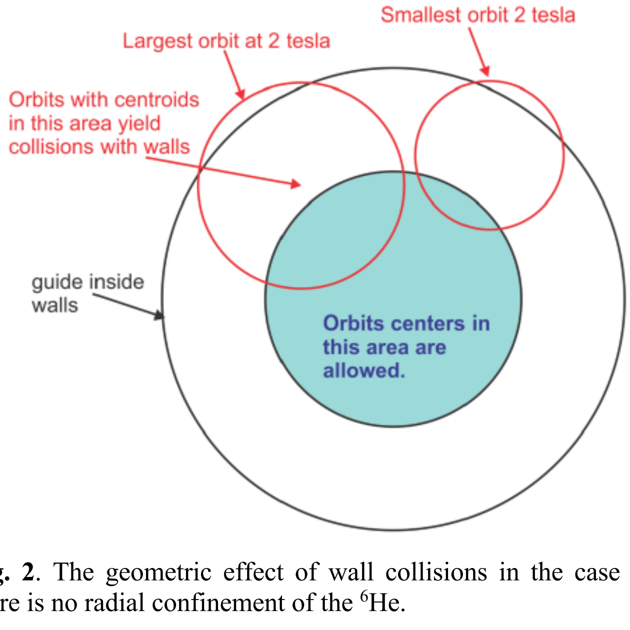

Fig. 2. The geometric effect of wall collisions in the case where there is no radial confinement of the ^{6}He.

a beam of ^{6}He ions to flow in and to the Penning trap. The issue here is making sure that the waveguide retains its ability to propagate the frequencies with minimal loss. Our goal is to remain below 1 dB of loss throughout the waveguide.

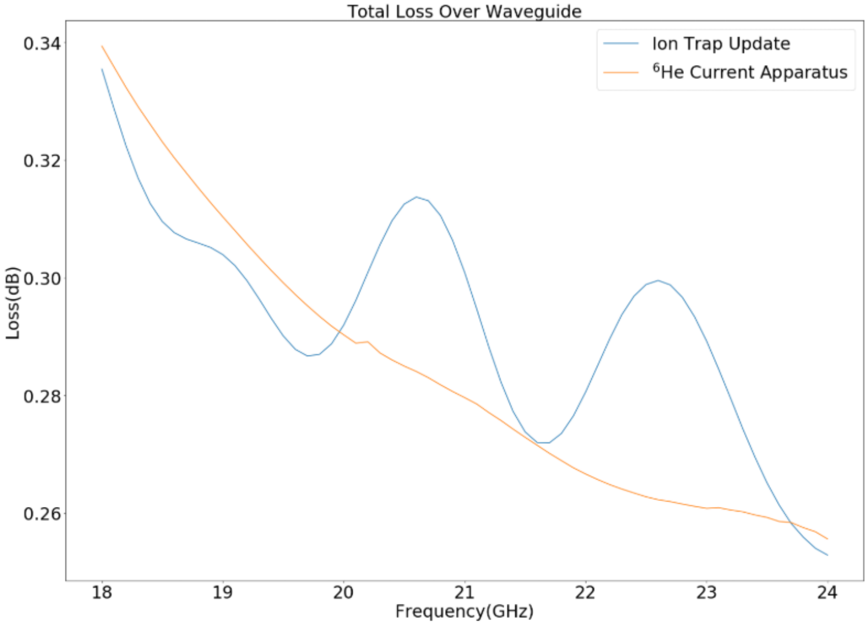

Fig. 3. The loss over the waveguide from the decay volume to the data collection waveport.

Using ANSYS' high-frequency structure simulator, HFSS, it was possible to create the waveguide within the environment and analyze the propagation of a given frequency band between two wave ports. Initially we attempted to minimize losses by testing different mesh densities over a hole cut into the waveguide. The results showed that there was no discernible difference between the different mesh densities. Next it was necessary to check how the loss over the Penning trap would differ from the loss of the current decay volume. Though the trap would not have the 25 holes for helium injection, it does contain Kapton spacers between each electrode. It was shown that the Kapton adds a small amount of loss to the system. Overall the system needs to remain below 1 dB of loss for the experiment to be viable, and though the loss of the system increased, we are still well below this threshold with the expected changes to the apparatus as shown in Fig. 3. From here, to update the experiment the Penning trap must be developed, along with an electron cyclotron resonance source and a radio-frequency quadrupole cooler buncher.

[1] J.D. Jackson, S.B. Treiman, and H.W. Wyld Jr, Nucl. Phys. **4**, 206 (1957).
[2] D.M. Asner *et al.*, Phys. Rev. Lett. **114**, 162501 (2015).
[3] A.A. Esfahani *et al.*, J. Phys. G **44**, 054004 (2017).
[4] A. García, private communication.

Measurement of the half-life of the *T=1/2* mirror decay of ^{29}P

P.D. Shidling, V.E. Iacob, V.S. Kolhinen, D. Melconian, M. Nasser, A. Ozmetin, and B. Schroeder

The consistency of *ft* values of pure Fermi transitions are well-known to demonstrate the conserved vector current and to determine the value of V_{ud} for probing the standard model via a test of the unitarity of the CKM matrix. Mixed Fermi and Gamow-Teller transitions between $T = 1/2$ mirror nuclei are being studied as a complementary and independent measure of V_{ud}. As these decays are mediated by both the vector and axial-vector component of the weak interaction, in addition to the *ft* value, (any) one of the angular-correlation coefficients must be measured to determine V_{ud}. The mirror decay of ^{29}P is one of five candidates of $T=1/2$ mirror nuclei which has been used as an independent measure of V_{ud} [1]. The relatively large uncertainty of its contribution is dominated by the precision of ρ, the ratio of Gamow-Teller to Fermi matrix elements, which was obtained from a ±12% measurement of the beta asymmetry parameter, A_β [2]. The ft value [3] is known much better, to ±0.4%, with the largest contribution to its uncertainty being the lifetime of the decay: 4.142(15) s [4]. The aim of the present work is to improve the lifetime of ^{29}P so that it no longer dominates the uncertainty in the deduced ft value.

The half-life of ^{29}P was measured using the Momentum Achromatic Recoil Spectrometer (MARS) and a fast-tape-transport system equipped with a 4π continuous-gas-flow proportional counter. The secondary beam of ^{29}P was produced via the $p(^{30}\mathrm{Si}, 2n)$ ^{29}P reaction in inverse kinematics at a primary beam energy of 24 MeV/u. MARS was used to produce a secondary beam of ^{29}P with a purity of 99.8%, with impurity levels of ^{27}Si and ^{25}Al both at the 0.1% level. The total data set was divided into several runs with different settings of the experimental parameters: bias voltage, discriminator threshold and dominant dead-times. The initial activity of ^{29}P for each cycle was in the range of 4000 − 9000 cps. All runs were composed of 100 − 200 cycles with $\approx 4\times10^6$ counts in each run. In addition, a background measurement was performed where all of the experimental conditions were the same as for normal data taking except that the tape motion was disabled.

The selection of data for final analysis was made according to following criteria. First, cycles with too few counts – less than 5000 – were rejected. Second, the number of βs recorded in each cycle was compared to the corresponding number of heavy ions recorded in the scintillator at the exit of MARS. If their ratio was abnormally low, it meant that the tape did not stop with the activity positioned correctly within the 4π proportional gas counter. In that case, the cycle was rejected. The decay data from accepted cycles are currently being analyzed by summed analysis method. In this analysis method, the first step is to correct the measured decay spectrum in each cycle channel-by-channel for deadtime, based on the measured rate in each channel. Next, the cycles of a given run are summed into two decay curves, one for each imposed dominant deadtime. Finally, these spectra are fitted to function composed of an exponential and flat background. Fig. 1 show a typical deadtime-corrected decay curve for one cycle.

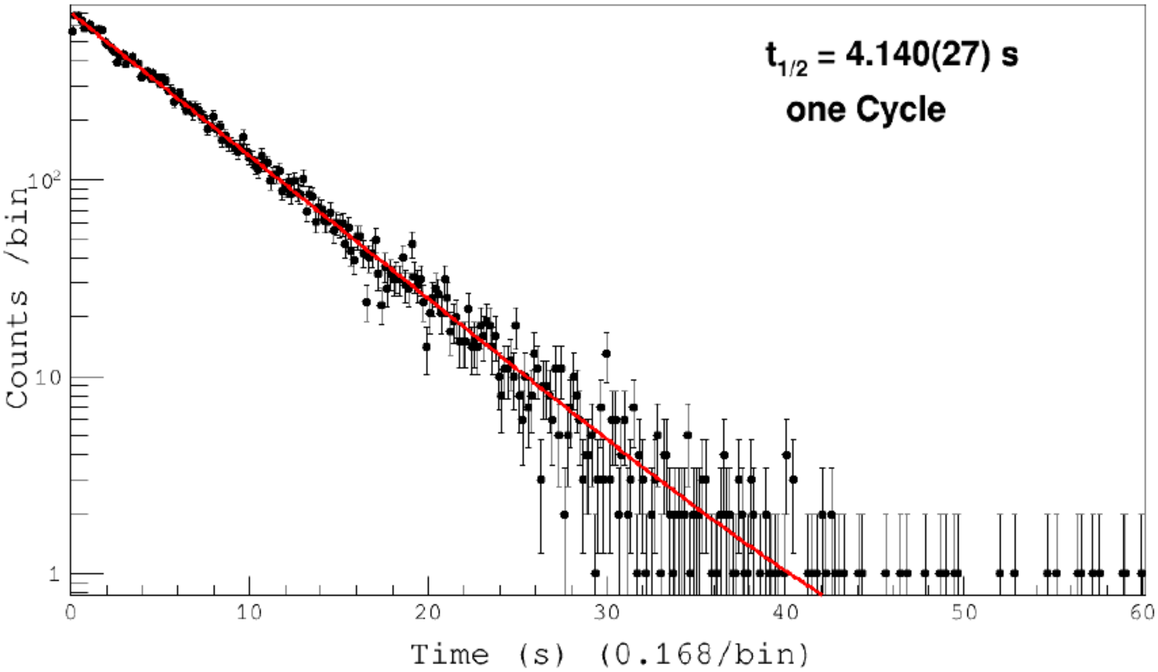

Fig. 1. Typical deadtime-corrected β-decay curve for ^{29}P from one cycle. The reduced χ^2 of the fit is 1.02.

The preliminary analysis indicates that the statistical uncertainty is at the 0.015% level. The analysis is in progress to extract the final value of the half-life along with an associated systematic error budget.

[1] O. Naviliat-Cuncic and N. Severijns, Phys. Rev. Lett. **102**, 142302 (2009).
[2] G.S. Masson and P.A. Quin, Phys. Rev. C **42**, 1110 (1990).
[3] N. Severijns, M. Tandecki, T. Phalet, and I.S. Towner, Phys. Rev. C **78**, 055501 (2008).
[4] M.S. Basunia, Nucl. Data Sheets **113**, 909 (2012).

Update on the TRIUMF Neutral Atom Trap (TRINAT) experiment

D. Melconian

The TRINAT collaboration continues to utilize neutral atom trapping and optical pumping techniques on short-lived β-decaying isotopes to probe the electroweak sector of the standard model.

Our analysis of the Fierz interference parameter [1] is ongoing. Our GEANT4 Monte Carlo for analysis is fully developed, however the computational time needed is exorbitant and cannot be used to fully analyze the data directly. We have therefore developed a relatively simple Monte Carlo with minimal overhead that is significantly faster (hours versus weeks). To minimize the bias this less-detailed simulation necessarily introduces, we have generated four separate response functions as a function of β energy in GEANT4: one for each of the upper and lower telescopes, both for each polarization state separately. We are about to benchmark our 'simple' MC to the full GEANT4 simulation and confirm that small variations of new physics around the best fit of the data using the standard model (*i.e.* $-0.25 \leq C_S \leq 0.25$) are the same for both MCs. Once this is confirmed, the final analysis should proceed quickly.

We also continue to analyze data taken from the decay of ^{92}Rb, which dominates the neutrino energy spectrum from reactors in the 5–7 MeV range where there is currently an unexplained excess of events [2]. By measuring the momenta of the charged recoil and β, and knowing the decay occurred from rest at the trap centre, we are able to directly reconstruct β-ν correlation parameter. Although $a_{\beta\nu}$ is naïvely expected to be ≈1, two separate approaches of analyzing of our data indicate $a_{\beta\nu} = 0.4(1)$ [3]. This result constains the difficult-to-calculate matrix elemnts of ^{92}Rb's first-forbidden $0^- \rightarrow 0^+$ ground-state to ground-state decay. This analysis did not utilize the information of the position-sensitive Si-strip β detectors; along with a higher-resolution spatial calibration of our MCP recoil-detector, our momentum analysis will have greater resolution. In parallel with these improvements, we are developing GEANT4 simulations of this decay so that we can reconstruct the Q value of the decay and better isolate the ground-state transition.

Looking forward, our next beamtime at TRIUMF is likely to be a search for time-reversal violation (TRV) in the radiative β decay of ^{45}K. When parity violation was discovered in the late 1950's in beta and muon decay, people immediately proposed experiments testing time-reversal symmetry, hoping its violation might also be large. Any scalar triple product of momenta $\vec{p}_1 \cdot \vec{p}_2 \times \vec{p}_3$ flips sign with the sign of time: if its value does not average to zero, that indicates a violation of time-reversal symmetry. However, this scalar trivially vanishes from momentum conservation if there are only three momenta in the final state. To nontrivially test time-reversal symmetry without involving spin, we must look for a correlation of three momenta from a four-momentum final state. Our sensitivity to TRV is through a unique observable using our trap: the triple-vector correlation $\vec{p}_\beta \cdot \vec{p}_\nu \times \vec{p}_\gamma$, where we deduce $\vec{p}_\nu$ from the recoild momentum. The geometry of the proposed system is shown in Fig. 1, as well as preliminary GEANT4 simulations of our sensitivity to c_5, the parameter that is non-zero if TRV exists [4]. Since this observable does not involve spin, it is actually more directly sensitive to certain sources of TRV than electric dipole moments. This 3-momentum correlation has never been measured in the first generation of particles, so could still be large.

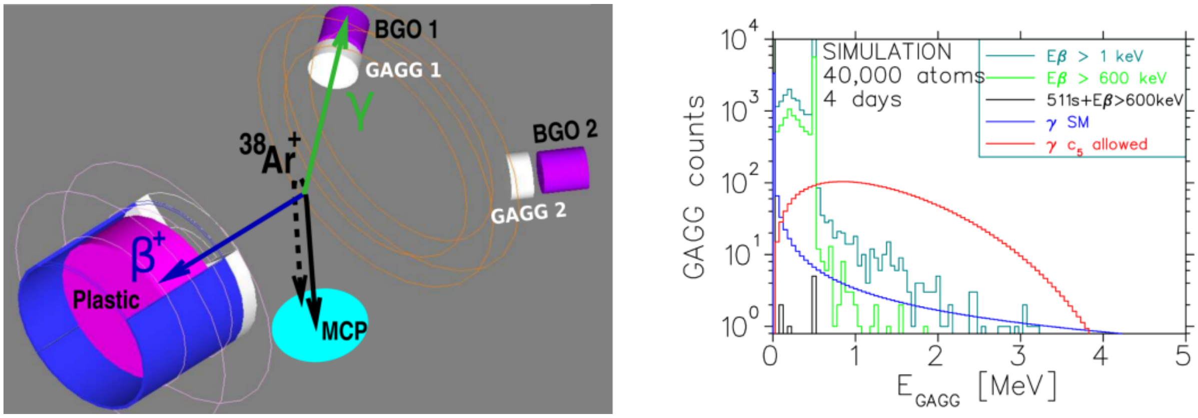

Fig. 1. The TRV experiment with TRINAT. Left: geometry of the detectors used to observe the triple-correlation. Right: GEANT4 simulation of the signal in the BG0 detector showing the sensitivity of the experiment.

[1] D. Melconian, *Progress in Research*, Cyclotron Institute, Texas A&M University (2018-2019), p. I-27.

[2] D.A. Dwyer and T.J. Langford, Phys. Rev. Lett. **114**, 012502 (2015).

[3] J.C. McNeil, M.Sc. Thesis, University of British Columbia, 2019.

[4] S. Garnder and D. He, Phys. Rev. D **87**, 116012 (2013).

Decay properties of ^{22}Ne + α resonances with TIARA and MDM spectrometer

S. Ota,[1] G.A. Christian,[1] E.A. Bennett,[1] S. Dede,[1] D.T. Doherty,[2] H. Jayatissa,[1]
J. Hooker,[1] C. Hunt,[1] C. Magana,[1] G. Rogachev,[1] A. Saastamoinen,[1] S. Upadhyayula,[1]
W.N. Catford,[2] S. Hallam,[2] G. Lotay,[2] M. Mouhkaddam,[2] J.A. Tostevin,[2] and R. Wilkinson[2]
[1]*Cyclotron Institute, Texas A&M University, College Station, Texas 77843*
[2]*University of Surrey, Guildford GU2 5XH, United Kingdom*

In core He burning and C-shell burning of massive stars (> 8 solar mass), the ^{22}Ne(α,n)^{25}Mg reaction is considered to be a dominant neutron source for the weak s-process during which nuclides in the A=60-90 mass range are produced [1]. The reaction also plays a secondary role in the neutron production for the main s-process in He-low and intermediate mass asymptotic giant branch (AGB) stars during which nuclides in the A~90-209 are produced [1]. While various attempts to experimentally determine the rate for this reaction at the *s* process temperatures (T = 0.2-0.3 GK, equivalent to $E_{\alpha,\mathrm{lab}}$ = 400 – 900 keV, namely, E_x=10.9-11.5 MeV in the excitation energy of ^{26}Mg) have been made by direct (^{22}Ne+^{4}He or α+^{22}Ne) measurements [e.g., 2], they have been hindered by the small cross sections due to the Coulomb barrier. Thus the resonance at $E_{\alpha,\mathrm{lab}}$ ~ 830 keV (E_x ~ 11.32 MeV) is the lowest resonance identified with this method. Although indirect methods such as ^{26}Mg(α,α')^{26}Mg, ^{22}Ne(^{6}Li,*d*)^{26}Mg, ^{25}Mg(n,γ), ^{26}Mg(γ,γ') reactions [e.g., 3-7] have been used to identify lower-energy resonances, there remain many uncertainties in spin-parity (J^π), partial widths of respective decay channels (Γ_γ, Γ_n, and Γ_α) of these resonances. Since past studies identified particularly two resonances, E_x=11.32 and 11.17 MeV above neutron separation energy (S_n=11.093 MeV), have the largest impact on the neutron production during the s-process [e.g., 7], unambiguously determining J^π, Γ_γ, Γ_n, and Γ_α for these resonances is important.

To determine these resonance parameters, we performed an experiment using the ^{6}Li(^{22}Ne,^{26}Mg)d α-transfer reaction with a large Si detector array, TIARA [8], and HPGe detector array, and the MDM spectrometer [9,10]. Because both the α and ^{22}Ne have ground states with $J^\pi=0^+$, the α-transfer reaction preferentially populates natural parity states in ^{26}Mg. This helps us selectively study the resonance parameters of astrophysically relevant natural parity states in ^{26}Mg, and J^π of these resonance states can be determined by measuring the angular distribution of deuterons. Furthermore, the inverse kinematics approach enables us to determine Γ_n / Γ_γ by direct measurements of the ratio of produced ^{25}Mg (^{26}Mg*$\rightarrow$^{25}Mg + n) and ^{26}Mg (^{26}Mg*$\rightarrow$^{26}Mg + γ) ions at the resonance states. Determining Γ_n / Γ_γ is important to understand the neutron yield of these resonances. The ^{22}Ne(α,γ)^{26}Mg reaction competes with the ^{22}Ne(α,n)^{25}Mg reaction at E_x=11.32 and 11.17 MeV resonances and therefore may significantly suppress neutron production for the s-process.

The experiment was performed at Cave 3 using a 7 MeV/u ^{22}Ne beam from the K150 cyclotron. ^{6}Li-enriched (95%) lithium fluoride (LiF) targets with the thickness of 30 μg/cm^2 on a graphite backing foil (10 μg/cm^2) were prepared and bombarded with the beam at an intensity of about 3 nA. Details of the experiment can be found in [11].

The ^{26}Mg excitation spectrum measured in the present experiment is shown in Fig. 1 [12]. It is evident that the resonance of our interest (E_x=11.32 MeV) is clearly observed and we concluded the branching ratio of Γ_n / Γ_γ = 1.14±0.26 from the ratio of ^{25}Mg/^{26}Mg ions observed by the MDM at the resonance energy after the efficiency correction. This result indicates Γ_n / Γ_γ is largely overestimated in past direct measurements as discussed below, which performed the (α,n) and (α,γ) measurements independently. Since the (α,γ) resonance of the resonance is relatively well constrained as 37±4 μeV [13,14], whereas (α,n) strength has large discrepancies among the past measurements, (α,n) strength was determined by multiplying the (α,γ) strength with the Γ_n / Γ_γ obtained in the present work. The obtained (α,n) strength is thus 42±11 μeV, which is much smaller than the past measurements (inflated weighted average of 140±30 eV [7]). The (α,γ) and (α,n) strengths of the E_x=11.17 MeV resonance are estimated from the Γ_α determined by [15] with the branching ratio (Γ_n / Γ_γ=0.2-0.6) and the J^π (2^+) from [6]. Fig. 2 shows the final stellar reaction rates (as a ratio to ones by Longland *et al.* [7]) as a function of stellar temperature. It is clearly seen that the obtained new reaction rates are about 3 times lower than the values conventionally used in the past nuclear astrophysics studies in the s-process temperature range.

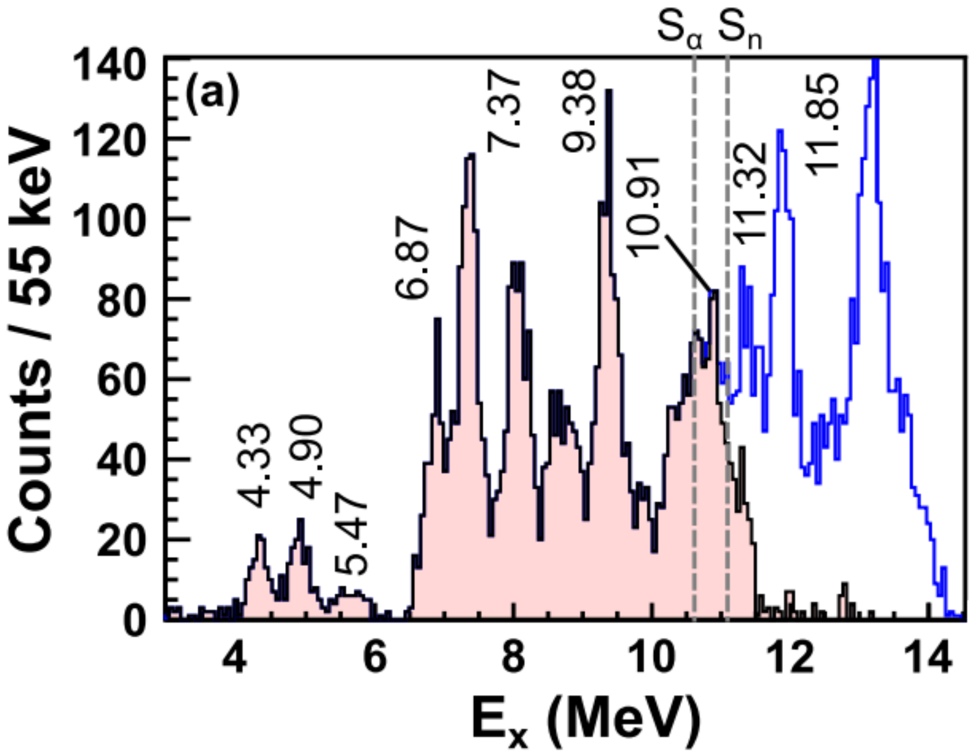

Fig. 1. ^{26}Mg excitation energy spectrum (red shadow: contribution from ^{22}Ne(^{6}Li,d)^{26}Mg, blue: sum of contributions from ^{22}Ne(^{6}Li,d)^{26}Mg and ^{22}Ne(^{6}Li,d+n)^{25}Mg). E_x=11.32 MeV resonance peak is distinct in both spectra.

Currently we are evaluating effects of our new results on s-process chemical abundances, and the results will be published soon.

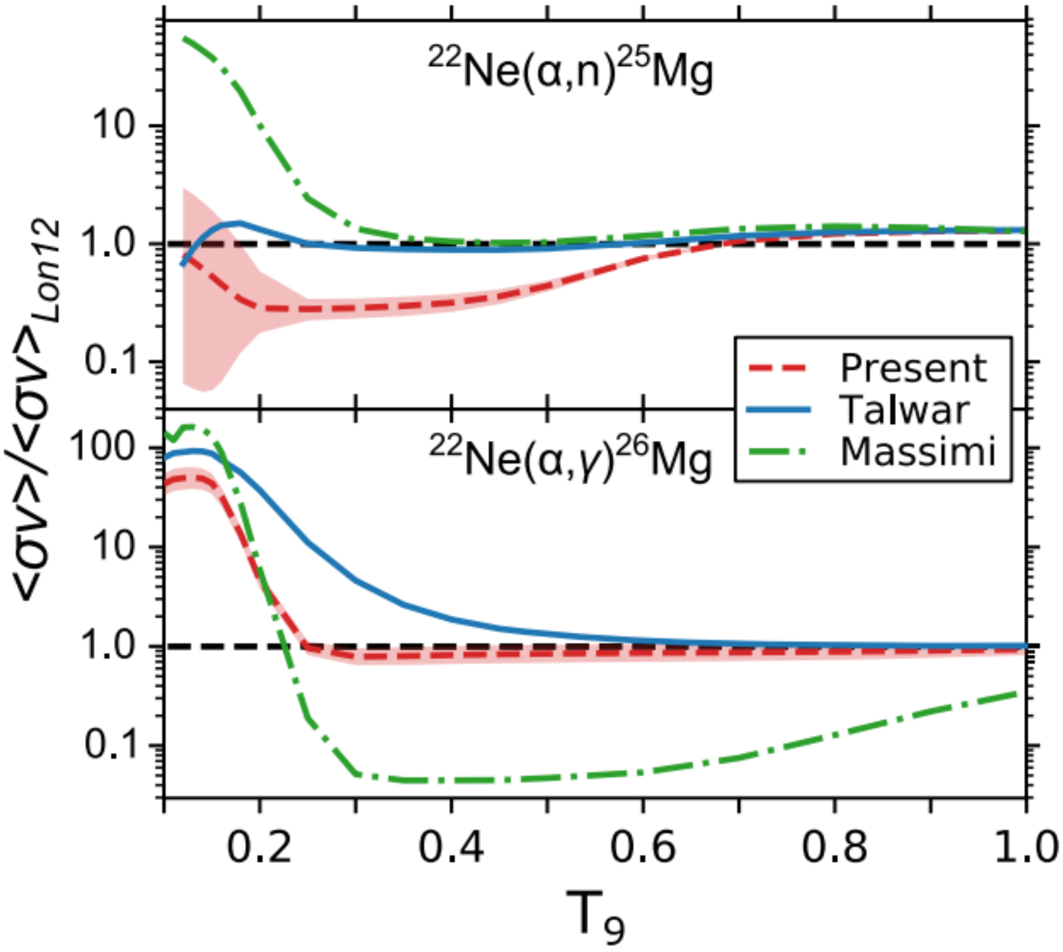

Fig. 2. Ratios of stellar reaction rates to Longland *et al.* [7] for $^{22}Ne(a,n)^{25}Mg$ (top) and $^{22}Ne(a,g)^{26}Mg$ (bottom) reactions as a function of temperature (in unit of GK).

[1] F. Kappeler, Prog. Part. Nucl. Phys. **43**, 419 (1999).
[2] M. Jaeger *et al.*, Phys. Rev. Lett. **87**, 20 (2001).
[3] P. Adsley *et al.*, Phys. Rev. C **96**, 055802 (2017).
[4] U. Giesen, J.D. King *et al.*, Nucl. Phys. **A561**, 95 (1993).
[5] R. Talwar *et al.*, Phys. Rev. C **93**, 055803 (2016).
[6] C. Massimi *et al.*, Phys. Lett. B **768**, 1 (2017).
[7] R. Longland *et al.*, Phys. Rev. C **80**, 055803 (2009).
[8] M. Labiche *et al.*, Nucl. Instrum. Methods Phys. Res. **A614**, 439 (2010).
[9] D.M. Pringle *et al.*, Nucl. Instrum. Methods Phys. Res. **A245**, 230 (1986).
[10] A. Spiridon *et al.*, Nucl. Instrum. Methods Phys. Res. **B376**, 364 (2016).
[11] S. Ota *et al.*, *Progress in Research*, Cyclotron Institute, Texas A&M University (2018-2019), p. I-29.

[12] S. Ota *et al.*, Phys. Let. B **802**, 135256 (2020).
[13] K. Wolke *et al.*, Z. Phys. A **334**, 491 (1989).
[14] S. Hunt *et al.*, Phys. Rev. C **99**, 045804 (2019).
[15] H. Jayatissa *et al.*, Phys. Lett. B **802**, 135267 (2020).

Shell structure and evolution through spectroscopy of ^{11}Be

M. Roosa, G. Christian, G. Rogachev, S. Ahn, E. Bennett, J. Bishop, S. Dede, C. Hunt, H. Jayatissa,
E. Koshchiy, R. Malecek, S. Ota, C. Parker, D. Scriven, and S. Upadhyayula

As the canonical example of shell-breaking in a neutron-rich nucleus ^{11}Be has been a focus for *ab-initio* calculations [1]. The largest component of its ground state, $\nu 1s_{1/2}$, is an inversion from the naive shell model's prediction and lacks a centrifugal barrier, producing ^{11}Be's famous one neutron halo. These studies will benefit from detailed spectroscopic information of ^{11}Be's low-lying states, some of which have been probed with neutron transfer studies [2]. We intend to provide a complementary measurement to neutron transfer studies with the proton pickup reaction (d, ^{3}He). Proton removal from ^{12}B will selectively populate p-wave states, making us particularly sensitive to the excited and unbound states of ^{11}Be.

Because the ^{11}Be system is well studied, this experiment will also help to establish the validity of using an Active Target Time Projection Chamber (AT-TPC) for transfer reaction studies [3]. We will extract differential cross sections from ^{12}B(d,^{3}He)^{11}Be in inverse kinematics to determine the spectroscopic factors of, and thus p-wave contributions to, low-lying states in ^{11}Be. Once the method is verified to work in the ^{11}Be case, we will extend it to the less-studied ^{12}Be system, where we will investigate occupancy of intruder shells in its low-lying states. The beam for this second experiment has already been developed – we expect 1.5×10^{4} pps of incident ^{13}B.

Data for the ^{11}Be study was taken during May of last year (2019) at the TAMU Cyclotron Institute using the K500 cyclotron and MARS [4]. Starting with a ^{14}C^{4+} beam at 30 MeV/u, we used the 1 mm ^{9}Be target to produce ~10^{5}pps of ^{12}B at 259.5 MeV/u ± 4%. This beam was delivered to the TexAT experimental set-up where it was impinged on a 200 torr deuterated methane target. TexAT includes a MicroMeGAS pad plane which provides full momentum reconstruction in the gas target, accompanied by

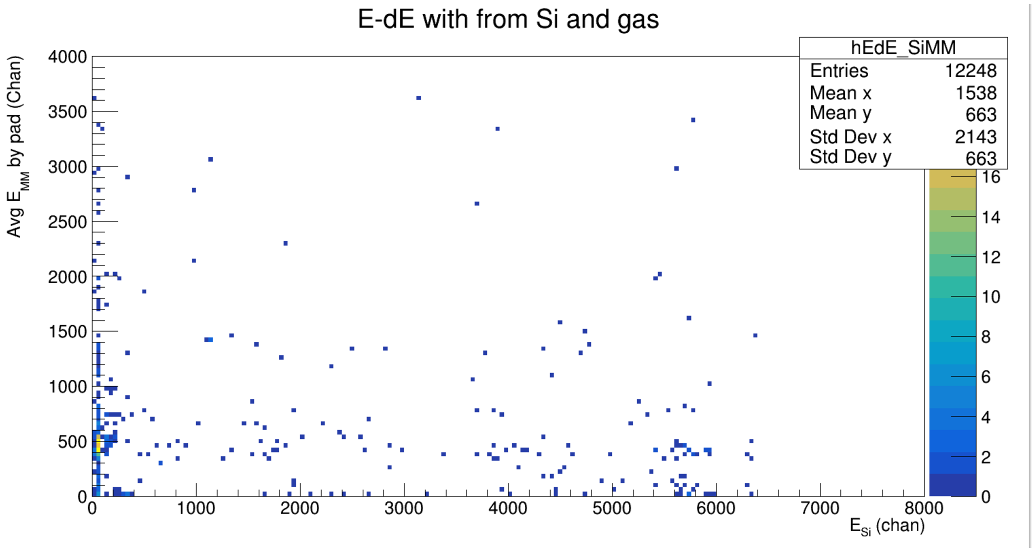

Fig. 1. Average energy loss in the gas(Arb) is plotted against remaining energy(Arb) measured in the silicon detectors for a small subset (<1%) of available data.

a wall of Si-CsI telescopes positioned perpendicular to the beam axis with a plastic scintillator at the 0° position relative to the beam axis. The solid-state detectors are used to identify particles, and thus events, that are not contained within the active volume.

At present, the project is in the analysis process; with focus on establishing reliable particle identification (PID). We optimistically plan to be able to identify protons, deutrons, tritons and alpha particles in addition to the ^{3}He of interest. We plan to use a traditional E-ΔE method (Fig. 1), in conjunction with a kinematics plot (Fig. 2) to separate the different particles.

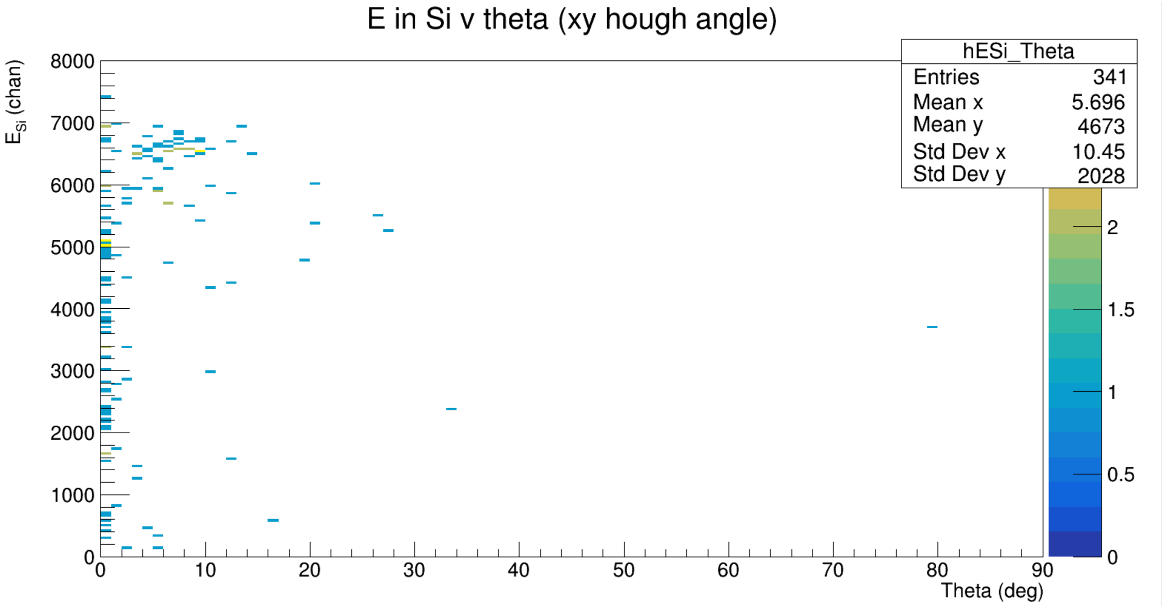

Fig. 2. Energy from the silicon detectors plotted against reconstructed angle for a small subset (<1%) of available data. ^{3}He will only be found with $\theta < 45^\circ$.

[1] A. Calci *et al.*, Phys. Rev. Lett. **117**, 242501 (2016).
[2] K.T. Schmitt *et al.*, Phys. Rev. Lett. **108**, 192701 (2012).
[3] E. Koshchiy *et al.*, arXiv:1906.07845.
[4] R.E. Tribble *et al.*, Nucl. Instrum. Methods Phys. Res. **A285**, 441 (1989).

Precise determination of the energy of the first excited state in ^{93}Nb

V. Horvat, J.C. Hardy, N. Nica, E.E. Tereshatov, and V.E. Iacob

The first excited state in ^{93}Nb is metastable, with a half-life of about 16 years. It decays to the ground state via an $M4$ transition. We are in the process of measuring the K-shell internal conversion coefficient (α_K) for this transition in order to test the validity of current methods of calculation. Compared to the transitions measured previously, the present one involves the lowest atomic number, the lowest transition energy, and the highest value of α_K.

The calculated α_K is sensitive to the transition energy E_t and its uncertainty is derived from the uncertainty of that energy. Therefore, it is important to know E_t as precisely as possible. Its presently adopted value is 30.77(20) keV, originating from an experiment preformed more than 40 years ago [1].

We are using x-ray/γ-ray spectroscopy to measure α_K. The same setup and technique are used to measure E_t at the same time. Nevertheless, this measurement is challenging for two main reasons: (*i*) because of the large value of α_K and the limited activity of the ^{93m}Nb source at hand, the gamma transition rate is very low. In order to overcome the limitations imposed by the counting statistics, the measurement has to be performed over a long period of time; and (*ii*) because the measurement takes a long time to complete, it has to be interrupted on a regular basis to determine the energy scale, monitor its stability, and make adjustments if necessary. We have acquired the spectrum of photons emitted from our ^{93m}Nb source for a total of 185 days.

The energy scale was determined using the sources of ^{241}Am and ^{109}Cd and finding centroids of the selected peaks in their spectra, with energies ranging from 11,870.8(21) eV (neptunium Ll x ray from the ^{241}Am source) [2] to 88,033.6(10) eV (^{109m}Ag γ ray following β decay of ^{109}Cd) [3]. Using this information, we determined the energy scale individually for every spectrum obtained in an uninterrupted measurement and then put all these spectra on a common energy scale by means of re-binning. We found no evidence of non-linearity and so all scale transformations were strictly linear. Because the slopes of individual energy scales were close to 10 eV per channel, we set the slope of the common energy scale to 10 eV per channel exactly. For the final analysis, individual re-binned spectra obtained under equivalent experimental conditions were combined into a single spectrum and the final energy scale was re-evaluated with increased scrutiny.

Four calibration points were used to establish an accurate energy scale in the region of interest. Two of these involved $K\alpha$ x rays of niobium (from the ^{93m}Nb source) and $K\alpha$ x rays of silver (from the ^{109}Cd source), whose weighted average energies are known with uncertainties of only ±0.27 eV and ±0.20 eV, respectively. Also, the corresponding peaks are well resolved from any other peaks, contain on the order of 10^8 events, and lie on a relatively low background, so that their centroids could be determined with uncertainty of only ±0.15 eV and ±0.07 eV, respectively.

The remaining two energy-calibration points were provided by the $K\alpha_1$ x ray of lanthanum and the ^{237}Np γ ray at 26.3 keV (both from the ^{241}Am source). Lanthanum was present in the ^{241}Am source as an impurity, in sufficient quantity to produce prominent K x-ray peaks in the spectrum by means of fluorescence. Peaks due to $K\alpha_1$ and $K\alpha_2$ x rays of lanthanum were well resolved from each other. However, a relatively small peak (accounting for less than 9% of the events) due to the ^{237}Np γ ray at 33.2

keV was not resolved from the lanthanum $K\alpha$ doublet, but it was properly taken into account by referring to an auxiliary measurement with a different ^{241}Am source that was not contaminated with lanthanum.

Energy of the measured ^{93m}Nb γ-ray peak was determined from its corresponding centroid and the scale based on the four calibration points referenced above. All relevant results from this analysis are given in Table I. The result we finally obtain for the ^{93m}Nb γ-ray energy (*i.e.*, the energy of the first excited state in ^{93}Nb) is

$$E_t = 30{,}760(5)\ \text{eV}. \qquad (1)$$

The quoted uncertainty includes statistical uncertainty of the corresponding peak centroid, as well as a minor contribution from uncertainty of the energy scale. Our result is in agreements with the currently accepted value, but its uncertainty is smaller by a factor of four.

Table 1. Calibration data and fit results used to determine the energy of the ^{93m}Nb γ ray. Symbols E, I, and C denote energy, intensity, and centroid, respectively. The centroids are given in channel units.

Quantity	Value	Source
$E(\text{Nb } K\alpha_1)$	16,615.16(33) eV	[2]
$E(\text{Nb } K\alpha_2)$	16,521.28(33) eV	[2]
$I(\text{Nb } K\alpha_2) / I(\text{Nb } K\alpha_1)$	0.5236 (26)	[4]
$E(\text{Nb } K\alpha)$	16,582.90(27) eV	deduced from above
$E(\text{Ag } K\alpha_1)$	22,162.917(30) eV	[2]
$E(\text{Ag } K\alpha_2)$	21,990.30(10) eV	[2]
$I(\text{Ag } K\alpha_2) / I(\text{Ag } K\alpha_1)$	0.5305 (27)	[4]
$E(\text{Ag } K\alpha)$	22,103.08(20) eV	deduced from above
$E(^{237}\text{Np } \gamma)$	26,344.6(2) eV	[5]
$E(\text{La } K\alpha_1)$	33,442.12(27) eV	[2]
$C(\text{Nb } K\alpha)$	1657.236(15)	fit
$C(\text{Ag } K\alpha)$	2209.771(7)	fit
$C(^{237}\text{Np } \gamma)$	2634.17(1)	fit
$C(\text{La } K\alpha_1)$	3344.33(3)	fit
$C(^{93m}\text{Nb } \gamma)$	3075.94(42)	fit
$E(^{93m}\text{Nb } \gamma)$	30,760(5) eV	deduced from above

Quality of the fit to the ^{93m}Nb γ-ray peak is illustrated in Fig. 1. This peak was fitted with a single Gaussian on a linear background, as shown. The centroid result was found to be stable against changes in the fitting region.

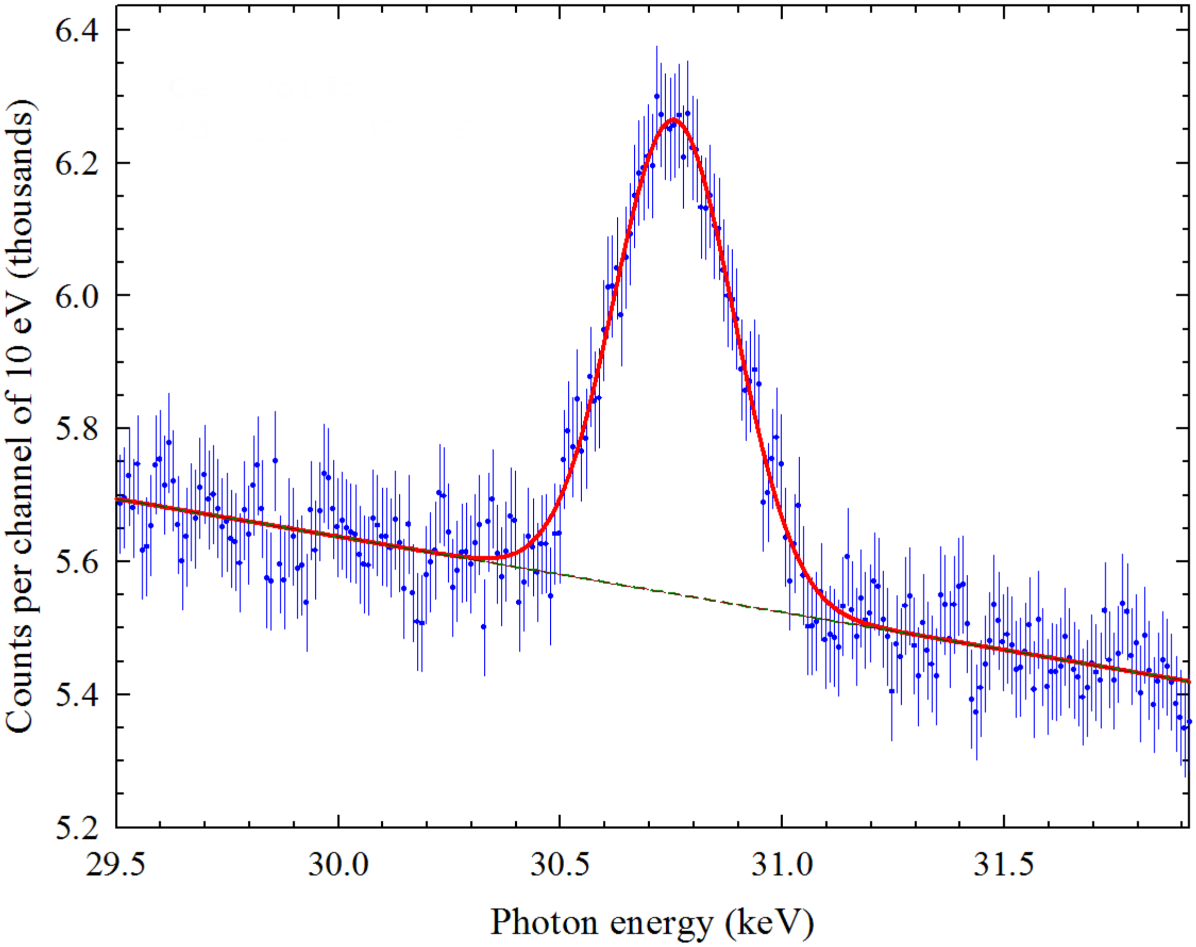

Fig. 1. Fit to the ^{93m}Nb γ-ray peak.

[1] J. Morel *et al.*, C.R. Acad. Sci. (Paris) B **284**, 223 (1977).

[2] R.D. Deslattes, E.G. Kessler Jr., P. Indelicato, L. de Billy, E. Lindroth, and J. Anton, Rev. Mod. Phys. **75**, 35 (2003).

[3] R.G. Helmer and C. van der Leun, Nucl. Instrum. Methods Phys. Res. **A450**, 35 (2000).

[4] E. Schönfeld and G. Rodloff, PTB Report: PTB-6.11-1999-1 (1999).

[5] C.M. Baglin, Nucl. Data Sheets **112**, 1163 (2011).

United States Nuclear Structure Data Program (USNDP) and Evaluated Nuclear Structure Data File (ENSDF) at Texas A&M University Evaluation Center of Cyclotron Institute

N. Nica and J.C. Hardy

Nuclear data evaluation fills a century-long chapter of nuclear science. A search in the *Nuclear Science Reference* (NSR) database maintained at the National Nuclear Data Center (https://www.nndc.bnl.gov/nsr/) on the author "M. Curie" produces a paper titled "*The Radioactive Constants as of 1930*" [1]. The introduction to this paper states that "*the need has arisen for the publication of special Tables of the Radioactive Constants*" and continues, "*This responsibility has been assumed by the International Radium Standards Commission chosen in Brussels in 1910 (...)*". Here we have the origin of what today is known as nuclear data evaluation.

Starting with the first generation of nuclear chemists and physicists, when measurements were already producing diverse and sometimes conflicting data, it became evident that assembling and reconciling the data from all across the published literature was a tedious and difficult task. Nevertheless, only after such a systematic analysis could the community arrive at recommended "practical standards," which could then be updated periodically to reflect the continuous improvements in knowledge and technology. Soon nuclear data evaluation became a specialized branch of research in its own right.

After the Second World War most of this activity was taken across the Atlantic and hosted by the United States Nuclear Structure Data Program (USNDP), which maintains the Evaluated Nuclear Structure Data File (ENSDF) database. While mostly undertaken by U.S. national laboratories, it has expanded to a relatively small number of university research labs, which has included the Texas A&M Cyclotron Institute since 2005. For more than a decade, the Texas A&M effort was financed by a contract with Brookhaven National Laboratory, but in 2017 it started to receive direct financing through the DOE Grant DE-FG03-93ER40773, "Cyclotron-based Nuclear Science". Moreover, since May 2017 Texas A&M Cyclotron Institute has been recognized and invested as an independent ENSDF Data Evaluation Center included within the Nuclear Structure and Decay Data international network.

Since 2005 we have completed and published the following full mass chain evaluations: the superheavy A=252 mass chain [2]; the very data-rich mid-mass chains, A=140 [3], A=141 [4], A=147 [5], and A=148 [6]; the relatively lighter chains, A=97 [7] and A=84 [8], the latter in a large international collaboration. In collaboration with B. Singh and a group of authors from McMaster University, Canada, we also published the A=77 [9], A=37 [10], A=36 [11], and A=34 [12] mass chains. At the beginning of 2016 another of our large mass chains, A=157, was published in Nuclear Data Sheets [13], followed by A=158 in 2017 [14], and the renewed full evaluation of A=140 in 2018 [15]. Finally, after its initial submission in September 2016, A=155 was corrected and updated after a long review process, and published after more than three years toward the end of 2019 [16]. In August 2019 we finalized and successfully first submitted A=147 which was our commitment for the USNDP data effort for FY 2019.

After the last decade crisis of new ENSDF evaluators, now it appears that the generational crisis moved to the ENSDF reviewers, which became critical in the last couple of years. This came by the retirement of many senior evaluators as well as by promoting an increased quality standard for the ENSDF published and on-line database data. The new standard consists of a pre-review process immediately after the first submission of a newly evaluated mass chain, which establishes whether the mass chain is admitted in the review pipe, followed by the review process itself, and by an editorial review before publication at the end. When combined with the large size mass chains as those in our responsibility, this generates typical intervals of more than three years spent by a mass chain in the publication pipe. This explains why the mass chains A=160, A=153, and A=147 submitted respectively in 2017, 2018, and 2019 are all in the publication process.

In September 2019 we started a new full evaluation for the mass chain A=141, covering all publications since January 2012. The mass chain consists of the following isobars, in total, 17 nuclei: Sb, Te, I, Xe, Cs, Ba, La, Ce, Pr, Nd, Pm, Sm, Eu, Gd, Tb, Dy, and Ho. Our bibliographical searches found that in the interval since January 2012, 206 papers have been published relating to this mass chain, of which 176 are primary references (most important). In all, 111 are experimental. This work is in progress.

[1] M. Curie, A. Debierne, A.S. Eve, H. Geiger, O. Hahn, S.C. Lind, S. Meyer, E. Rutherford, E. Schweidler, Rev. Mod. Phys. **3**, 427 (1931).
[2] N. Nica, Nucl. Data Sheets **106**, 813 (2005).
[3] N. Nica, Nucl. Data Sheets **108**, 1287 (2007).
[4] N. Nica, Nucl.Data Sheets **122**, 1 (2014).
[5] N. Nica, Nucl. Data Sheets **110**, 749 (2009).
[6] N. Nica, Nucl. Data Sheets **117**, 1 (2014).
[7] N. Nica, Nucl. Data Sheets **111**, 525 (2010).
[8] D. Abriola *et al.*, Nucl. Data Sheets **110**, 2815 (2009).
[9] B. Singh and N. Nica, Nucl. Data Sheets **113**, 1115 (2012).
[10] J. Cameron, J. Chen, B. Singh, and N. Nica, Nucl. Data Sheets **113**, 365 (2012).
[11] N. Nica, J. Cameron, and B. Singh, Nucl. Data Sheets **113**, 1 (2012).
[12] N. Nica and B. Singh, Nucl. Data Sheets **113**, 1563 (2012).
[13] N. Nica, Nucl.Data Sheets **132**, 1 (2016).
[14] N. Nica, Nucl.Data Sheets **142**, 1 (2017).
[15] N. Nica, Nucl.Data Sheets **154**, 1 (2018).
[16] N. Nica, Nucl.Data Sheets **160**, 1 (2019).

Beta-delayed charged-particle spectroscopy using TexAT

J. Bishop,[1] G.V. Rogachev,[1,2,3] S. Ahn,[1,2] E. Aboud,[1,2] M. Barbui,[1] P. Baron,[4] A. Bosh,[1,2] E. Delagnes,[4] J. Hooker,[1,2] C. Hunt,[1,2] H. Jayatissa,[1,2,*] E. Koshchiy,[1] R. Malecek,[5] S.T. Marley,[5] R. O'Dwyer,[1,2] E.C. Pollacco,[4] C. Pruitt,[6] B.T. Roeder,[1] A. Saastamoinen,[1] L.G. Sobotka,[6] and S. Upadhyayula[1,2,+]
[1]*Cyclotron Institute, Texas A&M University, College Station, Texas 77843,*
[2]*Department of Physics & Astronomy, Texas A&M University, College Station, Texas 77843,*
[3]*Nuclear Solutions Institute, Texas A&M University, College Station, Texas 77843,*
[4]*IRFU, CEA Université Paris-Saclay, F-91191, Gif-sur-Yvette, France*
[5]*Department of Physics and Astronomy, Louisiana State University, Baton Rouge, Louisiana 70803*
[6]*Department of Chemistry, Washington University, St. Louis, Missouri 63130,*
[*] Current address: Physics Division, Argonne National Laboratory, Argonne, Illinois 60439
[+] Current address: Department of Physics and Astronomy, University of Tennessee, Knoxville, Tennessee 37996

The experimental technique for measuring beta-delayed charged-particle spectroscopy in TexAT [1] – in this instance the ^{12}N→^{12}C*→3α reaction – has been previously detailed [2,3]. Analyzing data from this experiment, performed in March 2019, the efficacy of this technique has been proven.

To demonstrate the technique works well, a number of previously well-known observables were replicated [3]. Firstly, the '2p-mode' of the GET electronics allowed for a measurement of the time between the implant of the ^{12}N into TexAT and the subsequent decay branch to 3 α-particles. This allowed for a measurement of the ^{12}N half-life, shown in Fig. 1. From these data, a value of $t_{1/2}$ = 10.92 +/- 0.11 (stat.) +/- 0.11 (sys.) ms was obtained which is in good agreement with the literature value of 11.000 +/- 0.016 ms.

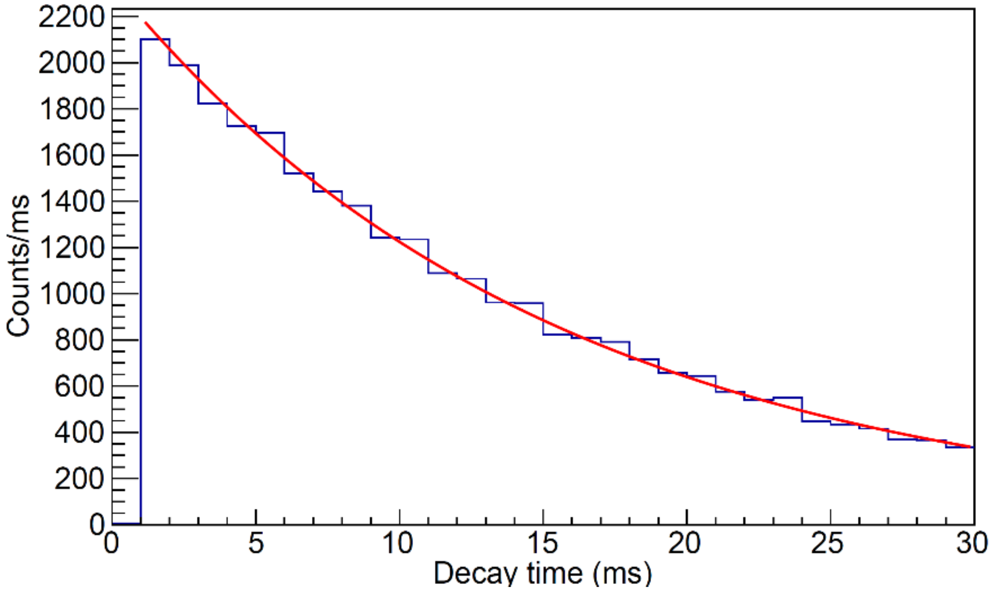

Fig. 1. Decay time spectrum for ^{12}N → ^{12}C(0_2^+). The fitted value is 10.92 +/- 0.11 (stat.) +/- 0.11 (sys.) ms.

Additionally, the beta-decay branching ratios to the excited-states in ^{12}C were also measured. As every implant was counted and the efficiency for measurement of α-unbound states was 100%, this allowed for a simple counting method to determine the branching ratio that doesn't rely on beta-particle or gamma-ray efficiencies as previous measurements have. The results in the current work are detailed in Table I below and can be seen to agree reasonably well with previously-measured values from KVI [4].

Table I. Branching ratios for ^{12}C states populated in ^{12}N β^+-decay from the present work and from KVI [4].

State	**KVI(%)**	**Current work(%)**
g.s.	96.17 ± 0.05	-
4.44 MeV – 2_1^+	1.90 ± 0.04	-
7.65 MeV – 0_2^+	1.44 ± 0.03	1.58 ± 0.01 (stat.) ± 0.11 (sys.)
7.3-16.3 MeV – 3α	2.11 ± 0.03	2.54 ± 0.01 (stat.) ± 0.18 (sys.)
0_2^+/3α	68 ± 2	62.1 ± 0.4 (stat.) ± 0.2 (sys.)

Finally, by reconstructing the events inside of TexAT and analyzing the energy partitions of the decays which proceed via the Hoyle state at 7.65 MeV in ^{12}C, the 'direct-decay mode' was measured whereby the ^{12}C* system decays directly into 3 α-particles without proceeding via the intermittent ^{8}Be ground state.

A GEANT4 simulation to model the direct-decay and sequential-decay modes was created and analyzed to generate a Dalitz plot which can differentiate the decay modes. The experimental results, in comparison for the GEANT4 simulations for both decay modes can be seen in Fig. 2 and the equivalency of the experimental data to the sequential decay mode is immediately visually apparent. A small branching ratio for the direct decay mode has been obtained and will be published in a soon-to-be-submitted article. This value allows for a benchmarking of the sensitivity available for future beta-delayed charged-particle spectroscopy studies with TexAT such as the planned ^{13}O experiment looking at 3α+p from ^{13}N.

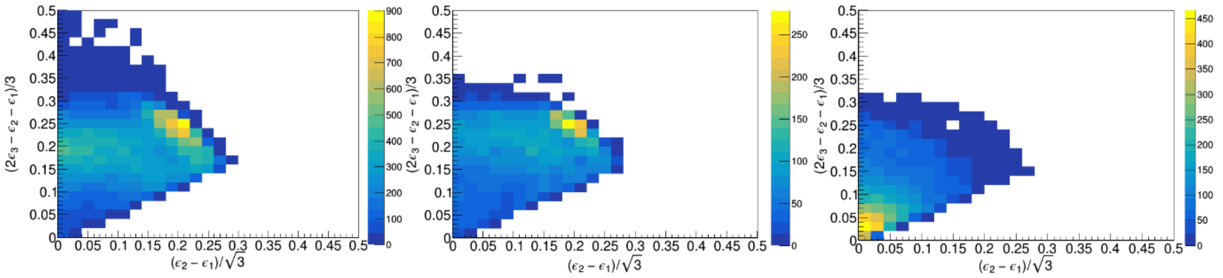

Fig. 2. Dalitz plots for the experimental data (left) against the GEANT4 simulated data for sequential-decay (middle) and direct-decay (right).

Additionally, this data set (in parallel with a previously-obtained Gammasphere data set [5] and an astrophysical argument) have been used to provide extremely strict limits on the existence of a potential Efimov state in ^{12}C at 7.458 MeV. These results will also be published soon.

In conclusion, the work performed this year demonstrated:

- The capability of TexAT to reconstruct 3 α-particle events at low gas pressure which allowed for the progression of an experiment to study ^{12}C(n,n$_2$)3α with TexAT at Ohio University (partially completed in March 2020).
- The possibility of using the beta-delayed charged-particle spectroscopy technique to study few-body systems in light nuclei – published in NIM [3].
- A measurement of the direct-decay Hoyle branching ratio and a prohibitive limit on the existence of an Efimov state in ^{12}C – to be published soon.

[1] E. Koshchiy *et al.*, Nucl. Instrum. Methods Phys. Res. **A957**, 163398 (2020).

[2] J. Bishop *et al.*, *Progress in Research*, Cyclotron Institute, Texas A&M University (2018-2019), p. I-45.

[3] J. Bishop *et al.*, Nucl. Instrum. Methods Phys. Res. **A964**, 163773 (2020).

[4] S. Hyldegaard *et al.*, Phys. Lett. B **678**, 459 (2009).

[5] M. Munch *et al.*, Phys. Rev. C **93**, 065803 (2016).

Experimental studies of nucleon-nucleus optical model potentials with rare isotope beams

A. Bosh,[1] G.V. Rogachev,[1] J. Holt,[1] S. Ahn,[1] Y. Koshchiy,[1] J. Bishop,[1] T. Whitehead,[1] L. Sobotka,[2]
E. Pollaco,[3] H. Jayatissa,[1] D. Scriven,[1] M. Roosa,[1] C. Parker,[1] E. Aboud,[1] and C. Hunt[1]
[1]*Cyclotron Institute, Texas A&M University, TAMU 3366, College Station, Texas 77843*
[2]*Department of Chemistry, Washington University in St. Louis, 1 Brookings Dr, St. Louis, Missouri 63130*
[3]*IRFU, CEA Saclay, Gif-sur-Yvette, France*

A better understanding of nucleon-nucleus interactions is crucial for nuclear reaction studies. The optical model potential (OMP) approximates the many-body interaction between a nucleon and a nucleus and allows one to describe the nucleon-nucleus scattering processes relatively well. The purely phenomenological approaches at establishing the optical model potentials is now being replaced by microscopic calculations. In particular, effective field theory is employed in [2] to establish the optical model potentials and dispersion theory is applied in [1,3].

The OMP has been calculated and is well studied for a plethora of stable nuclei. Naturally, much less experimental data is available for nucleon-nucleus OMPs for radioactive isotopes. Benchmarking the performance of microscopically-motivated OMPs with new experimental data on elastic scattering of nucleons (protons) off of radioactive nuclei is of paramount importance. We plan to use the Texas Active Target (TexAT) detector to perform these measurements [4].

Prior to running experiments, we have to study the best configuration of TexAT, i.e., silicon detectors, cesium iodide scintillation detectors, field cage, micromegas, etc. To accomplish testing the silicon detector parameters a versatile detector chamber was designed and built. We used the data collected from this chamber to determine which silicon detectors had the best resolution.

The first TexAT OMP related experiment was ^{14}O(p,p). A preliminary particle identification plot is shown in Fig. 1. A simulation of this experiment was performed and the analysis of the simulated data is currently underway to ensure the proper understanding of the information that must be extracted from the data collected in the experiment. During the experiment, the incoming beam energy was approximately 10 MeV/u of ^{14}O produced using the Momentum Achromat Recoil Separator (MARS). The active target consisted of methane gas at 200 Torr. To achieve an increased gain from the small proton signal, the thin Gas Electron Multipliers (GEMs) with a thickness of 50 μm were used. The analysis of this first test run is in progress. It has clear, however, that higher statistics run will be required and better angular resolution than the one TexAT can provide is highly desirable. Future OMP related experiments will be performed using high resolution TeBAT active target under development [5].

After the successful completion of the ^{14}O+p project with TeBAT we will move on to study isotopes of Ca: ^{48}Ca and ^{50}Ca.

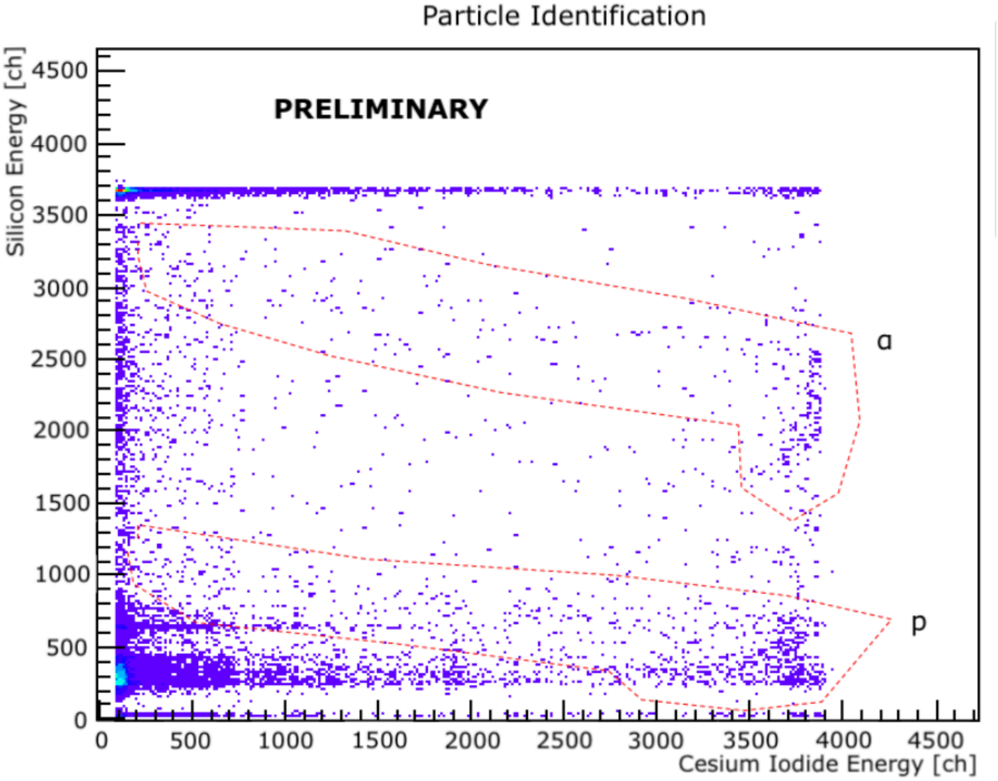

Fig. 1. Preliminary particle identification plot showing the energy deposited in the Si-CsI telescopes. There are two loci shown, representing alpha particles and protons. The shape of the loci is determined by signal saturation in CsI.

[1] W.H. Dickhoff and R.J. Charity, Prog. Part. Nuc. Phys. **105**, 252 (2019).

[2] T.R. Whitehead, Y. Lim, and J. W. Holt. Phys. Rev. C **100**, 014601 (2019).

[3] R.J. Charity, J.M. Mueller, L.G. Sobotka, and W.H. Dickhoff, Phys. Rev. C **76**, 044314 (2007).

[4] E. Koshchiy, G.V. Rogachev, E. Pollacco, S. Ahn, E. Uberseder, J. Hooker, J. Bishop, E. Aboud, M. Barbui, V.Z. Goldberg, C. Hunt, H. Jayatissa, C. Magana, R. O'Dwyer, B.T. Roeder, A. Saastamoinen, and S. Upadhyayula, Nucl. Instrum. Methods Phys. Res. **A957**, 163398 (2020).

[5] S. Ahn *et al.*, *Progress in Research*, Cycloton Institute, Texas A&M University (2019-2020), p. IV-118.

Experimental study of low-lying negative parity T=5 states in ^{48}Ca

S. Ahn,[1,2,3] G. Rogachev,[1] S. Upadhyayula,[1] M. Anastasiou,[4] S. Bedoor,[1] J.C. Blackmon,[5]
J. Browne,[2,6] C. Deibel,[5] A. Hood,[5] J. Hooker,[1] C. Hunt,[1] E. Koshchiy,[1] J. Lighthall,[5]
W.J. Ong,[2,6] N. Rijal,[4] D. Santiago-Gonzalez,[5] and I. Wiedenhover[4]
[1]*Cyclotron Institute, Texas A&M University, College Station, Texas*
[2]*National Superconducting Cyclotron Laboratory, Michigan State University, East Lansing, Michigan*
[3]*JINA-CEE, Michigan State University, East Lansing, Michigan*
[4]*Florida State University, Tallahassee, Florida*
[5]*Department of Physics & Astronomy, Louisiana State University, Baton Rouge, Louisiana*
[6]*Department of Physics & Astronomy, Michigan State University, East Lansing, Michigan*

A study of particle-hole excitation levels near closed shells provides important information on single-particle properties and on two-body interactions. Experimental information on these relatively simple excitations in neutron-rich nuclei provide good indications for models that describe structure of exotic nuclei [1]. Although the changes in nuclear structure near the doubly magic ^{4}He, ^{16}O, ^{40}Ca nuclei were extensively studied and are well known, information on charge-changing particle-hole excitations (T=5 negative parity states) in ^{48}Ca is not yet available. A recent study identified four low-lying negative parity states and suggested model-dependent tentative spin-parity assignments [2]. In order to establish the level scheme of the low-lying negative parity T=5 states in ^{48}Ca, which are isobaric analog states of the neutron-proton particle-hole excitations in ^{48}K, we performed an ANASEN (active target detector) [3] experiment of ^{47}K(*p,p*)^{47}K in inverse kinematics at NSCL using ReA3 reaccelerated beam of ^{47}K at energy of 4.6 MeV/u. By measuring the excitation function of the elastic scattering in the center of mass energy range from 1 MeV to 4.5 MeV, we expect to determine excitation energies, spin-parities and proton partial widths of T=5 states in ^{47}K using R-matrix analysis. The T=5 states are expected to show up in the excitation function as narrow resonances.

A schematic layout of the experimental setup is shown in Fig. 1. A 5 µm thick scintillator foil was installed on the upstream of the beamline to produce the first tag of the beam which is used for the Time-

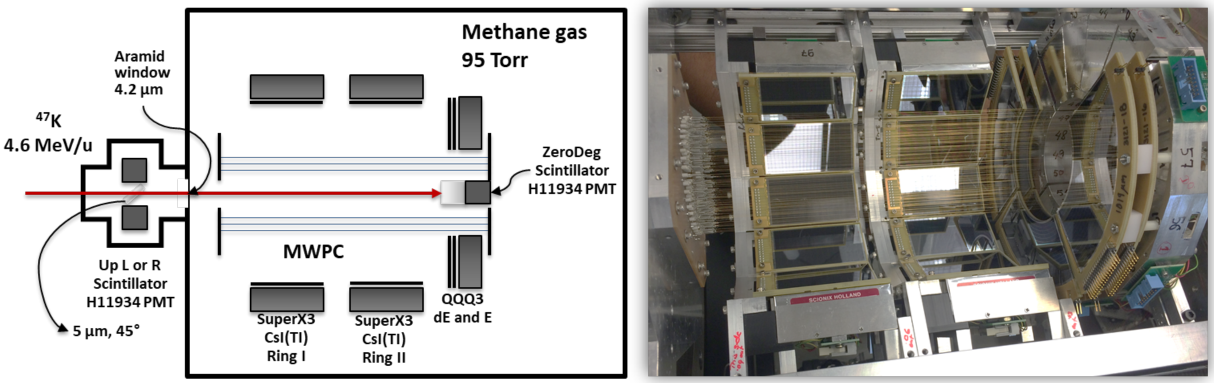

Fig. 1. Schematic drawing of ANASEN setup (left) and picture of detectors (right).

of-flight signal with either Silicon detector trigger signal or Zero-degree scintillator signal. A multi-wire proportional counter (MWPC) was installed around the beam axis to detect protons produced from elastic/inelastic scattering along the beam axis. SuperX3 and CsI(Tl) detectors were installed around the MWPC to measure final proton energies. Furthermore, QQQ3 dE and E detectors were set up at the downstream of the beam axis to cover forward focused protons. Finally, another thick scintillator was installed at zero degree of the downstream to produce the second tag of the beam.

The energy calibration of the QQQ3 dE and E detector was performed using ^{288}Th fission source under vacuum, which showed 5 strong alpha particle peaks with known energies from 5.18 MeV to 8.78 MeV. Fig. 2 shows an example of a calibrated energy spectrum on one QQQ3 dE detector and all strips of the QQQ3 were validated after the calibration. Another ^{288}Th fission source data was taken with the Methane gas of 60 Torr pressure. The source was located at 164 mm upstream from the QQQ3 dE

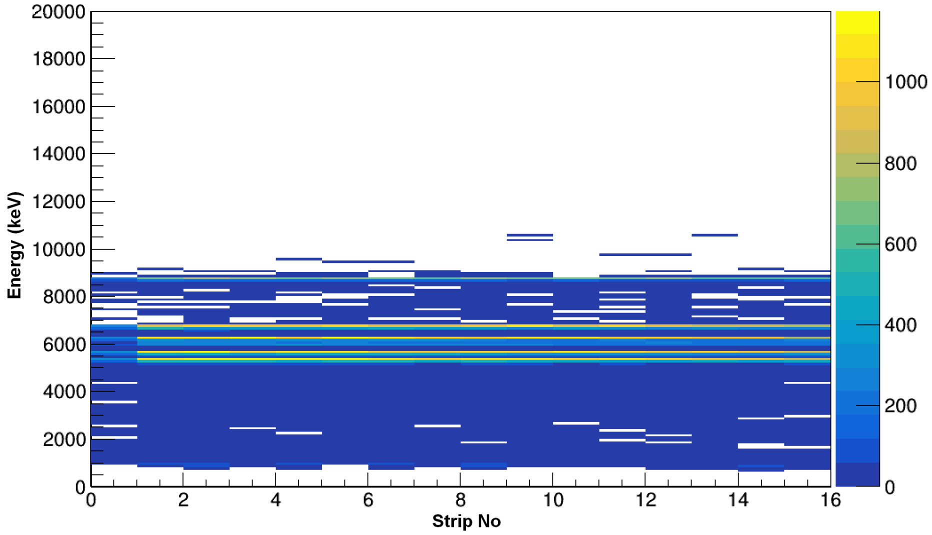

Fig. 2. QQQ3 Energy (keV) vs Front-side Strip No after the energy calibration.

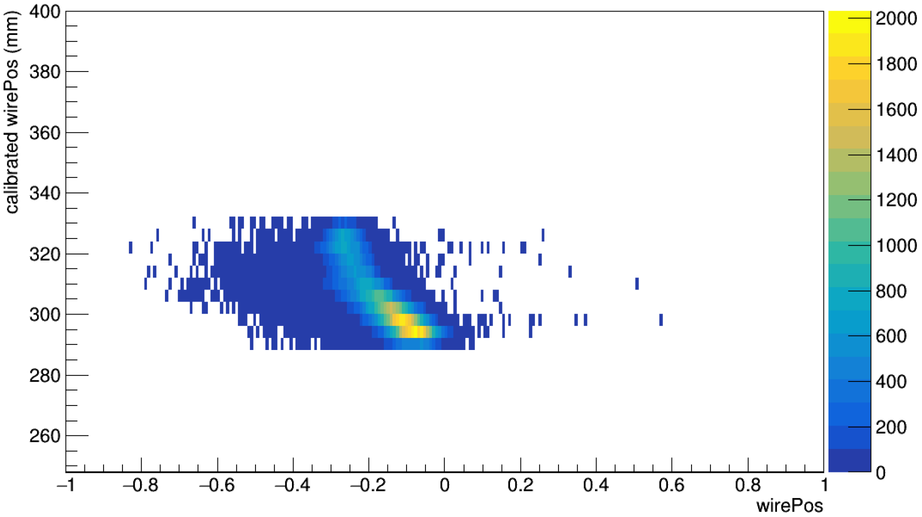

Fig. 3. Absolute wire hit position (mm) vs the ratio between wire-up and wire-down from the alpha source data.

detector (or 199 mm from the window). With the measured QQQ3 dE detector position of 363 mm from the window, each event in the source data provides an absolute hit position of wire from the source position and the Silicon detector hit position. Then, the wire hit position and the relative ratio between the upstream wire signal amplitude and the downstream wire signal amplitude could be calibrated as shown in Fig. 3. The data then fitted to the linear function to be used to find the wire hit position in the beam data.

After the position and energy calibration of the MWPC and QQQ3 dE and E detectors, we could plot the energy spectrum of the detectors from the beam data. The coincidence in time between the upstream scintillator and the QQQ3 detector was used to clean random background events. The particle identification (PID) plot was also very helpful to select high energy protons (using QQQ3 dE vs E) and all low energy protons (using QQQ3 dE vs wire E) as shown in Fig. 4. The energy of the high energy protons are used for further steps of data analysis.

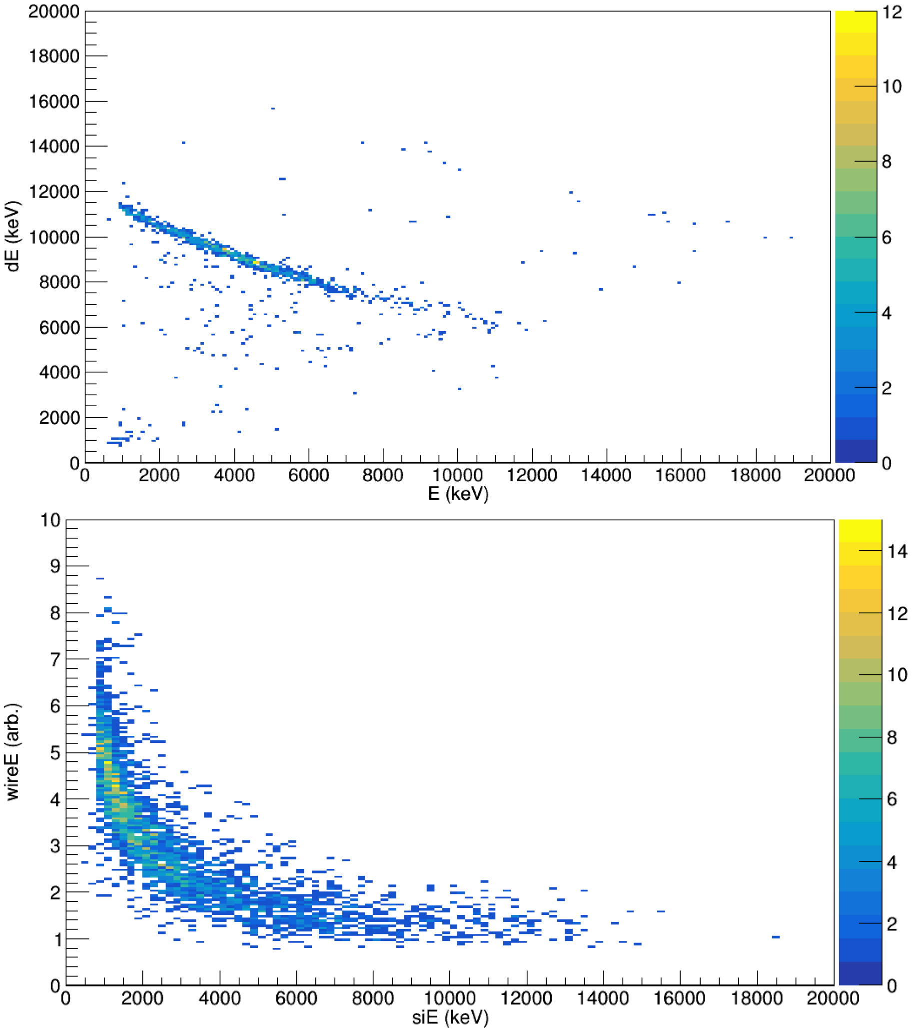

Fig. 4. QQQ3 PID plot for high energy protons gated on a QQQ3 Front Strip No. 6 (top) and PID from wire and QQQ3 to identify proton events gated on a QQQ3 Front Strip No. 6 (bottom).

With the clean proton events, the vertex of the reaction as well as angle of proton was calculated from the QQQ3 dE position and the wire hit position as shown in Fig. 5. Then, the center of mass (CoM) energy was calculated from the proton energy and angle shown in Fig. 6. Taking into account the beam energy loss in the gas after the window, target thickness at the vertex position, the effective solid angle of the QQQ3 detector as well as the total beam counts from the upstream scintillator scaler data, the excitation function will be calculated as a next step.

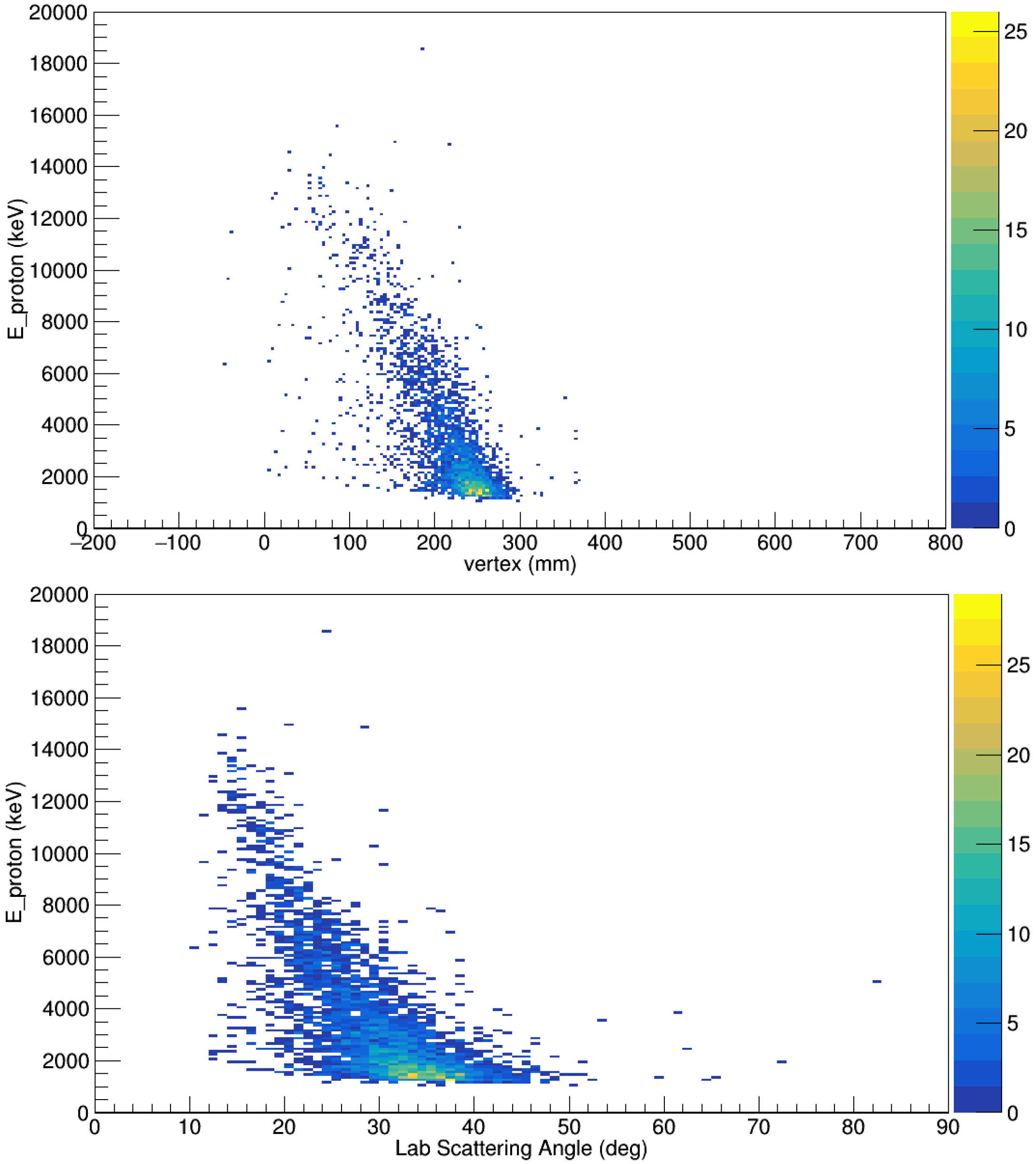

Fig. 5. Proton energy vs vertex position gated on a QQQ3 Front Strip No. 6 (top) and proton energy vs laboratory angle gated on a QQQ3 Front Strip No. 6 (bottom).

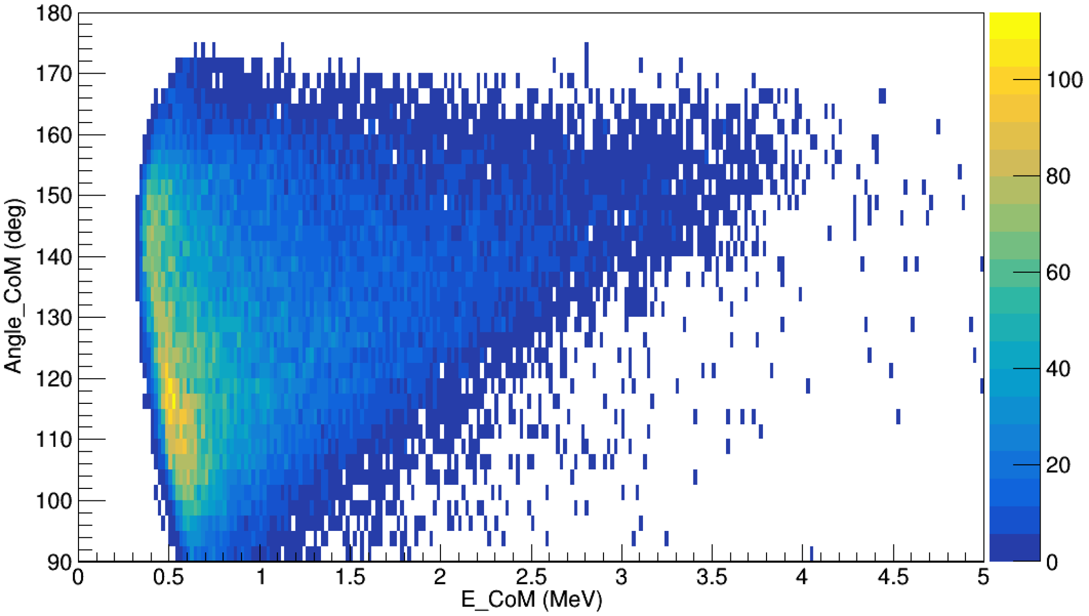

Fig. 6. Angle vs CoM energy from the angle and energy of protons.

In summary, in order to address excited states of the low-lying negative parity T=5 states in ^{48}Ca, we performed a ^{47}K(*p,p*)^{47}K reaction in inverse kinematics at NSCL using ReA3 reaccelerated beam of ^{47}K at energy of 4.6 MeV/u and the ANASEN detector system. By measuring the excitation function of the elastic, we expect to extract excitation energies, spin-parities and proton decay widths of ^{47}K. All of the calibration works are completed and examples of spectrums are shown. With additional steps, we will get a measured excitation function.

[1] T. Otsuka *et al.*, Phys. Rev. Lett. **95**, 232502 (2005).
[2] W. Krolas *et al.*, Phys. Rev. C **84**, 064301 (2011).
[3] E. Koshchiy *et al.*, Nucl. Instrum. Methods Phys. Res. **A870**, 1 (2017).

Neutron-induced triple-alpha enhancement: measuring neutron-induced reactions with TexAT

J. Bishop,[1] C.E. Parker,[1] G.V. Rogachev,[1,2,3] S. Ahn,[1,2] C.R. Brune,[4] K. Brandenburg,[4] R. Charity,[5]
J. Derkin,[4] N. Dronch,[5] G. Hamad,[4] Y. Jones-Alberty,[4] Tz. Kokalova,[6] E. Koshchiy,[1] V. Ohstrom,[5]
S. Paneru,[4] S.T. Marley,[7] T.N. Massey,[4] Z. Meisel,[4] R. Smith,[8] L.G. Sobotka,[5] D. Soltesz,[4]
A.V. Voinov,[4] and J. Warren[4]
[a]*Cyclotron Institute, Texas A&M University, College Station, Texas 77843,*
[b]*Department of Physics & Astronomy, Texas A&M University, College Station, Texas 77843,*
[c]*Nuclear Solutions Institute, Texas A&M University, College Station, Texas 77843,*
[d]*Department of Physics & Astronomy, Ohio University, Athens, Ohio 45701,*
[e]*Department of Chemistry, Washington University, St. Louis, Missouri 63130,*
[6]*School of Physics & Astronomy, University of Birmingham, Edgbaston B15 2TT, United Kingdom*
[7]*Department of Physics and Astronomy, Louisiana State University, Baton Rouge, Louisiana 70803*
[8]*College of Business, Technology and Engineering, Sheffield Hallam University, Sheffield S1 1WB, United Kingdom*

The triple-alpha reaction, by which helium is fused to form carbon, is an important reaction mechanism to overcome the A=5, 8 bottleneck which is facilitated by the Hoyle state at 7.65 MeV. The reaction rate is determined by the radiative width, i.e. how often the Hoyle state decays by γ-rays and electron-positron pair to end up with carbon-12 in the ground state. It was suggested that in certain astrophysical environments, an alternative decay path can dominate (by up to a factor of 100): that of neutron up-scattering [1]. In this situation, a low-energy neutron interacts with the excited nucleus and carries away a large amount of energy such that the nucleus can de-excite to the ground state (or the first-excited state). The cross section for this interaction is unknown due to the experimental difficulties in

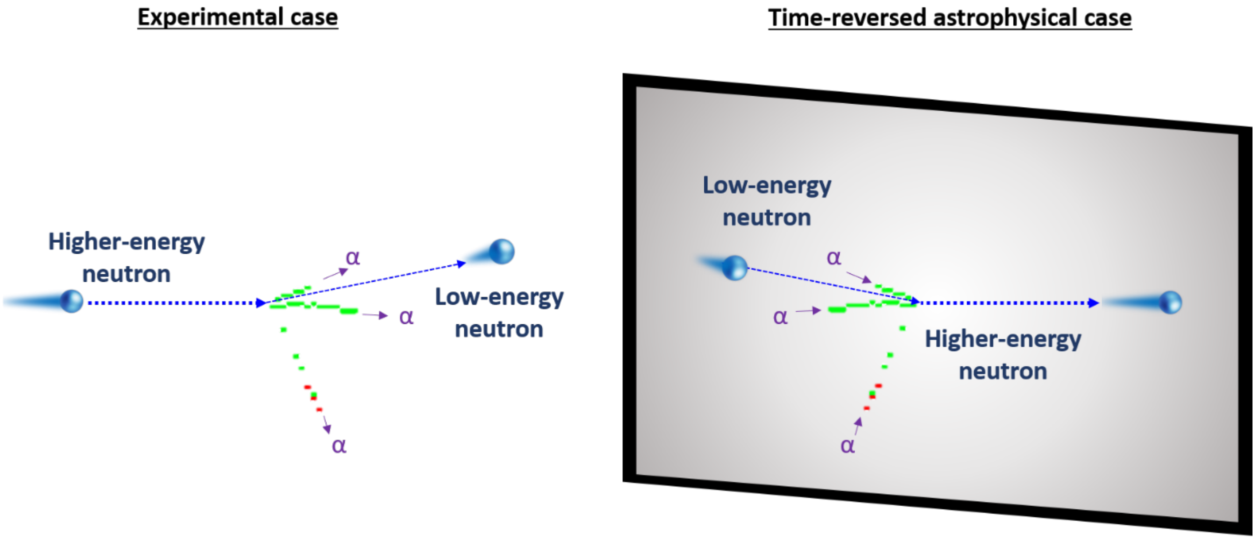

Fig. 1. Relation between the experimentally measured 12C(n,n_2)3a reaction studied with TexAT and the astrophysical case whereby a low-energy neutron enhances the triple-alpha reaction.

measuring it. To determine this cross section, the time-reversed reaction has been studied using TexAT [2] which will allow for a measurement of the enhancement of the triple-alpha rate via the effect of the neutrons. The relation between the astrophysical situation and our experiment is shown in Fig. 1.

The time-reversed reaction is that of $^{12}C(n,n_2)3\alpha$ and must be studied in the astrophysically-relevant energy regime of between the threshold at 8.3 MeV, and 10 MeV. This experiment therefore required a high-intensity, monochromatic, collimated neutron source such as that available at Ohio University [3] via the D(d,n) reaction. This well-suited neutron beam is then incident upon TexAT, filled with 50 Torr CO_2 where the charged-particle products can be measured.

Development and modelling (with MCNP and GEANT4) demonstrated the feasibility of this experiment with a neutron beam intensity of ~5000 n/s and a beam resolution of 300 keV (full-width). Additional efforts to provide precise beam normalization were also undertaken and was determined to be possible via:

- Measurement of $^{12}C(n,n_0)$ and $^{16}O(n,n_0)$ elastic scattering inside TexAT.
- Measurement of the $^{1}H(n,p)$ elastic scattering reaction using a CH_2 foil and a silicon detector.
- Activation of metal foils via the $^{27}Al(n,\alpha)$ reaction and measurement with a HPGe detector.
- Normalization using an NE-213 detector placed at 0^{o} after the TexAT detector.

This CENTAUR experiment represented a large collaboration between TAMU, LSU, and WashU as well as collaborators at Ohio University, Sheffield Hallam University (UK), and University of Birmingham (UK). The experiment was started in March 2020 and was 50% complete before being postponed due to COVID19. Preliminary results from a subset of neutron energies indicate the experiment was successful.

The code to reconstruct and analyze the $^{12}C(n,n_2)3\alpha$ events was developed and benchmarked with simulated data. An example of a real event can be seen in Fig. 1 where the 3 α-particles were reconstructed inside TexAT. Current efforts focus on automatic identification and separation of these 3α events from the more numerous (n,n_0) events.

Analysis of the data from the silicon detectors demonstrates the neutron flux rate is in agreement with that expected from the deuteron beam current and gas-cell details. Efforts are currently underway to unfold the neutron energy spectrum from the proton-recoil energy spectrum incorporating multiple effects using GEANT4.

This experiment not only demonstrates the measurement of an important astrophysical reaction but also the first measurement of a neutron-induced reaction with a Time Projection Chamber (TPC) which has garnered an article in Scientific American [4]. The preliminary successes pave the way for a multitude of additional studies using a similar technique.

[1] M. Beard, S.M. Austin, and R. Cyburt, Phys. Rev. Lett. **119**, 112701 (2017).

[2] E. Koshchiy *et al.*, Nucl. Instrum. Methods Phys. Res. **A957**, 163398 (2020).

[3] Z. Meisel *et al.*, Phys. Procedia **90** 448 (2017).

[4]https://www.scientificamerican.com/article/carbon-conundrum-experiment-aims-to-re-create-synthesis-of-key-element/

Resonant elastic scattering of ^{14}O on α particles studied with the TexAT active target

M. Barbui,[1] E. Aboud,[1] S. Ahn,[1] J. Bishop,[1] V.Z. Goldberg,[1] J. Hooker,[1] C.H. Hunt,[1] H. Jayatissa,[1]
Tz. Kokalova,[2] E. Koshchiy,[1] S. Pirrie,[2] E. Pollacco,[3] B.T. Roeder,[1] A. Saastamoinen,[1]
S. Upadhiayula,[1] C. Wheldon,[2] and G.V. Rogachev[1,4]
[1]*Cyclotron Institute, Texas A&M University, MS3366 College Station, Texas 77843*
[2]*School of Physics and Astronomy, University of Birmingham, Birmingham, United Kingdom*
[3]*IRFU, CEA, Saclay, Gif-Sur-Ivette, France*
[4]*Department of Physics&Astronomy, Texas A&M University, College Station, Texas 77843*

Isospin symmetry is an important concept in nuclear structure that has been extensively studied for many decades. It is well established that isospin is a good quantum number (with some exceptions) for nucleon degrees of freedom. However, applicability of this symmetry to cluster degrees of freedom is not obvious. The goal of this work is to explore if isospin symmetry still holds for alpha-cluster states by comparing the alpha-cluster states in ^{18}Ne with those in the mirror nucleus ^{18}O that were previously measured by Avila et al. [1]. The Coulomb shift in resonances of mirror pair nuclei can be used to probe the cluster structure of these states. For example, Baba and Kimura [3] performed an AMD calculation on the mirror pair ^{14}C-^{14}O to study molecular orbits in positive parity states. They found three types of configurations: the triangular, π-bond linear chain, and σ-bond linear chain. The excitation energy difference between ^{14}C and ^{14}O is very small for the π-bond linear chain while it is large for the σ-bond linear chain. This large energy shift is interpreted as Thomas-Ehrman shift in the σ-bond linear chain. Nakao et al. [4] studied the Coulomb shift in the mirror pair ^{18}O-^{18}Ne using the Orthogonality Condition Model. This calculation predicts suppressed excitation energy for the 0^+ resonant levels in ^{18}Ne and a larger alpha width compared to ^{18}O. This is also explained as Thomas-Ehrman effect.

In this work we studied the reaction ^{14}O+alpha using the TexAT active target [2] at Cyclotron Institute of Texas A&M University. The ^{14}O beam was produced using Momentum Achromat Recoil Separator (MARS) with the reaction ^{14}N(p,n)^{14}O. The ^{14}N primary beam with energy of 11 MeV/nucleon was delivered by the K500 Cyclotron. The energy of the ^{14}O beam was 61.8 MeV and the intensity was about 10^4pps.

Alpha particles were detected by the front-wall silicon detectors and identified using the energy loss in the last section of the active detector together with the residual energy deposited in the silicon. The interaction point inside the gas volume was obtained after reconstructing the trajectories of the incoming beam, the alpha particle and the recoiling ^{14}O. This information was used to select only the events corresponding to elastic scattering and rejecting the inelastic scattering events. The excitation function of ^{18}Ne was measured in the detectors placed at 5°, 9°, 12°, and 15°from the center of the entrance window. The corresponding differential cross sections are shown in Figure 1. The experimental cross sections were analyzed using the R-Matrix approach. Since the mirror nucleus ^{18}O has been already studied [1] we started the R-Matrix calculation with the parameters used to describe ^{18}O and we manually varied them to obtain the best reproduction of the experimental data. The result is shown by the blue line in Fig. 1. Although the statistics is low 50 resonances were identified with a reduced χ^2 of about 9 between experimental and calculated values. An almost complete correspondence between the levels in ^{18}O and

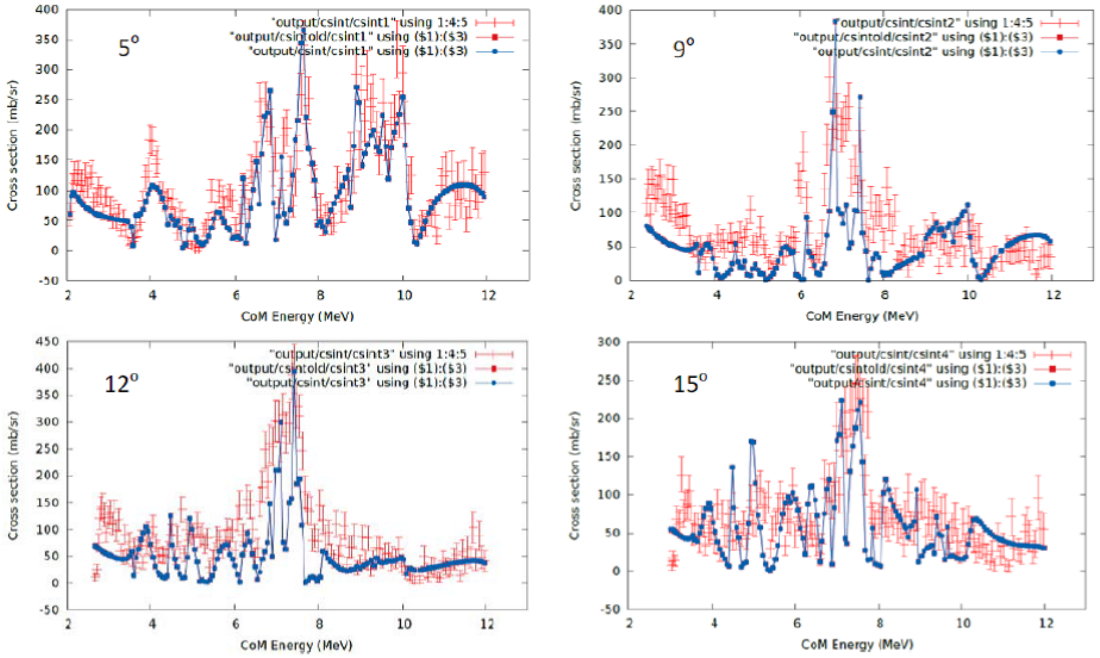

Fig. 1. ^{18}Ne excitation function measured at different angles (red points). The blu line shows the result of the R-matrix calculation.

^{18}Ne was found. This R-Matrix calculation was performed considering only the alpha exit channel, since there are no experimental data available for the p and p_1 channels in the energy range of interest. The dimensionless reduced alpha width and the excitation energy shift were calculated for all the corresponding levels in ^{18}Ne and ^{18}O. It is interesting to note that the states with the largest reduced alpha width in ^{18}Ne correspond to states with a large reduced alpha width in ^{18}O, signaling a pronounced alpha cluster structure of these states. The present R-matrix analysis does not show the drop of about 600 keV predicted by Nakao in the excitation energy of the 0^+_4 state in ^{18}Ne, but the width of the state is large (3.4 MeV). We also observe the tail of another 0^+ state at 2.2 MeV above the alpha threshold that is not seen in ^{18}O.

Calculation of the energy and width of the states in ^{18}O and ^{18}Ne have been performed using a simple potential model. These calculations are not able to reproduce at the same time the observed excitation energy shift and width of the states.

Further analysis work will be done to try to incorporate the p and p_1 exit channels in the R-Matrix calculation as well as a fit of the most significant resonances to improve the χ^2.

Comparison with the Monte Carlo shell model calculations performed by A. Volya will be also done.

[1] M.L. Avila *et al.*, Phys. Rev. C **90**, 024327 (2014).
[2] E. Koshchiy *et al.*, Nucl. Instrum. Methods Phys. Res. **A957**, 163398 (2020).
[3] T. Baba and M. Kimura, Phys. Rev. C **99**, 021303(R) (2019).
[4] M. Nakao *et al.*, Phys. Rev. C **98**, 054318 (2018).

Structure of ^{13}Be through isobaric analogue states in ^{13}B

C. Hunt,[1] G.V. Rogachev,[1] E. Koshchiy,[1] S. Ahn,[1] J. Bishop,[1] S. Upadhyayula,[1] E. Aboud,[1]
A. Bosh,[1] C. Parker,[1] M. Roosa,[1] B.T. Roeder,[1] M. Alcorta,[2] K. Hahn,[3] and S. Han[3]
[1]*Texas A&M University Cyclotron Institute, College Station, Texas*
[2]*TRIUMF, Vancouver, British Colombia, Canada*
[3]*Ewha Womans University, Seoul, South Korea*

Structure of ^{13}Be, exotic unbound isotope that has four more neutrons than the only stable beryllium isotope ^{9}Be, has been a major puzzle over the last decade. Naive shell model considerations indicate that ^{13}Be should have a $1/2^-$ ground state because it is well known that 2s1/2 shell is the lowest in ^{11}Be, it is filled in ^{12}Be, and the next valence neutron should occupy the unfilled 1p1/2 shell in ^{13}Be. However, it is known that valence nucleons in the ground state of ^{12}Be (^{10}Be+2n) are in the mixed $1p_{1/2}+2s_{1/2}$ configuration [1]. Moreover, theoretical calculations and experiments done on ^{13}Be have been unable to come to agreement with some finding a ground state of $1/2^+$ and others $1/2^-$ (see references in [2]). There is a general consensus only about a resonance at around 2 MeV above the neutron decay threshold, that was first observed in the ^{14}C(^{7}Li,^{8}B) reaction [3]. After that it has been observed in many other studies and based on indirect and/or theoretical arguments the spin-parity of the 2 MeV state is believed to be $5/2^+$. The rest of the ^{13}Be spectrum is still uncertain, as there are no conclusive experimental spin-parity assignments for any of the states in ^{13}Be, including the ground state. Three more states ($1/2^+$, $1/2^-$, and $5/2^+$) have been suggested below 2 MeV in various studies but neither can be considered as conclusively established (see for example [4-7] and Refs. therein). The experiments performed to date can be divided into two major groups: the experiments that use invariant mass or sequential neutron decay spectroscopy with rare isotope beams at high energy $\sim$100 MeV/u [4-7] and the multi-nucleon transfer reactions [3]. In either case the interpretation of the results is complicated by the uncertainties in the reaction mechanism resulting in ambiguities in spin-parity assignments. On top of that, at least some of the low-lying states are expected to be broad and overlapping resonances which are populated with different probability by different reactions. As a result, it has been very challenging to come up with conclusive and self-consistent interpretation of all of the experimental data so far.

To overcome the difficulties mentioned above, instead of studying ^{13}Be directly, we have studied the T=5/2 states in ^{13}B, the isobaric analogs of ^{13}Be. These states were populated in ^{12}Be+p resonance elastic scattering and measured using the state-of-the-art active target detector TexAT. In July of 2019 we moved the Texas Active Target (TexAT) detector [8] to TRIUMF to run ^{12}Be + p experiment using the ISAC II rare isotope beams facility. A beam of ^{12}Be with an energy of 6 MeV/u was used for the experiment with a target gas of isobutane at 260 Torr. This combination of beam energy and gas pressure allowed for a measurement of the excitation function from 6 MeV down to 1 MeV. This energy region is where the ^{13}Be low laying T=5/2 states are expected to be found.

The TexAT detector uses a highly segmented a Micro-Mesh Gaseous Structure (MicroMegas) detector to track particles in the chamber. For additional amplification a Gas Electron Multiplier (GEM) was placed in front of the MicroMegas plate. Tracks of the beam, heavy recoil, and light recoil particles are recorded by the TPC. An array of CsI backed Si detectors was placed at forward scattering angles to measure the energy of the light recoil particles. The particle tracks, in conjunction with the energy measured in the Si-CsI array, are used to reconstruct the reaction kinematics.

Analysis of the data is ongoing. Particle identification has been done for events where the light recoil particle has sufficient energy to pass through the Si detector into the CsI detector (Fig. 1). There is a clear distinction between protons, deuterons and tritons. Track reconstruction for the side regions in TexAT has been successful for the majority of events giving a measure of where the reaction occurred in the chamber. Using the reaction location with the energy deposited in the detectors the events of interest can be identified (Fig. 2). This will be used to create and excitation function from the energy of the protons in the Si-CsI array. R-Matrix analysis will be used to establish the structure of T=5/2 states in ^{13}B and infer the spin-parities of the low-laying states in ^{13}Be.

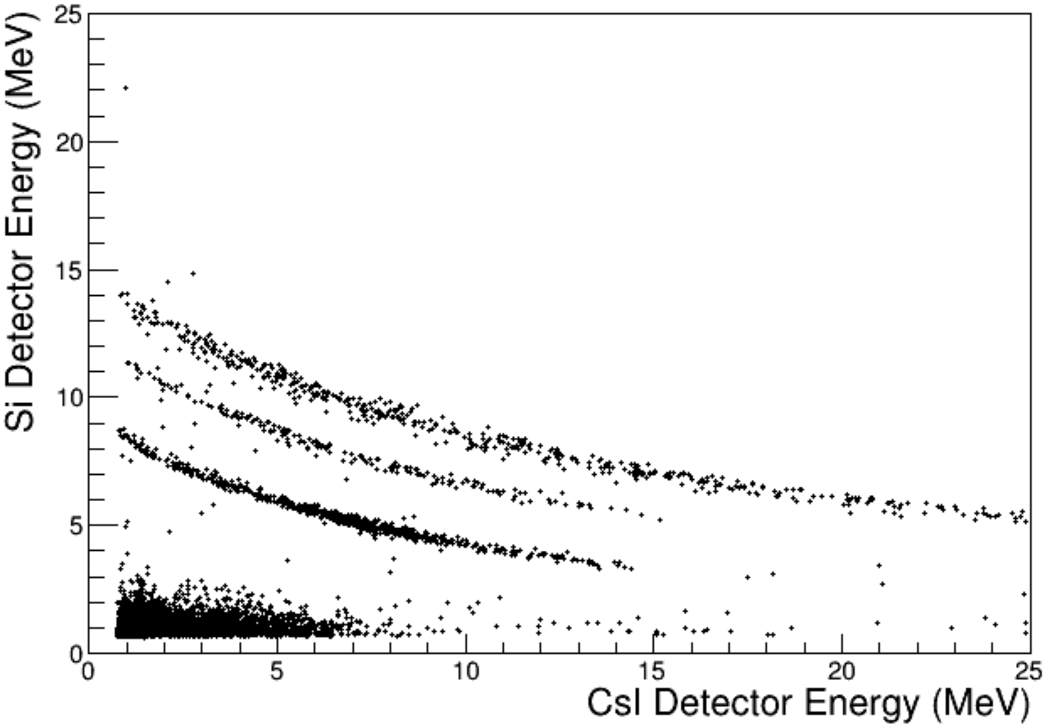

Fig. 1. Si Energy vs CsI Energy plot showing proton, deuteron and triton bands.

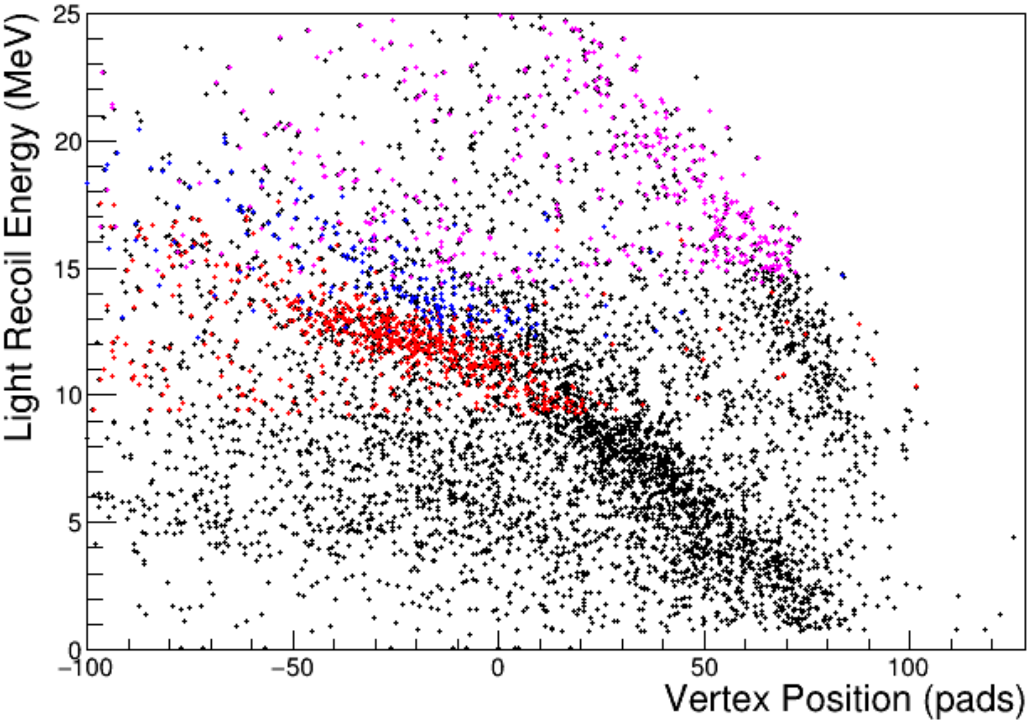

Fig. 2. Light Recoil energy plotted against the reaction position from track reconstruction. The colors correspond to protons (red), deuterons (blue), and tritons (magenta) as determined by the Si vs CsI energy plot. A strong band of protons corresponds to the 12Be + p elastic scattering reaction.

[1] R. Sherr and H.T. Fortune Phys. Rev. C, **60**, 064323, (1999).

[2] H.T. Fortune *et al.* Phys. Rev. C, **87**, 014305, (2013).

[3] D.V. Aleksandrov, E.A. Ganza, Y.A. Glukhov, V.I. Dukhanov, I.B. Mazurov, B.G. Novatskii, A.A. Ogloblin, D.N. Stepanov, V.V. Paramonov, and A.G. Trunov, Sov. J. Nucl. Phys. **37**, 474 (1983).

[4] Y. Kondo, T. Nakamura, Y. Satou, T. Matsumoto, N. Aoi, N. Endo, N. Fukuda, T. Gomi, Y. Hashimoto, M. Ishihara *et al.*, Phys. Lett. B **690**, 245 (2010).

[5] Y. Aksyutina, T. Aumann, K. Boretzky, M.J.G. Borge, C. Caesar, A. Chatillon, L.V. Chulkov, D. Cortina-Gil, U.D. Pramanik, H. Emling *et al.*, Phys. Rev. C **87**, 064316 (2013).

[6] G. Randisi, A. Leprince, H.A. Falou, N.A. Orr, F.M. Marques, N.L. Achouri, J.C. Angelique, N. Ashwood, B. Bastin, T. Bloxham *et al.*, Phys. Rev. C **89**, 034320 (2014).

[7] B.R. Marks, P.A. DeYoung, J.K. Smith, T. Baumann, J. Brown, N. Frank, J. Hinnefeld, M. Hoffman, M.D. Jones, Z. Kohley *et al.*, Phys. Rev. C **92**, 054320 (2015).

[8] E. Koshchiy, G.V. Rogachev, E. Pollacco, S. Ahn, E. Uberseder, J. Hooker, J. Bishop, E. Aboud, M. Barbui, V.Z. Goldberg, C. Hunta, H. Jayatissa, C. Magana, R. O'Dwyer, B.T. Roeder, A. Saastamoinen, and S. Upadhyayula. Nucl. Instrum. Methods Phys. Res. **A957**, 163398 (2020).

Simulation of multi-step γ cascade spectra from ^{59}Fe(d,pγ) reaction

S. Ota,[1] M. Krticka,[2] A. Abott,[1] E.A. Bennett,[1] A. Couture,[3] J. Gauthier,[1] K. Hagel,[1]
A.B. McIntosh,[1] A. Simon,[4] M. Sorensen,[1] and S.J. Yennello[1]
[1]*Cyclotron Institute, Texas A&M University, College Station, Texas 77843,*
[2]*Charles University in Prague, Prague, Czech Republic*
[3]*Los Alamos National Laboratory, Los Alamos, New Mexico 87545,*
[4]*University of Notre Dame, Notre Dame, Indiana 46556*

Cosmic γ rays from long-lived (τ (1/2) ~ Myrs) unstable nuclei such as ^{26}Al and ^{60}Fe are observed overall in the Galactic disk [1]. Understanding the origin of these nuclei will lead to greatly constrain and improve models of galactic chemical evolution and stellar nucleosynthesis.

These ^{60}Fe are believed to be produced by the ^{59}Fe(n,γ) reaction, e.g., in the He burning stage of massive stars. It is therefore important to determine the reaction cross sections at the stellar temperature (neutron energy (E_n) ~30 keV). However, since ^{59}Fe is short-lived (τ (1/2) = 44 days), indirect methods must be taken to determine the cross sections. We are developing a method using the ^{59}Fe(d,pγ)^{60}Fe reaction to indirectly constrain the ^{59}Fe(n,γ) cross sections. A charged particle detector with high energy-resolution (for ejectile protons) and a large γ-detector array with high detection efficiency are demanded for the method. Thus, a detector system composed of a Si detector and 128 BaF_2 crystals [2] is under development at the TAMU Cyclotron Institute [3].

Data analysis from the present method is highly similar to the one employed for (n,γ) experiments with the DANCE BaF_2 array at Los Alamos National Laboratory (LANL) [4]. In our case, highly excited states of a nucleus of interest are populated by (*d, p*) reactions instead of neutron capture reactions. Populated states and underlying states of a nucleus, ^{60}Fe in our case, are simulated by a Monte Carlo Simulation code named DICEBOX [5]. The simulation process, "Nuclear Realization", involves multiple nuclear realizations to accommodate the fact that many energy levels and decay properties of ^{60}Fe are not known in details. Realistic energy levels of ^{60}Fe from the ground state to a certain excitation energy (usually set to the neutron separation energy, 8.8 MeV for ^{60}Fe), with e.g., given spins, parities, γ partial width, are thus generated based on a nuclear level density model and photon strength function models provided in the input file. The multi-step (MS) γ cascades from the excitation energy to ground state are incorporated in our GEANT4 simulation in which the TAMU BaF2 array is built. The obtained GEANT4 spectra will be eventually compared with our experimental (*d,pγ*) spectrum. By iterating the simulation varying the models used, we will find the "best-match" level density and PSF models with the experimental spectra. ^{59}Fe(n,γ) cross sections can be determined using these models, e.g., with the TALYS code [6].

Figs. 1 show examples of simulated (generated) MS γ cascade spectra for ^{58}Fe, which were made to study data from the test experiments with the ^{57}Fe(d,pγ) reaction to benchmark the method. Note no detector responses have been included in the present simulations yet. The simulations are made from a nuclear level density available from [7] and PSFs theoretically calculated by Goriely *et al.* [8]. Each panel presents the overlaid spectra from different nuclear realizations for the cases of γ decay multiplicity

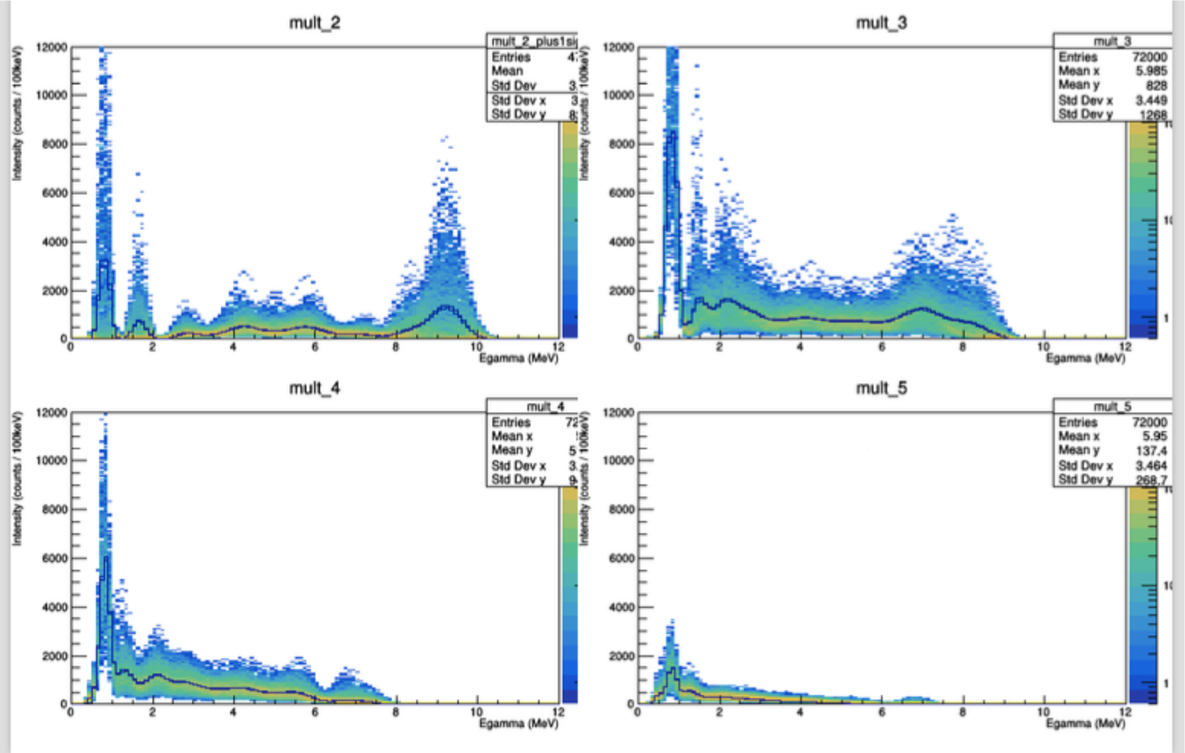

Fig. 1. Multi step γ cascade spectra from E_x=10 MeV ^{58}Fe J=2^+ state. Each panel shows a different γ source multiplicity.

equal to 2, 3, 4, and 5, respectively (see e.g., [9]). The lines in the panels correspond to average values at respective γ energies. It is clear the MS γ cascade spectra have intrinsic fluctuations derived from quantum mechanics (more specifically, e.g., the Porter-Thomas distribution). Therefore, a band corresponding to 66% (1 sigma) of the data will be extracted from each spectrum and then compared with the experimental data.

Fig. 2 shows the ^{57}Fe(n,γ) cross sections calculated using the models above with TALYS in comparison to past measurements [10, 11]. The calculations are preliminary, given no appropriateness of models used have been discussed yet. It can be seen, however, the (n,γ) cross sections can vary by a factor of two easily depending on models used. Thus, it is essential for the TAMU BaF_2 array to have the capability to distinguish different nuclear level density models and PSF models from the measured spectra. It is also noteworthy that the experimental cross-sections in the energy range of astrophysical interest (the range shown in the Fig. 2) have some discrepancies from different measurements. PSFs of ^{58}Fe currently being studied at LANL [12] may instead be a better guide for us to benchmark our method instead.

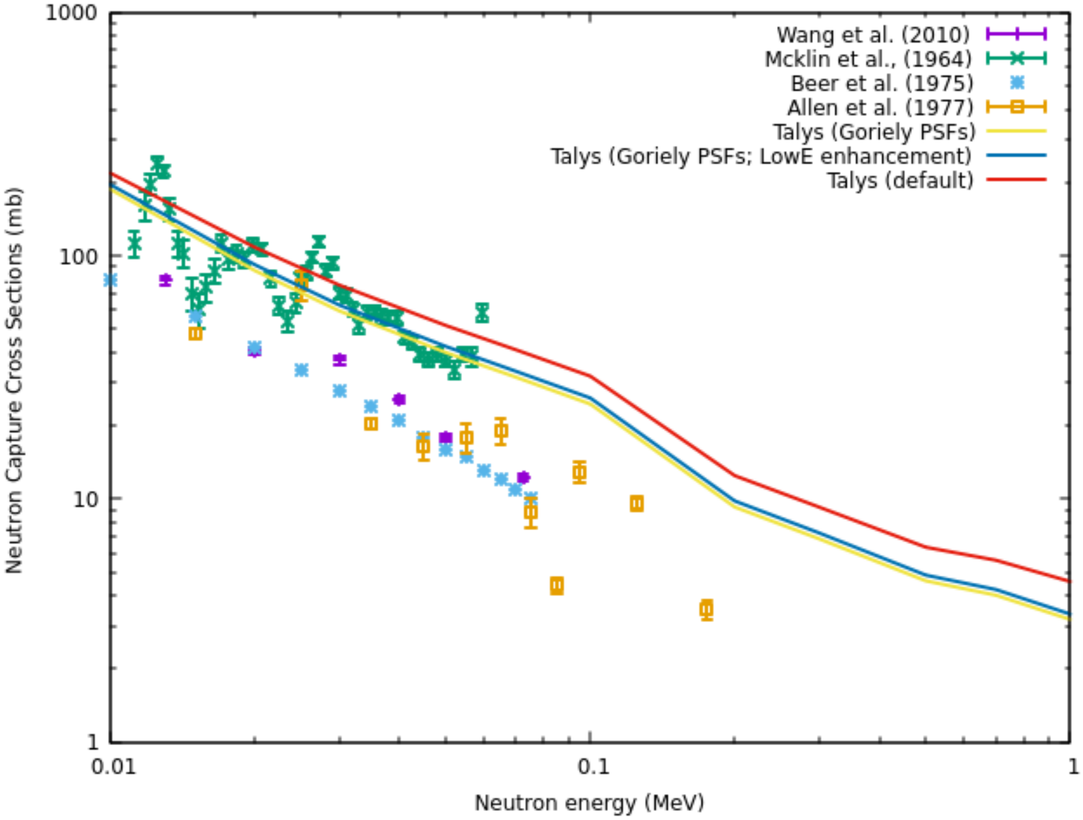

Fig. 2. ^{57}Fe(n,γ) cross sections from the past measurements and preliminary TALYS calculations.

[1] R. Diehl. Rep. Prog. Phys. **76**, 0263011 (2013).

[2] R. Varner, “Use of the ORNL-MSU-TAMU BaF$_2$ Array” (2004).

[3] A.B. McIntosh *et al., Progress in Research*, Cyclotron Institute, Texas A&M University (2018-2019), p. II-18.

[4] J. Kroll *et al.*, Phys. Rev. C **88**, 034317 (2013).

[5] F. Becvar, Nucl. IInstrum. Methods Phys. Res. **A417**, 434 (1998).

[6] A. Koning and D. Rochman, Nucl. Data Sheets **11**3, 2841 (2012).

[7] https://www-nds.iaea.org/RIPL-3/

[8] S. Goriely, S. Hilarie, S. Peru, and K. Sieja, Phys. Rev. C **98**, 014327 (2018).

[9] J.R. Winkelbauer *et al.*, Phys. Rev. C **99**, 024318 (2019).

[10] Experimental Nuclear Reaction Data (EXFOR).

[11] T. Wang *et al.*, Nucl. Instrum. Methods Phys. Res. **B268**, 440 (2010).

[12] E.A. Bennett, Ph. D Thesis, Texas A&M University (in preparation).

Background free measurement of β-delayed protons from ^{27}P for the astrophysical ^{26m}Al(p,γ)^{27}Si reaction

A. Saastamoinen, I. Stefanescu,[1] S. Hallam,[2] G. Lotay,[2] E. Pollacco,[2] B. Reed,[2] B.T. Roeder,
A. Spiridon,[1] L. Trache,[1] and R.E. Tribble
[1]*National Institute of Physics and Nuclear Engineering, Bucharest-Magurele, Romania*
[2]*IRFU, CEA Saclay, Gif-sur-Yvette, France*

The cosmic gamma-ray emitter ^{26}Al has been observed throughout the galactic plane of the Milky Way. Its short half-life of only about 720,000 years is an evidence about ongoing nucleosynthesis in our galaxy. The exact sites of creation and destruction of ^{26}Al are not pinpointed yet. The main candidates range from asymptotic giant branch stars to Wolf-Rayet stars to explosive scenarios such as oxygen-neon novae and core collapse supernovae. Nucleosynthesis in these hydrogen burning stellar scenarios occurs via network of radiative proton capture (p,γ) reactions. Among these reactions, proton capture from either the ground state, or the low-lying isomer state, of ^{26}Al to states in ^{27}Si can lead to depletion of ^{26}Al. Therefore, understanding of the properties of states beyond the proton separation threshold (S_p) in ^{27}Si is a crucial input for the modeling and understanding the origins of ^{26}Al in our galaxy. Several indirect and direct measurements have identified states relevant for both ^{26g,m}Al(p,γ)^{27}Si reactions. However some of the spin-parity assignments remain uncertain, especially in case of ^{26m}Al(p,γ)^{27}Si.

We have used selective nature of beta-decay of ^{27}P to populate states in ^{27}Si to improve the situation with the spin-parity assignments of the states just above the proton threshold in ^{27}Si. This decay was studied previously at the Cyclotron Institute by using the implantation-decay station utilizing Si and HPGe detectors [1,2]. As before, for this experiment the ^{27}P beam was produced through ^{1}H(^{28}Si,^{27}P)2n reaction with 40 MeV/u ^{28}Si beam from the K500 cyclotron impinging on LN$_2$ cooled H$_2$ target at 2 atm pressure. The reaction products were separated and identified with MARS resulting about 76% pure ^{27}P with average intensity of 1200 pps during the 7 day run. Immediately before and after the ^{27}P data taking run a beam of ^{25}Si was produced for calibration purposes through fragmentation with same primary beam hitting a 10 mil aluminum target.

β-delayed protons from ^{27}P were measured with the AstroBox2 detector [3,4] which suppresses the β-background down to ~100 keV and allows unambiguous measurement of low-energy β-delayed protons in the region of astrophysical interest. AstroBox2 was operated with ultra-pure P5 gas mixture (Ar/CH$_4$: 95%/5%) at 800 torr with drift field of about 200 V/cm and amplification field of about 30 kV/cm. While the ^{25}Si was spread throughout the active volume for calibration purposes, ^{27}P was tuned to over the centermost pads with the optimized background suppression capabilities. To ensure a pure sample impurity components of the beam with possible particle emitters (^{24}Al and ^{25}Si) were made to exit completely the main volume and only ^{27}P and ^{26}Si (only beta-gamma emission) impurity were stopped inside the active volume resulting 96% pure sample of ^{27}P over the centermost pads with most implants.

During the beam time total of 1.5e8 ^{27}P were implanted over the pads with best background rejection. Fig. 1. shows a preliminary sum spectrum of multiplicity one (only one pad triggering at the time) events from these pads. The main previously known β-delayed proton groups from decay of ^{27}P at 466(3), 612(2), and 731(2) keV [5] are clearly visible. In addition, several previously unobserved low energy particle groups are present. Detailed analysis of the data is work in progress.

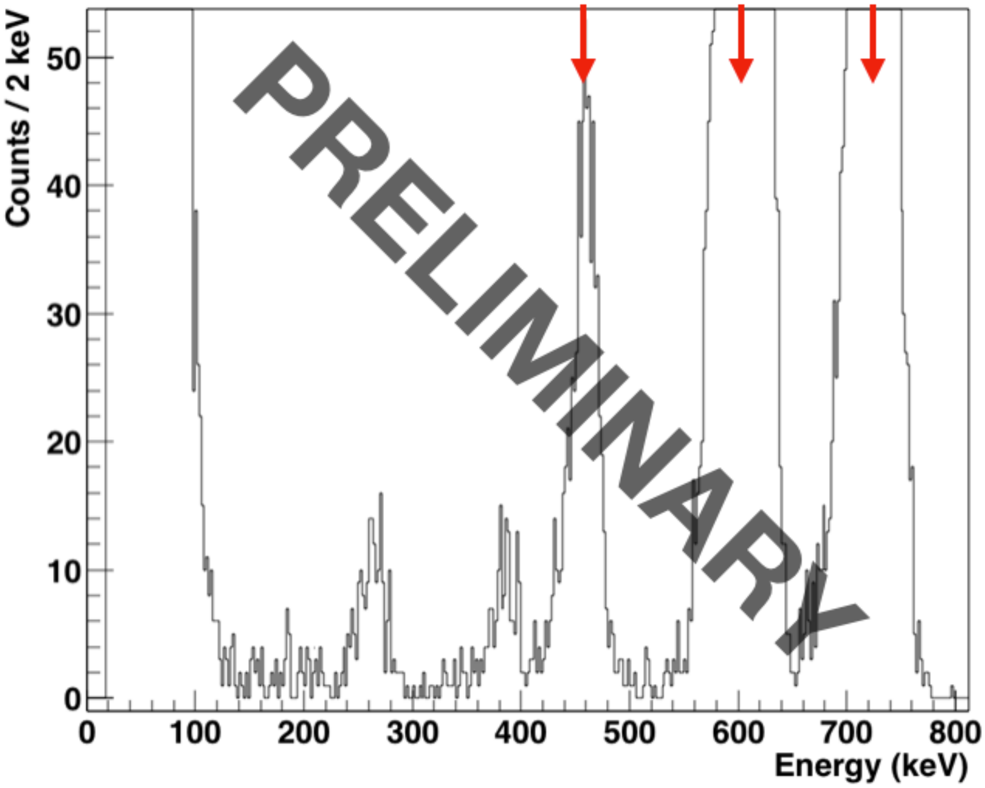

Fig. 1. Preliminary sum spectrum of the centermost pads with multiplicity one condition (only one pad firing at a time). The main previously known β-delayed proton groups from decay of ^{27}P at 466(3), 612(2), and 731(2) keV [5] are indicated with arrows. Several previously unobserved low-energy proton groups are present in the spectrum.

[1] E. Simmons, PhD Thesis, Texas A&M University, 2013.
[2] E. McCleskey *et al.*, Phys. Rev. C **94.** 065806 (2016).
[3] A. Saastamoinen *et al.*, Nucl. Instrum. Methods Phys. Res. **B376**, 357 (2016).
[4] A. Saastamoinen *et al.*, Nucl. Instrum. Methods Phys. Res. **B463**, 251 (2020).
[5] T.J. Ognibene *et al.,* Phys. Rev. C **54** 1098 (1996).

Intensity of a weak 519-keV γ ray following β decay of the superallowed emitter ^{34}Ar determined via the ^{33}S(p,γ)^{34}Cl reaction

H.I. Park,[1] J.C. Hardy,[1] M. Bencomo,[1] K.T. Macon,[2] W. Tan,[2] M. Brodeur,[2] A. Boeltzig,[2] B. Frentz,[2]
S.L. Henderson,[2] J. Long,[2] S. McGuinness,[2] O. Olivas-Gomez,[2] P. O'Malley,[2] G. Seymour,[2]
B. Vande Kolk,[2] and A. Kayani[3]
[1]*Cyclotron Institute, Texas A&M University, College Station, Texas 77843*
[2]*Department of Physics, University of Notre Dame, Notre Dame, Indiana 46556*
[3]*Department of Physics, Western Michigan University, Kalamazoo, Michigan 49008*

In the late summer of 2018 we have conducted the ^{33}S(p,γ)^{34}Cl experiment proposed at the University of Notre Dame to investigate the effect that weak γ-ray transitions potentially have on the superallowed β decay of ^{34}Ar, the parent nucleus of ^{34}Cl. Our focus was on determining the gamma-branching of the 666-keV level populated in ^{34}Cl. A possible weak 519-keV γ-ray from this level can affect the ^{34}Ar superallowed branching-ratio result for which we seek 0.1 % precision to yield a ft value contributing meaningfully to the determination of V_{ud}, the up-down quark-mixing element of the Cabibbo-Kobayashi-Maskawa matrix.

For our experiment the ^{33}S(p,γ)^{34}Cl reaction was initiated by protons from the 5U 5-MV single-ended vertical Pelletron at the Nuclear Science Laboratory of the University of Notre Dame. The proton beam, with an energy spread of less than 1 keV, passed through a 90° dipole magnet on its way to the water-cooled ^{33}S target, which was installed at the center of the compact germanium-detector array GEORGINA [1]. After exploring several candidate resonances, we chose the proton beam energy to be 1072 keV, which corresponds to a resonance in ^{34}Cl at an excitation energy of 6181 keV. This resonance was previously known [2] to preferentially decay to the state at 666 keV, whose decay we wished to study. Throughout our two-week measurement the beam current was limited to a maximum of 10.0 μA to prevent damage to the ^{33}S target.

The GEORGINA array consists of 5 Canberra n-type germanium detectors, each with a relative γ-ray of 100%. In our measurement, the beam was stopped in the tantalum containing the target material, so one of the detectors could be placed directly downstream from the target; the other four were arranged symmetrically in close geometry around the target and slightly upstream of it. The preamplified signals from each detector were directly read by a Mesytec MDPP-16 [3] fast high-resolution time and amplitude digitizer. We began the measurement with all five detectors in operation, but unfortunately were limited to four for most of the data taking.

Immediately following the end of data collection, we made calibration measurements with ^{6}Be, ^{60}Co, ^{137}Cs, ^{133}Ba, and ^{152}Eu. These sources provided us with the twenty well-known γ peaks covering energy range from 120 keV to 1410 keV, and therefore our energy calibration for all five Ge detectors was well established in the region of our interest between 500 keV and 700 keV. The efficiency calibration was done for each individual Ge detector using ^{60}Co, ^{137}Cs, and ^{152}Eu sources. The ^{60}Co and ^{137}Cs sources have a simple decay scheme to permit clean determination of detector's efficiency. A very complicated decay of the ^{152}Eu (to ^{152}Sm by electron capture and to ^{152}Gd via positron emission) source, on the other hand, made us consider only the 244-keV, 344-keV, 444-keV, 779-keV, 867-keV, 964-keV, 1086-keV, 1090-keV, 1112-keV, 1299-keV, and 1408-keV γ -rays. This provided detection efficiency in each detector for the most important 519-and 666-keV peaks of interest.

Data collected from the ^{33}S(p,γ)^{34}Cl measurement were processed to extract prompt γ-γ coincidence events, which were then stored in a database that could be accessed by analysis software developed at Texas A&M University. Each entry in the database consisted of the energies and time-stamps of two coincident γ-rays, the time difference between their arrivals, and an identifier of the two germanium detectors from which the signals originated. As the firrst step in analysis, all detector spectra were adjusted so as to place them on a common energy scale. Next, six two-dimensional γ-γ coincidence spectra were created, each with $2^{15}\times2^{15}$ channels and having 0.25 keV per channel. These spectra corresponded to the six possible pairs of our four operating germanium detectors.

The 6181-keV state we had populated in ^{34}Cl decays predominantly to the state at 666 keV via a 5515-keV transition, so by gating on the observed 5515-keV γ ray in one detector of a pair we could observe in the other detector the γ rays emitted in the subsequent decay of the 666-keV state. Peaks at 519 and 666 keV were clearly visible in each projected spectrum, and the relative intensity of the former to the latter was evaluated and found to be statistically consistent from one pair to another, thus indicating that any possible effects of angular correlations between the coincident γ rays can be neglected. As a result, we could safely add together all the projections for a given detector and determine the relative γ-ray intensities using the appropriate efficiency curve for that detector. Indeed, the relative efficiency curves of the four detectors were similar enough that we could also sum all of the detector projections into a single spectrum and use an averaged calibration curve for an analysis with the highest statistical precision.

We determined the areas of the 519- and 666-keV γ-ray peaks using GF3, the least-squares peak fitting program in the RADWARE [4] package. A Gaussian peak with a constant background in the peak region was sufficient to properly describe the data in the spectrum. The ratio of peak areas was determined to be $N\gamma_{519}/N\gamma_{666}$ = 0.0155(20), where the uncertainty includes provision for both counting statistics and systematic uncertainties associated with the spectral background and our specific choice of gates in the region of the 5515-keV peak. Taking this result together with the corresponding detector efficiency ratios, we found that the intensity of the 519-keV transition to the 146-keV isomeric state is 1.46(19) % relative to the dominant 666-keV transition to the ground state. Our result has made important contributions to new precise measurements of the superallowed decay of ^{34}Ar [5, 6].

[1] A. Aprahamian, P. Collon, and M. Wiescher, Nuclear Physics News **24**, 5 (2014).

[2] F.B. Waanders, J.P.L. Reinecke, H.N. Jacobs, J.J.A. Smit, M.A. Meyer, and P.M. Endt, Nucl. Phys. **A411**, 81 (1983).

[3] Mesytec, https://www.mesytec.com/products/nuclear-physics/MDPP-16.html.

[4] D.C. Radford, http://radware.phy.ornl.gov/main.html.

[5] V.E. Iacob, J.C. Hardy, H.I. Park, M. Bencomo, L. Chen, V. Horvat, N. Nica, B.T. Roeder, and A. Saastamoinen, Phys. Rev. C **101**, 015504 (2020).

[6] V.E. Iacob, J.C. Hardy, H.I. Park, M. Bencomo, L. Chen, V. Horvat, N. Nica, B.T. Roeder, A. Saastamoinen, and I.S. Towner, Phys. Rev. C **101**, 045501 (2020).

Spin physics with STAR at RHIC

C.A. Gagliardi, T. Lin, R.E. Tribble,
and the STAR Collaboration

Our group continues to play major roles in STAR investigations of both longitudinal and transverse spin phenomena in polarized *pp* collisions at RHIC, with a particular focus on spin asymmetries involving jet production.

A major goal of the RHIC spin program is to determine the gluon polarization (*i.e.*, helicity) in the proton over a wide range of x. The longitudinal double-spin asymmetry, A_{LL}, for inclusive jet production is an ideal tool in this effort because the cross section is large and dominated by quark-gluon and gluon-gluon scattering processes, both of which have large partonic asymmetries. Texas A&M has played a leading role in STAR gluon polarization measurements for over a decade. During the past year, STAR published "Longitudinal double-spin asymmetry for inclusive jet and dijet production in *pp* collisions at $\sqrt{s}$ = 510 GeV" [1]. This describes the results of our former graduate student (now BNL post-doc) Dr. Zilong Chang's dissertation research, together with the results of former University of Kentucky graduate student Dr. Suvarna Ramachandran.

The paper provides a detailed description of the high-statistics STAR measurement of mid-rapidity jet and di-jet A_{LL} in 510 GeV *pp* collisions, based on data recorded during the 2012 RHIC run. Notably, it describes several substantial improvements in STAR jet asymmetry measurement techniques that were developed by Dr. Chang while he was a TAMU graduate student. These improvements lead to by far the best match that STAR has ever obtained for a wide range of jet properties in data *vs*. simulation, including detailed comparisons of the jet p_T spectra, the longitudinal (z) and transverse (j_T) fragmentation distributions within the jets, and the observed electromagnetic energy fractions. (See [1] for details.) They also lead to much smaller systematic uncertainties than were practical in any previous STAR jet A_{LL} measurement, as illustrated in the left panel of Fig. 1, and they enable completely new observables to be

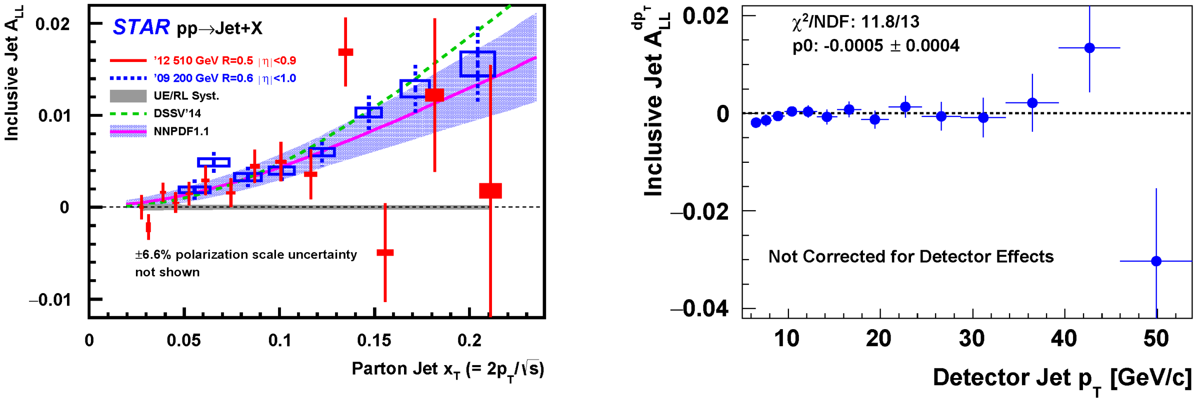

Fig. 1. (Left) The inclusive jet A_{LL} vs. jet p_T from the 510 GeV *pp* collision data that STAR recorded during 2012. (Right) A_{LL} for the underlying event from the same data set. See [1] for details.

investigated, such as the first-ever measurement of A_{LL} for the underlying event that accompanies jet production at RHIC, shown in the right panel of Fig. 1. These inclusive jet results provide important new constraints on the magnitude of the gluon polarization, especially in the range $0.015 < x < 0.1$. The di-jet results, which are separated into four different topology categories depending on the individual jet pseudorapidities, provide important new constraints on the shape of $\Delta g(x)$ over the same x range [1].

In parallel, we have been working on analysis of the azimuthal transverse single-spin asymmetries of identified hadrons within jets to measure the Collins effect, which involves the convolution of the quark transversity in the proton with the Collins fragmentation function. STAR recorded about 52 pb^{-1} of transversely polarized pp data at $\sqrt{s} = 200$ GeV during 2015, which is twice the luminosity sampled during 2012. These results will provide the most precise measurement of the Collins effect at this collision energy.

We have developed several new techniques to reduce systematic uncertainties. For the particle identification (PID), we use the particle ionization energy loss (dE/dx) and particle mass measured with the Time Projection Chamber (TPC) and Time of Flight (TOF). A new likelihood method has been developed to calculate the corresponding particle fractions in the sample that makes full use all of the information we can get from the detector. Pure samples of charged pions and protons are identified as the weak decay daughters of Λ and K_S. TOF has a very good ability to select the low momentum charged kaons and electrons. We also use the electromagnetic calorimeter to identify high momentum electrons. With these four types of particles well determined, we are able to constrain the PID with very good precision.

The underlying events are also studied in this analysis using the off-axis cone method [1]. Underlying event subtractions are made for each reconstructed jet. The underlying event subtraction increases the matching fractions between the detector level jets and particle/parton level jets and reduces the differences in $\langle p_T \rangle$ between the different levels. We also set an upper limit on the j_T of hadrons included in the spin asymmetry measurements that substantially reduces the underlying event background while removing only a very small fraction of the true jet fragments. After these, we calculate the underlying event fractions in the sample and correct the measured asymmetries for these underlying event dilutions.

About 8M Pythia simulation events have been generated to correct for detector effects on the measured quantities and evaluate various systematic uncertainties. We found systematic deviations of the reconstructed *vs*. true jet pseudorapidity at the ends of the detector. This arises because the systematic missing jet energy at larger pseudorapidity biases the reconstruction of the thrust axis. We estimated the associated bias and make the corresponding corrections to the reconstructed jets. The systematic uncertainties due to the detector's non-uniform acceptance effect are significantly reduced after this correction.

Fig. 2 shows the preliminary results for the Collins asymmetries for identified $\pi^{\pm}$ as a function of the particle level jet p_T. These results are presented for jets that scatter both forward (top panel) and backward (bottom panel) relative to the polarized beam. The asymmetries are large and opposite in sign for π^+ and π^- with similar magnitude for jets coming from the polarized beam. These new asymmetries agree with previous reported results, and have 30% smaller uncertainties. In addition to Fig. 2, we have also obtained Collins asymmetries for charged pions *vs*. hadron z and j_T, Collins asymmetries for charged kaons *vs*. jet p_T, "Collins-like" asymmetries for charged pions, which are sensitive to the linear polarization of gluons in a transversely polarized proton convoluted with the gluon analog of the Collins fragmentation function, and various inclusive jet asymmetries. We are beginning to write the paper that will describe these various results.

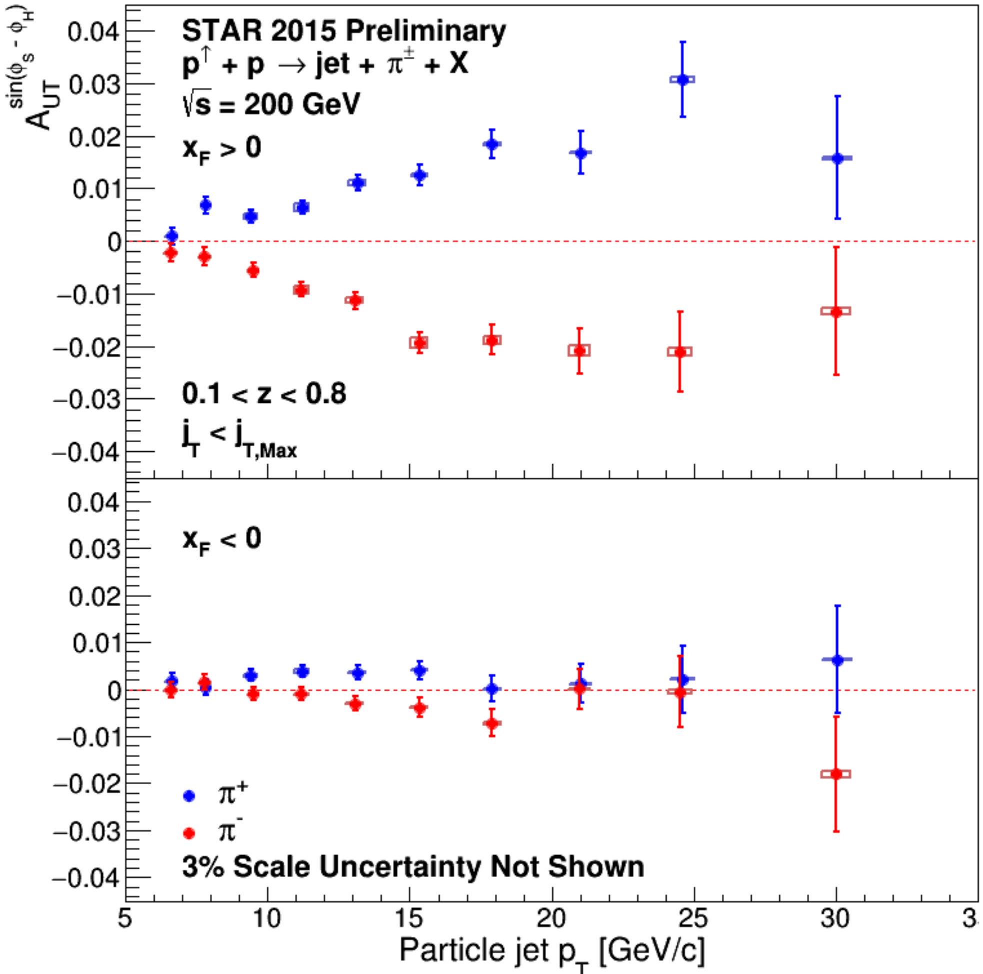

Fig. 2. Preliminary STAR Collins asymmetries in $\sqrt{s}$ = 200 GeV *pp* collisions for π^+ (blue) and π^- (red) as a function of particle-jet p_T.

Finally, we continue to carry various administrative responsibilities for STAR. Dr. Gagliardi is one of the two conveners of the STAR Cold QCD and Spin Physics Working Group. He is also serving on the god-parent committee for a STAR paper that describes measurements of weak boson cross sections and cross-section ratios in *pp* collisions at $\sqrt{s}$ = 510 GeV. Dr. Lin is serving as the software coordinator for the EEMC. He also served as STAR Period Coordinator for three weeks during the current RHIC run.

[1] J. Adam *et al*. (STAR Collaboration), Phys. Rev. D **100**, 052005 (2019).

SECTION II

HEAVY ION REACTIONS

A next generation study of the low density nuclear equation of state

K. Hagel, B. Harvey, A. Jedele, R. Wada, A.B. McIntosh, S.J. Yennello, J. Gauthier, L.A. McIntosh,
A. Hood, A. Hannaman, Z. Tobin, A. Abbott, M. Sorensen, and Y.-W. Lui

Characterization of the nuclear equation of state ranks among the most sought after information in all of nuclear physics. In particular, understanding the behavior of nuclear matter at low density has important implications in nuclear astrophysics because it has been shown that core collapse supernovae sample similar low density and temperature regions as those that can be created in the lab with heavy ion collisions [1-3].

A recent study reactions of 47 MeV/u ^{40}Ar + ^{112,124}Sn isolated a so-called femtonova, a hot source of early emitted light particles [4-8] that result from nucleon-nucleon collision. Coalescence analysis with an equilibrium assumption suggests that a very low density region is formed and that the time evolution of the reaction can be followed [9]. In particular, references [4, 7, 8] employed equilibrium constants of d, t, ^{3}He, and ^{4}He to compare to those of various astrophysical calculations and provided constraint on the assumptions of those models.

To study low density nuclear matter in more detail we note that correlation functions are another method that can be employed to extract an estimate of the size of the source. The size of the source extracted from a correlation function should reflect the size extracted using the coalescence model. If the two agree we will be able to put both methods on a firm footing. If the two methods are shown to not agree, we will be presented with an opportunity to gain further insight into results from coalescence analyses.

We have performed simulations that suggest that strip detectors in the angular region where particle production is dominated by products from the femtonova source provide adequate angular resolution to reconstruct a correlation function with sufficient accuracy.

To begin this process, we have acquired some sample silicon wafers that are of the same specifications as the silicon detectors used in the FAZIA [10] detector array. We are in the beginning stages of mounting and then testing these detectors to ensure that they meet the resolution needs to extract the correlation functions. Assuming a positive outcome, we are in discussion with CIS [11] in Germany to construct strip detectors using silicon wafers of similar specifications.

[1] E. O'Connor *et al.*, Phys. Rev. C **75**, 055803 (2007).
[2] M. Hempel *et al.*, Astrophys. J. **748**, 70 (2012).
[3] T. Fischer *et al.*, Eur. Phys. J. A **50**, 46 (2014).
[4] L. Qin *et al.*, Phys. Rev. Lett. **108**, 172701 (2012).
[5] R. Wada *et al.*, Phys. Rev. C **85**, 064618 (2012).
[6] K. Hagel *et al.*, Phys. Rev. Lett. **108**, 062702 (2012).
[7] K. Hagel *et al.*, Eur. Phys. J. A **50**, 39 (2014).
[8]. M. Hempel *et al.*, Phys. Rev. C **91**, 045805 (2015).
[9]. J. Wang *et al.*, Phys. Rev. C **72**, 024603 (2005).
[10] L. Bardelli *et al.*, Nucl. Instrum. Methods Phys. Res **A605**, 353 (2009);

FAZIA project: http://fazia.in2p3.fr.
[11] see https://www.cismst.de

A study of alpha knockout processes in alpha conjugate nuclei

R. Wada, A. Jedele, S.J. Yennello, K. Hagel, A.B. McIntosh, J. Gauthier, L.A. McIntosh, A. Hannaman, Z. Tobin, A. Abbott, M. Sorensen, A. Hood, B. Harvey, Y.-W. Lui, S. Hudan, and R.T. de Souza

Alpha clustering in nuclei has long been a topic of interest. Numerous works, both theoretical and experimental, shown evidence for cluster behavior [1-3]. Our group has performed a series of measurements on alpha conjugate nuclei in which we have shown that alpha conjugate nuclei have a propensity to break into alpha particles or other alpha conjugate nuclei [4-6].

We have embarked on a new experiment to further elucidate alpha clustering in alpha conjugate nuclei. We employ 60 MeV/u α-particles on various alpha conjugate nuclei and search for α - α elastic collisions in the reactions. We achieve this by searching for α - α coincidences where the summed energy of two α-particles traveling at 180° in the α - α center of mass frame (identical to the nucleon-nucleon center of mass frame, $\frac{1}{2}v_p$) is equal to the beam energy. Such processes would indicate that the impinging α- particle is, indeed, colliding with an alpha particle in the target nucleus. The experiment is similar in nature to a study reported many years ago [7].

The experiment is done using NIMROD [8], a 4π array composed of Silicon detectors and CsI crystals with photomultiplier readout having angles ranging from 3.6° to 170°. Particle identification is achieved using pulse shape discrimination. For the purpose of this experiment, only the CsI detectors in the angular range of 3.6° to 90°are used. Simulations have shown that the back to back alpha particle events of interest will populate detectors in the angular region of $15 < \theta_{lab} < 90$. The detectors at the more forward angles will be read in as extra particle production may give further insight into the reaction mechanism. For example, the incoming alpha particle may knock out one alpha particle from the ^{12}C leaving an ^{8}Be which would subsequently decay.

We began a first survey experiment in which we bombarded the 60 MeV/u alpha particles on a ^{12}C target as well as a cellulose ($C_6H_{10}O_5$) target. The statistics are expected to be such that further beam time is necessary. The analysis of these data is in progress in order to gain a sense of the level of statistics achieved as well as to refine the experiment if necessary.

[1] K. Ikeda *et al.*, Prog. Theor. Phys. Suppl. E, **68**, 464 (1968).
[2] M. Freer, Rep. Prog. Phys., **70,** 2149 (2007).
[3] W. von Oertzen *et al.*, Phys. Rep., **432**, 43 (2007).
[4] K. Schmidt *et al.*, Phys. Rev. C **95**, 054618 (2017).
[5] K. Schmidt *et al.*, Il Nuovo Cimento **39 C,** 394 (2017**).**
[6] K. Schmidt *et al.*, Eur. Phys. J. Web of Conferences **117**, 07021 (2016).
[7] B. Gottshcalk and S. L. Kannenberg, Phys. Rev C **2**, 24 (1970).
[8]. S. Wuenschel *et al.*, Nucl. Instrum. Methods Phys. Res. **A604,** 578 (2009).

Slope temperatures in Kr + C

A.B. McIntosh

Reactions of ^{78,86}Kr + ^{12}C @ 15, 25, 35 MeV/u have been carried out. Light charged particles were measured with the Forward Array Using Silicon Technology (FAUST), and heavy residues were measured in the Quadruple Triplet Spectrometer. The aim of the measurement is to investigate the asymmetry dependence of the nuclear caloric curve observed in [1-4].

Calibration of the data recorded for the reactions of ^{78,86}Kr + ^{12}C @ 15, 25, 35 MeV/u is well underway. Particle identification (PID) has been achieved for several detectors in rings C, D, and E of FAUST. Preliminary energy calibrations of the silicon detectors were obtained using ^{228}Th alpha source data and elastically scattered hydrogen and helium beams to calibrate the silicon detectors. Preliminary energy calibrations for the thallium-doped cesium iodide detectors coupled to photodiodes were obtained using the silicon calibration, the PID, and energy loss calculations. Preliminary calibration of the velocity of the heavy residues in the QTS has been carried out using cable timing delays anchored by the peak corresponding to elastically scattered beam particles.

Fig. 1 shows the 2-dimensional velocity distribution (transverse and parallel to the beam direction) of alpha particles measured in the calibrated detectors of rings C, D, and E of FAUST for reactions of ^{78}Kr + ^{12}C @ 35 MeV/u. There is an obvious Coulomb ring centered around 7.5 cm/ns, which

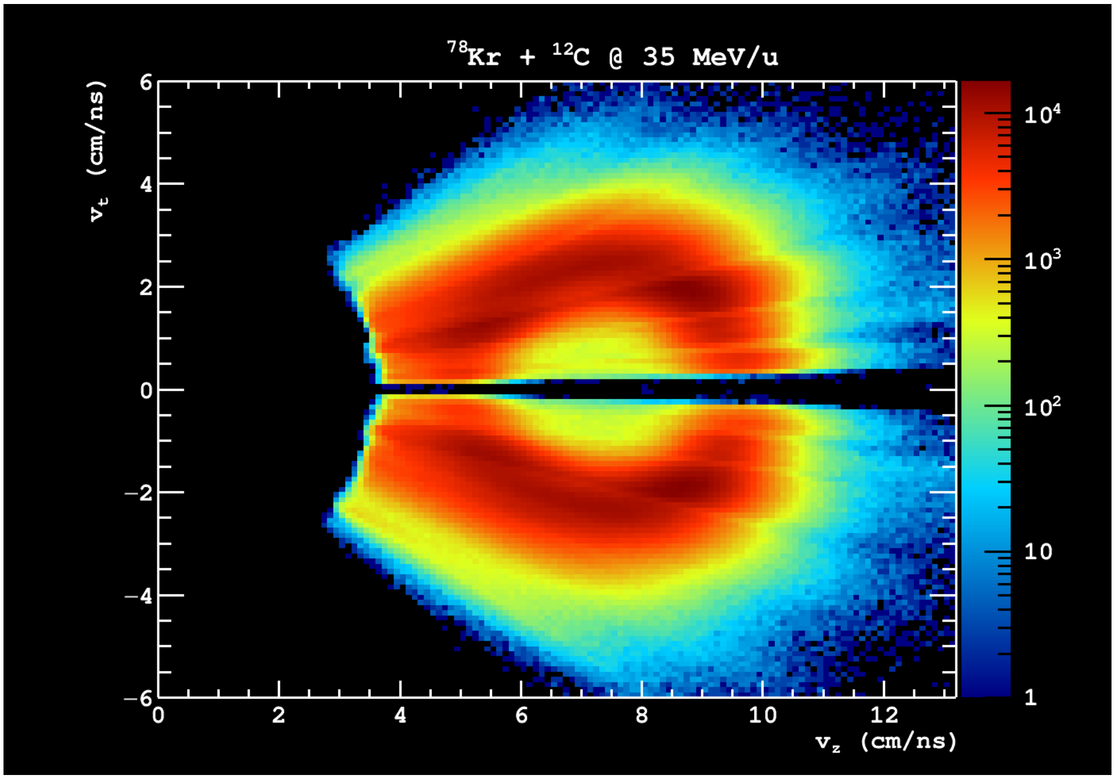

Fig. 1. 2D velocity distribution for alpha particles produced in reactions of ^{78}Kr + ^{12}C @ 35 MeV/u measured in FAUST.

is slightly damped from the 8.2 cm/ns beam velocity. Such a structure is expected when incomplete fusion takes place followed by charged particle evaporation. The evaporated charged particles are emitted with a Boltzman-like momentum distribution and receive a boost due to Coulomb repulsion from the heavy residue. This gives rise to a ridge centered around the average velocity of the residue with a de-populated Coulomb hole inside.

Further evidence for this mechanism is shown in Fig. 2. Here the yield of alpha particles is plotted as a function of the energy of the alpha particle in the frame of the coincidently measured heavy residue. This yield is shown for all alpha particles measured between 0 and 140 degrees in polar angle in the source frame (top distribution). This yield is also shown below for angular ranges every 10° (0-10°, 10-20°, 20-30° etc.). The shape, and particularly the exponential slope, does not show a dependence on

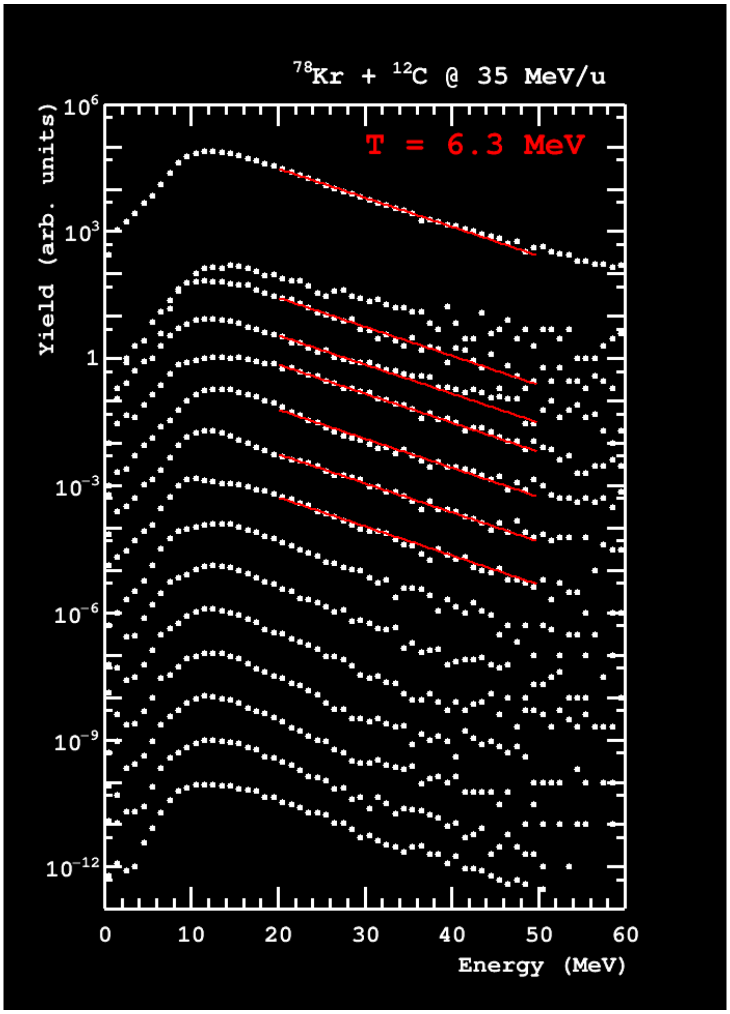

Fig. 2. Energy distributions of alpha particles in the frame of the heavy residue for reactions of ^{78}Kr + ^{12}C @ 35 MeV/u. Uppermost data points are integrated from 0° to 140° in polar angle in the source frame. Successively lower series of data point span the angular ranges 0-10°, 10-20°, 20-30° etc. up to 130-140°. Each data series is scaled by some factor to allow the shapes of the distributions to be compared. The red line corresponds to an exponential fit in between 20 and 50 MeV; these indicates a slope temperature of 6.3 MeV.

the angle. The yields are scaled by an arbitrary factor to allow comparison of their shape. The red overlaid line corresponds to an exponential fit between 20 and 50 MeV, with a slope temperature indicating 6.3 MeV.

Preliminary slope temperatures for alpha particles have been calculated also for ^{78}Kr + ^{12}C @ 15, 25 MeV/u as well, and all are plotted on the vertical axis in Fig. 3. The excitation energy for each system is deduced from the velocity damping according to the following equation [5,6]

$$\frac{E^*}{A} = \frac{1}{2}(v_B - v_R)v_R + Q$$

using the measured mean velocity of the heavy residues v_R (using a rough preliminary estimate), the velocity of the beam v_B and the Q value of the reaction that forms the compound nucleus from the target and projectile. The slope temperature clearly rises with the excitation energy.

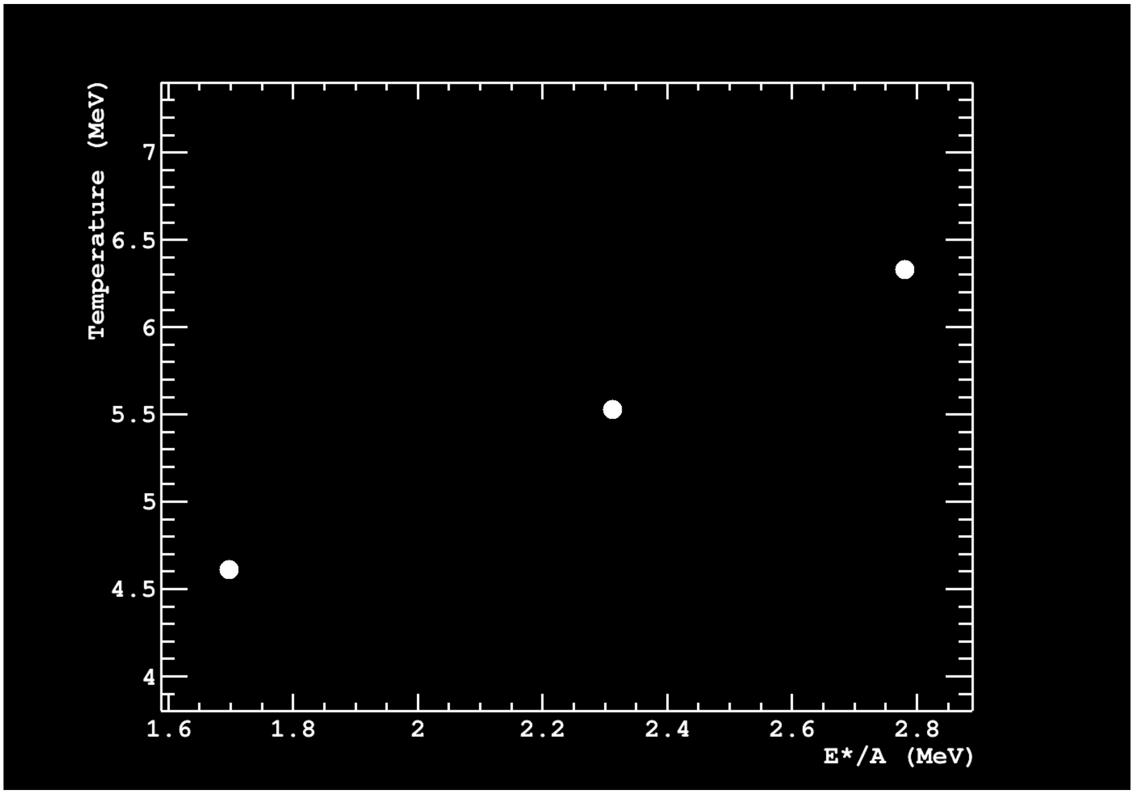

Fig. 3. Preliminary slope temperatures for alpha particles versus the excitation energy of the compound nucleus for ^{78}Kr + ^{12}C @ 15, 25, 35 MeV/u. Uncertainties have not been extracted since the calibrations are at this point preliminary.

Further work is underway to obtain reliable calibrations for all light charged particles and light intermediate mass fragments for all possible detectors, both for the ^{78}Kr + ^{12}C systems and the ^{86}Kr systems. This will then allow comparison of thermometric data for the neutron rich and neutron poor systems.

[1] A.B. McIntosh *et al.*, Phys. Lett. B **719**, 337 (2013).
[2] A.B. McIntosh *et al.*, Phys. Rev. C **87**, 034617 (2013).

[3] A.B. McIntosh *et al.*, Eur. Phys. J. A **50**, 35 (2014).

[4] A.B. McIntosh *et al.*, *Progress in Research*, Cyclotron Institute, Texas A&M University (2017-2018) p. IV-27

[5] W. Bohne *et al*., Phys. Rev. C **41**, R41 (1990).

[6] K. Hagel, Ph.D Thesis, Texas A&M University, 1986.

The effect of nuclear reaction dynamics on isoscaling properties

A. Hannaman, A.B. McIntosh, A. Jedele, J. Gauthier, K. Hagel, Z. Kohley, L.A. McIntosh,
R. Wada, M. Youngs, and S.J. Yennello

Isoscaling is a method that seeks to extract information about the asymmetry energy in the nuclear equation of state by comparing integrated yields of isotopes from two reaction systems that differ only in their isospin makeup according to the exponential scaling law $R_{21} = Y_2(N,Z)/Y_1(N,Z) = Cexp(\alpha N + \beta Z)$, where Y_2 is the yield from the more neutron-rich system and Y_1 is the yield from the less neutron-rich system while C, α, and β are fit parameters [1]. This methodology is typically applied under statistical and thermal equilibrium assumptions. However, molecular dynamics model studies have shown that isoscaling accurately describes fragment yields early in the reaction process where dynamical processes occur [2]. We have reported on an investigation as to how well isoscaling describes dynamically produced fragments in an experimental setting [3]. Further, by using the orientation of binary projectile-like fragment (PLF*) decays, we were able to distinguish between fragments primarily produced dynamically and statistically, showing how isoscaling properties change as a function of the mechanism of fragment production [3].

The systems used in this study were symmetric collisions of ^{70}Zn + ^{70}Zn and ^{64}Zn + ^{64}Zn [4]. In both systems, the beam was accelerated to 35 MeV/u by the K500 Cyclotron at Texas A&M University and was impinged on a thin target [4]. Reaction products were measured in NIMROD (Neutron Ion Multidetector for Reaction Oriented Dynamics) [5, 6]. The angle of PLF* rotation θ_{prox} = acos $[\vec{v}_{CM} \cdot \vec{v}_{REL}/(\| \vec{v}_{CM} \| \| \vec{v}_{REL} \|)]$ after separation from the target-like fragment (TLF*) and prior to binary breakup into the HF and LF is depicted in Fig. 1(b). The velocity vectors used in the calculation of θ_{prox} are the two-fragment center-of-mass velocity $\vec{v}_{CM} = (m_{HF}\vec{v}_{HF} + m_{LF}\vec{v}_{LF})/(m_{LF} + m_{HF})$ and the relative velocity between the HF and LF $\vec{v}_{REL} = \vec{v}_{HF} - \vec{v}_{LF}$. The LF yield distribution in Fig 1(c) shows excess yield at low θ_{prox} due to the dynamical process described favoring PLF* breakup aligned with the PLF*-TLF* separation axis.

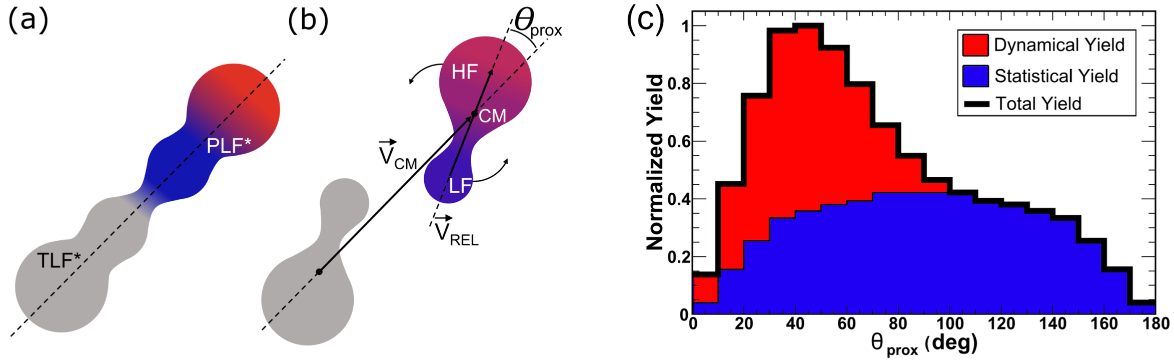

Fig. 1. Illustration depicting dynamical projectile and target interaction and decay. (a) Deformed PLF* and TLF* during the interaction. (b) At a later time, the PLF* will break after rotating relative to the TLF* (measured by the angle α) forming a heavy fragment (HF) and light fragment (LF) in the exit channel. The blue region denotes neutron richness while the red region denotes neutron deficiency. (c) The dynamical (red) and statistical (blue) fragment production yield distribution for the LF with $\boldsymbol{Z_L}$ = 6 in events with a measured $\boldsymbol{Z_H} \geq 12$ as a function of $\boldsymbol{\theta_{prox}}$.

In this work, focus was placed on isoscaling the LF with $4 \leq Z_L \leq 8$ in events containing a $Z_H \geq 12$. The isoscaling parameters α and $|\beta|$ obtained from fitting the isotopic yield ratios of the dynamically and statistically produced fragments as a function of θ_{prox} are shown in Fig 2.

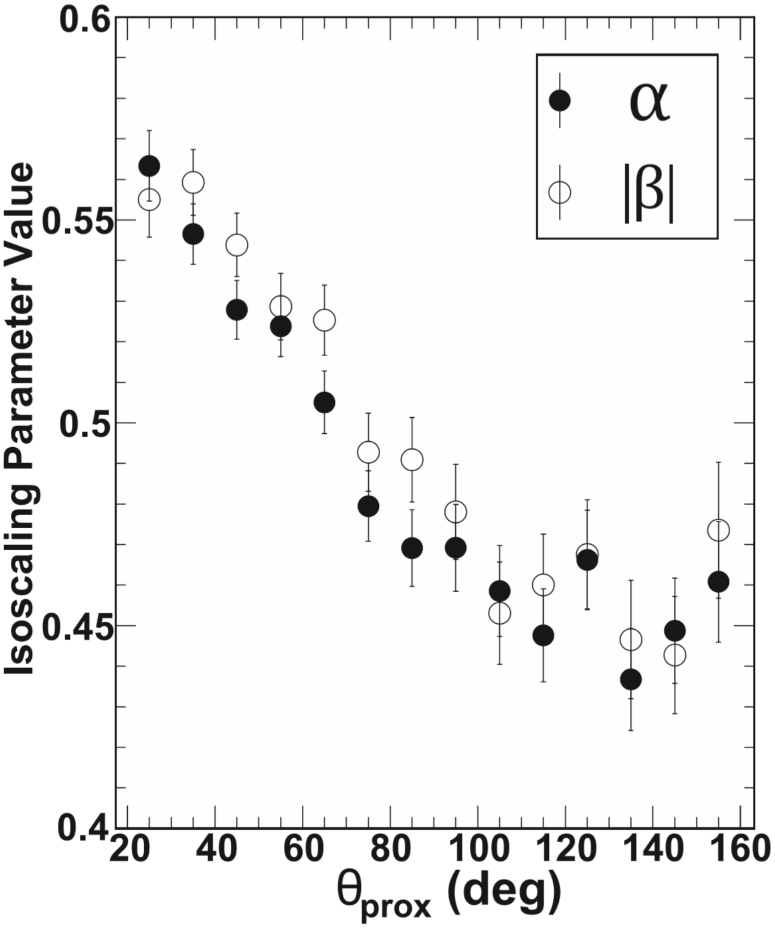

Fig. 2. Isoscaling parameters α and |β| as a function of $\boldsymbol{\theta_{prox}}$ for the total dynamical and statistical yield of $\mathbf{4} \leq \boldsymbol{Z_L} \leq \mathbf{8}$. Error bars contain statistical error from the fitting of R_{21} values.

The value of α is largest at θ_{prox} = 25° with a value of 0.563 ± 0.009 and decreases to an average value of 0.460 ± 0.008 in the statistical region of 80° < θ_{prox} < 160°. This decrease in α and |β|can be understood by the dynamics of the reaction mechanism. θ_{prox} functions as a clock for the extent of N-Z equilibration as described in prior work [7,8]. Smaller angles of θ_{prox} correspond to fragments originating from a largely unequilibrated system. Large values of α indicate that the difference in the mean of the mass distributions for the two systems is great relative to the width. The mass distributions are less aligned for dynamically produced fragments and are more aligned for statistically produced fragments. This directly supports the argument that neutrons are initially attracted to the low-density neck formed in the dynamic interaction, with this attraction being greater for the more neutron-rich system, and relaxing over time as the density gradient allows it to. The validity of the isoscaling model to dynamically produced fragments is a nontrivial result. Moreover, other transport model studies have shown similar isoscaling characteristics explicitly as a function of time [2].

The typical method of invoking statistical and thermodynamic equilibrium assumptions for the extraction of the asymmetry energy are difficult to apply to these results, as the system is evolving dynamically, and significant density gradients exist. However, dynamical transport models can produce data sets that can be treated in the same way as experimental data. These models can use different asymmetry energy inputs for comparison to this experimental result to determine which asymmetry energy is closest to reality. A more detailed description of these results can be found in the publication [3].

[1] M.B. Tsang *et al.,* Phys. Rev. Lett. **86**, 5023 (2001).

[2] C.O. Dorso *et al.,* Phys. Rev. C **74**, 044601 (2006).

[3] A. Hannaman *et al.,* Phys. Rev. C **101**, 034605 (2020).

[4] Z. Kohley, Ph.D. thesis, Texas A&M University, 2010, http://hdl.handle.net/1969.1/ETD-TAMU-2010-08-8495.

[5] R.P. Schmitt *et al.,* Nucl. Instrum. Methods Phys. Res. **A354**, 487 (1995).

[6] S. Wuenschel *et al.,* NIMRODISiS, Nucl. Instrum. Methods Phys. Res. **A604**, 578 (2009).

[7] A. Jedele *et al.,* Phys. Rev. Lett. **118**, 062501 (2017).

[8] A. Rodriguez Manso *et al.,* Phys. Rev. C **95**, 044604 (2017).

Time dependency of angular alignment

B.M. Harvey, M. Youngs, A.B. McIntosh, A. Jedele, R. Wada, and S.J. Yennello

In an experiment performed at Texas A&M University's Cyclotron Institute [1,2], a ^{70}Zn projectile beam was impinged on a ^{70}Zn target at 35 MeV/nucleon. During the collision, the projectile nucleus becomes an excited, deformed projectile-like fragment (PLF*). Before the PLF* separates from the target fragment, a low-density region between it and the target can form. This low-density region tends to be neutron-rich due to the action of the asymmetry energy. Part of this neutron-rich region can separate from the target as a relatively neutron-rich portion of the PLF*. The rate at which the nucleons redistribute themselves to reach chemical equilibrium is impactful to studies on the Nuclear Equation of State. This process occurs on the zeptosecond timescale, making it infeasible to take a direct measurement of this rate experimentally. Therefore, these experiments rely on the premise that angular alignment, α, which characterizes how much the PLF* rotates before breaking apart, is correlated linearly with the PLF* lifetime, Δt. The PLF* lifetime is the time that the equilibration process is allowed to continue before the PLF* breaks apart. The work presented here utilizes simulated nuclear collisions, through the Constrained Molecular Dynamics (CoMD) model, to properly characterize and quantify the dependency of α on Δt.

Like the experiment, we focus on the case where the breakup occurs dynamically and the PLF* separates into predominantly two primary fragments, the heaviest fragment (HF) and the lighter fragment (LF). The alignment angle is defined from these fragments' velocity.

$$\alpha = \arccos \frac{\overrightarrow{v_{cm}} \cdot \overrightarrow{v_{rel}}}{|\overrightarrow{v_{cm}}| \cdot |\overrightarrow{v_{rel}}|}$$

$$\overrightarrow{v_{cm}} = \frac{m_{HF}\overrightarrow{v_{HF}} + m_{LF}\overrightarrow{v_{LF}}}{m_{HF} + m_{LF}}$$

$$\overrightarrow{v_{rel}} = \overrightarrow{v_{HF}} - \overrightarrow{v_{LF}}$$

Two methods were used to study the same data set generated from CoMD simulations. The first method, called the Tree Method, was developed to directly track and identify fragments of interest through CoMD events. In particular, this tool was used to identify the PLF* at its time of separation from the target and the subsequent HF and LF when it decays at the time of its breakup. From this data, α and Δt (time from PLF* formation to PLF* breakup) can be found event-wise. The second analysis method implements the experimental assumptions, where the heaviest two fragments found at the end of the event are assumed to be the HF and LF. This analysis method has the same drawback as the actual experiments. In both cases, the PLF* lifetime is not directly measured, but the comparison of the results from both methods gives insight into the details of the dynamics.

Fig. 1 shows the angular distribution for two different collision energies and each analysis method modelled by a 3-term fit, including a sinusoidal statistical peak, a dynamic peak and a correctional flipped peak.

$$Y(\alpha) = A\sin\alpha + BY_{dyn}(\alpha) + CY_{dyn}(180^\circ - \alpha)$$
$$Y_{dyn}(\alpha) = \frac{1}{\sigma^2}\alpha e^{-\frac{\alpha^2}{2\sigma^2}}$$

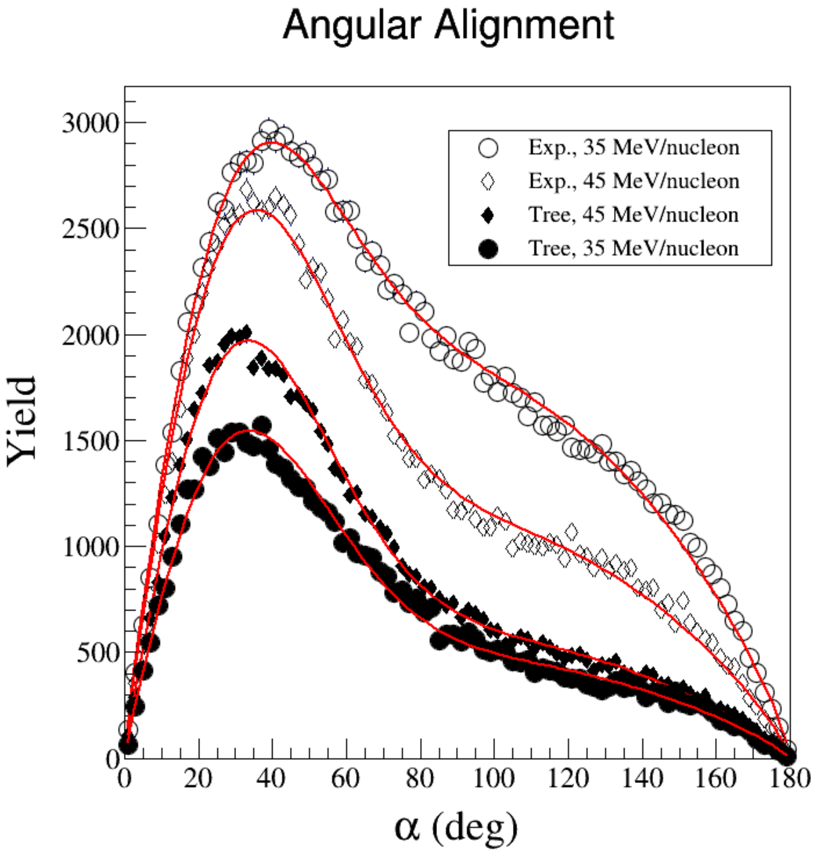

Fig. 1. Angular alignment for 35 and 45 MeV/nucleon simulated collisions utilizing the experimental assumptions (circles) and Tree Method (diamonds).

The model is shown to fit the data well for each distribution and demonstrates that the Tree Method is more selective to the dynamic events we are interested in, especially in the lower energy collisions. This model allows for the extraction of the average alignment angle due to dynamic breakup from the fit parameter, σ, as a function of PLF* lifetime. Fig. 2 shows α versus Δt, as well as the average alignment angle as blue data points, and the average alignment angle in the dynamic peak, $\langle\alpha_{dyn}\rangle$, are shown as black data points for both 35 and 45 MeV/nucleon collisions. The relationship between $\langle\alpha_{dyn}\rangle$ and Δt is explored through a linear fit and for both energies. It was found that $\frac{d\langle\alpha_{dyn}\rangle}{d\Delta t} = 2.0 \pm 0.2\frac{rad}{zs}$, demonstrating a correlation between angular alignment and PLF lifetime in good agreement with the assumptions used in [1,2].

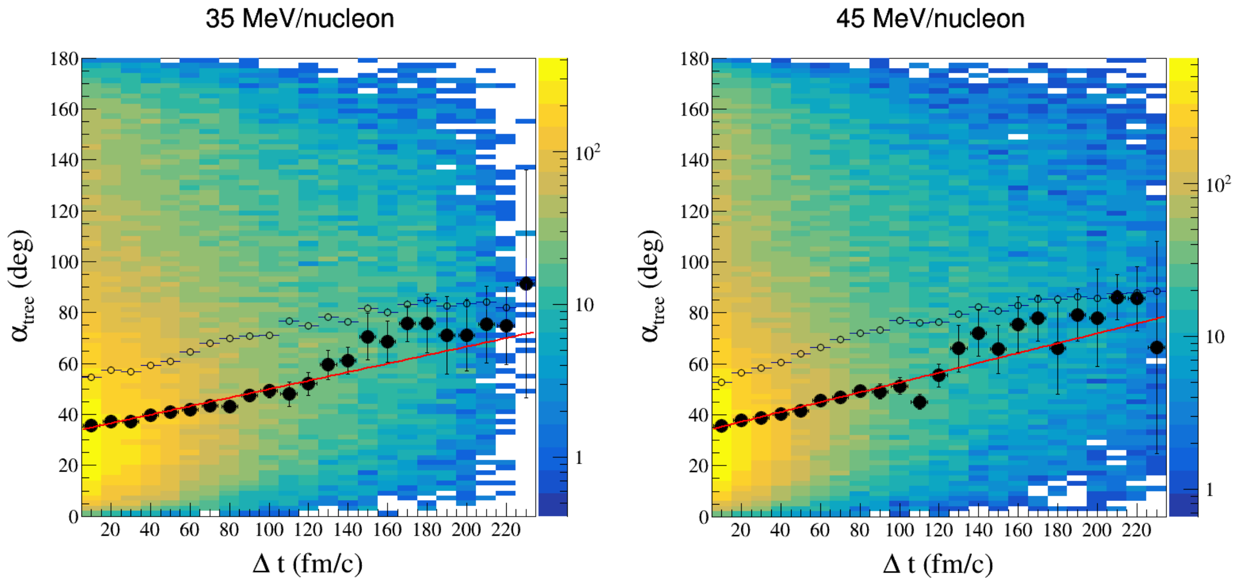

Fig. 2. Angular alignment versus time for 35 (left) and 45 (right) MeV/nucleon collisions utilizing the tree method. The solid data points show how the average alignment angle in the dynamic peak as a function of time, and the open data points represent the average of value in the entire angular alignment distribution as a function of time.

[1] A. Jedele *et al.*, Phys. Rev. Lett. **118**, 062501 (2017).

[2] A. Rodriguez Manso *et al.*, Phys. Rev. C **95**, 044604 (2017).

Experimental study of liquid-gas phase transition in Xe+Sn at 50A MeV

R. Wada, Guoyu Tian, Xueying Liu, Weiping Lin, Xingquan Liu, K. Hagel, and A. Chbihi

The experimental liquid-gas phase transition is studied for A~120 Quasi-Projectile(QP) system, using GANIL data of ^{129}Xe+^{nat}Sn at 50 MeV/nucleon, taken with a 4π detector array INDRA. The experimental details and data analysis are given in Refs.[1-4]. The methods used for characterizing the QP and constructing the caloric curve for this liquid-gas phase transition study are essentially same as those of the previous study, where the QP is reconstructed from the reactions of ^{40}Ar+^{27}Al, ^{48}Ti, ^{58}Ni at 47 MeV/nucleon, taken with NIMROD [5].

In order to characterize the QP source, a moving source analysis is used. In this study, the event centrality classification is made according to the mass of the projectile-like fragments, which has Z ≥ 3 with $v_z \geq 0.75\ v_{Beam}$, where v_z is the velocity of the fragment at the beam direction. All events are classified by ZBin=Z_{PLF}/10 from ZBin=0 to 4. Those with Z_{PLF}>=50 are included in ZBin4. In order to select out the QP particles, the velocity distribution of light charged particles are examined, which is shown in Fig.1 for p, d, α for ZBin=0, 2, 4. As one can see in the case of α particles, a well developed

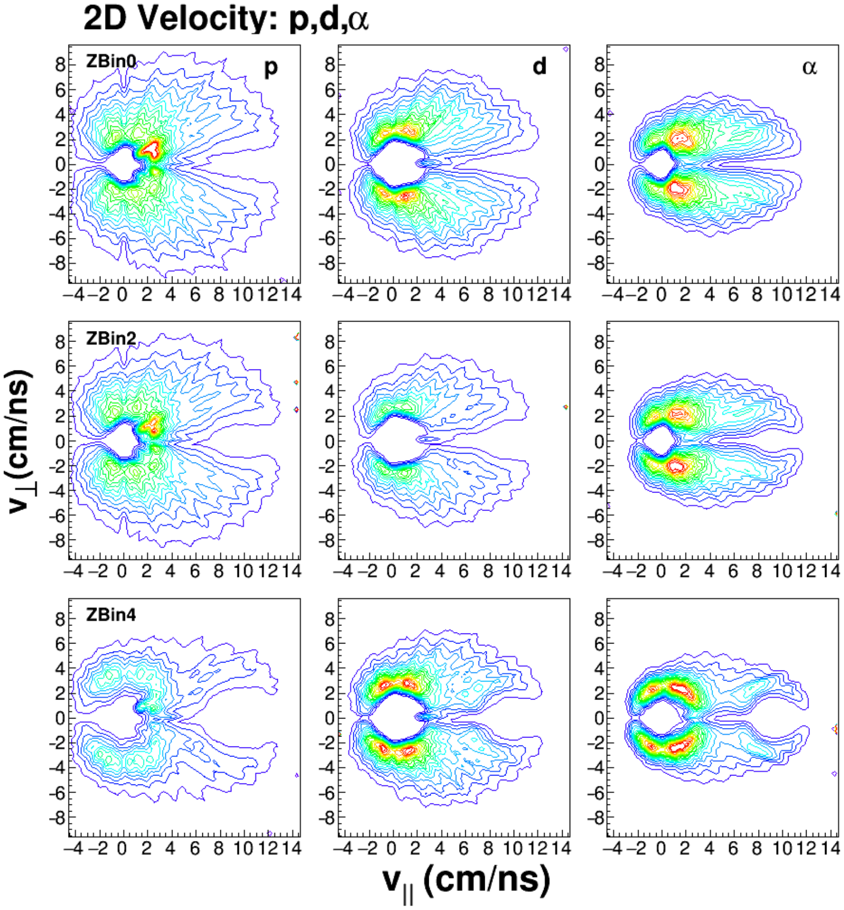

Fig. 1. Galilean invariant velocity distribution for p,d, α (from left to right) for ZBin 0,2,4 (from top to bottom, as indicated. Z axis is an arbitrary unit in logarithmic scale.

Coulomb ring is observed for ZBin 4, in which an observed large projectile-like fragment (PLF) characterizes the QP events. On the other hand for ZBin 0 no such a Coulomb ring is observed, though many particles from a PLF source are observed. The Coulomb ring is less prominent for the lighter LCPs. For protons for all ZBins show a large Coulomb-like ring around the beam velocity, but this is caused by the fact that the most forward ring, Ring 1, in the INDRA array is not capable to identify p,d,t and all these particles are assigned as protons and therefore the yield of protons enhanced at the most forward angle and causing like a ring when the contour is smoothed between the neighboring rings. In order to reproduce these features, all particles are fit with four sources, a target-like source (TLF) with a very small velocity, an intermediate velocity source (IV) and two PLF sources. One of PLF sources represents a binary sequential decay source (PLFB) which shows a clear Coulomb ring and the other is to represent a multifragmented PLF source and therefore a Coulomb ring is significantly reduced or is not seen.

Typical results of the four source fits are shown in Fig.2 for p, α, and ^{12}C at selected angles from left to right for ZBin3, where differential multiplicity of a given particle is plotted as a function of kinetic

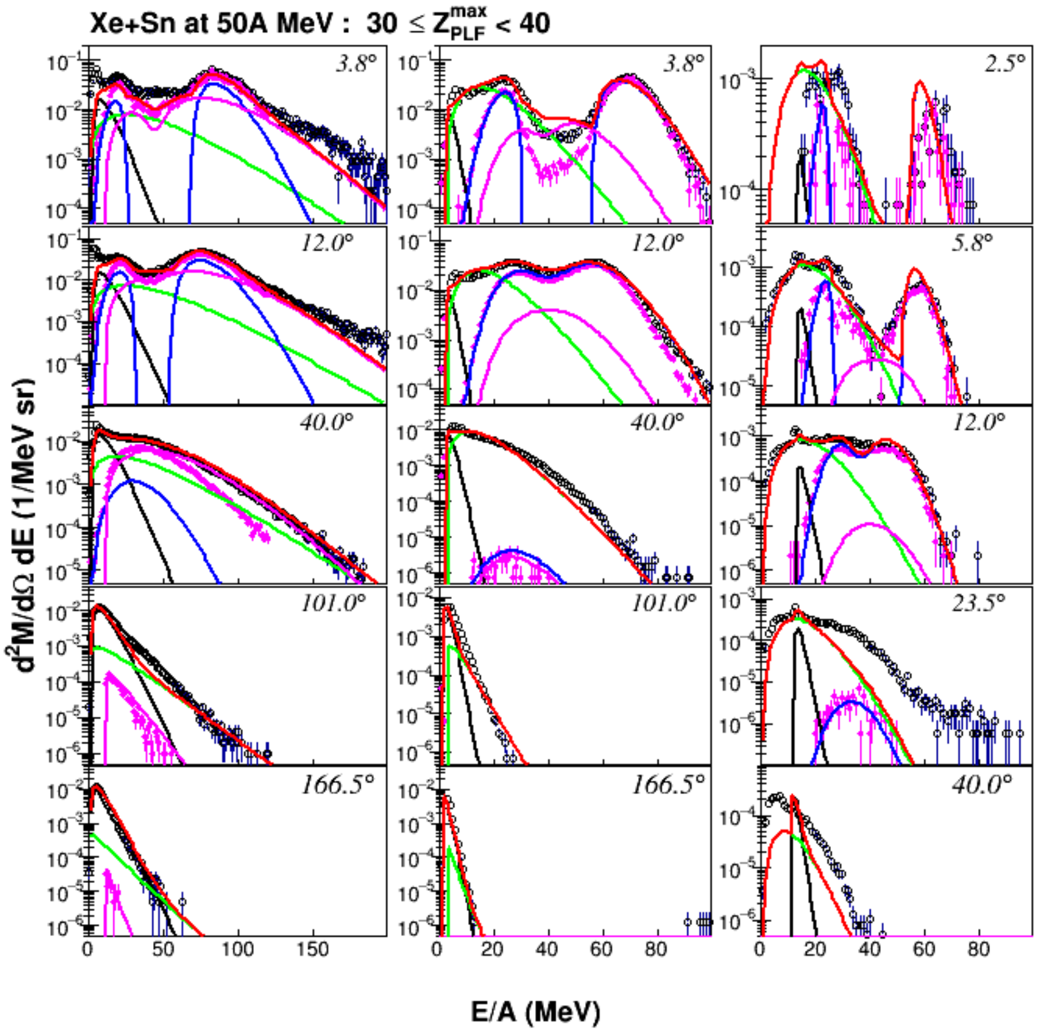

Fig. 2. Typical MS fits for p, α, and ^{12}C at the selective angles. See details in the text.

energy per nucleon (E/A) in the Laboratory frame. The experimental data are shown by black open circles. The curves are; TLF (black curves), IV (green), PLFB (blue), PLFM (magenta), sum of all four (Red). Generally, the PLF sources are dominated at forward angles of the energy spectra near the beam velocity. The binary PLFB dominates in ZBin4 events and multi-fragment PLFM dominates at ZBin0-2 as expected. For LCPs, the PLFB multiplicity becomes comparable to that of PLFM in ZBin3. The trends are similar for IMFs, but the multiplicity values change more drastically as ZBin changes, because in ZBin3-4, many of IMFs in PLFB are from a partner of the fission-like binary decay of the parent PLF and therefore accompanies with another large PLF.

In a similar manner in Ref.[5], the extracted moving source parameters are used to select out the QP particles, in which the MS fits are assumed to represent the probability of each component of each particle at a given angle. Using this probability selection method, the QP particles are selected as the PLFM+PLFB components from all particles in the entire energy and the entire angulaer range in each ZBin. The dots with magenta in Fig. 2 represent those QP particles.

The next step is to evaluate the excitation energy of the extracted QP source and their temperature will be evaluated, using the fluctuation thermometer to examine the caloric curves. The study is underway as a collaboration work of GANIL-TAMU-IMP.

[1] J. Pauithas *et al.*, Nucl. Instrum. Methods Phys. Res. **A357**, 418 (1995).

[2] J. Łukasik *et al.*, Phys. Rev. C **55**, 1906 (1995).

[3] N. Marie *et al.*, Phys. Lett. B **391**, 15 (1997).

[4] E. Plagnol *et al.*, Phys. Rev. C **61**, 014606 (1997).

[5] R. Wada, W. Lin, P. Ren, H. Zheng, X.Liu, M. Huang, K. Yang, and K. Hagel, Phys. Rev. C **99**, 024616 (2019).

^{93m}Nb target characterization for K-shell internal conversion coefficient measurements

E.E. Tereshatov,[1] K.J. Glennon,[1,2] V. Horvat,[1] N. Nica,[1] V.E. Iacob,[1] J.C. Hardy,[1,2] and C.M. Folden III[1,2]
[1]*Cyclotron Institute, Texas A&M University, College Station, Texas 77843,*
[2]*Department of Chemistry, Texas A&M University, College Station, Texas 77843,*
[3]*Department of Physics, Texas A&M University, College Station, Texas 77843*

Reliable nuclear decay schemes are important in fundamental physics, which also include information on internal conversion coefficients (ICC). This work is aimed at a target characterization that was specifically prepared for ICC measurements of ^{93m}Nb. This element represents the lowest atomic number and transition energy among those studied for K-shell ICC evaluation.

The molecular electroplating technique was successfully utilized in a series of target preparations for the ICC measurements performed in our group [1]. The same approach was used for the Nb target fabrication. To develop the Nb electrodeposition procedure, a non-radioactive inductively coupled plasma mass spectrometry (ICP-MS) standard niobium solution (1 mg/mL in nitric acid) was used. Isopropanol was chosen as the organic solvent for the target preparation. A 170 μL aliquot of the Nb standard solution was evaporated down to ~50 μL, diluted in 10 mL of isopropanol and transferred to the target cell. The Nb electrodeposition on an aluminum disk (2.275 cm^2, 10 μm thickness) was performed for 40 min with a stepwise increasing bias in the range from 500 V to 700 V. The prepared source (~50 μg air dried, shown in Fig. 1) was characterized at the Texas A&M University Materials Characterization Facility by means

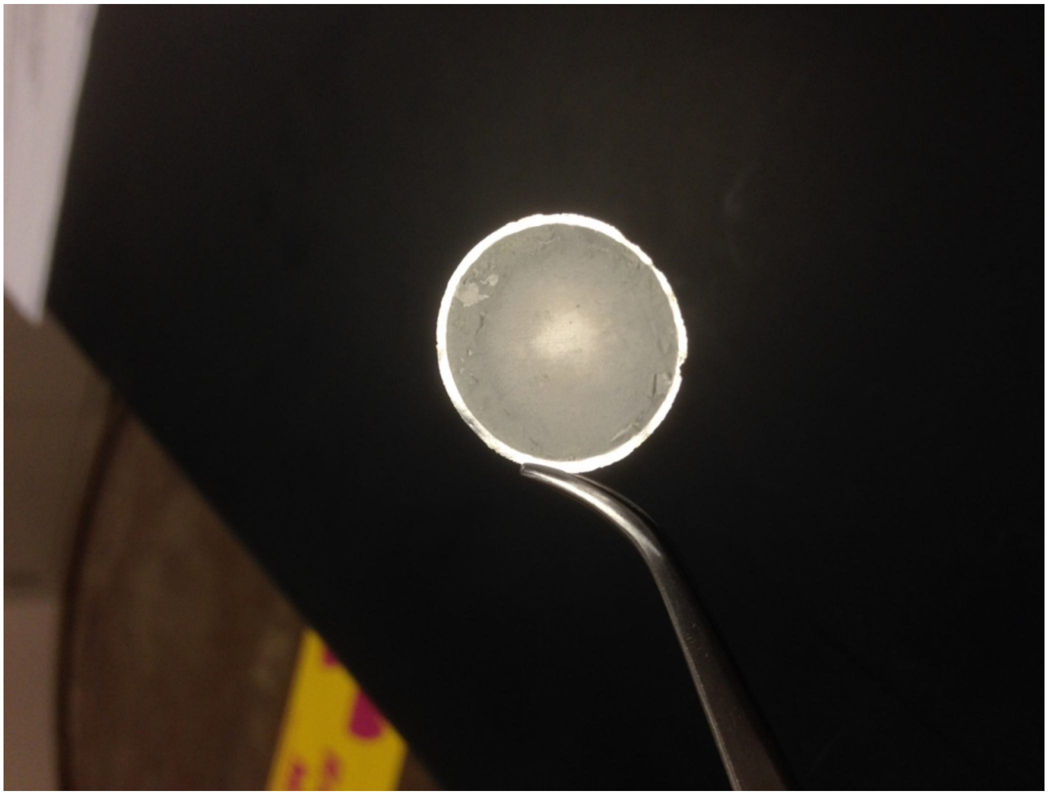

Fig. 1. Picture of Al-disk after stable Nb electrodeposition.

of scanning electron microscope (SEM), energy dispersive spectroscopy (EDS), and x-ray photoelectron spectroscopy (XPS), as well as by visual inspection of the color of deposited layer. Results of these analyses are shown in Figs. 2–4 and Tables I–II. Despite the presence of nitric acid, the EDS and XPS analyses showed that Nb was not electrodeposited as a corresponding nitrate salt. This conclusion is in agreement with literature data on electrodeposition of the metal [2-4]. However, trace amounts of HF in the ICP-MS standard lead to formation of a very stable oxyfluoro complex, $NbOF_3$ [5], which was most likely deposited along with niobium pentoxide, Nb_2O_5. Increasing the Nb content (1.3 mL aliquot of the Nb standard solution) and electrodeposition at an average current of 9.5 mA for the first 4 h followed by 3 h more at constant 800 V resulted in an overall electroplating yield of ~50 % [6]. The Nb concentration in the isopropanol solution was determined by neutron activation analysis.

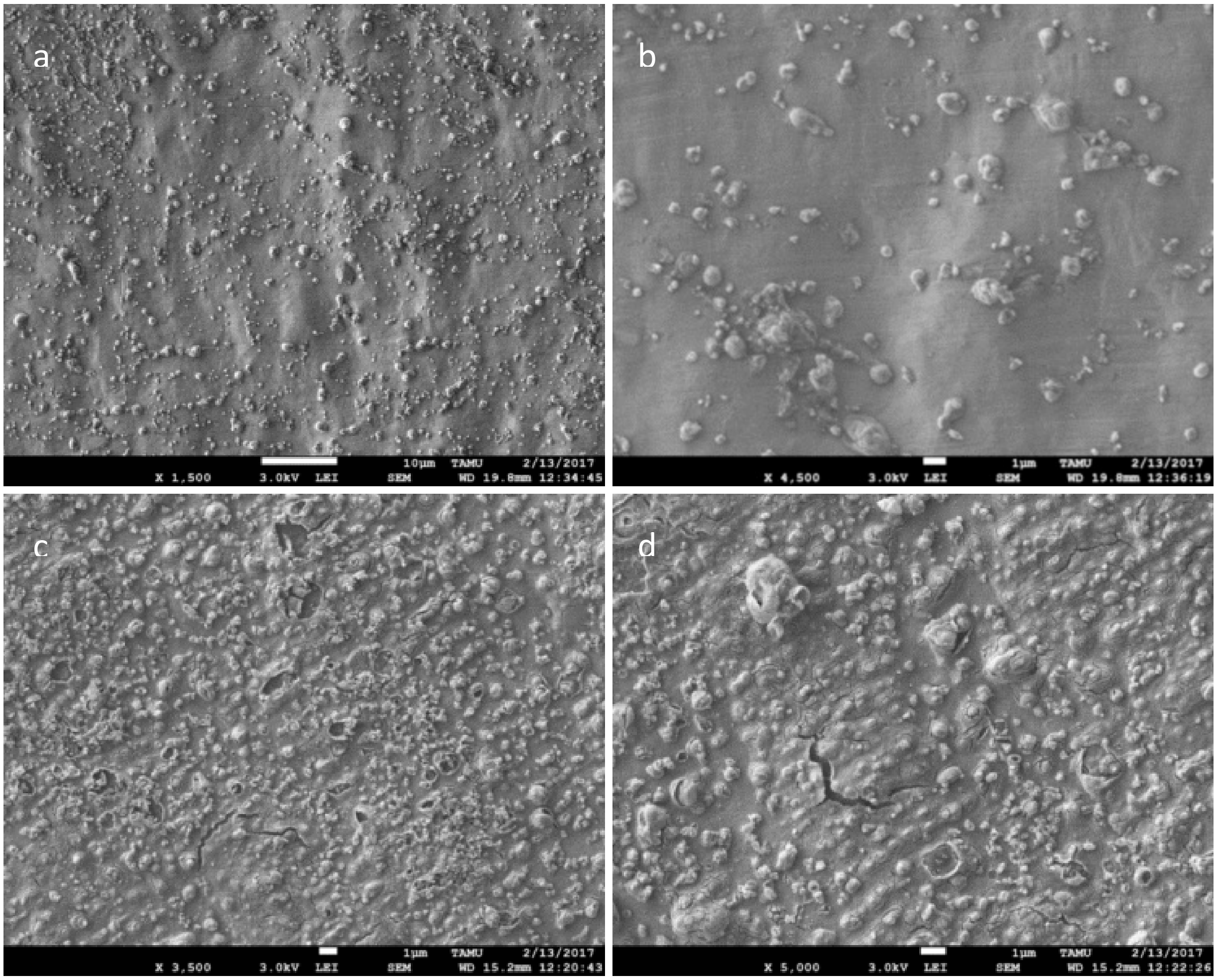

Fig. 2. SEM images of the Al disk at a) x1500 and b) x4500 magnification after bias was applied when pure isopropanol (no stable Nb) was in the target cell; SEM images of Al-disk at c) x3500 and b) x5000 magnification after bias was applied when isopropanol and Nb ICP-MS standard were in the target cell.

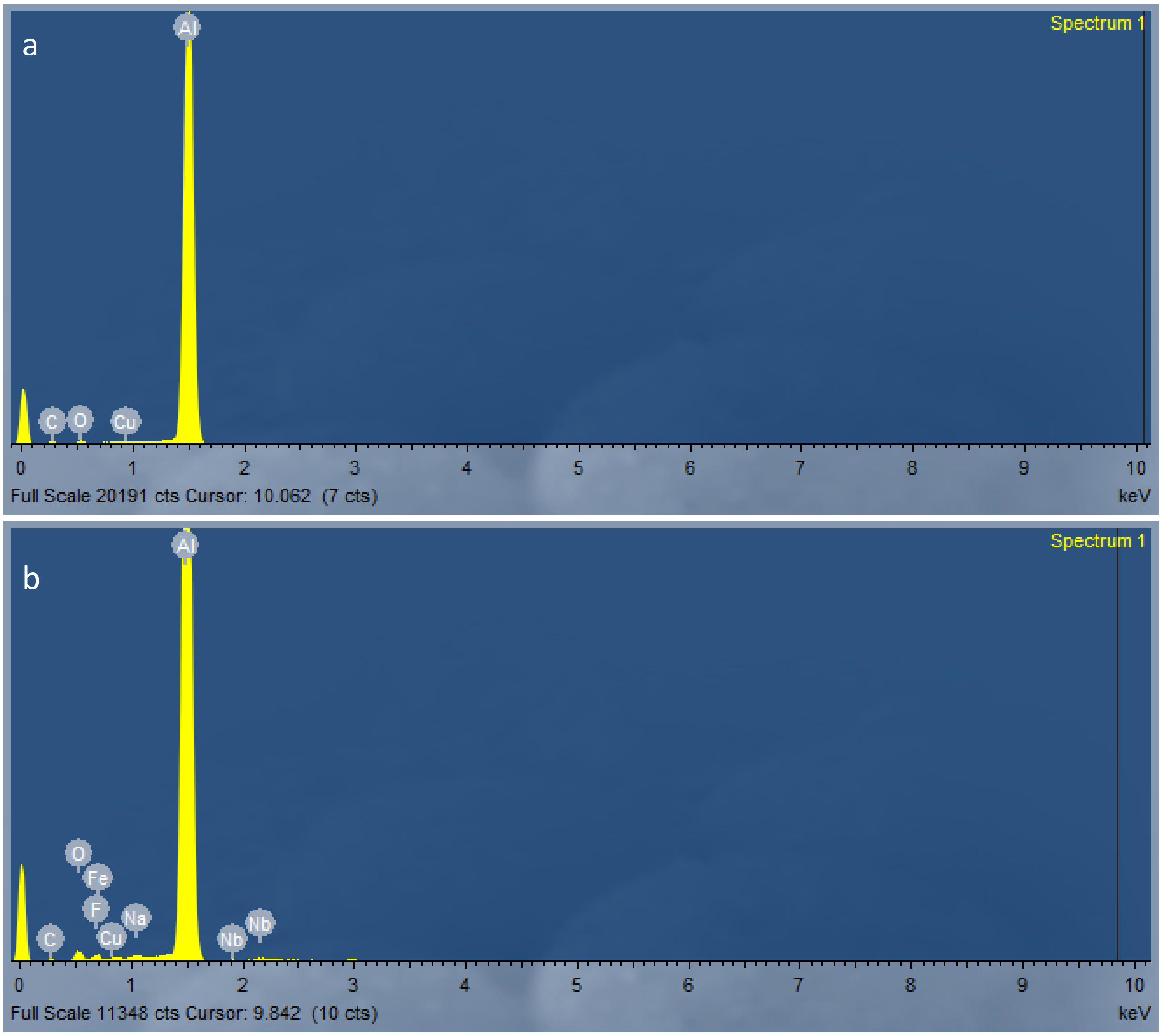

Fig. 3. EDS spectra of the Al disk corresponding to: a) SEM Fig. 2a [isopropanol (no stable Nb) was in the target cell] and b) SEM Fig. 2c (isopropanol and Nb ICP-MS standard were in the target cell).

Table I. EDS report attributed to the spectrum shown in Fig. 3a.

Element	**Approximate Concentration**	**Intensity Correction**	**Weight%**	**Weight% Sigma**	**Atomic%**
C K	10.54	0.1659	13.62	0.80	25.52
O K	10.84	0.5457	4.26	0.27	5.99
Al K	478.98	1.2506	82.12	0.79	68.49
Totals			100.00		

Table II. EDS report attributed to the spectrum shown in Fig. 3b.

Element	Approximate Concentration	Intensity Correction	Weight%	Weight% Sigma	Atomic%
C K	4.58	0.1640	6.17	0.75	12.21
O K	22.07	0.6155	7.92	0.30	11.77
F K	5.89	0.3998	3.26	0.21	4.07
Na K	3.12	1.4120	0.49	0.05	0.50
Al K	433.10	1.1863	80.67	0.73	71.06
Nb L	3.47	0.5135	1.49	0.19	0.38
Totals			100.00		

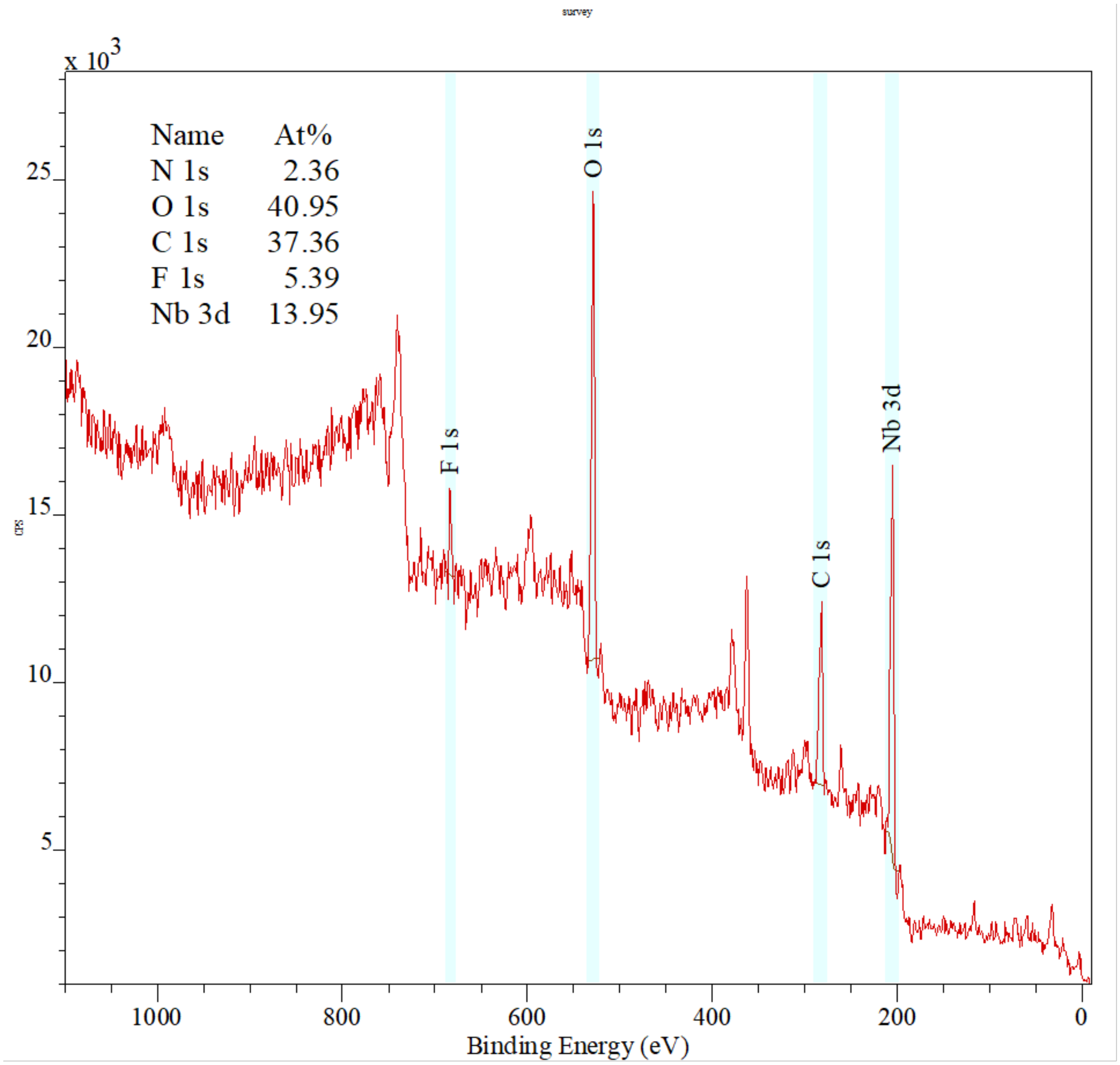

Fig. 4. XPS spectrum of Al-disk after stable Nb was electrodeposited from isopropanol.

After the preparatory step was finished, we purchased 0.85 mL of ^{93m}Nb (40 µCi) dissolved in 1 M HNO_3 + 0.3 M HF solution from Eckert and Ziegler Products, Atlanta, Georgia, USA. A small aliquot (10 µL) of the initial ^{93m}Nb solution was used to spike the solution in the target cell. During the electrodeposition, isopropanol aliquots were taken from the target cell and measured by an NaI γ-counter to simplify the control of electroplating. The efficiency of the Nb electrodeposition was optimized at a current density of 3-5 mA/cm^2, reaching ~95 % for 2 h in the case of relatively low carrier concentration.

The next step was to check the content of stable materials in the purchased ^{93m}Nb sample. For this purpose, an ICP-MS measurement with the radioactive sample was performed at Texas A&M University. The results (Fig. 5) show that the purchased ^{93m}Nb source had 4.1 ± 0.2 mg/mL of stable Nb carrier along with trace amounts of Sb and Ta that usually accompany stable Nb and most likely were added to the solution with the former. Also, 0.43 ± 0.04 µg/mL ^{238}U were found in the sample.

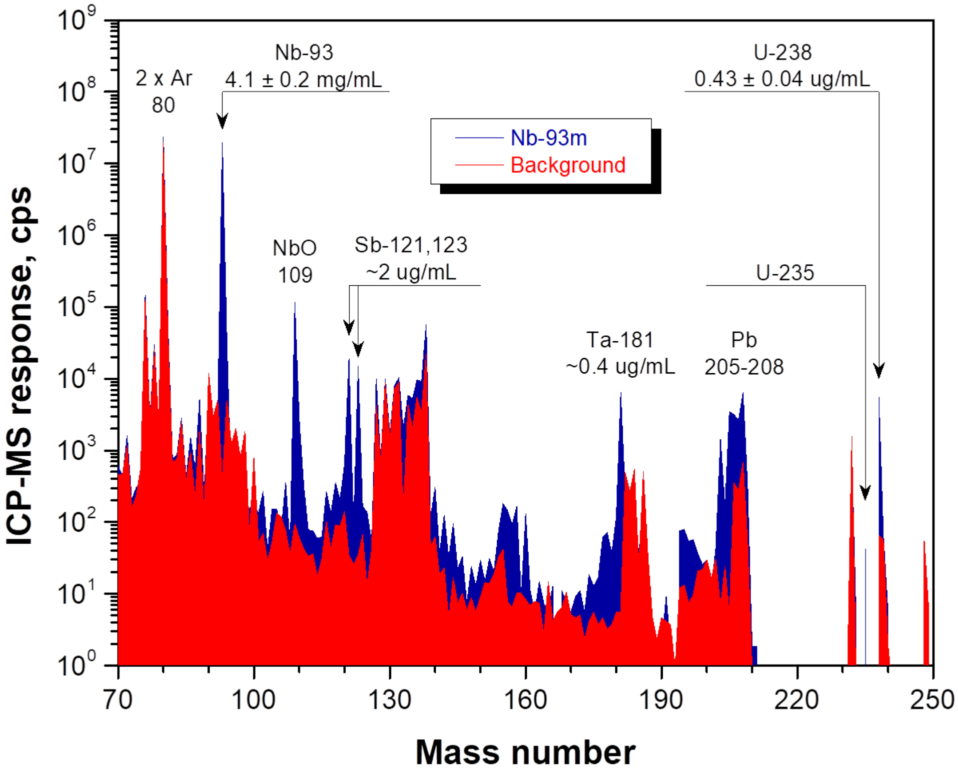

Fig. 5. ICP-MS spectrum of the ^{93m}Nb aliquot.

Finally, we prepared a reliable and convenient ^{93m}Nb source for the ICC measurement. The ICP-MS standard was not used in these experiments. An aliquot of radioactive solution was dried down to a small drop in a Teflon beaker using a heating plate and then transferred to the target cell. The electrodeposition method we employed is limited to 1-2 mg/cm^2 of material deposited. It was decided not to exceed this layer thickness in order to avoid flaking, cracking, and/or peeling of the film. The procedure to achieve the most active source took 15 h at ~10 mA resulting in a deposition efficiency of ~50 % [7].

The mass of the deposited layer (3.0 mg) was determined by weighing of the backing foil before and after deposition. The use of this foil for ICC measurements is described in another paper submitted to Phys. Rev. C (2020).

[1] D.A. Mayorov, E.E. Tereshatov, T.A. Werke, M.M. Frey, and C.M. Folden III, Nucl. Instrum. Methods Phys. Res., Sect. **B407**, 256 (2017). doi:10.1016/j.nimb.2017.07.012

[2] N. Getoff, H. Bildstein, and E. Proksch, Nucl. Instrum. Methods **46**, 305 (1967). doi:10.1016/0029-554X(67)90088-2

[3] K. Kamada, M. Mukai, and Y. Matsumoto, Electrochim. Acta **49**, 321 (2004). doi:10.1016/j.electacta.2003.08.014

[4] I. Sieber, H. Hildebrand, A. Friedrich, and P. Schmuki, Electrochem. Commun. **7**, 97 (2005). doi:10.1016/j.elecom.2004.11.012

[5] R. Caletka and V. Krivan, J. Radioanal. Nucl. Chem. **142**, 359 (1990). doi:10.1007/BF02040306

[6] E.E. Tereshatov and C.M. Folden III, *Progress in Research*, Cyclotron Institute, Texas A&M University (2016-2017), p.II-25; https://cyclotron.tamu.edu/progress-reports/2016-2017/2%20Heavy%20Ion%20Reactions/II_25-26_Development%20of%20niobium%20electroplating%20for%20a%20future%20radioactive%2093Nbm%20target.pdf.

[7] E.E. Tereshatov, N. Nica, V. Horvat, J.C. Hardy, and C.M. Folden III, *Progress in Research*, Cyclotron Institute, Texas A&M University (2017-2018), p.II-30; https://cyclotron.tamu.edu/progress-reports/2017-2018/2%20Heavy%20Ion%20Reactions/II_30_31_Preparation%20and%20characterization%20of%20a%20Nb-93m%20target.pdf.

Mathematical model describing solubility of hydrophobic ionic liquids in hydrochloric acid media

E.E. Tereshatov,[1] V. Mazan,[2,*] M. Boltoeva,[2] and C.M. Folden III[1,3]
[1]*Cyclotron Institute, Texas A&M University, College Station, TX 77843 USA*
[2]*Université de Strasbourg, CNRS, IPHC, UMR 7178, F-67000 Strasbourg, France*
[3]*Department of Chemistry, Texas A&M University, College Station, TX 77843 USA*
[*]*Present address: Université de Strasbourg, CNRS, LIMA, UMR 7042, F-67087 Strasbourg, France*

A mathematical model to explain cations' solubility of both protic (betainium-) and aprotic (pyrrolidinium- and imidazolium-based) ionic liquids with common *bis*(trifluoromethanesulfonyl)imide anion in a wide range of hydrochloric acid solutions has been developed. The concept of this model is based on an assumption of the mineral acid extraction into the organic phase [1], formation of a chloride-containing salt there due to ionic liquid and extracted acid ions recombination and partial salt back-extraction [2]. The proposed approach allows for estimating corresponding extraction constants. Comparison of calculated and experimentally measured solubility product constants shows that they are in good agreement. It was found also that the lower the hydrophilicity of the ionic liquids' cation the more hydrochloric acid is extracted. Fig. 1 shows some results of this work. It can be seen that experimentally measured solubility product constants and the calculated constant of hydrochloric acid extraction into a series of imidazolium based ionic liquid ([$C_n$mim][Tf_2N], where n = 2, 4, 6, and 8) decreases with increasing cation hydrophobicity. These are preliminary data submitted to a peer reviewed journal.

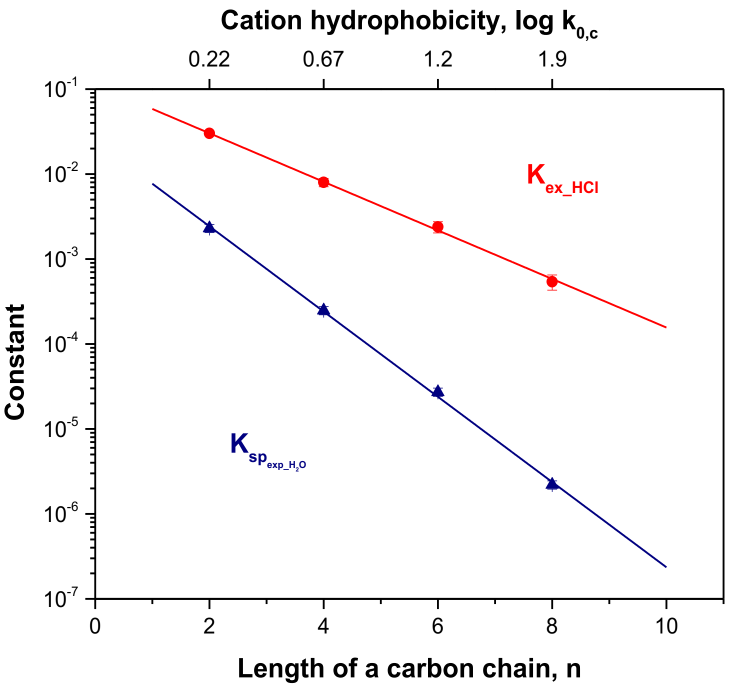

Fig. 1. Influence of the carbon chain length on the solubility and HCl extraction into imidazolium-based ionic liquids [$C_n$mim][Tf_2N], where n = 2, 4, 6, and 8. The imidazolium-based cations hydrophobicity data are taken from [3].

[1] C. Gaillard, V. Mazan, S. Georg, O. Klimchuk, M. Sypula, I. Billard, R. Schurhammer, and G. Wipff, Phys. Chem. Chem. Phys. **14**, 5187 (2012). doi:10.1039/c2cp40129k

[2] E.E. Tereshatov, M. Boltoeva, V. Mazan, C. Baley, and C.M. Folden III, New J. Chem. **43**, 8958 (2019). doi:10.1039/c9nj00689c

[3] J. Ranke, A. Othman, P. Fan, and A. Muller, Int. J. Mol. Sci. **10**, 1271 (2009). doi:10.3390/ijms10031271

Menthol-based eutectic solvent for indium and thallium partition from hydrochloric acid media

M.F. Volia,[1,2] E.E. Tereshatov,[1] and C.M. Folden III[1,3]
[1]*Cyclotron Institute, Texas A&M University, College Station, Texas 77843,*
[2]*Department of Nuclear Engineering, Texas A&M University, College Station, Texas 77843,*
[3]*Department of Chemistry, Texas A&M University, College Station, Texas 77843*

Eutectic mixtures have been considered as an alternative green solvent due to their similar characteristics with ionic liquids [1, 2]. Some of these solvents were reported to be hydrophobic [3, 4] and were able to extract metal ions from aqueous media through a liquid-liquid extraction process [5]. This report is to highlight the ability of a hydrophobic eutectic mixture composed of DL-menthol and lauric acid (ES-MLA) to extract In(III), Tl(I, III) from hydrochloric acid media. The most promising results were obtained for Tl(III). Addition of HDEHP into ES-MLA was able to significantly improve the extraction yields of In(III) and Tl(I), particularly at low acidity, but had a minor effect on Tl(III) extraction. The metal extraction decreases in the order Tl(III) > Tl(I) > In(III) for the entire HCl range in the case of pure ES-MLA and above 1 M HCl for the HDEHP + ES-MLA systems (Fig. 1). A mathematical model to explain the metal extraction has been developed. The effect of HDEHP diluents (the eutectic mixture ES-MLA or kerosene) on In(III) and Tl(III) extraction was also studied. It was found that the kerosene-containing system was able to improve In(III) extraction at low acidity by two orders of magnitude while Tl(III) behavior in this acidity region was not affected. However, at high acid concentrations the eutectic-based system shows an increase in D-values. A paper on these results is in the late stages of preparation.

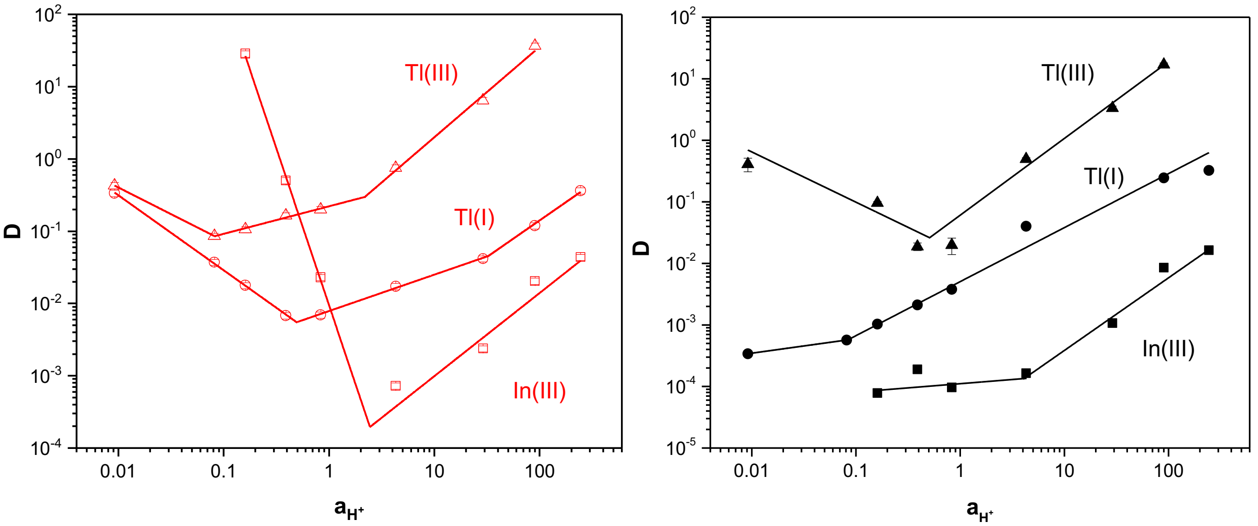

Fig. 1. The results of In(III) and Tl(I, III) extraction into ES-MLA (2:1 molar ratio) in the presence (left) and absence (right) of HDEHP. The lines are drawn to guide the eye.

[1] E.L. Smith, A.P. Abbott, and K.S. Ryder, Chem. Rev. **114**, 11060 (2014). doi:10.1021/cr300162p

[2] Q. Zhang, K. De Oliveira Vigier, S. Royer, and F. Jerome, Chem. Soc. Rev. **41**, 7108 (2012). doi:10.1039/c2cs35178a

[3] D.J.G.P. van Osch, L.F. Zubeir, A. van den Bruinhorst, M.A.A. Rocha, and M.C. Kroon, Green Chem. **17**, 4518 (2015). doi:10.1039/c5gc01451d

[4] B.D. Ribeiro, C. Florindo, L.C. Iff, M.A.Z. Coelho, and I.M. Marrucho, ACS Sustain. Chem. Eng. **3**, 2469 (2015). doi:10.1021/acssuschemeng.5b00532

[5] E.E. Tereshatov, M.Y. Boltoeva, and C.M. Folden III, Green Chem. **18**, 4616 (2016). doi:10.1039/c5gc03080c

Toward understanding relativistic heavy-ion collisions with the STAR detector at RHIC

D.M. Anderson, Y. Liu, S. Mioduszewski, N.Sahoo, and the STAR Collaboration

This project is a study of high-energy heavy-ion collisions at the Relativistic Heavy Ion Collider (RHIC). The focus of the study is on two probes of the dense, partonic matter created in these collisions: 1) direct-photon-triggered jets (and their correlations) and 2) heavy-quarkonium production and suppression.

1 Investigating Energy Loss through Photon-Triggered Jet Measurements

The hard production of a direct photon back-to-back with a jet (γ-jet) is a probe of the parton energy loss in heavy-ion collisions [1]. In the "γ-jet" coincidence measurement, the measured energy of the trigger particle (the photon) serves as a calibrated baseline for the total energy of the jet particles on the recoil side (i.e. opposite in azimuth) of the trigger. The mean-free path of the γ in the medium is large enough so that its momentum is preserved, regardless of the position of the initial scattering vertex. Thus it does not suffer from the geometric biases, i.e. the non-uniform spatial sampling of hadron triggers due to energy loss in the medium, of e.g. π^0 triggers. Because of the difference in path length traversed, on average, between a direct-γ and a π^0 trigger, comparisons of γ-jet to hadron(π^0)-jet measurements can provide insight into the path-length dependence of the energy loss.

As the dominant background to direct photons are π^0 (decaying to two photons), the Barrel Shower Maximum Detector (BSMD) has provided the capability of distinguishing direct photons from neutral pions via the transverse shower shape. Our group has used this method in the measurement of direct photon+hadron correlations [2]. The γ-hadron correlation studies can be extended to studies of γ-triggered jet reconstruction measurements (as has been done at the LHC [3, 4]). The away-side jet will then be reconstructed in coincidence with triggers selected as direct photon candidates or (for p_T<20 GeV using the shower shape with the BSMD) identified π^0 triggers. The advantage of this should be the ability to reach lower energy fragments in the jet to study jet-shape modification and possible redistribution of energy.

The Run-14 photon-triggered data set in Au+Au collisions has been fully analyzed for charged jets recoiling from a high-energy neutral (π^0 or γ) trigger. We have chosen to concentrate initially on charged-particle jets, for simplicity, recoiling from the trigger particle. Charged-jet reconstruction is performed using the anti-k_T algorithm from the Fastjet package [5]. A fiducial cut in jet pseudorapidity, $|\eta_{\text{jet}}| < 1-R_{\text{jet}}$, where R_{jet} is the jet resolution parameter associated with the radial size of the jet.

Fig. 1 shows the ratio (I_{AA}) of per-trigger charged recoil-jet yields in Au+Au collisions to those in PYTHIA [6] for π^0 triggers and γ triggers. The comparison of I_{AA} for Rjet=0.2 and Rjet=0.5 seems to indicate recovery of the lost energy at larger radii. However, this conclusion depends on the PYTHIA, and we have found that different settings in PYTHIA result in different conclusions. It is therefore essential to have the measurement in p+p collisions. As a baseline measurement, we have analyzed Run-9 p+p collisions. We are currently finalizing the determination of the energy scale and systematic uncertainties for this measurement.

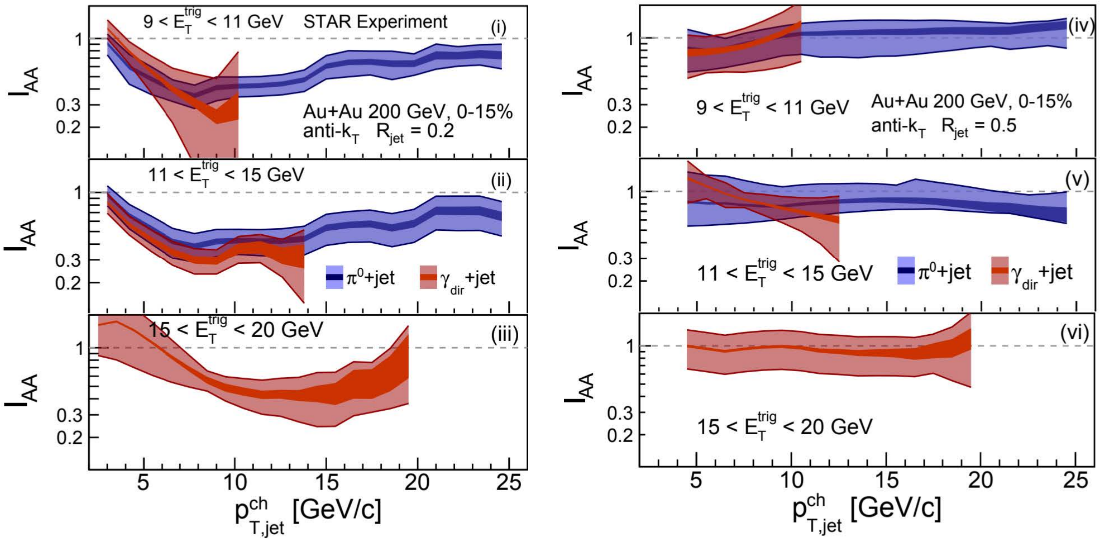

Fig. 1. Ratio (I_{AA}) of charged recoil-jet yields Au+Au collisions to those in PYTHIA (p+p collisions). The left panel are for jet resolution parameter R_{jet}=0.2, and the right panels are for R_{jet}=0.5. The blue bands are for π^0 triggers, and the red are for γ triggers. In the top panels the trigger energy E_T=9-11 GeV, in the middle panels E_T=11-15 GeV, and in the lower panels E_T=15-20 GeV.

2 Unraveling Cold Nuclear Matter Effects in J/ψ Suppression

The J/ψ has long been considered one of the most promising direct probes of deconfinement. According to theoretical predictions in 1986 [7], the produced $c\bar{c}$ pair will not be able to form a J/ψ bound state in the QGP, if a sufficiently high temperature is reached where the screening radius is smaller than the binding radius of the J/ψ resonant state. The "Debye" screening radius is the distance at which the color charges of two quarks are screened from one another, so that the confinement force is not able to hold the quarks together. A suppression in the yield of J/ψ was first observed in Pb+Pb collisions by the NA50 experiment at the CERN SPS (see, for example, [8]).

At RHIC, the predicted suppression of J/ψ due to screening in the QGP is much larger than the suppression observed at SPS due to the higher initial density of the produced medium [9]. The RHIC measurements, however, show a level of suppression similar to NA50 at mid-rapidity [10], which is significantly smaller than expectations due to color screening effects alone. This can be understood in a scenario where charmonium is regenerated due to the large initial production of charm + anti-charm quarks at $\sqrt{s_{NN}}$= 200 GeV, in conjunction with their possible thermalization in the created medium [11]. If charm quarks (partially) thermalize in RHIC collisions, then the coalescence of $c\bar{c}$ could lead to a smaller than expected suppression [12].

With counteracting effects, it is a challenge to disentangle the suppression from the regeneration. In addition, there are cold nuclear matter effects [13], including modification of the parton distribution functions ("shadowing") and partonic multiple scattering, that also lead to suppression of heavy quarkonium and need to be disentangled from QGP suppression. In order to quantify effects of deconfinement, cold nuclear matter effects (via p+Au collisions) must be measured and disentangled

Our goal is to measure charmonium production in p+Au collisions as a function of "centrality". Ideally, centrality would be determined using the event activity in the forward region, away from the mid-rapidity region where the J/ψ is reconstructed. However, due to the performance of the STAR Beam-Beam Counters (BBC) in the p+Au running period, we have concluded that we cannot use the BBC for this purpose. Alternatively, we based the centrality determination on an event multiplicity of the number of good primary tracks (NGPT) at mid-rapidity ($|\eta|<1$). With NGPT as the centrality measure, the results are difficult to interpret due to the correlations between the physics signal and the centrality determination. Fig. 2 shows this result, which we decided not to show at the Quark Matter conference last year, because of this auto- correlation. We are currently restricting our centrality determination to the NGPT outside of the rapidity region in which the J/ψ is reconstructed and anticipate having results soon.

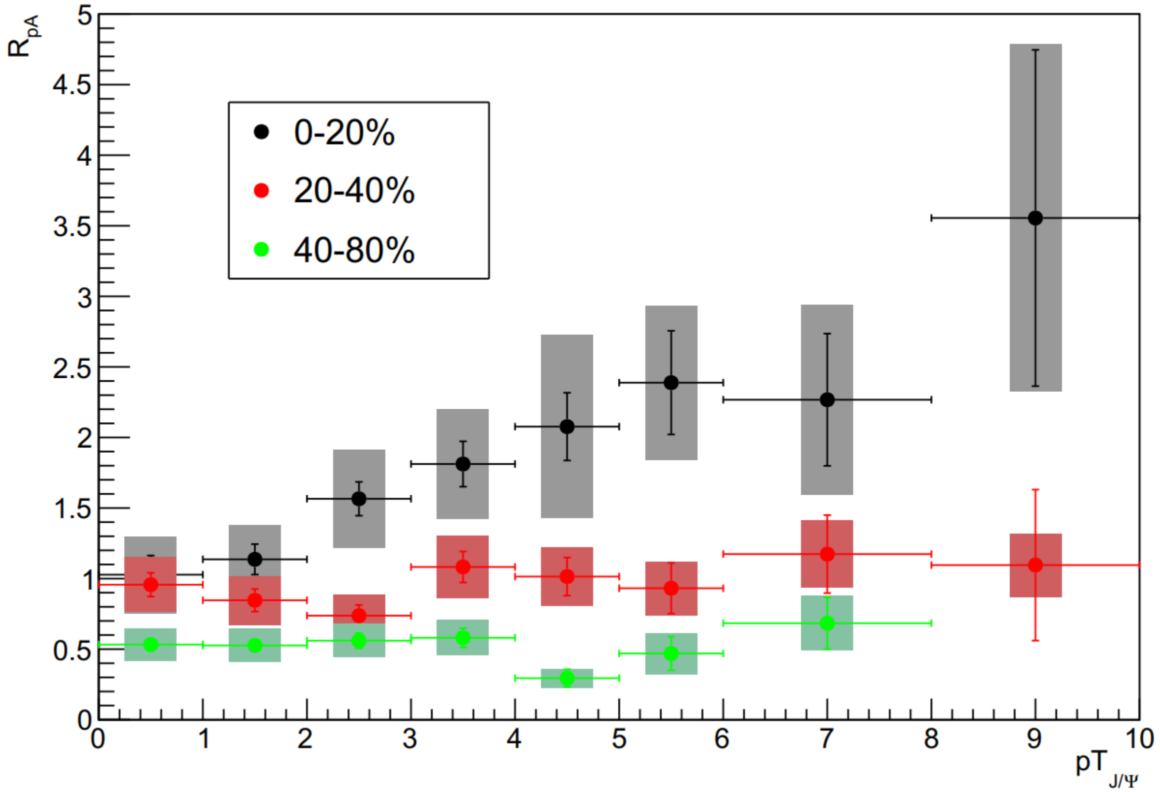

Fig. 2. Nuclear modification factor R_{pA} of J/ψ yields as a function of p_T (ratio in p+Au collisions to that in p+p collisions scaled by the mean number of binary collisions) for 3 different centrality classes. Since the centrality is determined by the multiplicity in the mid-rapidity region, there are auto-correlations with the J/ψ signal, making it difficult to interpret this result.

[1] X.N. Wang, Z. Huang and I. Sarcevic, Phys. Rev. Lett. **77**, 231 (1996).

[2] L. Adamczyk *et al.* (STAR Collaboration), Phys. Lett. B **760**, 689 (2016).

[3] S. Chatrchyan *et al.* [CMS Collaboration], Phys. Lett. B **718**, 773 (2013).

[4] [ATLAS Collaboration], ATLAS-CONF-2012-121.

[5] M. Cacciari and G. Salam, Phys. Lett. B **641**, 57 (2006); M. Cacciari, G. Salam and G. Soyez, JHEP **0804** 005 (2008); http://fastjet.fr.

[6] T. Sjöstrand, S. Mrenna, and P. Skands, Comput. Phys. Commun. **178**, 852 (2008).

[7] T. Matsui and H. Satz, Phys. Lett. B **178**, 416 (1986).

[8] M.C. Abreu *et al.* (NA50 Collaboration), Eur. Phys. J. C **39**, 335-345 (2005).

[9] L. Grandchamp, R. Rapp, and G.E. Brown, Phys. Rev. Lett. **92**, 212301 (2004); A. Capella and E.G. Ferreiro, Eur. Phys. J. C **42**, 419 (2005).

[10] A. Adare *et al.* (PHENIX Collaboration), Phys. Rev. Lett. 98, 232301 (2007).

[11] P. Braun-Munzinger and J. Stachel, Phys. Lett. B **490**, 196 (2000).

[12] L. Grandchamp and R. Rapp, Phys. Lett. B **523**, 60 (2001).

[13] R. Vogt, Phys. Rev. C **71**, 054902 (2005).

SECTION III

NUCLEAR THEORY

Nuclear theory – nuclear astrophysics

J.W. Holt

Introduction:

The structure, phases, and dynamics of nuclear matter are crucial to understand stellar explosions, the origin of the elements, patterns in observed gravitational waves, and the composition of the densest observable matter in the universe. The appropriate tool to study strongly interacting matter at the typical scales relevant in nuclear astrophysics (well below the scale of chiral symmetry breaking $\Lambda_\chi \approx 1$ GeV) is chiral effective field theory [1-3]. In recent years, chiral effective field theory (EFT) has become a cornerstone of the modern approach to nuclear many-body dynamics that provides a systematic framework for describing realistic microphysics, such as multi-pion exchange processes and three-body forces, within a well-defined organizational hierarchy. The long and intermediate-range parts of the nuclear potential result from one- and two-pion exchange processes, while short-distance dynamics, not resolved at the wavelengths corresponding to typical nuclear Fermi momenta, are introduced as contact interactions between nucleons. Chiral effective field theory is unique in its multichannel methods for quantifying uncertainties and especially in its ability to estimate the importance of missing physics.

Chiral three-body forces at next-to-next-to-next-to-leading order

Three-nucleon forces are an indispensable ingredient for accurate few-body and many-body nuclear structure and reaction theory calculations. While the direct implementation of chiral 3N forces

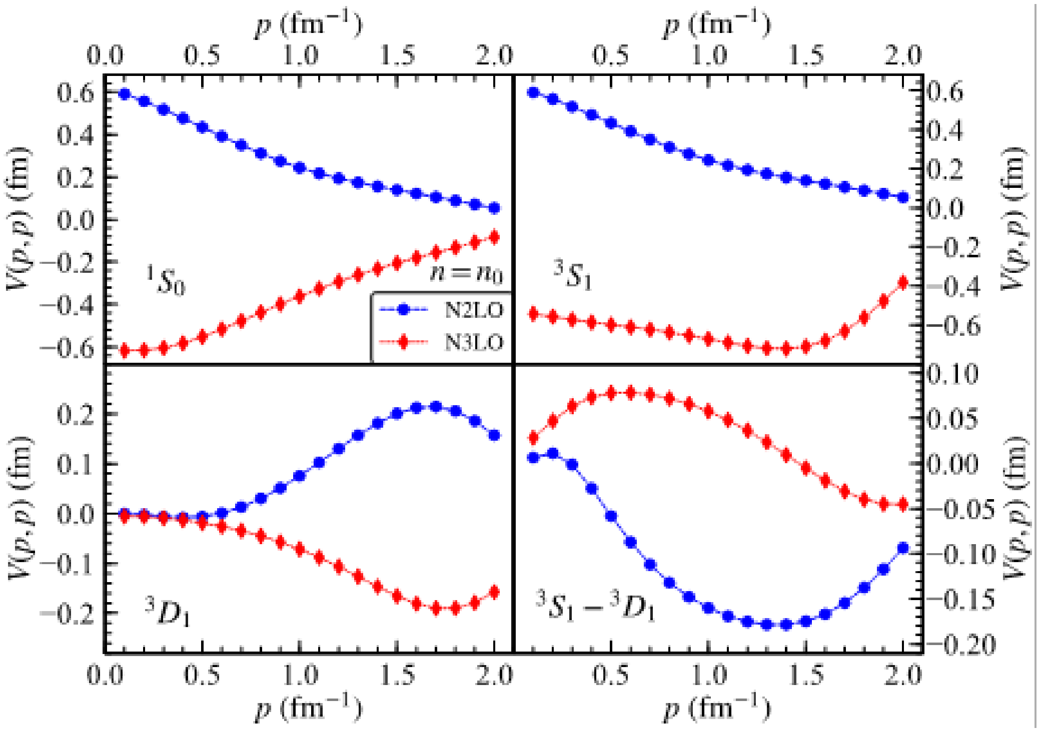

Fig. 1. Diagonal momentum-space matrix elements of the in-medium NN interaction associated with the N2LO and N3LO three-body forces in the $^1S_0$ and $^3S_1$ – $^3D_1$ partial-wave channels at saturation density in symmetric nuclear matter.

can be technically very challenging, a simpler approach is given by employing instead a medium-dependent NN interaction [4] that reflects the physics of three-body forces at the two-body normal-ordered approximation. In particular, the structure of three-body forces at next-to-next-to-next-to-leading order (N3LO) in the chiral expansion have in many cases been prohibitively challenging to implement in modern nuclear structure and reaction calculations. In recent work [5], we have constructed density-dependent nucleon-nucleon interactions from the N3LO chiral three-body force. Overall, we found that the 3N force at this order is strongly attractive in the lowest partial-wave channels. In Fig. 1 we plot the diagonal momentum-space matrix elements associated with both the total N2LO and total N3LO three-body force in the $^1S_0$ and $^3S_1$ – $^3D_1$ partial-waves in isospin-symmetric nuclear matter at saturation density. Interestingly, the N2LO and N3LO three-body force contributions have nearly equal magnitude but opposite sign. We note, however, that a relevant comparison can only be performed after the three-body N2LO low-energy constants, c_D and c_E, are refitted to the properties of three-body systems including the effects of the N3LO terms.

Adiabatic index of hot and dense matter from chiral effective field theory

Dynamical simulations of core-collapse supernovae [6-8] and neutron star mergers [9-12] require modeling of the nuclear equation of state up to densities $n \approx 5 - 10n_0$, where $n_0 - 0.16$ fm^{-3} is the saturation density of nuclear matter, and temperatures up to $50 - 100$ MeV. Such simulations are crucial for interpreting observable electromagnetic, neutrino, and gravitational wave emissions as well as understanding the origin of many heavy elements through r-process nucleosynthesis [13-15]. Presently there exist a number of equation of state tabulations derived from Skyrme mean field phenomenology and relativistic mean field models appropriate for astrophysical simulations. To explore an even wider range of parameterizations, polytropic equations of state have been coupled with an ideal gas ansatz for the thermal contribution to the pressure $p_{th} = (\Gamma_{th} - 1)\varepsilon_{th}$, where ε_{th} is the internal energy density and Γ_{th} is the so called adiabatic index. The resulting analytical equations of state have numerical advantages over tabulations and allow for a more thorough exploration of the correlations among bulk neutron star properties, features of gravitational wave signals, and properties of the equation of state. In particular, thermal effects have been shown to modify the dominant peak frequency and intensity of the post-merger gravitational wave signal [11] and lead to a delay in the remnant collapse time to a black hole [11].

Previous numerical simulations of neutron star mergers have employed a constant value of the thermal index, and recently we have provided [16] a general parameterization for Γ_{th} based on finite-temperature calculations of the equation of state from microscopic chiral effective field theory. In Fig. 2 we show uncertainties in the density- and temperature-dependent adiabatic index obtained from mean field models constrained by chiral effective field theory. We find in particular that microscopic chiral effective field theory yields a consistently larger adiabatic index compared to traditional Skyrme force models and especially relativistic mean field models.

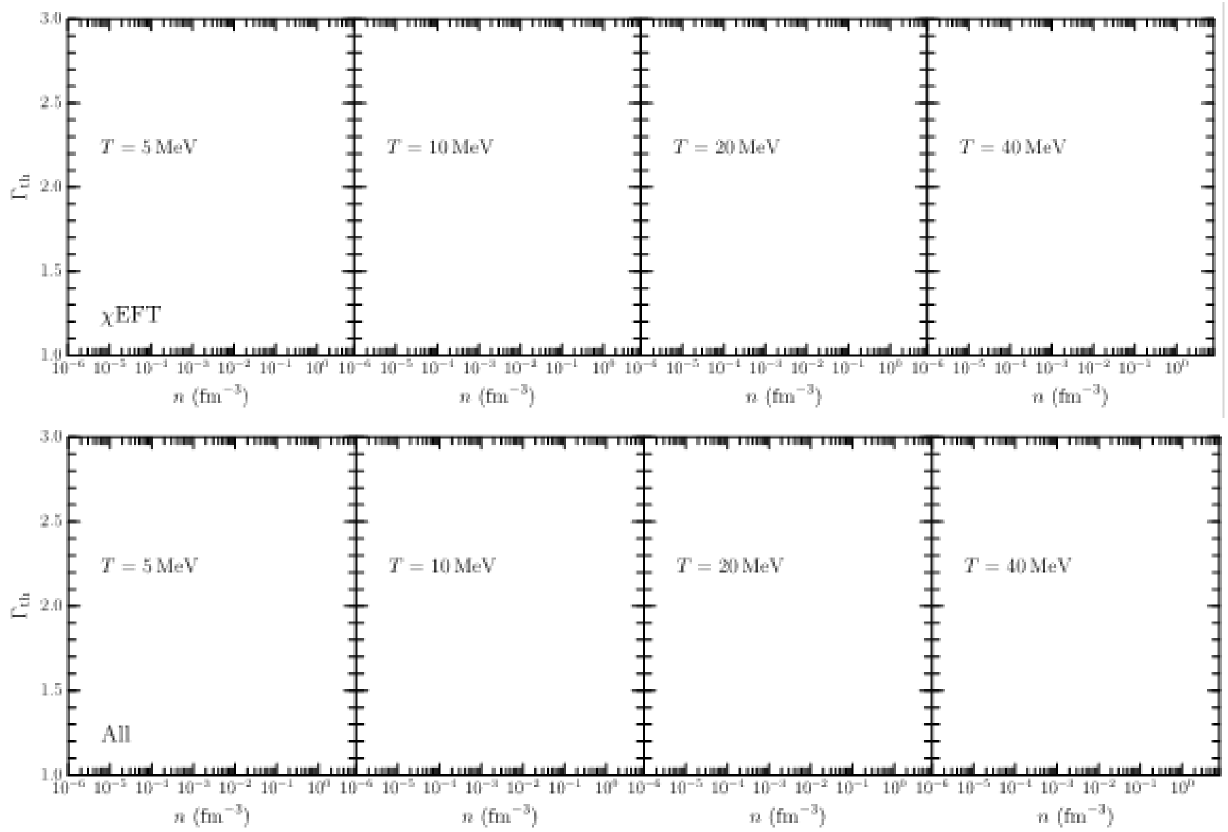

Fig. 2. Adiabatic index confidence intervals of $\pm 1\sigma$ and $\pm 2\sigma$ obtained from Skyrme and Relativistic Mean Field models ("ALL") as well as models constrained by chiral effective field theory ("χEFT").

Neutron-nucleus optical potentials from chiral two- and three-body forces

Numerical simulations of r-process nucleosynthesis are essential for identifying the astrophysical site of the r-process, the primary candidates being the wind-driven ejecta from accretion disks surrounding binary neutron-star mergers or collapsars as well as the neutrino-driven winds of core-collapse supernovae. Neutron-capture rates on exotic neutron-rich isotopes are particularly important during the non-equilibrium freeze-out phase of r-process nucleosynthesis, but direct experimental studies at rare-isotope facilities remain unfeasible. The large uncertainties in these capture rates, due in part to difficulties in extrapolating phenomenological optical model potentials far from the valley of stability, limit the precision of predicted heavy-element abundances. Previously we have computed proton-nucleus optical potentials [17] by combining the improved local density approximation with chiral effective field theory calculations of the nucleon self energy in homogeneous nuclear matter. Differential elastic scattering cross sections on calcium isotopes were found to be in quite good agreement with experimental data for projectile energies up to 150 MeV.

More recently, we have computed also neutron-nucleus optical potentials [18] for calcium isotope targets. Given the important role of the Coulomb potential at small scattering angles in the case of proton elastic scattering, testing our approach with a neutron projectile was a nontrivial extension. We also computed for the first time in our formalism vector analyzing powers. This is an important test of the quality of our spin-orbit optical potential that was not benchmarked in our previous calculations. The real spin-orbit optical potential was constructed within the density matrix expansion [19] from consistent chiral two-body and three-body forces. In Fig. 3 we show the analyzing powers for n-40Ca elastic scattering at projectile energies E = 11.9, 16.9 MeV. Results from the chiral optical potential are given by the blue bands obtained by varying the smearing length in the improved local density approximation. We find quite good agreement with our results and experimental data (shown as red dots with error bars in Fig. 3) and the results from the Koning-Delaroche phenomenological optical potential [20] (green dashed curves).

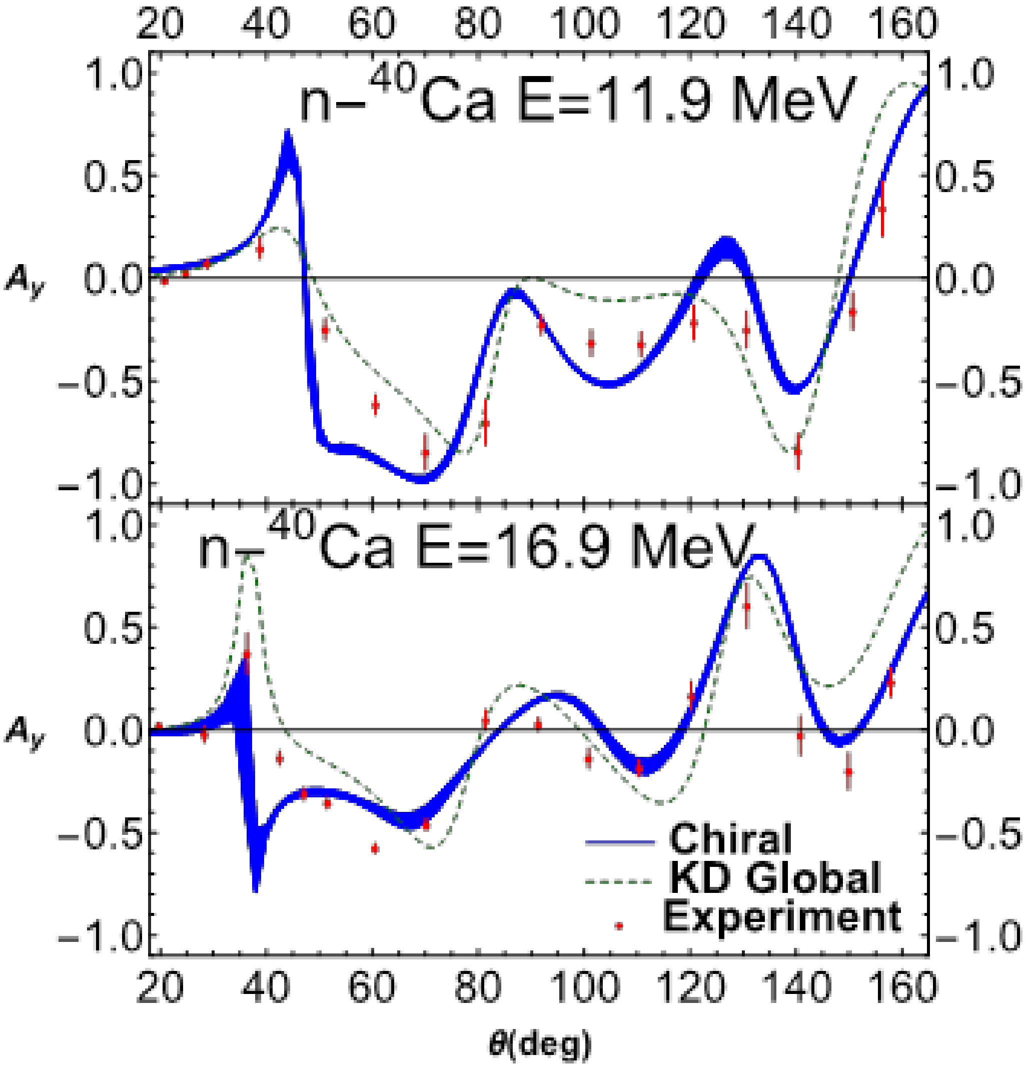

Fig. 3. Vector analyzing powers for elastic n-40Ca scattering at projectile energies E = 11.9, 16.9 MeV. Results from the chiral optical potential are given by the blue bands, while those from the Koning-Delaroche phenomenological optical potential are given by the green dashed curves. Experimental data are represented by red circles with error bars.

[1] S. Weinberg, Physica A **96**, 327 (1979).

[2] E. Epelbaum, H.-W. Hammer, and U.-G. Meissner, Rev. Mod. Phys. **81**, 1773 (2009).

[3] R. Machleidt and D.R. Entem, Phys. Rep. **503**, 1 (2011).

[4] J.W. Holt, N. Kaiser, and W. Weise, Phys. Rev. C **79**, 054331 (2009).

[5] J.W. Holt, M. Kawaguchi, and N. Kaiser, Front. Phys. **8**, 100 (2020).

[6] H.-T. Janka, K. Langanke, A. Marek, G. Martínez-Pinedo, and B. Müller, Phys. Rep. **442**, 38 (2007).

[7] C.D. Ott, E. Abdikamalov, P. Mösta, R. Haas, S. Drasco, E.P. O'Connor, C. Reisswig, C.A. Meakin, and E. Schnetter, Astrophys. J. **786**, 115 (2013).

[8] T. Melson, H.-T. Janka, R. Bollig, F. Hanke, A. Marek, and B. Müller, Astrophys. J. **808**, L42 (2015).

[9] M. Ruffert and H.T. Janka, Astron. Astrophys. **338**, 535 (1998).

[10] R. Oechslin, H.-T. Janka, and A. Marek, Astron. Astrophys. **467**, 395 (2007).

[11] A. Bauswein, H.-T. Janka, and R. Oechslin, Phys. Rev. D **82**, 084043 (2010).

[12] D. Kasen, B. Metzger, J. Barnes, E. Quataert, and E. Ramirez-Ruiz, Nature **551**, 80 EP (2017).

[13] J.M. Lattimer and D.N. Schramm, Astrophys. J. **192**, L145 (1974).

[14] F.-K. Thielemann, M. Eichler, I. Panov, and B. Wehmeyer, Ann. Rev. Nucl. Part. Sci. **67**, 253 (2017).

[15] D. Radice, A. Perego, K. Hotokezaka, S.A. Fromm, S. Bernuzzi, and L.F. Roberts, Astrophys. J. **869**, 130 (2018).

[16] Y. Lim and J.W. Holt, arXiv:1909.09089.

[17] T.R. Whitehead, Y. Lim, and J.W. Holt, Phys. Rev. C **100**, 014601 (2019).

[18] T.R. Whitehead, Y. Lim, and J.W. Holt, Phys. Rev. C **101**, 064613 (2020).

[19] J.W. Holt, N. Kaiser, and W. Weise, Eur. Phys. J. A **47**, 128 (2011).

[20] A.J. Koning and J.P. Delaroche, Nucl. Phys. **A713**, 231 (2003).

Four α correlations in nuclear fragmentation: a game of resonances

M. Huang, A. Bonasera, S. Zhang, H. Zheng, D.X. Wang, J.C. Wang, N. Song,
X. Tang, L. Lu, G. Zhang, Z. Kohley, M.R.D. Rodrigues, Y.G. Ma, and S.J. Yennello

Today, clustering is still a hot topic in nuclear structure for C, O and more complex nuclei [1–4]. This is true in nuclear dynamics as well, for instance in fragmentation reactions [5–10], together with the possibility of observing a Bose Einstein Condensate (BEC) and Efimov states [3,11]. Following Ref. [12], we can identify the HS as an Efimov State (ES) [11, 13-14] because of its 100% decay into ^{8}Be+α, i.e, with the lowest relative energy of two αs equal to 92 keV. The mechanism at play is that an α particle is exchanged between the other two αs. The Boson exchange produces an effective field that binds the 3 particles system [15]. This mechanism might be extended to 4 or more Bosons [16] and provide new insight into many body interactions. In particular, if ^{16}O can be described as 4α clusters, we can study the relative energy distributions of all 2α possible combinations. To put this idea on a firm ground, we extend the ^{12}C case to ^{16}O and write its excitation energy as:

$$E^{*} = \frac{1}{2}\sum_{i=1,j<i}^{4} E_{ij} - Q. \tag{1}$$

where E_{ij} are the two αs relative energies and we have classified the (undistinguishable) particles according to their relative energies in such a way that $E_{ij}^{1} \leq E_{ij}^{2} \leq \cdots E_{ij}^{6}$; Q = -14.44 MeV is the Q-value for the decay into 4α. If the six E_{ij} relative energies combinations equal to 92 keV (the ^{8}Be ground state) then we expect from eq. (1) an excited level at E^{*}=14.72 MeV [16]. Similarly, to the ^{12}C [17-18], we might expect an excited level of ^{16}O, which decays sequentially to ^{12}C(HS)+α with the ^{12}C(HS) decaying into ^{8}Be+α [19–22]. In this case the available excitation energy is not divided democratically (equally) among all the αs. Only the lowest relative energy of two αs is equal to 92 keV (the last ^{8}Be decay).

To study `in medium' 4α correlations and link them to the 'fission' of ^{16}O in two ^{8}Be in the ground state or ^{12}C*(Hoyle State) + α, events with only 4α particles emitted amongst other particles were analyzed at the same time for the system of 35 MeV/nucleon ^{70}Zn+^{70}Zn, ^{64}Zn+^{64}Zn and ^{64}Ni+^{64}Ni measured using the NIMROD array [7,10]. To assign a position to the fragment in the single detector, two possible avenues are commonly followed [10, 23-24]. One is to assign the fragment position at the center of the single detector(CD), the second is to assign a random position on the surface of the single detector (RD). In fact, we can randomly choose the position of the real events N>>1 times (RDN). In this way we can uniformly explore the surface of the detector and, if we normalize the number of events to one, it becomes the probability of finding a fragment at a certain angle and energy. Another detector feature to consider is double hits (DH). Because of the finite granularity it is possible that two fragments hit the same detector in the same event. For α-particles the detector response to DH is quite unique and there is no possibility to confuse those events with other fragments (say $^{6;7}$Li etc.) [24]. This together with the CD method automatically produces a 'resonance' for relative energies E_{ij}(DH)=0 MeV. The RD(N) method, on the other hand, might give non-zero relative energy since the positions of the two particles in the single detector are randomly chosen. The next step in the data analysis is to generate mixing events for each assumption discussed above. This is achieved by choosing four different α-particles from four different events. This procedure can be repeated many times (more than the number of real events) in order to get a smooth paving of the available phase space. As for the real events, we normalize the total number of mixing events to 1. A four-body correlation function can be defined as:

.

$$1 + R_4 = \frac{Y_R}{Y_M} \tag{2}$$

where Y_R is the yield of real events and Y_M is the yield of mixing events. Similarly, the three-body (1+R_3) or the two-body (1+R_2) correlation functions can be obtained. The ratio can be performed as function of the ^{16}O excitation energy defined in eq. (1) or other relevant physical quantities

In Fig. 1, we plot the correlation function as function of the ^{16}O excitation energy. In the left panel, the E_{ij}(DH)=92 keV is adopted while the E_{ij}(DH)=0 keV is given in the center panel. The results without DH are displayed in the right panel. The CD (black full circles) and RD (green open squares) choices give a positive correlation function around 15 MeV. A peak at 15.1 MeV is clearly seen when the E_{ij}(DH)=92 keV assumption is adopted. If we generate a large number of RDN events (red open circles) we obtain a smoothing of the RD case (see also the insets). The interesting feature is that two clear peaks appear at 14.85 and 15.1 MeV in the left panel, while the two peaks are smoothed in the middle one. These results confirm the resonance at 15.1 MeV and give some circumstantial evidence for a peak at lower E =14.72 MeV consistent with the decay of ^{16}O into four alpha particles all with energies 92 keV (see eq. (1)), i.e, all combinations of two αs result in the g.s. of ^{8}Be. The right panel (no DH) shows the positive correlation function above 15 MeV but no data points are found for lower energies thus

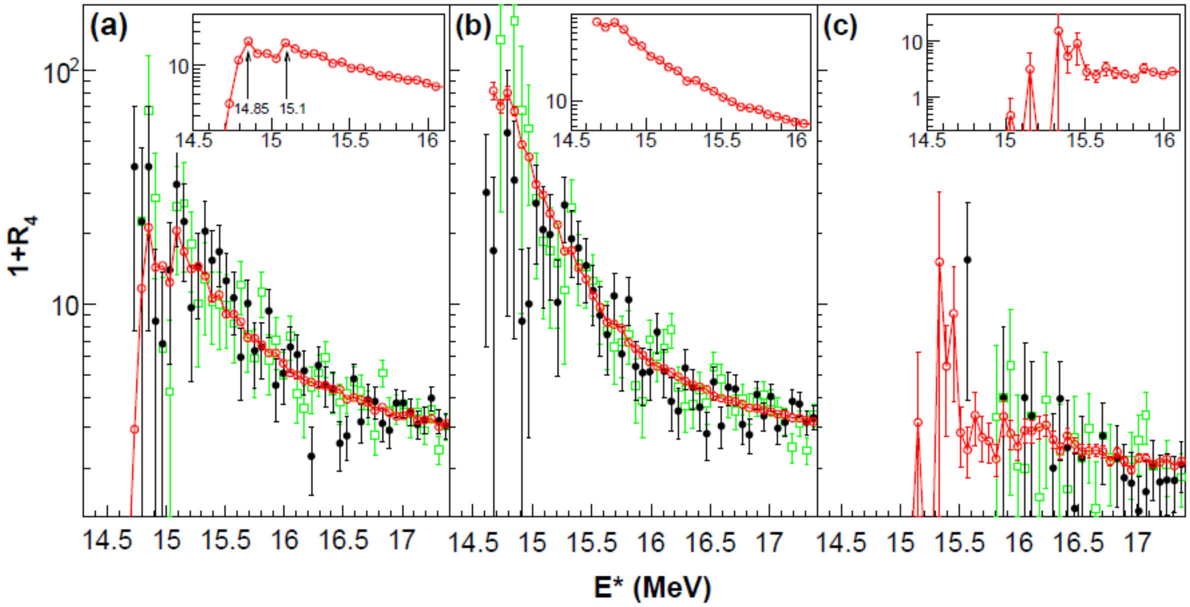

Fig. 1. Four αs energy correlation function of 16O: (a) relative energy for DH is equal to 92 keV and (b) equal to zero. No double hits in panel (c). In all cases, the bin-width is 60 keV. In the insets we display the results for the RDN cases only.

suggesting that DH relevant with the decay of ^{8}Be are crucial to determine the exact position of the resonance(s).

In Fig. 2, we have repeated the analysis of the previous Fig. 1 for different bin-widths ((a),(b),(c),(d) correspond to the bin-widths of 60 keV, 80 keV, 120 keV, 200 keV, and the middle and bottom panels are similar) and for the CD case only. The 15.1 MeV is clearly visible in the two top panels with some hint in the bottom panel where DH are not included. Some data points are also present near the 14.85 MeV excitation energy but error bars are too large. In the inset of figure 2(d) we have indicated the positions and widths of some observed excited levels coming from the decays into ^{8}Be+^{8}Be (black full lines) and α+^{12}C*(HS) (red dashed lines) [19–22]. We notice the large bump below 16 MeV which might be dominated by the suggested resonances plus the detector acceptance. For larger excitation energies, resonances are embedded into the BEC thus are not clearly distinguishable [5, 8-9]. Of course repeating the experiment with an improved detector granularity might shed more light on these in medium levels. In such a scenario the RDN method proposed in this work might be crucial.

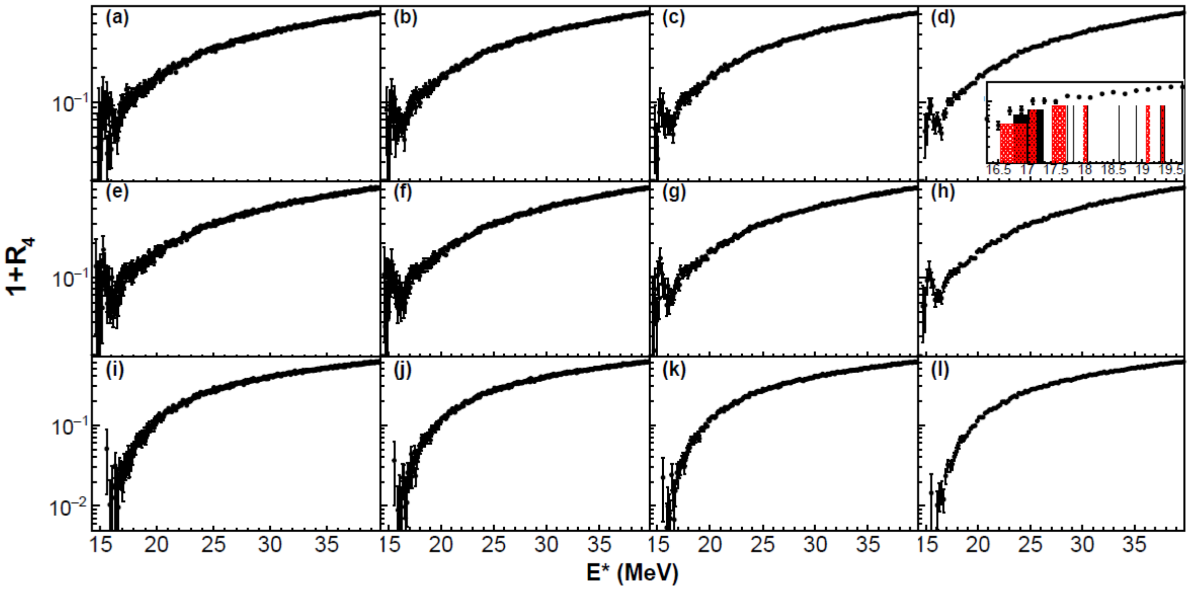

Fig. 2. Excitation energy distribution for the CD choice: (top) Eij(DH)=92 keV, (middle) Eij(DH)=0 keV and (bottom) no double hits.The (a),(b),(c),(d) correspond to the bin-widths of 60 keV, 80 keV, 120 keV, 200 keV, and the middle and bottom panels are similar. In the inset of (d), the positions and widths of known resonances are indicated as well, see text.

[1] D.J. Marín-Lámbarri *et al.*, Phys. Rev. Lett. **113**, 012502(2014).
[2] T. Ichikawa *et al.*, Phys. Rev. Lett. **107**, 112501(2011).
[3] J. Bishop *et al.*, Phys. Rev. C **100**, 034320 (2019).
[4] M. Barbui *et al.*, Phys. Rev. C **98**, 044601 (2018).
[5] G. Giuliani, H. Zheng, and A. Bonasera, Progress in Particle and Nuclear Physics **76**, 116 (2014).
[6] A. Bonasera, F. Gulminelli, and J. Molitoris, Phys. Rep. **243**, 1 (1994).
[7] K. Schmidt *et al.*, Phys. Rev. C **95**, 054618 (2017).
[8] J. Mabiala, H. Zheng, A. Bonasera, Z. Kohley, and S. J. Yennello, Phys. Rev. C **94**, 064617 (2016).
[9] P. Marini *et al.* [INDRA Collaboration], Phys. Lett. B **756**, 194 (2016).

[10] Z. Kholey, PhD Thesis, Texas A&M University, 2010.
[11] V. Efimov, Phys. Lett. B **33**, 563 (1970).
[12] H. Zheng and A. Bonasera, arXiv:1811.10412.
[13] V. Efimov, Nat. Phys. **5**, 533 (2009).
[14] A.Tumino, A.Bonasera, G.Giuliani *et al.*, Phys. Lett. B **750**, 59 (2015).
[15] L.H. Thomas, Phys. Rev. **47** 903 (1935).
[16] C.H. Greene, Phys. Today **63** (3), 40 (2010).
[17] S. Zhang, A. Bonasera, M. Huang *et al.*, Phys. Rev. C **99**, 044605 (2019).
[18] S. Zhang, J.C. Wang, A. Bonasera *et al.*, Chinese Phys. C **43**, 064102 (2019).
[19] P. Chevallier *et al.*, Phys. Rev. **160** (4), 827 (1967).
[20] F. Brochard *et al*., Phys. Rev. C **13** (3), 967 (1976).
[21] M. Freer *et al.*, Phys. Rev. C **51**, 1682 (1995).
[22] M. Freer *et al.*, Phys. Rev. C **70**, 064311 (2004).
[23] Ad. R. Raduta *et al.*, Phys. Lett. B **705**, 65 (2011).
[24] R. Wada *et al.*, Phys. Rev. C **69**, 044610 (2004).

Systematic investigation of the particle spectra in heavy-ion collisions at the Large Hadron Collider

H. Zheng,[1] X.R. Zhu,[2] L.L. Zhu,[3] and A. Bonasera
[1]*School of Physics and Information Technology, Shaanxi Normal University, Xi'an 710119, China*
[2]*School of Science, Huzhou University, Huzhou 313000, China*
[3]*Department of Physics, Sichuan University, Chengdu 610064, China*

We investigate the charged particle spectra produced in the heavy-ion collisions at nine centralities from different systems, i.e., Pb+Pb at $\sqrt{s_{NN}} = 2.76$TeV and 5.02 TeV as well as Xe+Xe at $\sqrt{s_{NN}} = 5.44$ TeV, at Large Hadron Collider (LHC) using one empirical formula inspired by the stationary solution of the Fokker-Planck equation, dubbed as the generalized Fokker-Planck solution (GFPS) [1]. Our results show that the GFPS can reproduce the experimental particle spectrum up to transverse momentum p_T about 45 GeV/c with the maximum discrepancy 30% covering 10 orders of magnitude. The discrepancy between the data and the results from the GFPS decreases to 15% when the maximum of the charged particle transverse momentum is cut to 20 GeV/c. We confirmed that the Tsallis distribution derived from the non-extensive statistics, which can reproduce the particle spectra produced in small collision systems, such as p+p, up to few hundreds GeV/c, can only apply to systematically study the particle spectra up to 8 GeV/c in A+A collisions at LHC, as pointed out in the study of identified particle spectra in Pb+Pb collisions at $\sqrt{s_{NN}} = 2.76$TeV [2]. A brief discussion on GFPS is also given.

Recently, the experimental data of charged particle spectra at different centralities in Pb+Pb collisions at $\sqrt{s_{NN}} = 2.76$TeV and 5.02 TeV as well as Xe+Xe collisions at $\sqrt{s_{NN}} = 5.44$TeV with a wide p_T range up to 45 GeV/c, which is twice larger than the previous experimental measurements [3], have been released by the ALICE Collaboration at LHC [4, 5]. More systems and more colliding energies with particle spectra in wider p_T range will be the new challenges to all the models. Therefore, we investigate whether the GFPS proposed by us can reproduce the new experimental data, which can shed the light on understanding the particle production mechanism at LHC.

The generalized Fokker-Planck solution (GFPS) adopted is

$$\left(E\frac{d^3N}{dp^3}\right)_{|\eta|<a} = A\frac{e^{-\frac{b}{T}\arctan\frac{E_T}{b}}}{[1+(\frac{E_T}{b})^d]^c}$$

It has five parameters A, b, c, d and the effective temperature T. E_T is the transverse energy of the particle. The asymptotic behavior of GFPS at high p_T is the power-law and at low p_T is the Boltzmann thermal distribution. A crossover from the exponential law at low p_T to the power law at high p_T takes place at $E_T \sim b$. In Fig. 1, we show the typical results for the charged particles produced in Pb+Pb collision at $\sqrt{s_{NN}} = 2.76$ TeV using GFPS and Tsallis distribution.

By conducting detailed investigation of the transverse momentum spectra of charged particle spectra produced in Pb+Pb at $\sqrt{s_{NN}} = 2.76$TeV and 5.02 TeV as well as Xe+Xe at $\sqrt{s_{NN}} = 5.44$TeV using GFPS and the Tsallis distribution, our results show that the GFPS can nicely describe the charged particle spectra from central to peripheral collisions with p_T up to 45 GeV/c, while the Tsallis distribution

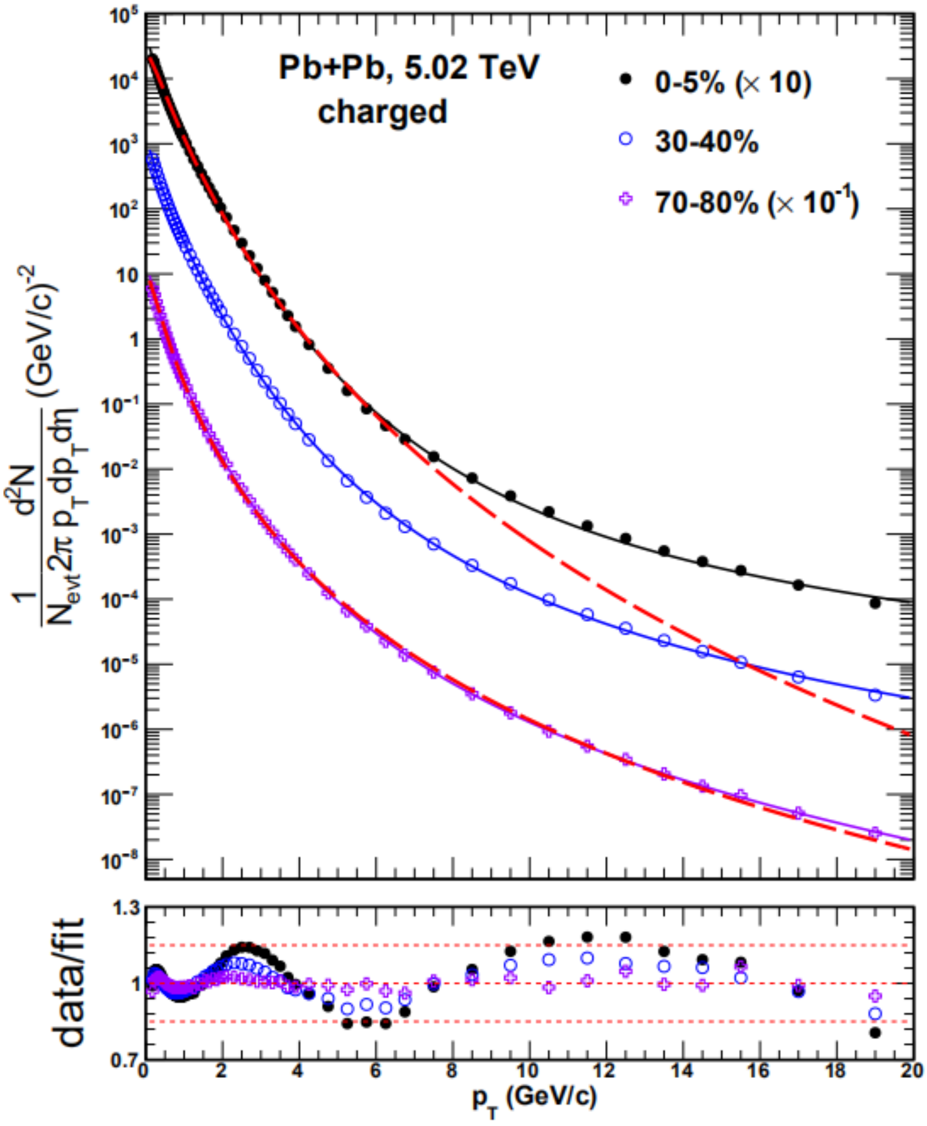

Fig. 1. (Color online) Fitting results showed by solid lines using the GFPS and dashed lines using Tsallis distribution for Pb+Pb collisions at 5.02 TeV.

can only fit the spectra at $p_T < 8$ GeV/c for central collisions and it has the same performance as the GFPS for the peripheral collisions.

[1] H. Zheng, X.R. Zhu, L.L. Zhu, and A. Bonasera, Mod. Phys. Lett. A (Accepted); arXiv: 1905.08623.
[2] H. Zheng, L.L. Zhu, Adv. High Energy Phys. **2015**, 180491 (2015).
[3] The ALICE Collaboration, Phys. Lett. B **736**, 196 (2014).
[4] S. Acharya *et al.* (The ALICE Collaboration), J. High Energy Phys. **11**, 013 (2018).
[5] S. Acharya *et al.* (The ALICE Collaboration), Phys. Lett. B **788**, 166 (2019).

Yield ratio of neutrons to protons in ^{12}C(d, n)^{13}N and ^{12}C(d,p)^{13}C from 0.6 MeV to 3 MeV

Wu-Jie Li,[1,2] Yu-Gang Ma,[3,1] Guo-Qiang Zhang,[4,1] Xian-Gai Deng,[3,1] Mei-Rong Huang,[5]
Aldo Bonasera,[6,7] De-Qin Fang,[3,1] Jian-Qing Cao,[1] Qi Deng,[1]
Yong-Qi Wang,[1] and Qian-Tao Lei[1]
[1]*Shanghai Institute of Applied Physics, Chinese Academy of Sciences, Shanghai 201800, China*
[2]*University of the Chinese Academy of Sciences, Beijing 100080, China*
[3]*Key Laboratory of Nuclear Physics and Ion-Beam Application (MOE), Institute of Modern Physics, Fudan University, Shanghai 200433, China*
[4]*Shanghai Advanced Research Institute, Chinese Academy of Sciences, Shanghai 201210, China*
[5]*College of Physics and Electronics information, Inner Mongolia University for Nationalities, Tongliao, 028000, China*
[6]*Cyclotron Institute, Texas A&M University, College Station, Texas 77843, USA*
[7]*Laboratori Nazionali del Sud, INFN, via Santa Sofia, 62, 95123 Catania, Italy*

The neutron yield in the ^{12}C(d,n)^{13}N reaction and the proton yield in the ^{12}*C*(d,p)^{13}C reaction have been measured using deuteron beams of energies 0.63 MeV, some of the results are shown in Fig. 1. The deuteron beam is delivered from a 4 MeV electrostatic accelerator and bombarded on a thick carbon target. The neutrons are detected at 0°, 24°, and 48° and the protons at 135° in the lab frame. Further, the ratio of the neutron yield to the proton yield was calculated. This can be used to effectively recognize the resonances. The resonances are found at 1.4 MeV, 1.7 MeV, and 2.5 MeV in the ^{12}C(d,p)^{13}C reaction, and at 1.6 MeV and 2.7 MeV in the ^{12}C(d,n)^{13}N reaction. The proposed method provides a way to reduce systematic uncertainty and helps confirm more resonances in compound nuclei.

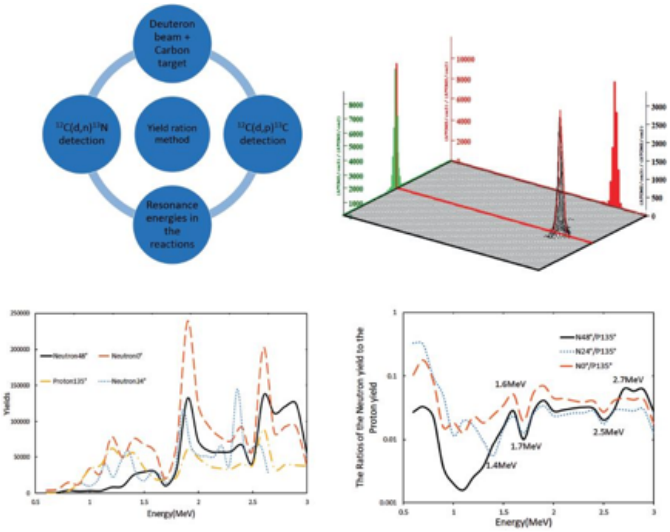

Fig. 1. Yield of neutron and ratio of neutron yield to proton yield from this experiment [1].

[1] W.-J. Li, Y.-G. Ma, G.-Q. Zhang, X.-G. Deng, M.-R. Huang, A. Bonasera, D.-Q. Fang, J.-Q. Cao, Q. Deng, Y.-Q. Wang, and Q.-T. Lei, Nuclear Science and Techniques **30**, 180 (2019).

Cumulative nuclear level density within a micro-macroscopic approach

A.G. Magner,[1] A.I. Sanzhur,[1] S.N. Fedotkin,[1] A.I. Levon,[1] and S. Shlomo
[1]*Institute for Nuclear Research of the NAN Ukraine, Kyiv, Ukraine*

Many nuclear properties can be described in terms of the statistical level density. We have derived the nuclear level density in the micro-macroscopic approximation (MMA) beyond the saddle-point method (SPM), obtaining $\rho \propto I_\nu(S)/S^\nu$, where $I_\nu(S)$ is the modified Bessel function of the entropy S of order $\nu = (n+1)/2$, where n is the number of integrals of motion, taken n=3 in our case. This level density goes to the well-known *SPM* grand-canonical ensemble limit $\rho \propto \exp(S)$ for large entropy *S,* and to the finite micro-canonical limit at low excitation energy.

The MMA expressions for the one-parametric cumulative level density, $N = \int d\,W'\rho(W')$, where the integral is taken from 0 to the excitation energy W, provides a good fit, using a standard mean-least-square (MLS) code, to the experimental two-neutron-transfer reaction data for *N(W)* values shown (see the left panels of the Fig. 1) for different angular momenta $I^\pi = 0^+$, 2^+ and 4^+. The $N(W)$ is used for the unfolding procedure by transferring the spectrum W_i to the uniform states $w_i = \widetilde{N}(W_i)$,

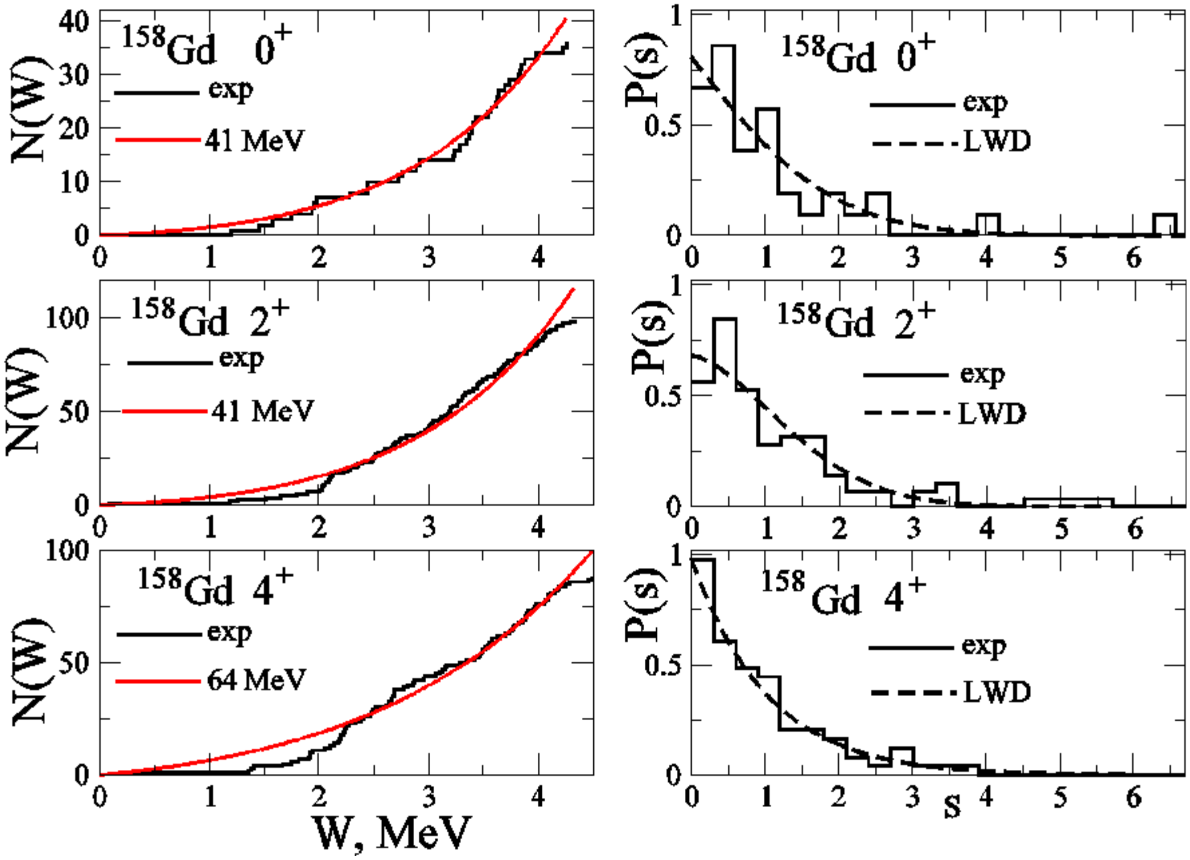

Fig. 1. Cumulative energy level density N(W) as function of the excitation energy W (left panels) and the nearest neighbor spacing distribution P(s) as a function of energy spacing s (right panels) for state with different angular momentum, 0^+, 2^+ and 4^+ in ^{158}Gd.

where the tilde means averaging over states i, and determining $s_i = w_{i+1} - w_i$. Using this result in the statistical analysis of the collective excitation states i in terms of the nearest neighbor spacing distribution (NNSD) $P(s)$ we obtained the experimental NNSD (see the right panels of the Fig. 1). From a good MLS fit to our one-parameter theoretical linear-repulsion-density NNSD within the Wigner-Dyson (LWD) theory for ^{158}Gd, as example, we finds the parameters of contributions of the Wigner chaos and Poisson order distributions for different angular momenta I^+. As seen from Fig. 1, with increasing I^+, there is an anomaly behavior of the NNSD $P(s)$ as a shift from the Poisson order with a sharp peak at zero spacing s to the side of the Wigner chaos distribution with the maximum at $s > 0$ for the angular momentum 2^+ and, then, again for 4^+ to the Poisson order, in contrast of a monotonical I^+ dependence found for the collective states in actinide nuclei. For perspectives, the moment of inertia for the collective rotational bands and K-symmetry breaking phenomenon is a challenge for study.

[1] A.G. Magner, A.I. Sanzhur, S.N. Fedotkin, A.I. Levon, and S. Shlomo, to be published.

Properties of isoscalar giant multipole resonances in medium-heavy closed-shell nuclei: a semi-microscopic description

M.L.Gorelik,[1] S. Shlomo, B.A. Tulupov,[2] and M.H. Urin[3]
[1]*Moscow Economic School, Moscow 123022, Russia*
[2]*Institute for Nuclear Research, RAS, Moscow 117312, Russia*
[3]*National Research Nuclear University "MEPhI", Moscow 115409, Russia*

The particle-hole (p-h) dispersive optical model (PHDOM) [1], was adopted and implemented [2] for describing main properties of Isoscalar Giant Multipole Resonances (ISGMPR) up to L=3 in medium-heavy closed-shell nuclei. The overtones of the monopole and quadrupole isoscalar giant resonances were also studied. The main properties, considered in a large excitation-energy interval., include the following energy-averaged quantities: (i) the strength function related to an appropriate probing operator; (ii) the projected one-body transition density (related to the corresponding operator), and; (iii) partial probabilities of direct one-nucleon decay. Unique abilities of PHDOM are conditioned by a joint description of the main relaxation processes of high-energy p-h configurations associated with a given giant resonance (GR). Two processes (Landau damping and coupling the mentioned configurations to the single-particle continuum [3]) are described microscopically in terms of Landau-Migdal p-h interaction and a phenomenological mean field, partially consistent with this interaction. Another mode, the coupling to many quasiparticle states (the spreading effect) is described phenomenologically in terms of the imaginary part of the properly parameterized energy-averaged p-h self-energy term. The imaginary part determines the real one via a microscopically-based dispersive relationship. The model parameters related to a mean field and p-h interaction are taken from independent data with the isospin symmetry, and translation invariance of the model Hamiltonian also taking into account. Parameters of the strength of self-energy term imaginary part were adjusted to reproduce in PHDOM-based calculations of total width (the full width at half maximum) of ISGMPR for the considered closed-shell nuclei ^{40,48}Ca, ^{90}Zr, ^{132}Sn, ^{208}Pb. The calculation results were compared with available experimental data. Some of results were compared with those obtained in microscopic Hartree-Fock based RPA calculations [4]. These comparisons confirm the statement that PHDOM is a powerful tool for describing ISGMPR in medium-heavy closed-shell nuclei. Extension of the model by taking nucleon-nucleon pairing interaction into account in open-shell nuclei is in order.

As an example we present in the Fig. 1 below the relative energy-weighted strength functions, $y_L(\omega)$, (Fig. 1a) and the projected transition density, $\rho_{V_L}(r,\omega)$ (Figure 1b) for the overtone of the isoscalar giant monopole resonance (ISGMR2) in the closed shell nuclei ^{40,48}Ca, ^{90}Zr, ^{132}Sn and ^{208}Pb. Evaluated within PHDOM, the transition densities were taken at the peak energy of the respective ISGMR2.

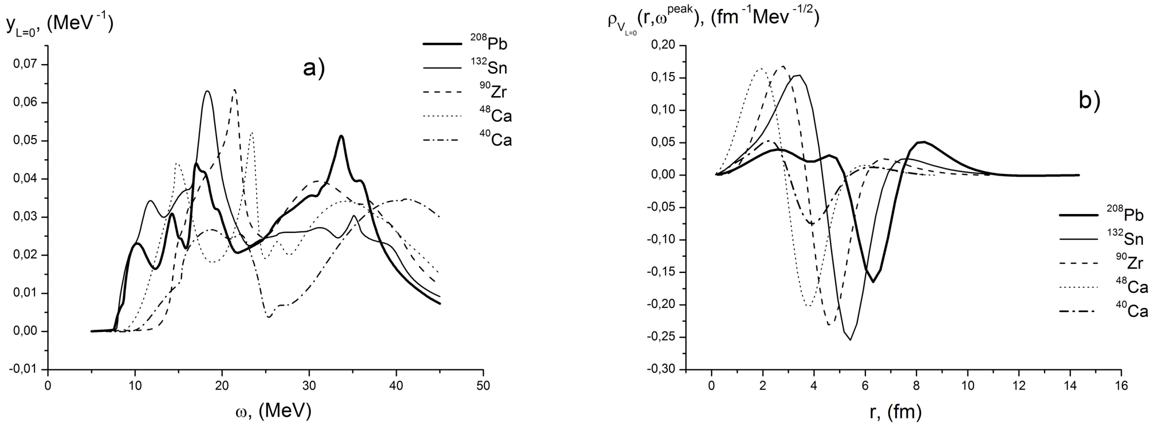

Fig. 1. Evaluated within PHDOM for the overtone of the isoscalar giant monopole resonance (ISGMR2) in ^{40,48}Ca, ^{90}Zr, ^{132}Sn and ^{208}Pb nuclei : a) the relative energy-weighted strength function; b) the projected transition density taken at the resonance peak-energy.

[1] M.H. Urin, Phys. Rev. C **87**, 044330 (2013).
[2] M.L. Gorelik, S. Shlomo, B.A. Tulupov, and M.H. Urin, to be published.
[3] S. Shlomo and G. Bertsch, Nucl. Phys. **A243,** 507 (1975).
[4] G. Bonasera, M.R. Anders, and S. Shlomo, Phys. Rev. C **98**, 054316 (2018).

Shell and collective effects in the nuclear level density

A.G. Magner,[1] A.I. Sanzhur,[1] S.N. Fedotkin,[1] A.I. Levon,[1] and S. Shlomo
[1]*Institute for Nuclear Research of the NAN Ukraine, Kyiv, Ukraine*

It is well known that the nuclear level density is an important ingredient in determining nuclear cross sections needed for describing various phenomena in nuclei and Astrophysics objects. Continuing our long term investigation, of taking into accounts effects of the continuum and the temperature dependence of the level density parameter, *a*, [1,2], we have investigated the shell effect on the level density [3]. We derived the statistical level density $\varrho(S)$ as function of the entropy *S* within the micro-macroscopic approximation (MMA) using the mixed micro- and grand-canonical ensembles. This function can be applied for small and, relatively, large entropies *S,* or excitation energies *U* of a nucleus. For a large entropy (excitation energy), one obtains the standard exponential asymptotics, however, with the significant inverse $1/S$ power corrections. For small *S* one finds the usual finite combinatoric expansion in powers of *S*. The transition from small to large *S* is sufficiently rapid in a small region of $S \approx 3-4$. This analytically derived level density is specified for the simplest example of the “classical rotation” as alignment of the single particle (s.p.) angular momenta of nucleons in a spherical infinitely deep potential within the semiclassical periodic orbital theory (POT), and taking into account the shell effects.

The calculations was carried out within the semi-classical extended Thomas Fermi (ETF) approximation, using the POT which unifies the smooth ETF part and oscillating (shell) corrections in terms of short periodic orbits which occupy larger phase-space volume in the potential well. We added the smooth self-consistent ETF values of the level density parameter *a* for the KDE0v1 and SkM* Skyrme forces with accounting for the effective mass m^* from Ref. [2] to the shell corrections in *a* through the level density, and also determined the inverse level density parameter $K(A)=A/a$. As shown in Ref. [2], the effect of the effective mass m^* on the inverse level density $K(A)$ is very strong, by decreasing $K(A)$ by about a factor about 2, that leads approximately to the mean values deduced from the experimental data for neutron resonances [4]. We found qualitatively good agreement between semiclassical POT and quantum-mechanical results with experimental data on $K(A)$ after an overall shift of all $K(A)$ curves by only one parameter betwen particle numbers $A \approx 80=150$. We suggest to use the MMA for small excitation energies to remove descrepancy near the double magic nuclei ^{40}Ca and ^{208}Pb.

We note that the neutron-proton asymmetries and large deformations of the rare earth and actinide nuclei should be also taken into account to improve the theoretical results in comparison with the experimental data on the nuclear level density parameter for neutron resonances.

[1] S. Shlomo, Nucl. Phys. **A539**, 17 (1992).
[2] V.M. Kolomietz, A.I. Sanzhur, and S. Shlomo, Phys. Rev. C **97,** 064302 (2018).
[3] A.G. Magner *et al.*, to be published.
[4] T. von Egidy and D. Bucurescu, Phys. Rev. C **80**, 054310 (2009).

Astrophysical factors of $^{12}C + ^{12}C$ fusion extracted using the Trojan horse method

A.M. Mukhamedzhanov, D.Y. Pang, and A.S. Kadyrov

Carbon-carbon burning plays an important role in many stellar environments. Recently, Tumino *et al.* [1] reported a sharp rise of the astrophysical S factor for carbon-carbon fusion determined using the indirect Trojan horse method. We demonstrate that the rise at low energies seen in the aforementioned work is an artifact of using an invalid plane-wave approximation that neglects the Coulomb interactions between charged particles. Our analysis shows that such a rise disappears if the Coulomb (or Coulomb-nuclear) interactions in the initial and final states are included [2].

[1] Tumino *et al.* Nature **557**, 687 (2018).
[2] A.M. Mukhamedzhanov, D.Y. Pang, and A.S. Kadyrov, Phys. Rev. C **99**, 064618 (2019).

New method of analytic continuation of elastic-scattering data to the negative - energy region, and asymptotic normalization coefficients for ^{17}O and ^{13}C

L.D. Blokhintsev, A.S. Kadyrov, A.M. Mukhamedzhanov, and D.A. Savin

A new method is proposed for extrapolation of elastic-scattering data to the negative-energy region for a short-range interaction [1]. The method is based on the analytic approximation of the modulus-squared of the partial-wave scattering amplitude and can serve as an alternative to the traditional one based on continuation of the effective-range function. The new method has been applied to determine the asymptotic normalization coefficients for the ^{17}O and ^{13}C nuclei in the n+^{16}O and n+^{12}C channels, respectively. The asymptotic normalization coefficients obtained by the new method are compared with the ones obtained in the effective-range function approach.

[1] L.D. Blokhintsev, A.S. Kadyrov, A.M. Mukhamedzhanov, and D.A. Savin, Phys. Rev. C **100**, 024627 (2019).

Proton-beam stopping in hydrogen

J.J. Bailey, I.B. Abdurakhmanov, A.S. Kadyrov, I. Bray, and A.M. Mukhamedzhanov

The stopping cross section for protons passing through hydrogen is calculated for the energy range between 10 keV and 3 MeV [1]. Both the positive and neutral charge states of the projectile are accounted for. The two-center convergent close-coupling method is used to model proton collisions with hydrogen. In this approach, electron-capture channels are explicitly included by expanding the scattering wave function in a basis of both target and projectile pseudostates. Hydrogen collisions with hydrogen are modeled using two methods: the single-center convergent close-coupling approach is used for the calculation of one-electron processes, while two-electron processes are calculated using the Born approximation. The aforementioned approaches are also applied to the calculation of the charge-state fractions. These are then used to combine the proton-hydrogen and hydrogen-hydrogen stopping cross sections to yield the total stopping cross section for protons passing through hydrogen.

[1] J.J. Bailey, I.B. Abdurakhmanov, A.S. Kadyrov, I. Bray, and A.M. Mukhamedzhanov, Phys. Rev. A **99**, 042701 (2019).

Status on ^{12}C + ^{12}C fusion at deep subbarrier energies: impact of resonances on astrophysical S* factors

C. Beck, A.M. Mukhamedzhanov, and X. Tang

Since the discovery of molecular resonances in $^{12}C+^{12}C$ in the early sixties a great deal of research work has been undertaken to study α-clustering and resonant effects of the fusion process at sub-Coulomb barrier energies. The modified astrophysical S∗ factors of $^{12}C+^{12}C$ fusion have been extracted from direct fusion measurements at deep subbarrier energies near the Gamow window. They were also obtained by the indirect Trojan horse method (THM). A comparison of direct measurements and the THM, which elucidates problems in the analysis of the THM, is discussed in this Letter to the Editor [1].

[1] C. Beck, A.M. Mukhamedzhanov, and X. Tang, Eur. Phys. J. A **56**, 87 (2020).

Theory of surrogate nuclear and atomic reactions with three charged particles in the final state proceeding through a resonance in the intermediate subsystem

A.M. Mukhamedzhanov and A.S. Kadyrov

Within a few-body formalism, we develop a general theory of surrogate nuclear and atomic reactions with the excitation of a resonance in the intermediate binary subsystem leading to three charged particles in the final state. The Coulomb interactions between the spectator and the resonance in the intermediate state and between the three particles in the final state are taken into account. Final-state three-body Coulomb multiple-scattering effects are accounted for using the formalism of the three-body Coulomb asymptotic states based on the work published by one of us (A.M.M.) under the guidance of L. D. Faddeev. An expression is derived for the triply differential cross section. It can be used for investigation of the Coulomb effects on the resonance line shape as well as the energy dependence of the cross section. We found that simultaneous inclusion of the Coulomb effects in the intermediate and final state decreases the effect of the final-state Coulomb interactions on the triply differential cross section [1].

[1] A.M. Mukhamedzhanov and A.S. Kadyrov, Few-Body Systems **60**, 9 (2019).

Charmed hadron production in an improved quark coalescence model

Sungtae Cho,[1] Kai-Jia Sun, C.M. Ko, Su Houng Lee,[2] and Yongseok Oh[3]
[1]*Division of Science Education, Kangwon National University, Chuncheon 24341, Korea*
[2]*Department of Physics and Institute of Physics and Applied Physics, Yonsei University, Seoul 03722, Korea*
[3]*Department of Physics, Kyungpook National University, Daegu 41566, Korea and Asia Pacific Center for Theoretical Physics, Pohang, Gyeongbuk 37673, Korea*

Using the charm quark coalescence and fragmentation model with the inclusion of the effect of collective flow on the transverse momentum spectra of produced charmed hadrons, we have studied the transverse momentum spectra of charmed mesons and baryons as well as the Λ_c^+/D_0 ratio [1]. As shown in Fig.1, by tuning the oscillator constants in the charmed hadron Wigner functions in the quark coalescence model, which models their changing sizes in hot dense matter, to use up all the charm quarks at $p_T \approx 0$ GeV and fragmenting the remaining charm quarks into charmed hadrons, we have obtained the ratio Λ_c^+/D_0 as a function of p_T (dashed line) that successfully describes the experimental data measured at RHIC (solid stars) [2]. This is in contrast to previous studies that did not include the effect of collective flow on charmed hadrons formed from quark coalescence, which underestimated substantially this ratio at

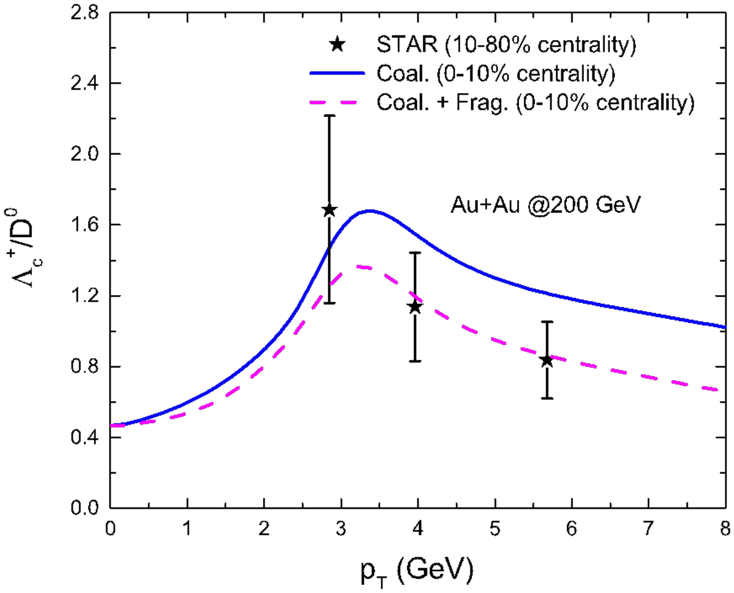

Fig. 1. The yield ratio $\boldsymbol{\Lambda_c^+/D_0}$ as a function of transverse momentum for Au + Au collisions at $\sqrt{s_{NN}} = 200$ GeV. Solid and dashed lines denote the ratio from only charm quark coalescence and the sum of charm quark fragmentation and coalescence contributions at 0-10% centrality. The experimental data from Ref. [2] for the (10-80%) centrality are shown by solid stars with combined statistical and systematic uncertainties.

$p_T > 4.5$ GeV [3]. Compared to results from these studies, the contribution from fragmentation is less important in the present approach. As a result, we have obtained a much larger value for Λ_c^+/D_0 at $p_T > 6$ GeV than that from the conventional approach. Our study thus provides an alternative description of the measured p_T dependence of the ratio Λ_c^+/D_0 at RHIC without the inclusion of a large number of unknown charmed baryon resonances as assumed in Ref. [4].

[1] S. Cho, K.J. Sun, C.M. Ko, S.H. Lee, and Y. Oh, Phys. Rev. C **101**, 024909 (2019).
[2] G. Xie (on behalf of the STAR Collaboration), Proc. Sci. **345**, 142 (2018).
[3] Y. Oh, C.M. Ko, S.H. Lee, and S. Yasui, Phys. Rev. C **79**, 044905 (2009).
[4] M. He and R. Rapp, Phys. Rev. Lett. **124**, 042301 (2020).

Constraining the in-medium nucleon-nucleon cross section from the width of nuclear giant dipole resonance

Rui Wang,[1,2] Zhen Zhang,[3] Lie-Wen Chen,[4] C.M. Ko, and Yugang Ma[1,2]
[1]*Key Laboratory of Nuclear Physics and Ion-beam Application (MOE), Institute of Modern Physics, Fudan University, Shanghai 200433, China*
[2]*Shanghai Institute of Applied Physics, Chinese Academy of Sciences, Shanghai 201800, China*
[3]*Sino-French Institute of Nuclear Engineering and Technology, Sun Yat-Sen University, Zhuhai 519082, China*
[4]*School of Physics and Astronomy and Shanghai Key Laboratory for Particle Physics and Cosmology, Shanghai Jiao Tong University, Shanghai 200240, China*

By incorporating the stochastic NN collision term into the previous lattice-Hamiltonian Vlasov framework [1], we have solved the Boltzmann-Uheling-Ulenbeck (BUU) transport equation with nuclear mean field obtained from the N3LO Skyrme pseudopotential [2]. With the use of a sufficiently large number of test particles, the present lattice-Hamiltonian BUU (LBUU) method treats the Pauli blocking in the collision term of BUU equation with very high precision and thus significantly increases the accuracy in solving the BUU equation. From the accurately calculated giant dipole resonance (GDR) width of

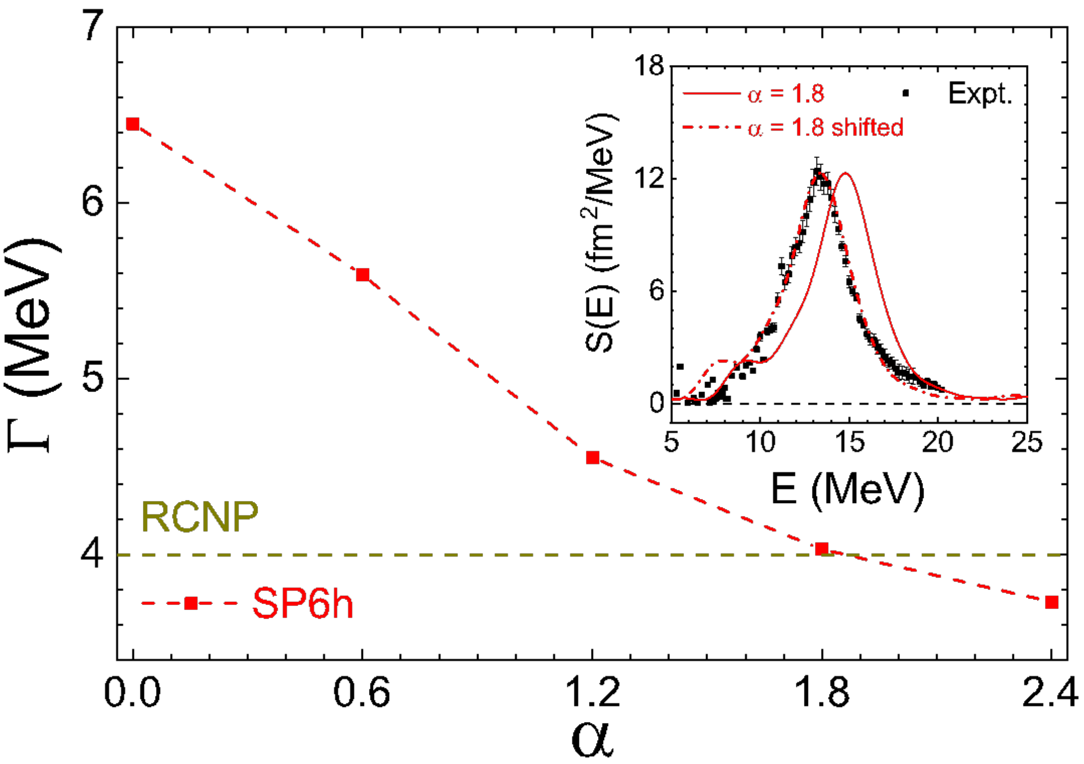

Fig. 1. The GDR width of ^{208}Pb from LBUU calculations for different values of $\boldsymbol{\alpha}$ in $\boldsymbol{\sigma}^*_{NN} = \boldsymbol{\sigma}^{\rm free}_{NN}\mathbf{exp}\left[-\boldsymbol{\alpha}\frac{\rho/\rho_0}{1+(\mathrm{T_{c.m.}}/\mathrm{T_0})^2}\right]$. The horizontal line represents the RCNP experimental value of 4.0 MeV [3]. The inset shows the strength function with $\boldsymbol{\alpha}$ =1.8 (solid line) and the shifted one (dash-dotted line) to match the experimental GDR peak energy.

^{208}Pb, we have found that it depends strongly on the magnitude of the in-medium NN cross section σ_{NN}^{*}, and the experimentally measured GDR width of ^{208}Pb from the ^{208}Pb($\vec{p},\overrightarrow{p'}$) reaction at RCNP [3] can only be reproduced with a NN cross section that is significantly reduced in nuclear medium as shown in Fig.1. The large medium reduction of the free-space NN scattering cross section $\sigma_{NN}^{\text{free}}$ raises challenges to microscopic calculations based on realistic NN interactions. Also, the effects of such a large medium reduction of $\sigma_{NN}^{\text{free}}$ on the widths of other modes of giant resonances in nuclei and on the dynamics of HICs need to be studied as it may significantly affect the extracted information on the properties of nuclear matter at various densities.

[1] R. Wang, L.-W. Chen, Z. Zhang, Phys. Rev. C **99**, 044609 (2019).
[2] R. Wang, Z. Zhang, L.W. Chen, C.M. Ko, and Y.G. Ma, Phys. Lett. B **807**, 135532 (2020).
[3] A. Tamii *et al.*, Phys. Rev. Lett. **107**, 062502 (2011).

Isospin splitting of pion elliptic flow in relativistic heavy-ion collisions

He Liu,[1,2] Feng-Tao Wang,[1,2] Kai-Jia Sun, Jun Xu,[1,2,3] and C.M. Ko
[1]*Shanghai Institute of Applied Physics, Chinese Academy of Sciences, Shanghai 201800, China*
[2]*University of Chinese Academy of Sciences, Beijing 100049, China*
[3]*Shanghai Advanced Research Institute, Chinese Academy of Sciences, Shanghai 201210, China*

We have studied the effect of the vector-isovector interaction on the elliptic flow difference between π^+ and π^- based on the framework of an extended multiphase transport model, in which the partonic mean-field potentials are obtained from a 3-flavor Nambu-Jona-Lasinio model including isovector couplings, and the hadronization algorithm is improved by considering the coalescence of partons close in phase space [1]. We have found that the time component of the vector-isovector potential leads to a more repulsive (attractive) potential for d (u) quarks in the baryon-rich and d-quark-rich medium, thus enhancing the elliptic flow v_2 of d quarks and π^- while reducing that of u quarks and π^+. The space component of the vector-isovector potential and the hadronic potentials are, however, found to have less important effect on the isospin splitting of v_2. With increasing strength of the vector-isovector coupling, the v_2 difference between $\pi^+$and π^- tends to saturate. As shown in Fig.1, results from our transport approach (solid circles) reproduce the decreasing v_2 splitting with increasing collision energy seen in experiments (solid stars) [2], and the experimentally observed v_2 difference between $\pi^+$and π^- favors a strong vector-isovector coupling, with its coupling strength larger than twice the scalar-isoscalar

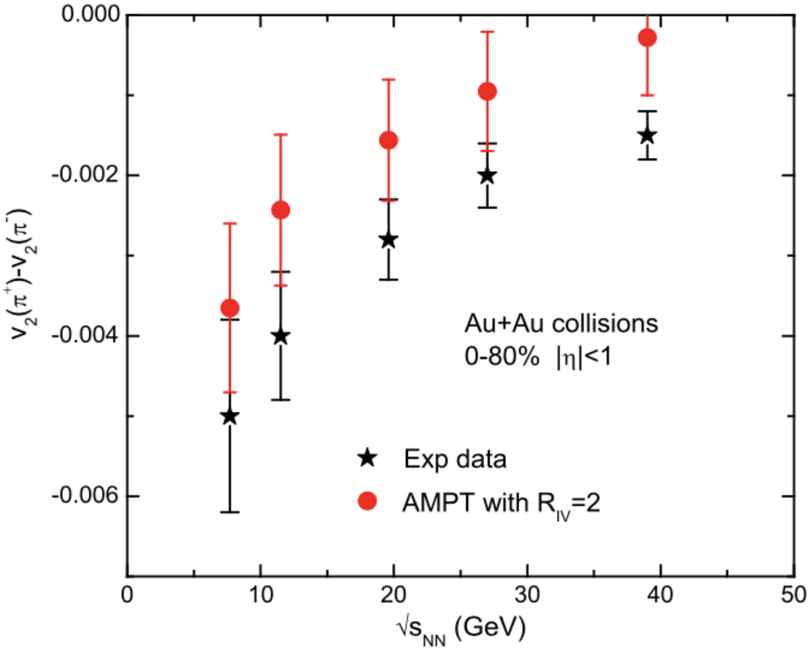

Fig. 1. Comparison of the elliptic flow v_2 difference between mid-pseudorapidity ($|\eta|$ <1) $\pi^+$and π^-at different RHIC-BES energies from the extended AMPT model with those measured by the STAR Collaboration [2].

coupling strength. In the *d*-quark-rich matter, a stronger vector-isovector coupling disfavors the splitting of *u* and *d* quark chiral phase transition boundary, leads to a critical point at higher temperatures, and results in a larger quark matter symmetry energy [3]. Further studies to understand the observed dependence of the total isospin splitting of pion v_2 on the charge asymmetry [3] and to include the isospin-independent Polyakov-loop potential, which is essential for describing the QCD deconfinement phase transition and the thermodynamic properties of QGP [4], are needed.

[1] H. Liu, F.T. Wang, K.J. Sun, J. Xu, and C.M. Ko, Phys. Lett. B **798**, 135002 (2019).
[2] L. Adamczyk *et al.* [STAR Collaboration], Phys. Rev. Lett. **110**, 142301 (2013).
[3] L. Adamczyk *et al.* [STAR Collaboration], Phys. Rev. Lett. **114**, 252302 (2015).
[4] H. Liu, J. Xu, L.W. Chen, and K.J. Sun, Phys. Rev. D **94**, 065032 (2016).

Light nuclei production in relativistic heavy ion collisions from the AMPT model

Kai-Jia Sun and C.M. Ko

Based on an improved multiphase transport (AMPT) model [1,2], which gives a good description of proton production with a smooth quark matter to hadronic matter transition in relativistic heavy ion collisions, we have studied deuteron and triton production from the coalescence of nucleons at the kinetic freezeout of these collisions [3]. For Au+Au collisions at center-of-mass energies $\sqrt{s_{NN}}$ from 7.7 GeV to 200 GeV available at the Relativistic Heavy Ion Collider (RHIC), we have found that the ratio N_tN_p/N_d^2 of the yield N_p of protons, N_d N_d of deuterons, and N_t of tritons is essentially a constant as a function of collision energy as shown by the solid squares in Fig.1. Our result confirms the expectation in Refs.[4,5] that without a first-order quark to hadronic matter phase transition in the produced matter or its approach to the critical point of the QCD matter, this yield ratio does not show any non-monotonic behavior in its collision energy dependence, which is, however, seen in the data from the STAR experiments [6] shown by the solid stars in Fig.1.

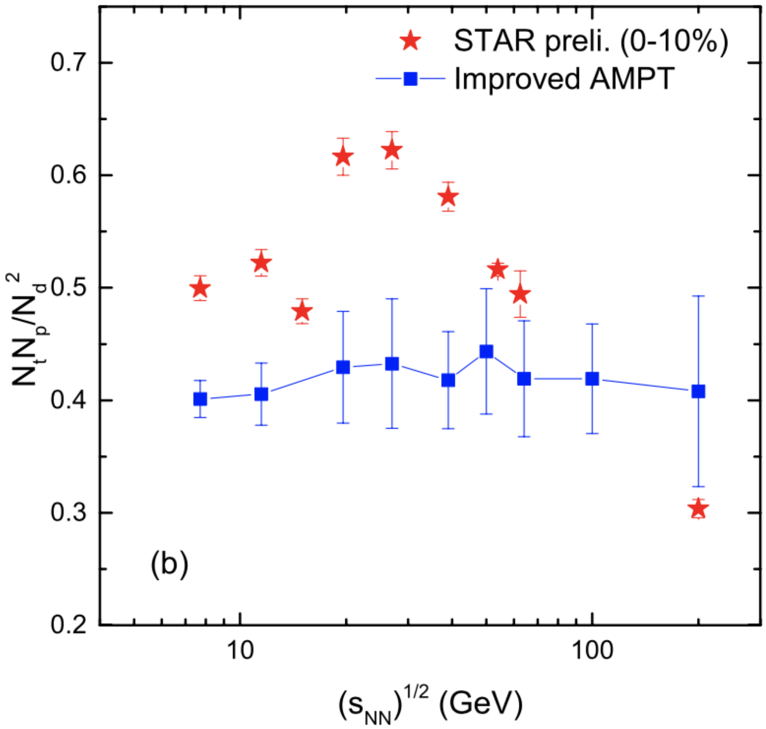

Fig. 1. The yield ratio N_tN_p/N_d^2 as functions of the collision energy $\sqrt{s_{NN}}$ in central Au+Au collisions. Results from the AMPT model are shown by solid squares, and experimental data from Ref. [6] are shown by solid stars.

[1] Z.-W. Lin, C.M. Ko, B.-A. Li, B. Zhang, and S. Pal, Phys. Rev. C **72**, 064901 (2005).
[2] Y. He and Z.-W. Lin, Phys. Rev. C **96**, 014910 (2017).

[3] K.J. Sun and C.M. Ko, arXiv: 2005.00182 [nucl-th].
[4] K.-J. Sun, L.-W. Chen, C.M. Ko, and Z. Xu, Phys. Lett. B **774**, 103 (2017).
[5] K.-J. Sun, L.-W. Chen, C.M. Ko, J. Pu, and Z. Xu, Phys. Lett. B **781**, 499 (2018).
[6] D. Zhang (STAR), arXiv:2002.10677 [nucl-ex].

Nuclear matter properties at finite temperatures from effective interactions

Jun Xu,[1] Arianna Carbone,[2] Zhen Zhang,[3] and C.M. Ko
[1]*Shanghai Institute of Applied Physics, Chinese Academy of Sciences, Shanghai 201800, China*
[2]*European Centre for Theoretical Studies in Nuclear Physics and Related Areas (ECT*) and Fondazione Bruno Kessler, Strada delle Tabarelle 286, I-38123 Villazzano (TN), Italy*
[3]*Sino-French Institute of Nuclear Engineering and Technology, Sun Yat-Sen University, Zhuhai 519082, China*

To study if the commonly used nucleon-nucleon effective interactions, which are usually constructed from fitting the properties of cold nuclear matter and of finite nuclei, can properly describe nuclear matter at finite temperatures, we have used the improved isospin- and momentum-dependent interaction ImMDI-GF [1,2] and the recently constructed Skyrme interaction Skχm* [3] to evaluate the nucleon occupation probabilities, the equations of state, and the mean-field potentials in symmetric nuclear matter and pure neutron matter at finite temperatures using the Hartree-Fock approach [4]. These results have been compared with those from the microscopic self- consistent Green's function method [5] and the chiral effective many-body perturbation theory [6] using chiral nuclear forces [7]. We have found that differences start to appear more strongly at higher temperatures between results for nuclear matter properties from the two effective interactions and also between these two and those from the microscopic theories. The deviations seen in the nucleon occupation probabilities have been understood from the different momentum dependence in the single-nucleon potential obtained within these approaches, while the latter is strongly suppressed at high momenta in the microscopic calculations based on chiral forces compared to those from the effective interactions, especially for Skχm∗ that has a quadratic momentum dependence. These differences in the nucleon momentum distributions lead to deviations in the kinetic energy contribution and also partially in the potential energy contribution to the nuclear equation of state. The energies per nucleon for symmetric nuclear matter and pure neutron matter from these two effective interactions, shown in the left and right windows of Fig.1, respectively, are roughly consistent with those from the self-consistent Green's function approach, although the equation of state for symmetric nuclear matter from Skχm* remains softer at higher temperatures. Using the ImMDI-GF model in the Hartree-Fock calculation reproduces remarkably well the mean-field potential from the microscopic approaches at various temperatures for both symmetric nuclear matter and pure neutron matter. Our study thus shows that effective interactions with the correct momentum dependence in the mean-field potential, such as the one from the ImMDI-GF model, can properly describe the properties of hot dense nuclear matter and is thus suitable for use in transport models to extract the equation of state of cold nuclear matter, which is needed for describing the properties of neutron stars [8], from intermediate-energy heavy-ion collisions [9,10].

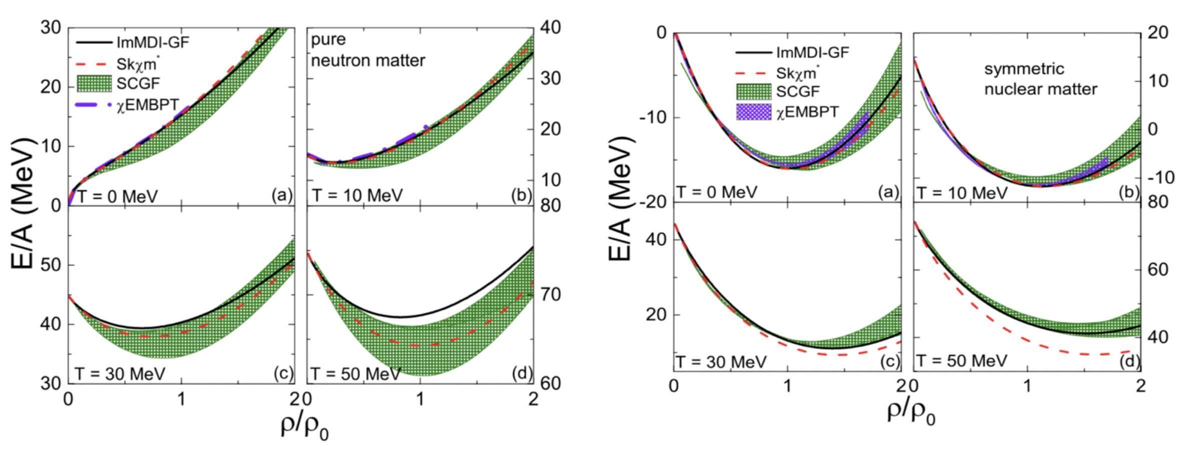

Fig. 1. Total energy per nucleon as a function of reduced nucleon density for symmetric nuclear matter (left window) and pure neutron matter (right window) at various temperatures from ImMDI-GF and Skχm* compared with results from the self self-consistent Green's function approach and from the chiral effective many-body perturbation theory using chiral nuclear forces.

[1] C.B. Das, S. Das Gupta, C. Gale, and B.A. Li, Phys. Rev. C **67**, 034611 (2003).

[2] J. Xu, L.W. Chen, and B.A. Li, Phys. Rev. C **91**, 014611 (2015).

[3] Z. Zhang, Y. Lim, J.W. Holt, and C.M. Ko, Phys. Lett. B **777**, 73 (2018); Phys. Rev. C **98**, 054614 (2018).

[4] J. Xu, A. Carbone, Z. Zhang, and C.M. Ko, Phys. Rev. C **100**, 024618 (2019).

[5] A. Carbone, A. Rios, and A. Polls, Phys. Rev. C **90**, 054322 (2014).

[6] C. Wellenhofer, J.W. Holt, and N. Kaiser, Phys. Rev. C **92**, 015801 (2015); **93**, 055802 (2016).

[7] R. Machleidt and D.R. Entem, Phys. Rep. **503**, 1 (2011).

[8] Y. Lim and J.W. Holt, Phys. Rev. Lett. **121**, 062701 (2018).

[9] P. Danielewicz, R. Lacey, and W.G. Lynch, Science **298**, 1592 (2002).

[10] J. Aichelin and C.M. Ko, Phys. Rev. Lett. **55**, 2661 (1985).

Probing QCD critical fluctuations from the yield ratio of strange hadrons in relativistic heavy-ion collisions

Tianhao Shao,[1] Jinhui Chen,[2] C.M. Ko, and Kaijia Sun

[1]*Shanghai Institute of Applied Physics, Chinese Academy of Science, Shanghai 201800, China and University of Chinese Academy of Science, Beijing 100049, China*

[2]*Key Laboratory of Nuclear Physics and Ion-beam Application (MOE), Institute of Modern Physics, Fudan University, Shanghai 200433, China*

By analyzing the available data on strange hadrons in central Pb+Pb collisions from the NA49 Collaboration at the Super Proton Synchrotron (SPS) [1] and in central Au+Au collisions from the STAR Collaboration at the Relativistic Heavy-Ion Collider (RHIC) [2] in a wide collision energy range from $\sqrt{s_{NN}}$ = 6.3 GeV to 200 GeV, we have found a possible non-monotonic behavior in the ratio $[N(K^+)N(\Xi^-)]/[N(\phi)N(\Lambda)]$ of K+, Ξ−, φ, and Λ yields as a function of $\sqrt{s_{NN}}$ [3] as shown by open and filled circles in Fig.1. Based on the quark coalescence model with the inclusion of the effect of quark density fluctuations on hadron production, a possible non-monotonic behavior in the dependence of the

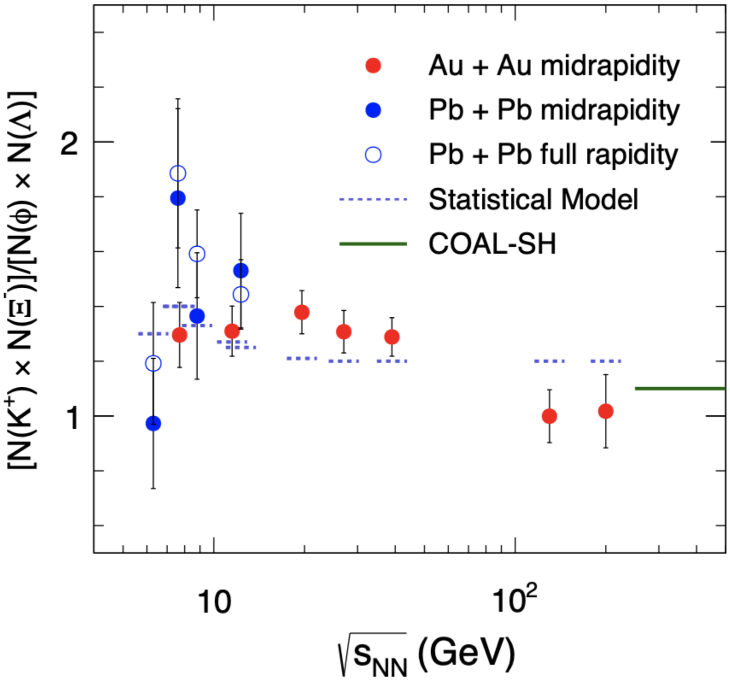

Fig. 1. Collision energy dependence of the ratio $[N(K^+)N(\Xi^-)]/[N(\phi)N(\Lambda)]$ in central Pb+Pb collisions at SPS energies and in central Au+Au collisions at RHIC energies from experimental data from Ref.[1] and Ref.[2], respectively. Filled and open circles denote, respectively, the ratio obtained from midrapidity and in full rapidity space. Error bars represent the statistical uncertainties. The horizontal line on the right side of the figure show the ratio calculated from the coalescence model without quark density fluctuations [4]. The dash lines are the ratio calculated from the statistical model [5].

strange quark density fluctuation on $\sqrt{s_{NN}}$ is obtained. This is in contrast to the coalescence model that does not include quark density fluctuations [4] and also to the statistical hadronization model [5], shown by short solid and dashed lines, respectively, in Fig.1, as both fail to describe even qualitatively the collision energy dependence of the ratio $[N(K^+)N(\Xi^-)]/[N(\phi)N(\Lambda)]$. Our finding thus confirms the suggestion in Refs.[6-8] that the signal and location of a possible critical endpoint in the QCD phase diagram, which is expected to result in large quark density fluctuations, can be found in the on-going Bean Energy Scan program at RHIC.

[1] C. Alt *et al.* (NA49), Phys. Rev. C **77**, 024903 (2008); C **78**, 044907 (2008); C **78**, 034918 (2008).

[2] X. Luo and N. Xu, Nucl. Sci. Tech. **28**, 112 (2017).

[3] T.H. Shao, J.H. Chen, C.M. Ko, and K.J. Sun, Phys. Lett. B **801**, 137177 (2020).

[4] K.-J. Sun and L.-W. Chen, Phys. Rev. C **95**, 044905 (2017).

[5] S. Wheaton and J. Cleymans, Comput. Phys. Commun. **180**, 84 (2009).

[6] K.-J. Sun, L.-W. Chen, C.M. Ko, and Z. Xu, Phys. Lett. B **774**, 103 (2017).

[7] K.-J. Sun, L.-W. Chen, C.M. Ko, J. Pu, and Z. Xu, Phys. Lett. B **781**, 499 (2018).

[8] C.M. Ko, Proceedings, 17th International Conference on Strangeness in Quark Matter (SQM 2017), Eur. Phys. J. Web Conf. **171**, 03002 (2018).

Probing the partonic degrees of freedom in high multiplicity p-Pb collisions at $\sqrt{s_{NN}}$ = 5.02 TeV

Wenbin Zhao,[1,2] C.M. Ko, Yuying Liu,[1,2,3] Guangyou Chen,[4,5] and Huichao Song[1,2,3]
[1]*Department of Physics and State Key Laboratory of Nuclear Physics and Technology, Peking University, Beijing 100871, China*
[2]*Collaborative Innovation Center of Quantum Matter, Beijing 100871, China*
[3]*Center for High Energy Physics, Peking University, Beijing 100871, China*
[4]*Institute of Particle Physics and Key Laboratory of Quark and Lepton Physics (MOE), Central China Normal University, Wuhan, Hubei 430079, China*
[5]*Nuclear Science Division, Lawrence Berkeley National Laboratory, Berkeley, CA, 94270*

We have carried out the first quantitative and timely study [1] of the number of constituent quark (NCQ) scaling of elliptic flow v_2 of pions, kaons and protons at intermediate $p_{\rm T}$ in high multiplicity *p*-Pb collisions at $\sqrt{s_{NN}} = 5.02$ TeV via the coalescence of soft thermal partons from the VISH2+1 hydrodynamics [2] and hard partons from the energy loss LBT model [3]. As shown in Fig. 1, adding low $p_{\rm T}$ hadrons from the hydrodynamically expanding fluid and high $p_{\rm T}$ hadrons from jet fragmentation to these intermediate p_T hadrons from quark coalescence, our Hydro-Coal-Frag hybrid model can simultaneously describe the $p_{\rm T}$ spectra (left window) and differential elliptic flow $v_2(p_{\rm T})$ (middle window) of identified hadrons over the $p_{\rm T}$ range from 0 to 6 GeV. We have also demonstrated that the inclusion of the quark coalescence contribution to the production of hadrons is essential in reproducing the measured $v_2(p_T)$ of these identified hadrons and their observed approximate NCQ scaling at intermediate p_T (right widow). Results from the present study thus provides a strong indication for the existence of the partonic degrees of freedom and the possible formation of the QGP in high multiplicity *p*-Pb collisions at $\sqrt{s_{NN}} =$ 5.02 TeV.

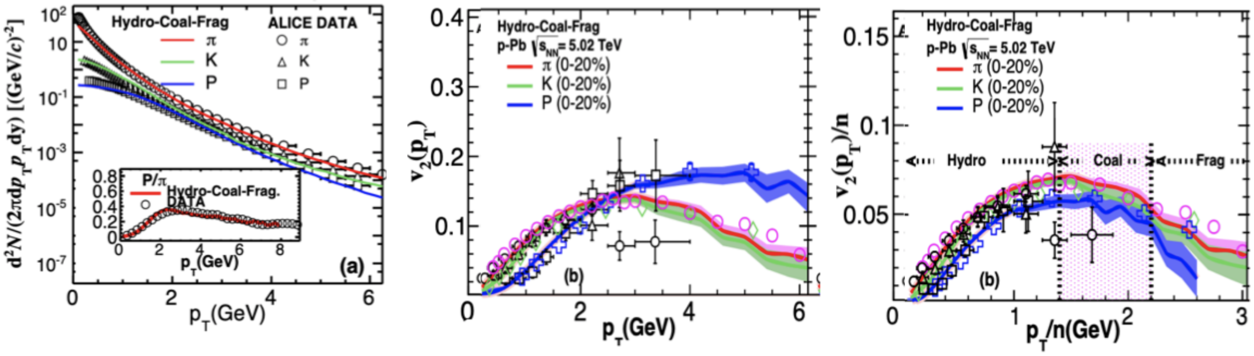

Fig. 1. Transverse momentum p_T spectra (left window), elliptic flow v_2 (middle window) and NCQ scaled elliptic flow (right window) of pions, kaons and protons in 0-20% *p*-Pb at $\sqrt{s_{NN}}$ = 5.02 TeV. ALICE data on p_T spectra are from Ref.[4], and ALICE, CMS, and ATLAS data on elliptic flow are from Refs.[5], [6], and [7], respectively.

[1] W.B. Zhao, C.M. Ko, Y.X. Liu, G.Y. Chen, and H.C. Song, arXiv:1911.00826 [nucl-th].
[2] H. Song and U.W. Heinz, Phys. Rev. C **77**, 064901 (2008); Phys. Lett. B **658**, 279 (2008).
[3] X.N. Wang and Y. Zhu, Phys. Rev. Lett. **111**, 062301 (2013).

[4] J. Adam *et al.* [ALICE Collaboration], Phys. Lett. B **760**, 720 (2016).
[5] B.B. Abelev *et al.* [ALICE Collaboration], Phys. Lett. B **726**, 164 (2013).
[6] A.M. Sirunyan *et al.* [CMS Collaboration], Phys. Rev. Lett. **121**, 082301 (2018).
[**7**] M. Aaboud *et al.* [ATLAS Collaboration], Phys. Rev. C **96**, 024908 (2017).

Properties of strange quark stars with isovector interactions

He Liu,[1,2] Jun Xu,[1,2,3] and C.M. Ko
[1]*Shanghai Institute of Applied Physics, Chinese Academy of Sciences, Shanghai 201800, China*
[2]*University of Chinese Academy of Sciences, Beijing 100049, China*
[3]*Shanghai Advanced Research Institute, Chinese Academy of Sciences, Shanghai 201210, China*

We have studied the properties of strange quark stars by employing a 3-flavor Nambu-Jona-Lasinio model with both scalar-isovector and vector-isovector interactions [1]. Using the constraint on the vector-isoscalar interaction strength obtained from the elliptic flow splitting between particles and their antiparticles in relativistic heavy-ion collisions [2], we have investigated the dependence of the properties of strange quark stars on the vector-isovector and the scalar-isovector interactions, and compared the results with the state-of-art astrophysical constraints on the compact star radius and mass as well as its tidal deformability from the GW170817 event [3]. Results from our study reinforce the prospect of using both heavy-ion collisions and astrophysical observations to provide constraints on the isovector coupling strength in quark matter and thus the quark matter equation of state as well as the QCD phase structure at finite isospin chemical potentials as shown in Fig.1.

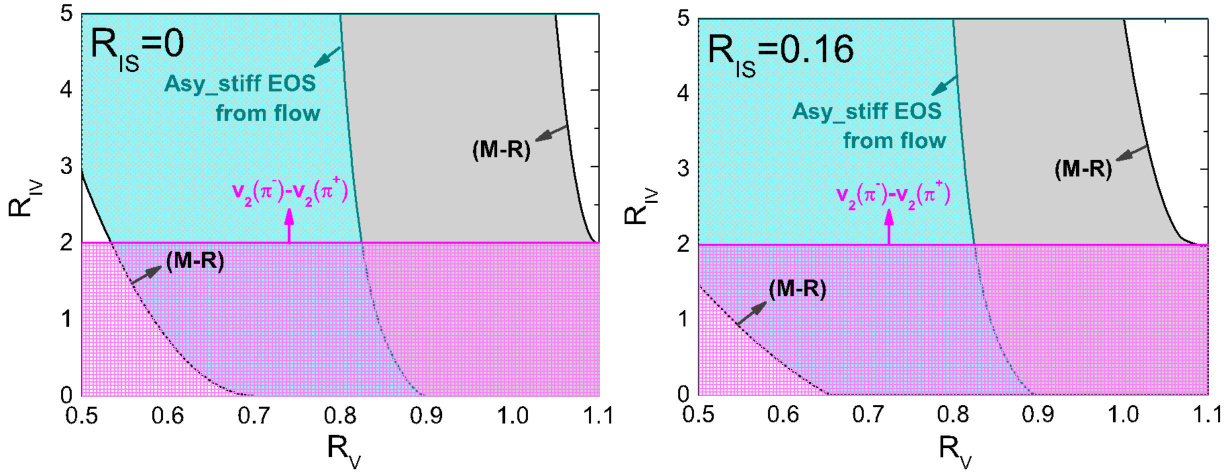

Fig. 1. Constraints on the strengths of the vector-isoscalar interaction R_V and the vector-isovector interaction R_{IV} from comparing with the hadronic matter EOS, the v_2 splitting results in relativistic heavy-ion collisions, and the mass-radius relation for strange quark stars. The left window is the case without the scalar-isovector interaction R_{IS} = 0, while the right window is for R_{IS} = 0.16.

[1] H. Liu, J. Xu, and C.M. Ko, Phys. Lett. B **803**, 135343 (2020).

[2] J. Xu, T. Song, C.M. Ko, and F. Li, Phys. Rev. Lett. **112**, 012301 (2014).

[3] B.P. Abbott *et al.* [LIGO Scientific Collaboration and Virgo Collaboration], Phys. Rev. Lett. **121**, 161101 (2018).

Spin polarizations in a covariant angular momentum conserved chiral transport model

Shuai Y.F. Liu,[1,2] Yifeng Sun,[3] and C.M. Ko

[1]*Quark Matter Research Center, Institute of Modern Physics, Chinese Academy of Sciences, Lanzhou, Gansu, 073000, China*

[2]*University of Chinese Academy of Sciences, Beijing, 100049, China*

[3]*Laboratori Nazionali del Sud, INFN-LNS, Via S. Sofia 62, I-95123 Catania, Italy*

Based on the side-jump formalism for the scattering of chiral fermions, we have constructed a transport model that conserves the total angular momentum of the quark matter created in relativistic heavy-ion collisions [1]. Via the introduction of a covariant angular momentum tensor, the spin polarization of massless quarks then has both spin and orbital contributions. In the case of an expanding

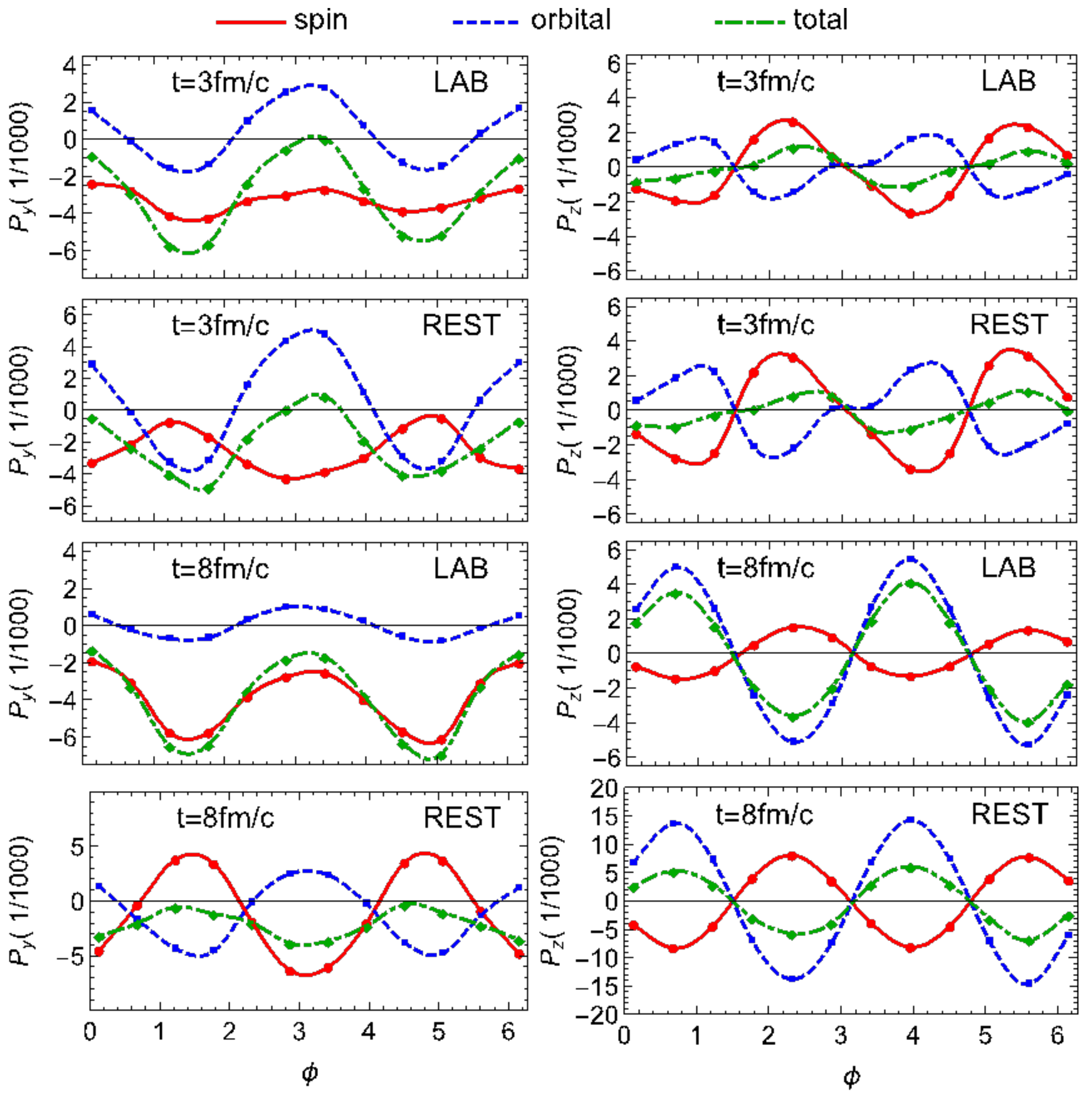

Fig. 1. Azimuthal angle φ dependence of spin polarizations P_y along the y-direction and P_z along the z-direction in the LAB and medium rest (REST) frame at times $t = 3$ and 8 fm/c.

box with a given vorticity field, we have found that the final quark spin polarization is consistent with that expected from the thermal model. For the case of a heavy ion collision using initial conditions from the realistic AMPT model [2], the chiral vortical effect is found to lead to a redistribution of the axial charges in the produced quark matter, resulting in the appearance of dipole and quadrupole structures in the transverse plane of heavy ion collisions. As shown in Fig. 1, including both the spin and orbital contributions of these redistributed quarks to the quark local spin polarizations, we have found that their azimuthal angle dependence along the transverse (P_y) and longitudinal (P_z) directions in the medium rest frame are similar to those obtained from a chiral kinetic theory [3] and also of Lambda hyperons observed in experiments [4].

[1] S.Y.F. Liu, Y.F. Sun, and C.M. Ko, arXiv:1910.06774 [nucl-th].
[2] Z.-W. Lin, C.M. Ko, B.-A. Li, B. Zhang, and S. Pal, Phys. Rev. C **72**, 064901 (2005).
[3] Y. Sun and C.M. Ko, Phys. Rev. C **99**, 011903 (2019).
[4] J. Adam *et al.* (STAR Collaboration), Phys. Rev. Lett. **123**, 132301 (2019).

The QCD critical point from the Nambu-Jona-Lasinio model with a scalar-vector interaction

Kai-Jia Sun, C.M. Ko, Shanshan Cao,[1] and Feng Li[2]
[1]*Department of Physics and Astronomy, Wayne State University, Detroit, MI, 48201, USA*
[2]*School of Physical Science and Technology, Lanzhou University, Lanzhou, Gansu, 073000, China*

Based on the NJL model with both two flavors and three flavors as well as with the inclusion of the Polyakov loop (PNJL), we have studied the effect of the eight-fermion scalar-vector coupled interaction, which has no effects on the QCD vacuum properties, on the critical endpoint of the first-order QCD phase transition line in the QCD phase diagram [1]. We have found that the location of the critical point in the temperature and baryon chemical potential plane is sensitive to the strength of this interaction and can be easily shifted by changing its value as shown in Fig.1 by the dashed and dash-dotted lines in Fig. 1 for the NJL and the PNJL models, respectively. This flexible dependence of the quark equation of state due to the quark scalar-vector coupled interaction is very useful for locating the phase boundary in

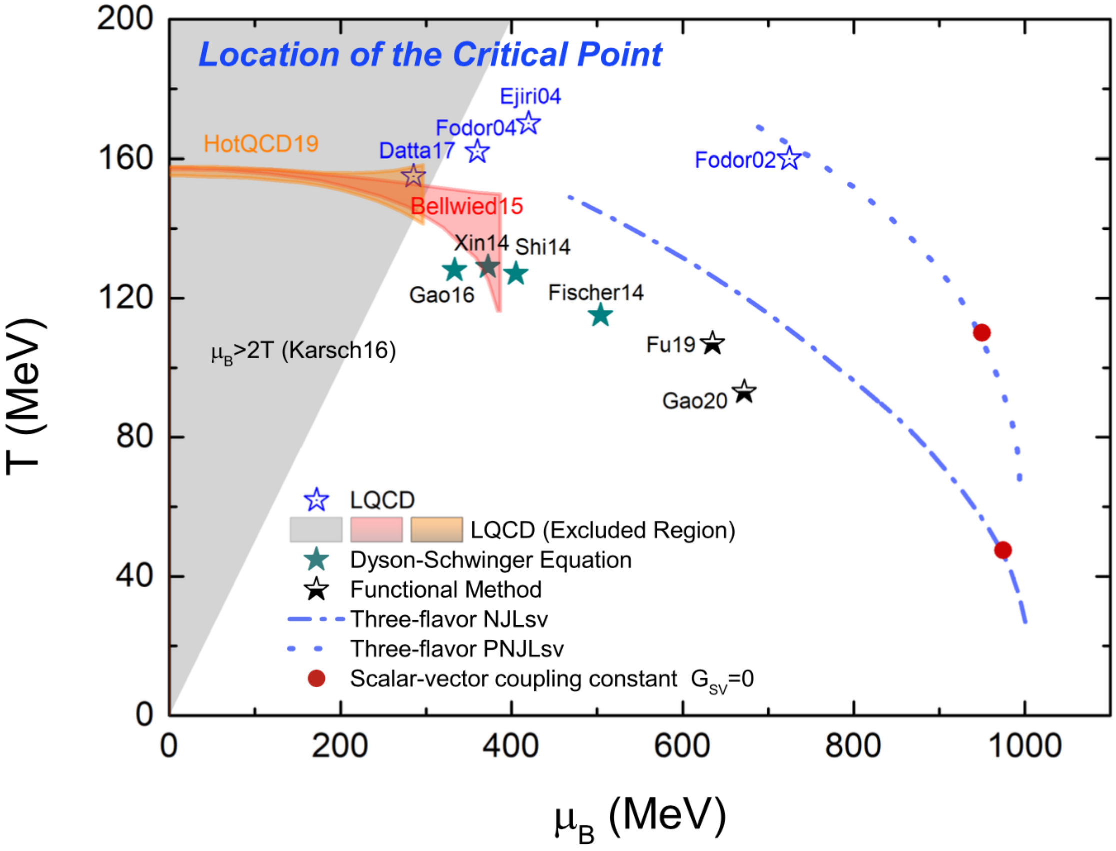

Fig. 1. Comparison of the location of the critical point in the plane of temperature T versus baryon chemical potential μ_B from the three-flavor NJL (dash line) and PNJL (dash-dotted line) models by varying the value of the scalar-vector coupling constant G_{SV}, with red solid circles denoting that obtained with $G_{SV} = 0$, with predictions from LQCD [2–8], Schwinger-Dyson equation [9–12], and the functional renormalization method [13, 14].

QCD phase diagram by comparing the experimental data with results from transport model simulations or hydrodynamic calculations based on equations of states from such generalized NJL and PNJL models.

[1] K.J. Sun, C.M. Ko, S.S. Cao, and F. Li, arXiv:2004.05754 [nucl-th].

[2] S. Ejiri, C.R. Allton, S.J. Hands, O. Kaczmarek, F. Karsch, E. Laermann, and C. Schmidt, Prog. Theor. Phys. Suppl. **153**, 118 (2004).

[3] Z. Fodor and S.D. Katz, JHEP **04**, 050 (2004).

[4] S. Datta, R.V. Gavai, and S. Gupta, Nucl. Phys. **A904-905**, 883c (2013).

[5] F. Karsch *et al.*, Nucl. Phys. **A956**, 352 (2016).

[6] S. Datta, R.V. Gavai, and S. Gupta, Phys. Rev. D **95**, 054512 (2017).

[7] R. Bellwied, S. Borsanyi, Z. Fodor, J. Günther, S.D. Katz, C. Ratti, and K.K. Szabo, Phys. Lett. B **751**, 559 (2015).

[8] A. Bazavov *et al.* (HotQCD), Phys. Lett. B **795**, 15 (2019).

[9] X.-y. Xin, S.-x. Qin, and Y.-x. Liu, Phys. Rev. D **90**, 076006 (2014).

[10] C.S. Fischer, J. Luecker, and C.A. Welzbacher, Phys. Rev. D **90**, 034022 (2014).

[11] C. Shi, Y.-L. Wang, Y. Jiang, Z.-F. Cui, and H.-S. Zong, JHEP **07**, 014 (2014).

[12] F. Gao, J. Chen, Y.-X. Liu, S.-X. Qin, C.D. Roberts, and S.M. Schmidt, Phys. Rev. D **93**, 094019 (2016).

[13] W.-j. Fu, J.M. Pawlowski, and F. Rennecke, arXiv:1909.02991 [hep-ph].

[14] F. Gao and J.M. Pawlowski (2020), arXiv:2002.07500 [hep-ph].

Hadronization and charm-hadron ratios heavy-ion collisions

Min He and Ralf Rapp

Understanding the hadronization of the quark-gluon plasma (QGP) remains a forefront challenge in the study of strong-interaction matter as produced in ultra-relativistic heavy-ion collisions. Due to their large mass, heavy quarks are excellent tracers of the color neutralization process of the QGP when they convert into various heavy-flavor (HF) hadrons, see, e.g., Ref. [1] for a recent review.

In the present work [2] we have developed an energy-momentum conserving recombination model for HF mesons and baryons that obeys the benchmarks of thermal and chemical equilibrium limits and accounts for space-momentum correlations (SMCs) of heavy quarks with the thermal partons of the hydrodynamically expanding QGP, thereby resolving a long-standing problem in quark coalescence models [3]. The SMCs enhance the recombination of fast-moving heavy quarks with high-flow thermal quarks in the outer regions of the fireball. We have furthermore employed an improved hadro-chemistry which includes "missing" charm-baryon states [4] (i.e., those not listed by the particle data group but predicted by lattice QCD [5] and the relativistic quark model [6]). These were previously found to describe the large Λ_c/D^0 ratio measured in proton-proton (pp) collisions at the LHC [4], and thus we establish a consistent treatment of the hadronization process in pp and nucleus-nucleus (AA) collisions. The SMCs are implemented on an event-by-event basis for the charm-quark distribution functions obtained from our hydro-Langevin simulations of heavy-quark diffusion in the strongly coupled QGP which allows for exact charm-quark conservation. The diffusion process is described by non-perturbative T-matrix interactions, which for the current purpose have been augmented by a K-factor of 1.6 to roughly account for radiative interactions which are presently not included in our set up.

Our results for the Λ_c/D^0 and D$_s$/D^0 ratios are shown in the left and middle panel of Fig. 1, respectively, in comparison to ALICE data from the LHC and STAR data from RHIC, showing fair agreement. The main effect of the SMC's is a much increased reach of the recombination process in transverse momentum, p$_T$, causing a significant enhancement over the pp values of the two ratios. In

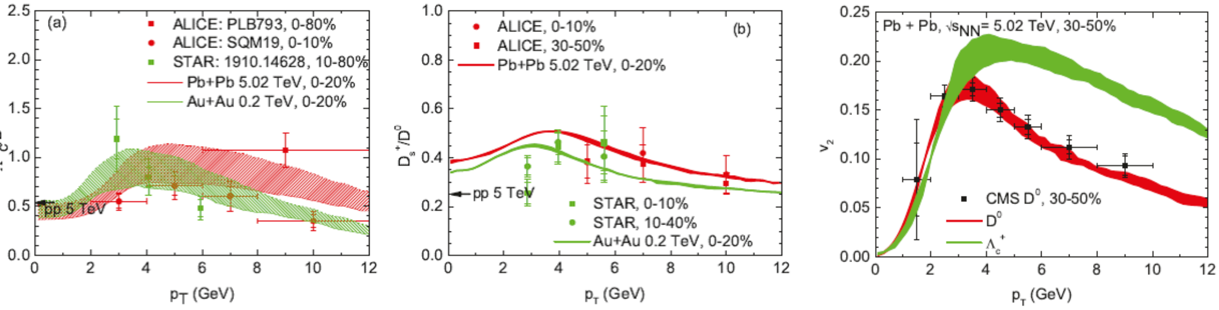

Fig. 1. Transverse-momentum dependence of the L$_c$/D^0 (left) and D$_s$/D^0 (middle) ratio (green bands: 0.2 TeV Au-Au at RHIC, red bands: 5 TeV Pb-Pb collisions at the LHC), compared to ALICE (red symbols) and RHIC (green symbols) data. Right panel: Elliptic flow coefficient, v$_2$(p$_T$), for D^0 mesons (red band) and Λ_c baryons (green band), compared to CMS D^0 data (black symbols).

addition, the near-equilibration of strange-quark production in AA collisions increases the total D_s production also at low p_T [7]. Finally, the SMCs lead to an improved description of the measured high-p_T elliptic flow (see right panel in Fig. 1), which was underestimated in our previous calculations without SMCs [7].

[1] X. Dong, Y.-J. Lee, and R. Rapp, Ann. Rev. Nucl. Part. Sci. **69**, 417 (2019).
[2] M. He and R. Rapp, Phys. Rev. Lett. **124**, 042301 (2020).
[3] R.J. Fries, V. Greco, and P. Sorensen, Ann. Rev. Nucl. Part. Sci. **58**, 177 (2018).
[4] M. He and R. Rapp, and Phys. Lett. B **795**, 117 (2019).
[5] P. Madanagopalan, R.G. Edwards, N. Mathur, and M.J. Peardon, PoS LATTICE **2014**, 084 (2015).
[6] D. Ebert, R.N. Faustov, and V.O. Galkin, Phys. Rev. D **84**, 014025 (2011).
[7] M. He, R.J. Fries, and R. Rapp, Phys. Rev. Lett. **110**, 112301 (2013).

X(3872) transport in heavy-ion collisions

Biaogang Wu, Xiaojian Du, Matthew Sibila, and Ralf Rapp

Ever since its discovery, the internal structure of the X(3872) particle has remained under debate [1]. The production of the X(3872) in heavy-ion collisions has been contemplated as an alternative probe of its internal structure. To investigate this conjecture, we perform transport calculations of the X(3872) through the fireball formed in nuclear collisions at the LHC [2].

We employ the thermal-rate equation approach that we have used before to interpret and predict a wide variety of charmonium and bottomonium observables [3–5]. Here, we focus on the time evolution of the X(3872) abundance in the hadronic phase of the fireball; it is governed by two transport parameters: the equilibrium limit and the inelastic reaction rate. The former provides an important benchmark as the long-time limit of the transport equation, while the latter encodes the structure effects through its coupling to the medium. Specifically, we consider two scenarios for the X(3872): a compact tetraquark state as a bound state of a colored diquark (cq) and its anti-diquark, and a hadronic molecular state as a loosely bound state of a D and D* meson. The width of the tetraquark is estimated to be in the range of Γ_{tetra}=40-80 MeV at an initial temperature of T_0=180 MeV, but much larger for the molecule, Γ_{mol}=300-500 MeV. The temperature dependence is assumed to decrease proportional to $(T/T_0)^3$. For the initial conditions, we assume the equilibrium limit for the tetraquark at the initial temperature (based on its formation with large reaction rates in the quark-gluon plasma), and zero for the molecule. The calculation of the temperature-dependent equilibrium limit throughout the hadronic includes a large number of charm-hadron states which largely affect the evaluation of the charm-quark fugacity (which figures squared for states containing $c\bar{c}$).

Our results, summarized in Fig. 1, show rather moderate differences in the yields within the two X(3872) structure scenarios, by around a factor of 2, which is smaller than in most coalescence model calculations which predict differences of up to two orders of magnitude. Moreover, contrary to coalescence models, the tetraquark yields are larger than those for the molecule, a direct consequence of

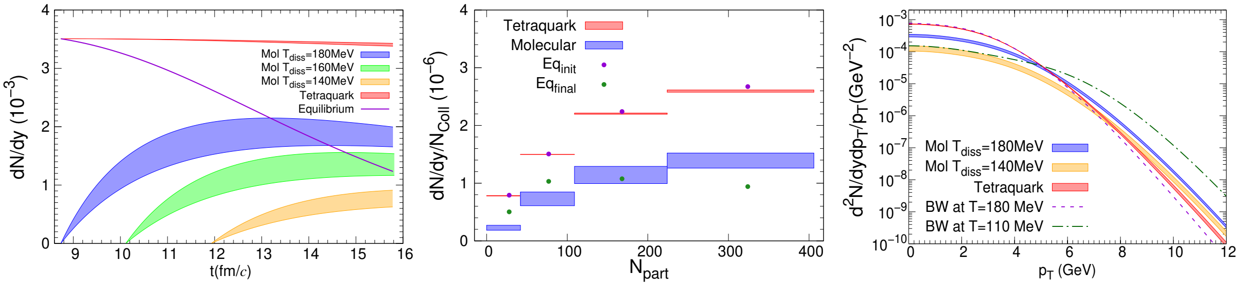

Fig. 1. Left panel: time evolution of the X(3872) equilibrium yield (solid line) and the solutions of the rate equation for the molecular (lower bands, for decreasing onset temperature of regeneration) and tetraquark (upper red band) scenarios in the hadronic phase of 0-20% Pb-Pb collisions at 5 TeV. Middle panel: centrality dependence of the production yields, normalized to the number of primordial NN collisions at each centrality (red bars: tetraquark scenario, blue bars: molecule scenario, symbols: equilibrium limit at chemical and thermal freezeout). Right panel: p_T-spectra in 0-20% central Pb-Pb collisions for the molecular (blue/orange band for T_{diss}=180/140MeV) and tetraquark (red band) scenarios, compared to blastwave spectra at chemical (dashed line) and thermal (dash-dotted line) freezeout.

the larger reaction rate for the molecule in connection with a decreasing equilibrium limit as the fireball cools down. Our calculations of the transverse-momentum (p_T) spectra provide additional constraints on the production time in the fireball evolution, with harder spectra indicating later production.

[1] A. Esposito, A. Pilloni, and A. Polosa, Phys. Rept. **668**, 1 (2017).
[2] B. Wu, X. Du, M. Sibila, and R. Rapp (2020), e-print arXiv:2006.09945.
[3] L. Grandchamp, R. Rapp, and G.E. Brown, Phys. Rev. Lett. **92**, 212301 (2004).
[4] X. Zhao and R. Rapp, Nucl. Phys. **A859**, 114 (2011).
[5] X. Du, R. Rapp, and M. He, Phys. Rev. C **96**, 054901 (2017).

Parameterizing smooth viscous fluid dynamics with a viscous blast wave

R.J. Fries and Zhidong Yang

We have studied how well viscous blast waves represent simulations of high energy nuclear collisions using relativistic viscous fluid dynamics. Previously we had introduced a blast wave with shear viscous corrections [1]. This blast wave ansatz extends the range of applicability to larger momenta, into a region beyond strict kinetic equilibrium. The blast wave fits are sensitive to the ratio of shear viscosity to entropy density η/s of hadronic matter at freeze-out. As reported previously one can use viscous blast wave fits to extract the specific shear viscosity of hadron matter as a function of temperature [1].

To further support our conclusions we have carried out this follow-up study. We have run many instances of viscous fluid dynamic simulations of nuclear collisions with η/s and the freeze-out temperature T_{fo} as parameters, sampling a region in the $\eta/s - T_{\mathrm{fo}}$-plane consistent with expectations in real collisions. Subsequently we have extracted η/s and T_{fo} by Bayesian analysis from the computed identified hadron spectra and elliptic flow using our viscous blast wave ansatz. We find that the fitted values of η/s are mostly consistent with the "true" values of η/s used in the fluid dynamic simulations. On the other hand the fitted freeze-out temperatures are only consistent with "true" values at lower temperatures (more central collisions), but they underpredict the "true" values for peripheral collisions by as much as 15 MeV. We have carefully assigned uncertainties to the fitted values which allow for a notion of consistency between points. The analysis was carried out for Au+Au collisions at energies of 200 GeV at the Relativistic Heavy Ion Collider (RHIC) and for Pb+Pb collisions with 5.02 TeV at the Large Hadron Collider (LHC).

We have parameterized maps M from "true" to fitted blast wave values of η/s and T_{fo} to quantify the systematic deviations of raw fit values. Fig. 1 shows an example of several points in the $\eta/s - T_{\mathrm{fo}}$-plane for Au+Au collisions, together with raw blast wave fits including uncertainty estimates, and the points obtained from the parameterized map for Au+Au applied to the "true" values. The maps M can be inverted and applied to the raw blast wave fit values to obtain corrected fit values which are very close to the "true" values used in fluid dynamics. In extension, raw values of η/s and T_{fo} obtained in blast wave fits from data can be corrected by applying the appropriate inverse maps. The corrected blast wave fit values can be surmised to be closer to the real values.

This correction has been applied to the raw values of η/s and T_{fo} extracted from experimental data in [1] as reported previously. Beyond this immediate application our study points to the possibility that blast wave fits, which are intuitive and numerically cheap tools of data analysis, can be made much more reliable by systematically studying and removing biases introduced by the simplifying assumptions made. The results of this study have been submitted for publication [2].

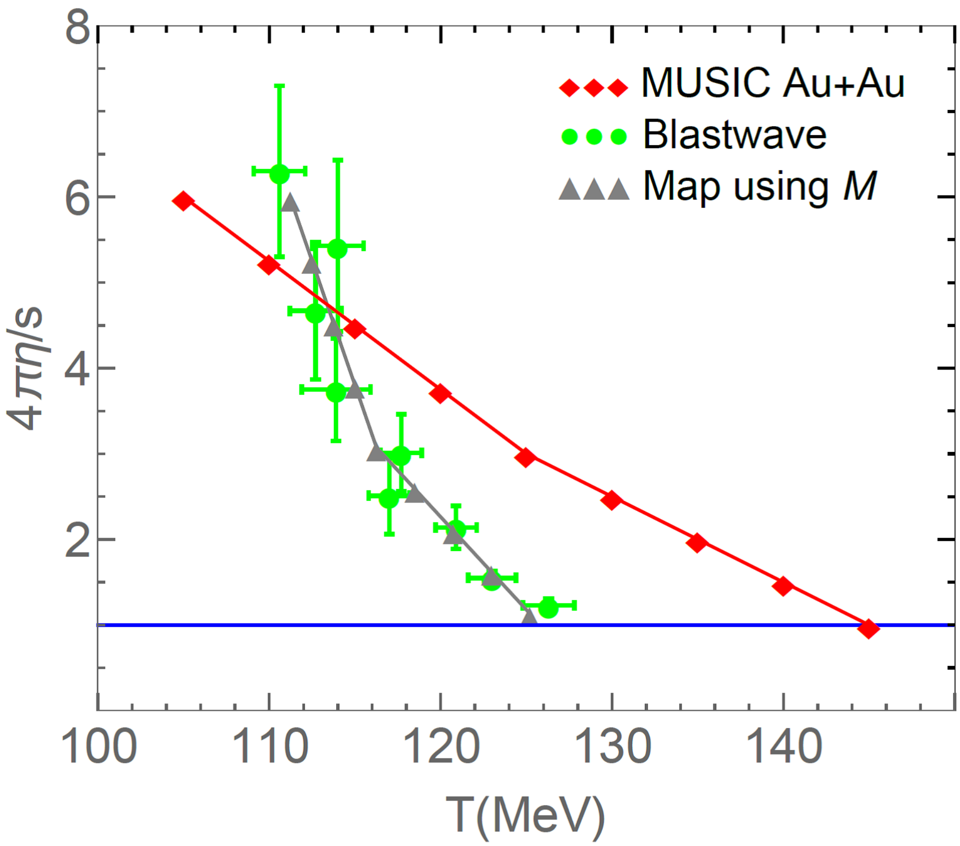

Fig. 1. Points in a plane spanned by specific shear viscosity $\boldsymbol{\eta/s}$ and freeze-out temperature used for viscous fluid dynamic simulations of Au+Au collisions at RHIC (red diamonds), the same parameters extracted from viscous blast wave fits of identified hadron spectra and elliptic flow calculated with these simulations (green circles), and parameterized map M applied to the original values (grey triangles). Lines are included to guide the eye.

[1] Z. Yang and R.J. Fries, arXiv:1807.03410.

[2] Z. Yang and R.J. Fries, arXiv:2007.11777.

The JETSCAPE collaboration: Recent updates and v3.0 release

R.J. Fries, Byunggyu Kim, Michael Kordell, and JETSCAPE Collaborators

We have previously reported on the first release of the JETSCAPE framework package (2018) [1] and the comprehensive study of jet observables in p+p collisions with JETSCAPE 1.0 and the JETSCAPE PP19 tune (2019) [2]. JETSCAPE stands for *Jet Energy-loss Tomography with a Statistically and Computationally Advanced Program Envelope*. It is a collaboration funded with \$3.6M through the *Software Infrastructure for Sustained Innovation* (SI2) program of the U.S. National Science Foundation. It involves theoretical and experimental physicists, computer scientists, and statisticians. R. J. Fries has been a PI on the proposal and is representing Texas A&M University in this multi-institutional effort.

Funding for the original proposal ends in 2020 and the current reporting period saw the release of the last major evolution of the JETSCAPE framework as version 3.0 [3]. v3.0 packs all the physics promised in the original proposal. Improvements and new additions include: (a) the hadronic transport model SMASH which can be used as an afterburner to fluid dynamic simulations in the soft sector; (b) the LIQUIFIER module which simulates the deposition of energy from jets into the background modelled by fluid dynamics; (c) 2-step running to simulate the effects of energy and momentum deposition into the medium enabled by the addition of the LIQUIFIER module; (d) improvements to hybrid hadronization; (e) improved user friendliness through a new XML structure.

With the initial p+p study published the focus of simulations has turned to nucleus-nucleus collisions. A tuning of the soft sector (initial conditions + fluid dynamics + hadronic afterburner) using a Bayesian analysis and tens of millions of CPU hours is currently being readied for publication. First jet results in A+A have been shown at conferences and will be officially released soon. JETSCAPE has also held three schools so far, focusing on students and young postdocs. In 2019 this school was hosted by Texas A&M with support from the Cyclotron Institute.

One of the contributions from members at Texas A&M has been the addition of color flow information into the Hybrid Hadronization model used in JETSCAPE. Color flow is important information for dilute systems of quarks and gluons about to hadronize. This has been established in measurements of e^++e^- and p+p collisions. This information is obscured in A+A collisions by the presence of a color bath. Hybrid Hadronization can take complete (e.g. in p+p) or partially available color flow information, compute recombination probabilities consistently with this color flow, and form remnant strings between quarks and gluons based on the initial color flow modified by recombination. A very simple example for a single string is discussed in Fig. 1. The improvement in the handling of color flow improves the description of dilute systems like e^++e^- and p+p, and p+A collisions.

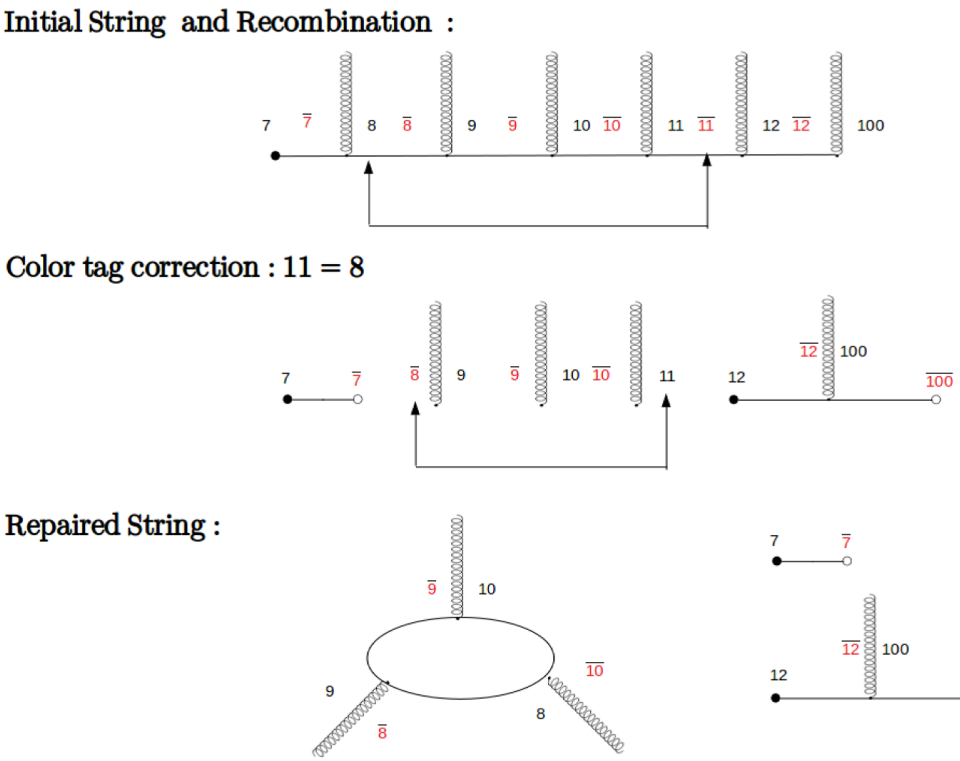

Fig. 1. New color flow in Hybrid Hadronization for a jet shower initiated by a quark with color tag 100 (top row). A quark and an anti-quark from decayed gluons with color tags and 8 and 11(bar) recombine into a meson (center row). The final string configuration after recombination consists of a gluon loop and two smaller strings which are given to PYTHIA 8 for string fragmentation. An anti-quark with color tag 100(bar) has to be added to make the system a color singlet (bottom row).

[1] J. Putschke *et al.* (JETSCAPE Collaboration), arXiv:1903.07706.

[2] A. Kumar *et al.* (JETSCAPE Collaboration), arXiv:1910.05481.

[3] The JETSCAPE 3.0 package, https://github.com/JETSCAPE.

SECTION IV

SUPERCONDUCTING CYCLOTRON AND INSTRUMENTATION

K500 operations and development

D.P. May, G.J. Kim, B.T. Roeder, H.L. Clark, and F.P. Abegglen

Introduction

During the 2019-2020 reporting period a total of 20 different beams, including 7 newly developed beams, were used for experiments, and there were a total of 23 beam tunings for these experiments. The SEE program and the radioactive-beam effort are treated separately in this progress report.

Ion Sources

During the shutdown the ion source that is used by the K500, ECR1, was opened for cleaning and examination. It was found that there had been further deterioration in the damaged spot, first noticed in 2008, that had developed over a plasma flute on the aluminum wall. The field measured at the wall over this spot was 3.7 kilogauss. This position measured 4.4 kilogauss over a small area corresponding to the joint between two NdFeB blocks after the initial assembly of the hexapole in 1995. It was the second weakest point in the wall field after that time. The bar with the weakest field point was damaged in that area by electron bombardment and was replaced in January of 2004. Since electron bombardment at this spot causes excessive heating, degrading performance, and could eventually permanently damage the wall of the plasma chamber, a new hexapole with more uniform magnets and more water-cooling is now being seriously considered.

Cyclotron Beams

New beams of ^{10}B at 25 AMeV, ^{13}C at 30 AMeV, ^{14}N at 14 AMeV, ^{15}N at 30 AMeV, ^{28}Si at 32 AMeV, ^{54}Fe at 36 AMeV, and ^{100}Mo at 12 AMeV were developed for experiments. The majority of experiments used the 2A line devoted to the recoil spectrometer MARS.

Operations

For the period April 1, 2019 through March 31, 2020, the operational time is summarized in Table I, while Table II lists how the scheduled time was divided. Unscheduled maintenance remained quite low. Scheduled time for outsider users, exclusively SEE customers remained about the same as in the last reporting period.

Table I. 2019-2020 operational time.

Time	Hrs.	%Time
Beam on target	6416	73.4
Beam development	560	6.4
Scheduled maintenance	1616	18.5
Unscheduled maintenance	144	1.7
Total	**8736**	**100**

Table II. 2019-2020 Scheduled Beam Time.

Time	Hrs.	%Time
Nuclear physics	1456	20.9
Nuclear chemistry	904	13.0
Outside collaboration	0	0.0
Outside users	4056	58.1
Beam development	560	8.0
Total	**6976**	**100.0**

K150 operations and development

G.J. Kim, B.T. Roeder, F.P. Abegglen, H.L. Clark, L. Gathings, D.P. May, and H. Peeler

We had another busy year operating the K150 cyclotron. For the reporting period as shown in Table I, we logged over 4024 hours of beam-on-target and 2888 hours for beam developments. Included in the beam-on-target time was 3672 hours (1676 for physics and 1996 for chemistry) for in-house science experiments and 352 hours for the SEE tests.

Table I. 2019-2020 operational time.

Time	Hours	% Time
Beam on target	4024	46.1
Beam development	2888	33.0
Scheduled maintenance	1656	19.0
Unscheduled maintenance	168	1.9
Total	8736	100

The big users of the K150 beams were: the SEE tests, the Yennello group, and the Folden and Melconian groups as they began their respective experiments.

The efforts to improve the K150 vacuum started in early 2019 and the vacuum readings ranged from $8\text{x}10^{-7}$ to $1.5\text{x}10^{-6}$ torr for the rest of 2019. With the vacuum improvement, heavier beams like ^{57}Fe, ^{63}Cu, and ^{78}Kr in 4.1 to 15 AMeV were developed and were used in experiments. The internal transmission improved with the vacuum improvement and this helped to achieve good beam intensities for various experiments; notably we achieved 24 μA of 15 MeV protons (from the H- source), 4 μA of 6.3 AMeV ^{40}Ar 11+, 5 μA of 10 AMeV $^{3}\text{He}^{1+}$, and 10 μA of 7.2 AMeV $^{4}\text{He}^{2+}$ beam. Early in 2020, the diffusion pump was removed from the cyclotron and cleaned in ordered to further improve the vacuum, however the initial cyclotron vacuum readings did not show improvement from those of 2019.

The SEE testings continued with 6 to 45 MeV proton beams using the H- source. In addition, we ran two ECR beams, 15 AMeV ^{4}He and 15 AMeV ^{40}Ar, for SEE customers on two separate occasions for the first time. The development of ECR SEE beams continued as time allowed, and to the 15 AMeV ^{14}N, ^{20}Ne and ^{40}Ar beams we developed last year, we were able to add 15 AMeV ^{63}Cu and 10 AMeV ^{78}Kr beams. We would like to develop 15 AMeV ^{78}Kr and even heavier ^{124}Xe beam in the 10 to 12 AMeV range.

The commissioning of the AGGIE spectrometer began with 6.3 AMeV $^{40}\text{Ar}^{11+}$ beam in July. The experiment would have preferred a 5.0 AMeV ^{40}Ar beam, but our difficulties with the 3rd harmonic beams, with tuning and beam intensity (conditioning the RF dee to high voltages has been difficult for frequencies above 14 MHz), pushed the experiment to use 1st harmonic 6.3 AMeV ^{40}Ar beam with a scheme to degrade the energy just in front of their target. We considered degrading the beam energy from 6.3 to 5 AMeV before the 160 degree Analyzing Magnet (AM) and then using AM to select one charge state with largest beam intensity after the degrader. While this method would have provided a clean 5 AMeV ^{40}Ar beam, the beam loss would have been substantial and hence was not tried. Prior to the July run we verified that we could obtain good beam intensities of about 360 particle nA of 6.3 AMeV ^{40}Ar^{11+} on FC02 and that the beam could be transported the experiment through the rather large 53 degree bend through the Maryland magnet. Through the fall, the Folden group used the argon beam 3 times, and the experimenters are now getting ready for their next campaign in the spring.

The commissioning of the TAMUTRAP gas cell, which shares with the Light Ion Guide (LIG) line, began with 10 AMeV ^{3}He^{1+} beam in August. The cell was designed to produce exotic ^{25}Si and ^{24}Si from ^{3}He beam on a ^{24}Mg target, and then stopping and collecting the product in a gas cell (a little larger one than for LIG). Due to the small cross sections for the production, and also due to the difficulty of collecting and transporting the product, having an intense ^{3}He beam was important for the experiment. The two beams of interest were 10 AMeV ^{3}He^{1+} and 23 AMeV ^{3}He^{2+} for producing ^{25}Si and ^{24}Si, respectively. After an initial study the Melconian group concentrated on the 10 AMeV beam. The production cross section for ^{25}Si is larger than that for ^{24}Si, and the lower energy beam produced lower energy recoils, which made the recoil collection more efficient in the gas cell. Thus far we were able to extract 5 μA of 10 AMeV ^{3}He^{1+} beam on FC02. To obtain an intense beam, a good flow of ^{3}He gas was needed into the ECR2 source, and we attached a large gas bottle to the source for a long and stable operation. The beam transport (from FC02) to the gas cell was carried out very similarly to transporting the beams to the LIG target – that is after verifying the beam on the viewer just upstream of the gas cell, we optimized the beam intensity on the faraday cup just downstream of the gas cell using the last 4 quadrupoles. Factoring in the fact that the beam particles would strip up to 2+ from 1+ charge state in going through a number of windows and a target material around the gas cell, around 80% transport efficiency from FC02 to the gas cell was obtained, which is comparable to the beam transport for LIG.

Texas A&M cyclotron radiation effects facility
April 1, 2019 – March 31, 2020

H.L. Clark, G. Avila, J. Brinkley, V. Horvat, B. Hyman, M. Kenna, H.I. Park, B. Roeder, and G. Tabacaru

The activity of the Radiation Effects Facility (REF) increased for record setting usage compared to any previous reporting year. In this reporting period, the facility was used for 3,982 hours, which is an 8.25% increase over the 3,678 hours used in the 2018-2019 reporting period. Users of the facility (and hours used) over the past year were: RTS (274), Boeing Corp (269.5), MDA Corp (242), NASA JPL (214), Texas Instruments (194.5), Infineon (178), Renesas (148.5), NAVSEA (118.25), AFRL (113), Microchip (101), Sandia National Laboratory (99), SEAKR (96), Northrop Grumman (95), Blue Origin

Table I. Radiation effects facility usage by commercial and government customers for this and previous reporting years.

Reporting Year	Total Hours	Commercial Hours (%)	Government Hours (%)
2019-2020	3,982	2,862 (72%)	1,120 (28%)
2018-2019	3,678	2,939(80%)	739(20%)
2017-2018	3,681	2,622 (71%)	1,059 (29%)
2016-2017	3,355	2,501 (75%)	854 (25%)
2015-2016	3,042	2,326 (76%)	716 (24%)
2014-2015	3,024	1,975 (65%)	1,049 (35%)
2013-2014	2,399	1,517 (63%)	882 (37%)
2012-2013	2,626	1,856 (71%)	770 (29%)
2011-2012	2,673	1,630 (61%)	1,043 (39%)
2010-2011	3,042	1,922 (63%)	1,121 (37%)
2009-2010	2,551	1,692 (66%)	859 (34%)
2008-2009	2,600	1,828 (70%)	772 (30%)
2007-2008	2,373	1,482 (62%)	891 (38%)
2006-2007	2,498	1,608 (64%)	890 (36%)
2005-2006	2,314	1,314 (57%)	1,000 (43%)
2004-2005	2,012	1,421 (71%)	591 (29%)
2003-2004	1,474	785 (53%)	689 (47%)
2002-2003	1,851	1,242 (67%)	609 (33%)
2001-2002	1,327	757 (57%)	570 (43%)
2000-2001	1,500	941 (63%)	559 (37%)
1999-2000	548	418 (76%)	131 (24%)
1998-1999	389	171 (44%)	218 (56%)
1997-1998	434	210 (48%)	224 (52%)
1996-1997	560	276 (49%)	284 (51%)
1995-1996	141	58 (41%)	83 (59%)

(92), Troxel Engineering (91), Lockheed Martin (87.5), Johns Hopkins (87), Raytheon (87), Analog Devices (83), NASA GSFC (68.5), BAE Systems (65), Honeywell (64), VPT Inc (64), COSMIAC (48), Freebird Semiconductor (48), Thales Alenia Space (48), Space X (46.5), Intel Corp (41), ReflexPhotonics (41), Howard University (40), Cobham (40), Teledyne DALSA (38.5), SMU (32), JD Instruments (32), Microsemi (32), Signal Analysis (32), Space Micro (32), STEE-SATSYS (32), UltraComm (31.5), GSI Technology (31), Rugged (30.5), Naval Post Graduate (30), Ryoei (28), Draper Labs (24), Millennium (24), Harris (21.5), Astranis (20), Amazon (18), Los Alamos (16), Criteria Labs (16), Cubic Aerospace (16), L3Harris (16), Nucletudes (16), Data Device Corp (15), Crane AE (14), General Dynamics (11.5), SWRI (11.5), U of Arkansas (8), Ball Aerospace (8), iSpace (8), Aria Labs (8), KAIST (8), OnSemi Conductor (8), Raitek (8), T2 Research (8), TRAD (8), and TAMU Physics (4). New users included Reflex Photonics, Howard University, SMU, Rugged, Naval Post Graduate, Amazon, U of Arkansas, and Raitek.

Table I compares the facility usage by commercial and government customers. While commercial hours still dominate, the ratio from this reporting year (72% to 28%) is similar to usage from previous reporting periods (see Fig 1). Commercial usage decreased slightly by 3% but was the second highest commercial usage ever. Government usage increased by 52% and was the second highest usage ever. The large increase in government hours was due to the work by Missile Defense Agency (242 hours). 15 MeV/u ions were the most utilized and especially 15 MeV/u Au. No new beams were added to

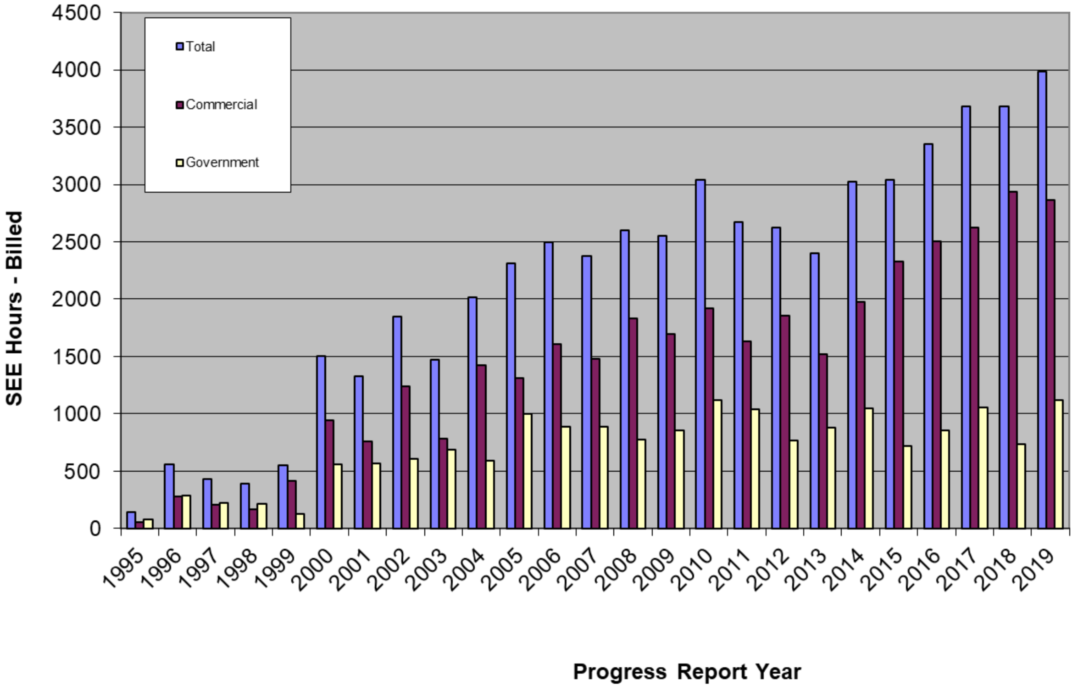

FIG. 1. Radiation Effects Facility usage by commercial and government customers for this and previous reporting years. While commercial hours still dominate, the ratio from this reporting year (72% to 28%) is similar compared to usage from prior reporting period. Almost 11% (316 hours) of the commercial hours were for foreign agencies from Canada, Japan, South Korea, France, and Singapore.

SEELine users list. Much of the testing conducted at the facility continues to be for defense systems by both government and commercial agencies. Almost 11% (316 hours) of the commercial hours were for foreign agencies from Canada, Japan, South Korea, France, and Singapore. It is expected that the facility will continue to be as active in future years.

Recent progress on the ECR4 ion source

D.P. May, S. Molitor, F.P. Abegglen, H.Peeler, H.I. Park, and R. Olsen

The construction of the new 6.4 GHz ECR4 ion source is nearing completion and will soon be installed and commissioned. Most significantly, the NdFeB permanent magnet bars that comprise the hexapole have been fitted into the ECR4 plasma chamber and the completed plasma chamber inserted into the yoke-and-coil structure. The power supplies, transmitters, stands and injection-line elements have all been installed.

The most crucial operation was the insertion of the permanent magnets in the hexapole structure. The insertion fixture is shown in Fig. 1. The plasma chamber was placed in the center, and the six radial arms controlled the movement of permanent magnet bars into their respective slots. A calculation had been performed with PANDIRA to determine the force radially inward on each bar in the hexapole configuration. This had been determined to be approximately 300 lbs. on each 22.4 in. long bar when all six bars are in their final positions. This force builds up rapidly to this maximum as the bars move radially inward, but if the bars are perfectly symmetric the azimuthal forces on any bar are balanced to zero. Each bar was constrained by its radially outward attraction to a 3.75 in. thick bar of soft steel. The magnetic force between each bar and its steel holder was determined by PANDIRA to be approximately 1140 lbs. giving a safety margin of almost a factor of four.

Fig. 1. Fixture used for inserting magnet bars into ECR4 plasma chamber.

To place each magnet on each steel bar first one permanent magnet bar was brought in by hand and, placed in its slot in the plasma chamber, and secured by brass rods in the slot. The control arm was then attached to the fixture and the steel holder brought radially up to the magnet until three long stainless screws threaded through the holder encountered an aluminum bar taped to the magnets outer face. With this arrangement, the screws could control the approach of the holder to the magnet. When the holder was flush with the magnet then they both were brought out to maximum radius. Next a magnet bar 120° in position from this bar was attached to its holder and brought out to full radius in this manner. The next magnet was attached 120° from this position, and then with their side forces balanced the remaining three magnets were attached After all six magnet bars were attached in turn to their holders and brought out to full radius, they were moved in slowly and symmetrically into their slots in the plasma chamber. This process required six lab personnel as each arm was cranked in by hand. At this point the steel holders were pushed outward with the long screws to the point where their attraction to the magnet bars no longer is capable of pulling them from their slots.

Now with all the magnets safely installed, the plasma chamber was withdrawn from the fixture, wrapped in a stainless-steel shell and covered with an insulating plastic film. Fig. 2 shows the insertion of the plasma chamber into the steel-yoke and axial coil structure along an aluminum guide pole, and Fig. 3 shows the chamber in its final position.

Fig. 2. Plasma-chamber/hexapole being inserted into yoke and coil structure.

At this point the magnetic field of the hexapole at the chamber wall was measured along each pole with a hand-held Hall probe. The field strength averaged a very uniform 4.94 kilogauss with 4.98 kilogauss for the strongest bar and 4.90 kilogauss for the weakest. The weakest point measured 4.73 kilogauss. This can be compared to the 4.76 kilogauss average pole strength measured for ECR1 with the weakest point descending to 4.39 kilogauss. These weak points on ECR1 have led to a gradual degradation of the performance of the ECR1 ion source even as the one bar with the weakest point was replaced. It should also be noted that the ECR4 hexapole does not exhibit the sudden dips in field strength at the joints between the blocks forming the bars as does the ECR1 hexapole. With a more uniform field profile and more cooling capacity, the ECR4 hexapole should prove to be much more robust.

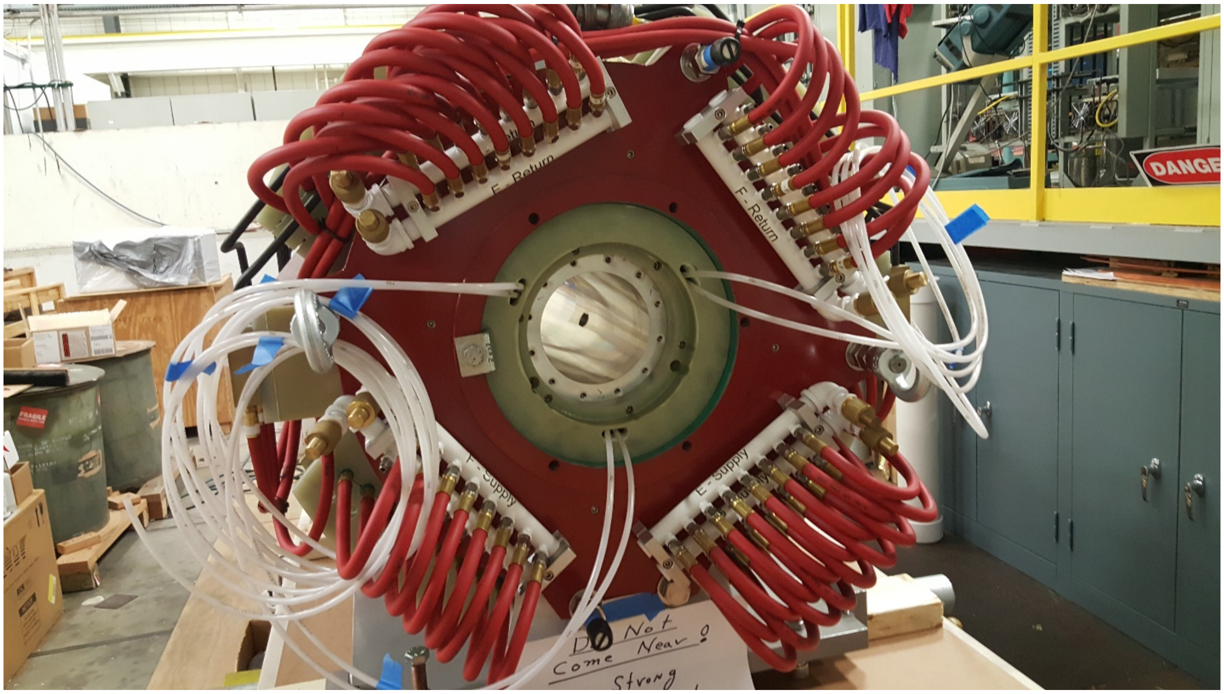

Fig. 3. Plasma chamber in its position inside the coils and steel yoke.

Progress on the light ion guide project

G. Tabacaru, J. Ärje, D.P. May, A. Saastamoinen, F.P. Abegglen, L.N. Gathings , G.J. Kim,
S. Molitor, and B.T. Roeder

The Light Ion Guide project [1] continues to be developed with the main focus on reliability, reproducibility and the finding of a set of functioning parameters for each ion studied, stable or radioactive. The Light Ion Guide was also retrofitted to serve and provide radioactive ions to the TAMUTRAP facility [2].

A search for the best conditions for the Light Ion Guide was made using a stable element heated ion source, as explained in the previous reports (see [1] and the references therein). We have very good results using a short section of the sextupole ion guide (SPIG) directly injecting ions into the plasma chamber of the Charge Breeding ECR (CBECR). Extending the SPIG to the full length (5 sections of approximately 2.4 meter) was the next test and this was also successfully proved to be a very good solution. One of the issues related to the long SPIG is the difficulty of mounting, connecting and aligning the five sections. The actual design of the vacuum chambers makes it difficult to service the SPIG sections, and a new design has been envisioned. The new design presented in figure 1 consists in two aluminum boxes with ample room inside to accommodate four SPIG sections. A platform will support the sections making it possible to align properly all the SPIG sections on a different table and then to place them into the boxes. After this baffles that manage the helium flow can be installed. This design will allow us to remove the SPIG and clean it when its performance degrades due to carbon deposition from the pumping system and from the CBECR extracted current.

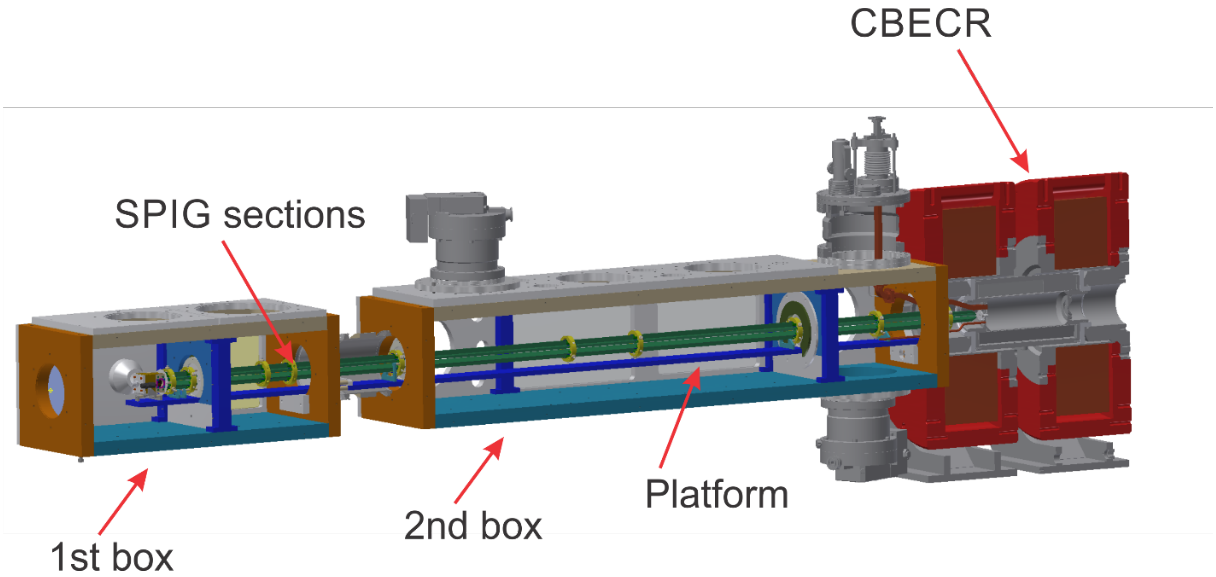

Fig. 1. CAD drawing of the new LIG design.

The new boxes were built by an outside vacuum parts supplier, and panels, covers and SPIG sections are going to be built in house.

In parallel with the new design work, we tested separately how sensitive the SPIG transport efficiency is dependent on the RF frequency. A new type of RF phase splitter was developed that allows the SPIG rods and the flat bars to be driven with a load of 50-ohm. Usually an RF amplifier needs a 50-ohm load, but the SPIG is mostly a capacitive load, and it is an open circuit. The new RF circuit splits the phase 180 degree and keeps a 50-ohm load such that the amplifier sees the correct load, and there is no reflected power with the ability to change the frequency to where the SPIG is resonating. With this new circuit we tested potassium and rubidium samples of the heated ion sources. We found out that there is no ion transport through the SPIG when the frequency is below 1 MHz. The transport efficiency is close to 90% between 1 MHz and 3.5 MHz for the same amplitude of the RF signal measured directly to the rods or flat bars. Multiple tests were performed showing that there is no dependence on the RF frequency and the ion species (atomic mass). Another result was that there is no difference in the transport efficiency when the SPIG was constructed out of rods or flat bars. The same result of no dependence in frequency was found when one SPIG section made out of rods was coupled to one section made out of flat bars. The main conclusions from these studies were that the SPIG transports the ions from the source with great efficiency, keeping the ions in a tight envelope.

As we mentioned in the beginning of this report, a few months of the LIG operation were dedicated to the TAMUTRAP facility. The TAMUTRAP group needed to test the ability of the LIG to produce ^{25}Si radioactive ions. ^{25}Si is a proton emitter with half-life of 220 ms and by detecting protons it is relatively easy to detect the production the ions. The reaction chosen for production was ^{3}He as beam and ^{24}Mg as target. Since the recoil ion ^{25}Si has a much higher energy than the recoil ions produced in (p,n) reactions, a new larger gas cell was designed. The Roots chamber stayed in the same position, the new gas cell was mounted, and a new SPIG was mounted in reverse direction compared with the normal LIG operation. An additional beam line equipped with electrostatic focusing elements was installed in order to transport the ^{25}Si into a more shielded location with very low background. The tests were successfully performed and now the TAMUTRAP can start developing the new phase comprising separation, beam cleaning and transport to the Penning trap.

[1] G. Tabacaru *et al.*, *Progress in Research*, Cyclotron Institute, Texas A&M University (2018-2019), p. IV-13.
[2] P.D. Shidling *et al.*, *Progress in Research*, Cyclotron Institute, Texas A&M University (2018-2019), p. IV-47.

Status of the light ion guide beam reacceleration and diagnostics

B.T. Roeder, F. Abegglen, J. Ärje, G.J. Kim, D.P. May, A. Saastamoinen, and G. Tabacaru

Following the success of re-accelerating ^{112}In from the Light Ion Guide (LIG) in November 2018 [1], this year we attempted to improve our tuning techniques for the re-accelerated beams. We also worked on reducing the stable beam background originating from intrinsic contamination in the Charge Breeding Electron Cyclotron Resonance Ion Source (CB-ECRIS), which was also studied with some detail last year [2]. Finally, we commissioned the new in-line BEam Analysis Station, or BEAST, which will allow re-accelerated beams to be identified and tuned without the use of the MARS spectrometer [3].

K500 Frequency Scaling Improvements

The main improvement in our re-accelerated beam tuning technique was the development and refinement of the K500 radiofrequency scaling (also known as "frequency jumping") to change from intense, stable pilot beams to the extremely weak, rare isotope beams (RIBs) from the LIG and CB-ECRIS. In previous years, the re-accelerated beam had to be extremely close in frequency to the pilot beam, within about 10 kHz, in order to be easily found and optimized [1]. A larger frequency change of 56 kHz was previously only achieved one time while changing from ^{16}O^{3+} to ^{85}Rb^{16+}, where ^{85}Rb^{16+} was a stable ion beam coming directly from the CB-ECRIS [4].

This year, we attempted larger frequency changes up to ±200 kHz away from the pilot beam. This will allow greater flexibility in the choice of pilot beam and perhaps allow for choosing the charge state of the RIB from the LIG with the least amount of background beam from the CB-ECRIS. For the test, the ECR1 ion source was used to make the tuning a bit easier. The pilot beam in the test run was ^{16}O^{3+} at 14 MeV/u. The K500 radiofrequency for this beam was 12.2366 MHz and the ECR1 extraction HV was 10.00 kV. For frequency changes greater than 12 kHz, or 0.1% in charge-to-mass ratio, it was found that the ECR1 extraction voltage also needed to be scaled by the same amount. Thus, for larger K500 frequency changes, two parameters needed to be changed to go from the pilot beam to the beam of interest.

With the two parameter change technique, changing the K500 frequency and ECR1 extraction HV for ^{16}O^{3+} frequency -1.2% (-147 kHz for the K500 frequency and -0.12 kV for the ECR1 voltage) allowed ^{27}Al^{5+} to be accelerated and observed at the end of the MARS spectrometer. Similarly, ^{63}Cu^{12+} and ^{84}Kr^{16+} are +1.668% higher in charge-to-mass ratio than ^{16}O^{3+}, and thus can be accelerated by changing the K500 frequency for ^{16}O^{3+} by +204 kHz and the ECRIS extraction voltage +0.17 kV).

It is important to note that other parameters, such as the cyclotron "dee" voltages and beam line magnets were not changed during this test. In the future, these parameters will need to be optimized also to maximize the intensity of the reaccelerated beams.

CB-ECRIS Coating and Liner Studies

It is hypothesized that the majority of the stable beam contamination originating from the CB-ECRIS arises from the interaction of the plasma in the ion source with its internal components, in particular, with its plasma chamber. The CB-ECRIS plasma chamber is composed of Al-7075 alloy, which contains 6% Zn, 2.5% Mg, 1.5% Cu, and other trace amounts of other metals [5]. This accounts for the contamination observed in previous tests [2]. While the ECR1 source plasma chamber is composed of somewhat cleaner Al-6061 alloy, contamination is measurable from that ion source as well.

This year, we tried two ideas to reduce or eliminate the stable beam contamination from ECR1 and the CB-ECRIS. The first idea was to leak silane gas (SiH_4) into the ion sources. Prolonged exposure of the ion source plasma chamber to SiH_4 has been shown in the past to improve the intensity for some ions. Also, through interaction with oxygen ions in the plasma, the SiH_4 is converted to solid SiO_2, which condenses on the walls of the plasma chamber. It was hoped that the SiO_2 would coat the inside surface of the plasma chamber and prevent the plasma from interacting with the aluminum alloy and thus reduce or eliminate the stable beam contamination. To test this possibility, a test was conducted with the K500 cyclotron and the MARS spectrometer to see if the rate of $^{64}Zn^{12+}$ from the CB-ECR was reduced after treatment with SiH_4. First, the rate of $^{64}Zn^{12+}$ was measured at MARS before the SiH_4 treatment. Then, the CB-ECR was treated with SiH_4 gas for about 36 hours. Initially, the CB-ECR did not function and could not support a plasma after the treatment with SiH_4. After treatment with oxygen gas for about 6 hours, the ion source became functional again and the measurement of the ^{64}Zn beam could be repeated with MARS. Unfortunately, there was no difference in the rate of $^{64}Zn^{12+}$ observed with MARS after the SiH_4 treatment; about $1.2 \cdot 10^4$ p/s according to the MARS measurements. The results of this test are summarized Fig. 1. It was also noted that the rate of ^{64}Zn measured increased with the amount of microwave power used for the CB-ECR, independent of the SiH_4.

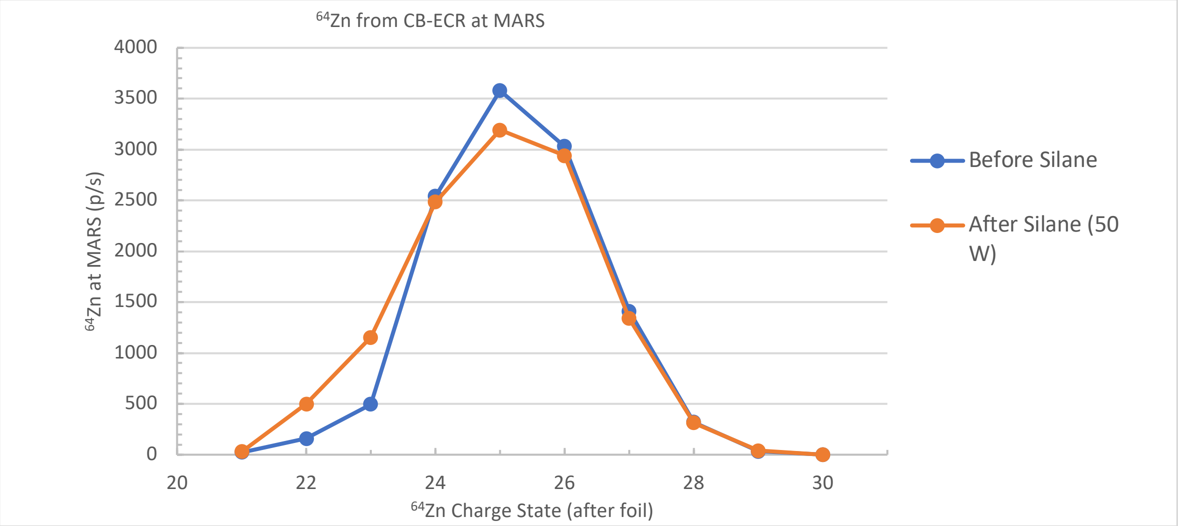

Fig. 1. Measurements of ^{64}Zn beam at 14MeV/u produced from the CB-ECR as observed at the MARS focal plane. The ^{64}Zn beam was stripped with a thin carbon foil at the entrance of MARS and the different charge states were measured individually. The sum of the charge states produced was $1.2 \cdot 10^4$ p/s both before and after the SiH_4 treatment. See text for further explanation.

Following the test, it was found that the SiO_2 coating drastically reduced the charge breeding efficiency for the Light Ion Guide beams. In order to restore the charge breeding performance, the CB-ECR needed to be completely disassembled and thoroughly cleaned.

The second idea to reduce the stable beam contamination from the ECR sources was to insert a thin aluminum liner composed of an alloy with less trace contaminants. Ideally, a “pure” aluminum sheet would have been used for the test, but pure aluminum is difficult to machine and manipulate. Thus, an aluminum liner, end plate, and bias plate made of aluminum 1050 series alloy [5] was made. This alloy is composed of 99.5% aluminum and contains, in particular, less than 0.05% zinc. The test was conducted on the ECR1 ion source and, if successful, could then be tried on the CB-ECR. Ideally, it would have been possible to completely cover all surfaces of ECR1 with the 1050 series aluminum. However, at the time of the test, the ion source extraction plate made of 1050 series aluminum was not ready. It was also not possible to cover all the surfaces of the plasma chamber with the 1050 series aluminum. Nevertheless, about 75% of the internal surface of the ECR1 plasma chamber was covered.

A similar test with the K500 cyclotron and the MARS spectrometer was conducted for testing the liner. The ^{64}Zn^{12+} at 14 MeV/u beam intensity was measured before and after the installation of the 1050 series aluminum liner. Again, no difference in the ^{64}Zn beam intensity at MARS was observed. This presents two possibilities: either the extraction plate of the ion source, which was not made of the 1050 series aluminum, was a significant source of the ^{64}Zn beam background, or the 0.05% Zn content of the 1050 series aluminum was still enough to generate the low rate of beam observed in the test. Thus, even though this method of reducing the Zn beam background did not produce favorable results, future investigation of this method with more extensive source coverage and/or more “pure” aluminum liners may be interesting.

BEam Analysis Station (BEAST)

A new chamber housing the Beam Analysis Station, or BEAST, with beam viewers, detectors, and a faraday cup has been installed for testing in cave 3 upstream of the MDM spectrometer. The BEAST will be used to identify and optimize the beam tunes of the relatively low intensity beams from the Light Ion Guide. The Light Ion Guides ideally will be tuned with the BEAST only and will not require use of the MARS spectrometer.

The BEAST contains the following components. First, a low-noise faraday cup on an actuator is

Fig. 2. The BEam Analysis Station (BEAST), and associated equipment, as installed in cave 3. See text for further explanation.

[1] B.T. Roeder *et al.*, *Progress in Research*, Cyclotron Institute, Texas A&M University (2018-2019), p. IV-17, http://cyclotron.tamu.edu/progress-reports/2018-2019/SECTION IV.html.

[2] B.T. Roeder *et al.*, *Progress in Research*, Cyclotron Institute, Texas A&M University (2018-2019), p. IV-23, http://cyclotron.tamu.edu/progress-reports/2018-2019/SECTION IV.html.

[3] R.E. Tribble, R.H. Burch, and C.A. Gagliardi, Nucl. Instrum. Methods Phys. Res. **A285**, 441 (1989).

[4] B.T. Roeder *et al.*, *Progress in Research*, Cyclotron Institute, Texas A&M University (2015-2016), p. IV-16, http://cyclotron.tamu.edu/progress-reports/2015-2016/SECTION IV.html.

[5] https://en.wikipedia.org/wiki/Aluminium_alloy

[6] https://www.tek.com/keithley-low-level-sensitive-and-specialty-instruments/keithley-high-resistance-low-current-electrom

Computing at the Cyclotron Institute

R. Burch, J. Gauthier, Y.-W. Lui, and K. Hagel

We have continued to expand the computational cluster with the addition of three new DELL R610 computers, each of them having 64 GB of RAM memory, 2 CPU with 6 cores/2 threads each, adding 72 available computing job slots to the cluster. These new servers are available to all lab personnel. CentOS 8 is the operating system and ROOT 6 is installed and available to all users upon login. These machines currently serve as test machines to enable Cyclotron users to transition to root 6 and the new compilers before the full CentOS-8 deployment on our systems scheduled for the coming months.

As mentioned above, the ROOT 6 implementation will coincide this year with the upgrade to CentOS 8 operating system on all the Cyclotron Linux computers. We have been working on this upgrade preparation since the new OS release in September 2019. CentOS 8 had to be configured and tested to be fully compatible with our identification (ldap) and authentication (Kerberos) systems as well as our centralized home directory configuration (autofs). All of those are now managed by the sssd central service.

During summer 2019, the old Cyclotron web server was replaced by a new computer (Protectli Vault Intel quad core Mini PC). This new server is running on CentOS 7 and is hosted at the West Campus Data Center. We have also implemented our web pages on a machine running CentOS-8 to be used as a backup in case the active web server fails.

There has been significant development of the data acquisition systems. Coincident with the computational server upgrade to CentOS-8, we have also upgraded the data acquisition front end as well as back end systems to CentOS-8. The upgrade of front-end computers which utilize the Struck 3104 controller connected via the PCI-e interface presented a challenge to identify the correct hardware driver for that board. Once the driver was identified, we also learned that the driver is very sensitive to the kernel version in that the driver, which had a clean build and worked for CentOS-8.0 did not even compile on CentOS-8.1.

We made the strategic decision to employ the latest version of ROOT 5 on the data acquisition front-end machines. The reasons for this include allowing more time to test the data acquisition software, but also importantly to be able to read the files acquired during an experiment with root 5 since there continues to be a fair number of users who utilize ROOT 5.

One of the backend servers was replaced, and the new one was installed with CentOS-8. The other backend server continues to run Scientific Linux 6 (SL6) in order to be sure that all software has been successfully ported to CentOS-8 before eliminating the possibility of using SL6 for experiment in case the port to CentOS-8 is not fully achieved.

In addition to upgrading the acquisition operating systems there has been significant development in the slow control of various devices. A control GUI was developed for the SIS 3316 Flash ADCs and is more or less complete although tweaks at a low level continue. In addition, a GUI for the MASE system borrowed from Indiana University Cyclotron Facility (IUCF) for NIMROD experiments was developed. Both of these control GUIs have increased the stability of the system and made its behavior more uniform across experiments. This is because the GUI now controls the devices as opposed to the users writing the setup functions which were easily changed in very non-transparent ways. The GUIs also keep a log of which parameters changed and when.

There was significant activity for Windows Desktop computers. Windows 7 reached End of Life (EOL) on 14-Jan-2020. It was therefore necessary to upgrade all desktop computers to Windows 10. Many users at the Cyclotron Institute had continued to employ Windows 7 and that made the upgrade a significant effort. Coincident with that effort, it was announced early in the year that the University had dropped the contract with Symantec for the campus wide virus protection and replaced it with CrowdStrike. This required again accessing all machines in order to remove Symantec and replace it with CrowdStrike. This effort is in progress.

Larger beam profile for K150 radiation effects facility testing

B.C. Hyman, H.L. Clark, G.J. Kim, and B.T. Roeder

A 4.5" diameter beam profile has been developed for proton testing with the K150 Radiation Effects Facility beam line. This new beam profile will allow for larger devices to be placed under test as well as a greater number of devices to be tested simultaneously. Most existing elements of the beam line have been remade to facilitate the beam profile enlargement.

All elements (shutters, viewers, etc.) of the beam line are housed in three ISO250 six-way crosses (Fig. 1). Pneumatic thrusters are used to move elements into and out of the beam path. Existing thrusters, all with 4" of travel, were replaced by thrusters with 5" or 7" of travel, as needed, to allow for elements to completely move out of the larger beam path.

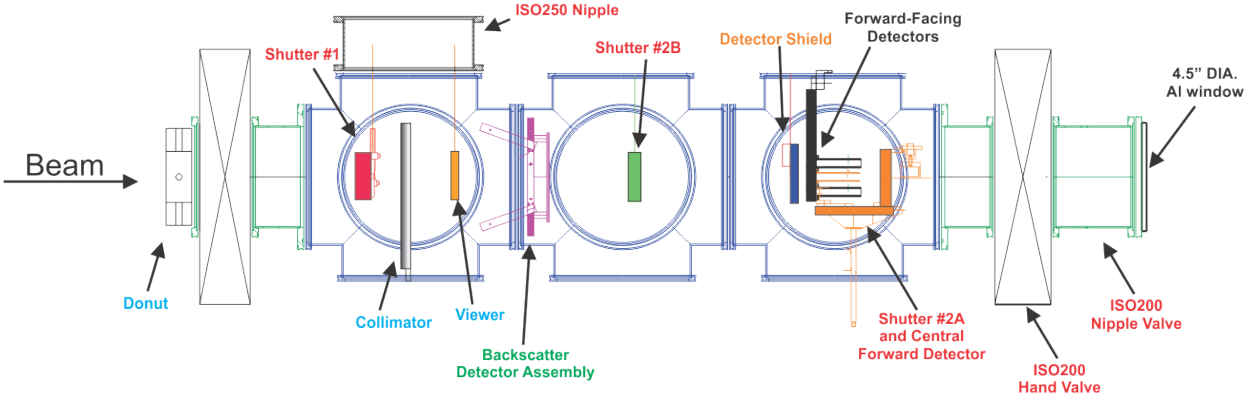

Fig. 1. K150 SEE Beam Line Components.

A ISO250 nipple was added to the top of first six-way cross to provide more space for shutter one and the beam viewer to move out of the beam path (Fig. 1) as there was not enough height in the six-way cross for complete removal. Shutter #1 (Fig. 1), a standard sized faraday cup, was replaced with a larger (6.5"x6.5") faraday cup. The existing beam viewer was mounted to a new longer support rod. In the second six-way cross shutter #2B (Fig. 1) was enlarged and mounted on a longer support rod.

During testing beam dosimetry is measured using a set of five forward-facing detectors. Four stationary detectors are mounted on a support frame and positioned on the outer edges of the beam profile. A new detector support frame was made with a larger diameter opening and with the four stationary detectors placed further out. During high intensity proton testing a movable aluminum shield is used to protect the stationary detectors from exposure. The exiting shield was replaced to accommodate the new detector holder geometry and was attached to a new longer support rod.

One removable detector is positioned on beam line center and is part of the Shutter #2A (Fig. 1) assembly. This shutter assembly also contains a tantalum plate used to block the beam from devices under test. The size of the tantalum plate was increased to completely block the new beam profile. A new longer support rod was also installed.

At the rear of the beam line, the ISO100 hand valve was replaced with an ISO200 hand valve (Fig. 1). A ISO200 Nipple (Fig. 1) was installed after the hand valve. New beam exit windows have been made by attaching aluminum foil (5 mil thick) to an aluminum support plate using double sided tape. This support plate is then mounted on to a modified ISO200 blank flange (Fig. 2). The flange and window were mounted to the backend of the ISO200 nipple.

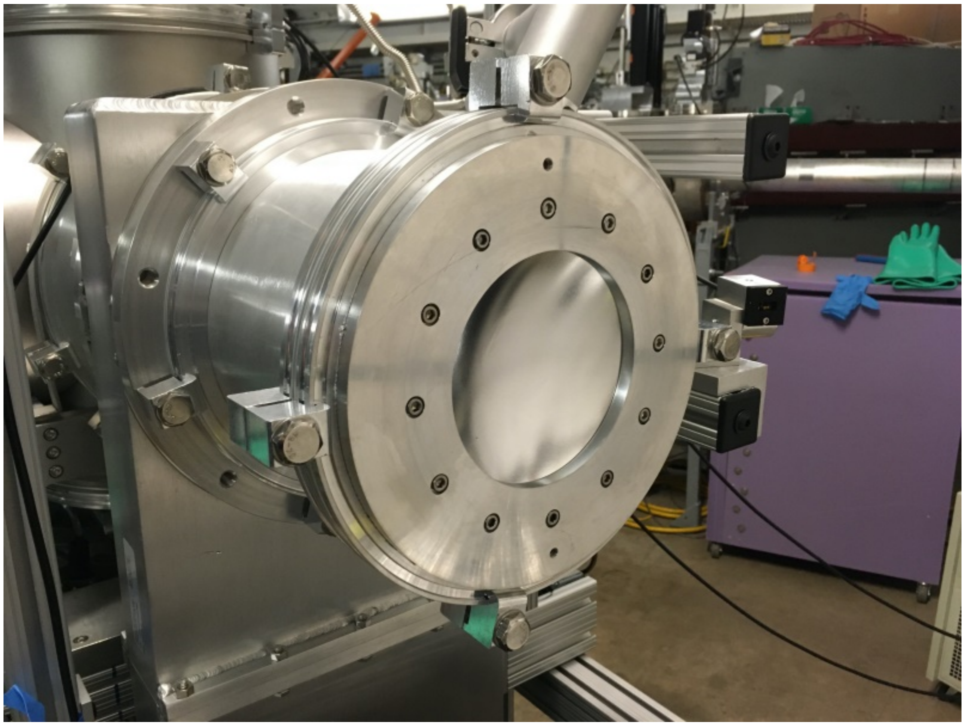

Fig. 2. Aluminum Exit Window mounted on an ISO200 nipple.

For high intensity proton testing a set four backscatter detectors are used for beam dosimetry [1]. As with the forward-facing detectors it was necessary to remake the geometry of the backscatter detector holder to accommodate the larger beam profile. Modifications were also made to the backscatter detector shielding features previously added to the beam line [2]. A new collimating "donut" was installed in front of the beam line isolation valve (Fig. 1). A flange-mounted collimator with a larger opening was placed in between shutter 1 and the viewer (Fig. 1). Individual aluminum detector shields were also remade to fit the new backscatter detector holder geometry.

Initial uniformity test with a 30 MeV proton beam using Gafchromic dosimetry film seems promising (Fig. 3), but beam uniformity is less than optimum. An aluminum beam collimator has been added to the rear ISO200 nipple to hopefully rectify this issue (Fig. 4). Additional test will be carried out in the near future to verify that the uniformity issues have been resolved.

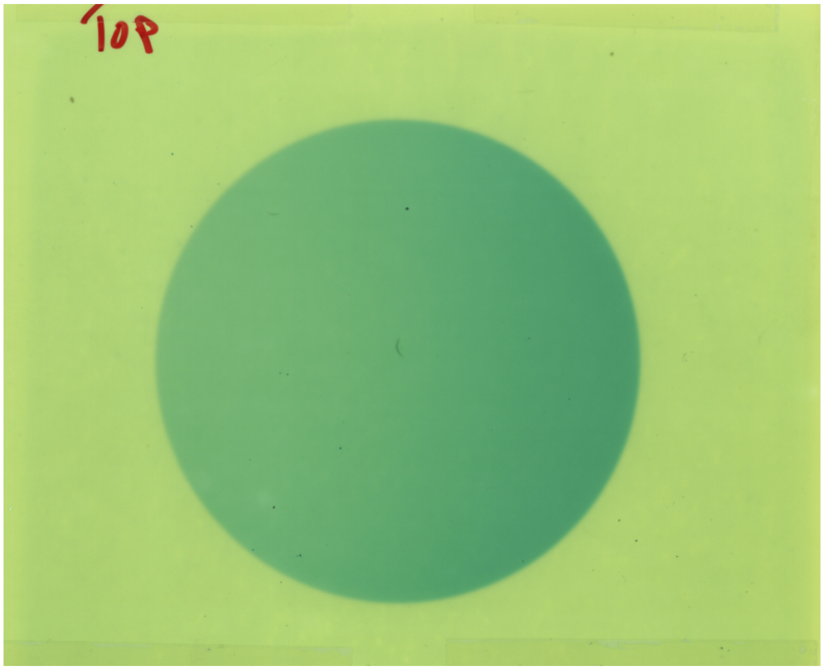

Fig. 3. Gafchromic film exposure of 4.5" diameter beam profile.

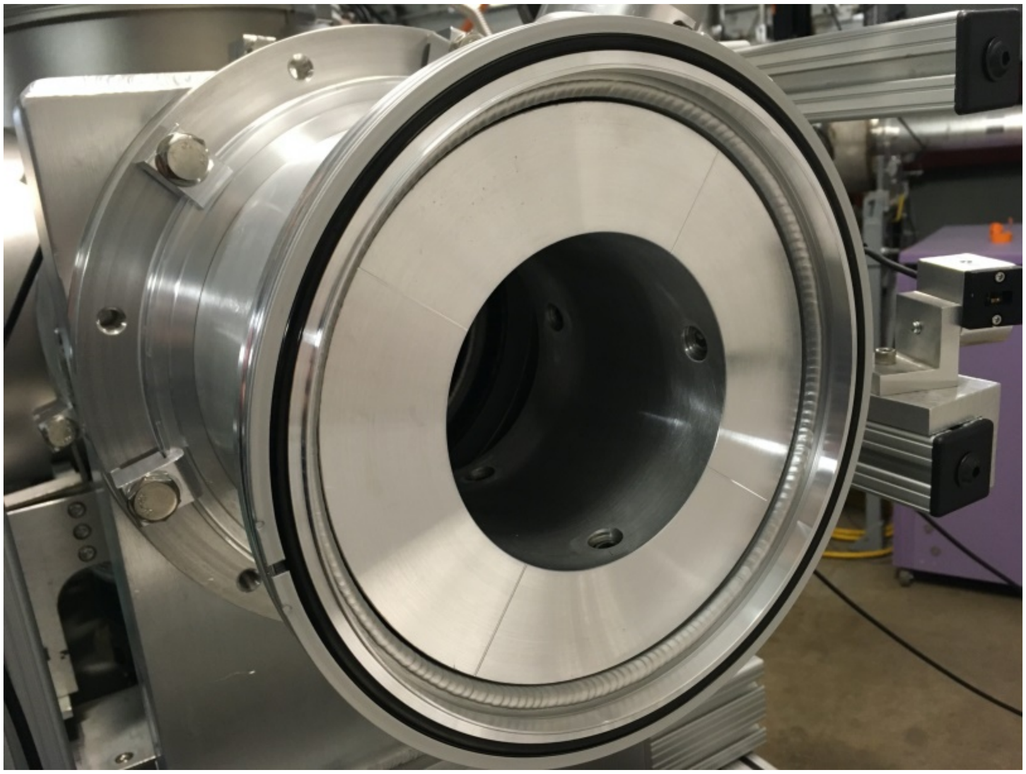

Fig. 4. Aluminum exit collimator.

The larger beam profile improvements to the K150 radiation effects beam line were made at the request of the United States Air Force/Ball Aerospace group. Additional radiation effects testing groups have also expressed interest in using the larger beam profile. These beam line improvements should provide increased testing flexibility. An increase in outside customer use of the K150 SEE Line is anticipated going forward.

[1] B.C. Hyman *et al.*, *Progress in Research*, Cyclotron Institute, Texas A&M University (2016-2017), p. IV-9.
[2] H.L Clark *et al.*, *Progress in Research*, Cyclotron Institute, Texas A&M University (2018-2019), p. IV-9.

Development of an electron cyclotron emission imaging system

L.E. Henderson, H.L. Clark, C.A. Gagliardi, and D.P. May

Development has continued for an Electron Cyclotron Emission (ECE) imaging system that will make measurements on the Cyclotron Institute's Electron Cyclotron Resonance Ion Sources (ECRIS). The ECE imaging system could give many new insights into ECRIS plasma dynamics by directly measuring the absolute energy distribution and relative number density of electrons in the plasma.

Much of the development over the past year was focused on using simulations to improve a central element of the camera, the Electronically Variable Reflective Surfaces (EVRS). These metamaterial arrays will be used as shutters and frequency-selective beamsplitters, able to bandpass ECE signals and overlay local oscillator reference signals. Compared to previous iterations, the new EVRS (Fig. 1) cell design simulations show no unwanted harmonic resonances and much lower out-of-band reflectivity.

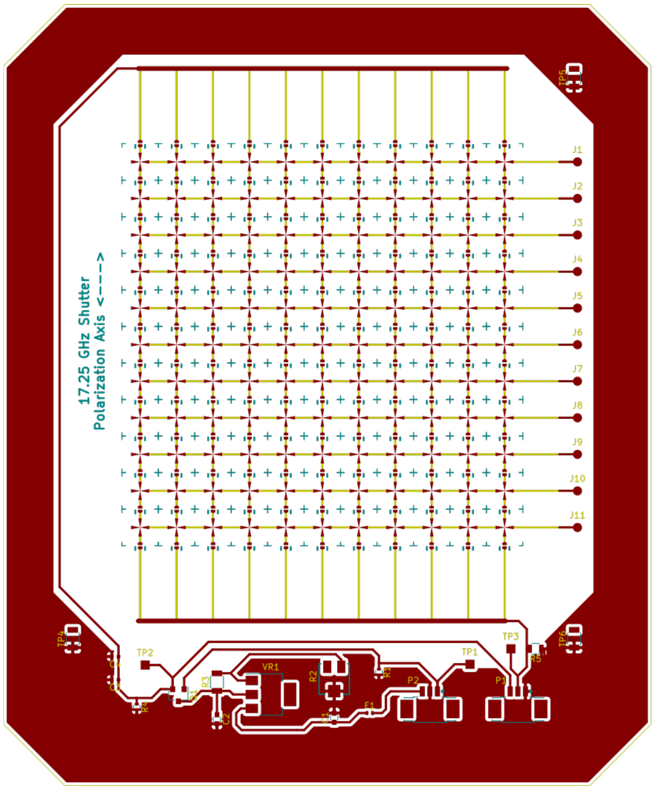

Fig. 1. EVRS board.

Once this satisfactory EVRS array cell was found, prototype printed circuit boards (PCB) were designed and fabrication was initiated. The EVRS PCB integrates the array with support electronics for cycling the power state and generating diagnostic signals. These EVRS boards will be driven, synchronized, and monitored in clusters by dedicated controller boards that are also in development.

Other critical components of the imaging system were also redesigned. The optical layout of the full ECE imaging system was changed and simplified in order to fit laboratory space constraints. The new layout (Fig. 2) routes the signal vertically out of the ECRIS and over the x-ray shield to the top of a server rack (containing the EVRS filters, detector array, and data capture computers). The vertical orientation of the vacuum optics in this new layout required a reconsideration of their mounting hardware and installation procedure, and the new mounting system is a substantial improvement. Besides mechanical simplicity, its lack of metal fixtures prevents a resonant heating mode in the primary lens assembly.

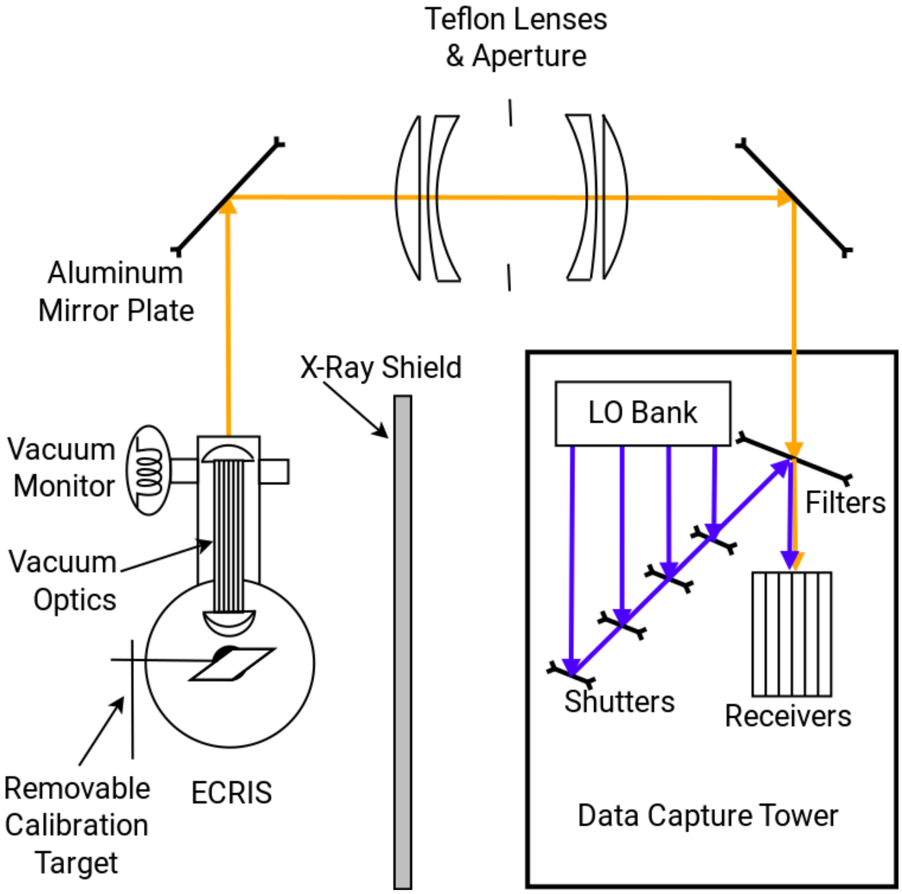

Fig. 2. New Optical Layout.

The ECE detector channel architecture has been made more practical. Each detector pixel will now be made independent by using more frequency step-down stages and readily available 250 MS/s Analog-to-Digital Converters (ADC). The detector channels will be driven by central controllers: Power supplies and timing signals will be supplied via daisy-chains, and the local oscillator signals will be supplied by a switched fanout board. Due to sheer data volume, samples acquired by each ADC will be routed to the data capture computer over a dedicated USB 3 connection.

Based on prototyping experience, it was determined that the non-vacuum optics should be mounted with 3D-printed plastic hardware. This simplifies manufacturing for many parts, but more importantly the use of plastic parts will greatly reduce ECE signal interference due to paraxial reflections.

The immediate future plan for this project is to fabricate and test components as rapidly as possible. Each component for the ECE imaging system, including each lens and EVRS, needs to be characterized across the full design band at various angles of incidence before final assembly integration. A turntable test stand is being built for this purpose. Interactions between components that are difficult to simulate accurately, such as the interaction between stacked EVRS, will be checked experimentally on the turntable as well.

Improvements in the radiation-testing hardware and software

V. Horvat, B. Hyman, M. Kennas, and H.L. Clark

In 2020 our software package (SEUSS), used for control of the hardware and characterization of the beams at the Radiation Effects (SEE-line) Facility, has undergone a major upgrade from its 2019 version. The main goal of the upgrade was to match SEUSS results for ion energy loss and range with those obtained using the latest version of the Stopping and Range of Ions in Matter (SRIM) code [1], while keeping an option to do the calculations using the pre-upgrade method. Keeping this legacy option is important to our customers for proper comparison between their new results and those they obtained previously.

We have been using the same method of energy-loss calculation consistently since 1996. That method was based on ion-energy dependence given by a semi-empirical formula and a table of the associated parameters specific for each ion species and each medium. They were made publicly available along with the 1995 version of SRIM. Meanwhile, SRIM methods of calculation evolved, but the updated formulas and the associated parameters were no longer made available. Therefore, to keep up, the new version of SEUSS has to rely on the energy-loss tables produced by the latest version of SRIM and on implementation of suitable methods of interpolation. The new method of calculation is conceptually very different from the old one and requires considerably more time to produce the results, so that most of the code had to be re-written and optimized for speed.

As an added benefit, the new method of calculation is much more flexible, and in the future, if needed, it can easily be updated just by preparing newer energy-loss tables, without having to update the software itself. The downside is that the new tables will have to be made for all SEE-line beams and for all substances these beams are expected to go though. While the number of beams that we offer for radiation testing is relatively small, the number of different substances in use could be extensive. However, a search through the archived "layer" files, which contain information on the substances our customers had used in the past, identified the substances that were used most frequently. These involve aluminum, aramica, air and silicon, as well as GaAs, GaN, SiC, SiGe, InP, and NaI. All of them are currently supported by the updated version of the SEUSS software, while other substances can be added to this list if needed. Alternatively, the calculations for the unsupported substances can be done using the legacy method.

All graphs of energy loss vs. depth and the associated tables posted on our web site [2] and around the building have been updated to reflect the new SEUSS calculations. Other software improvements are minor and include the following:

(*a*) The energy loss vs. depth tables produced by SEUSS are now more refined and more precise. The first row of the table reflects the current setting and the table caption contains the Bragg-peak information.

(*b*) All reports that include accumulated fluence now also include the accumulated dose in rad. (*c*) Our customers now can choose the default run number increment.

Additionally, progress has been made regarding the migration toward a complete hardware and software solution supported by the Windows 10 operating system. To reach this goal, a new hardware has to be acquired and set to be controlled by the software in order to perform the following tasks: (*i*) generate suitable output voltages for input to nine detector power supplies, as well as provide an indicator that the beam path is clear all the way to the target; (*ii*) count the signals originating from at least ten detectors; and (*iii*) physically move the target and the beam-energy degraders. The hardware for items (*i*) and (*ii*) already has been obtained from National Instruments [3], while the hardware for item (*iii*) is expected to become available soon.

The software solution is expected to be compatible with our SEUSS software package, which means that the hardware should have drivers that are compatible with the Microsoft Visual Studio C++ compiler and linker. For items (*i*) and (*ii*) such drivers have been adopted from the provided examples in ANSI C and made to work in the Visual Studio C++ environment. A trial window-based application, illustrated in Fig. 1, was developed to test one channel of the hardware that generates voltage output. Further development of the application and completing the set of hardware connections to include all available channels is in progress and no major problems are expected on the way to full functionality.

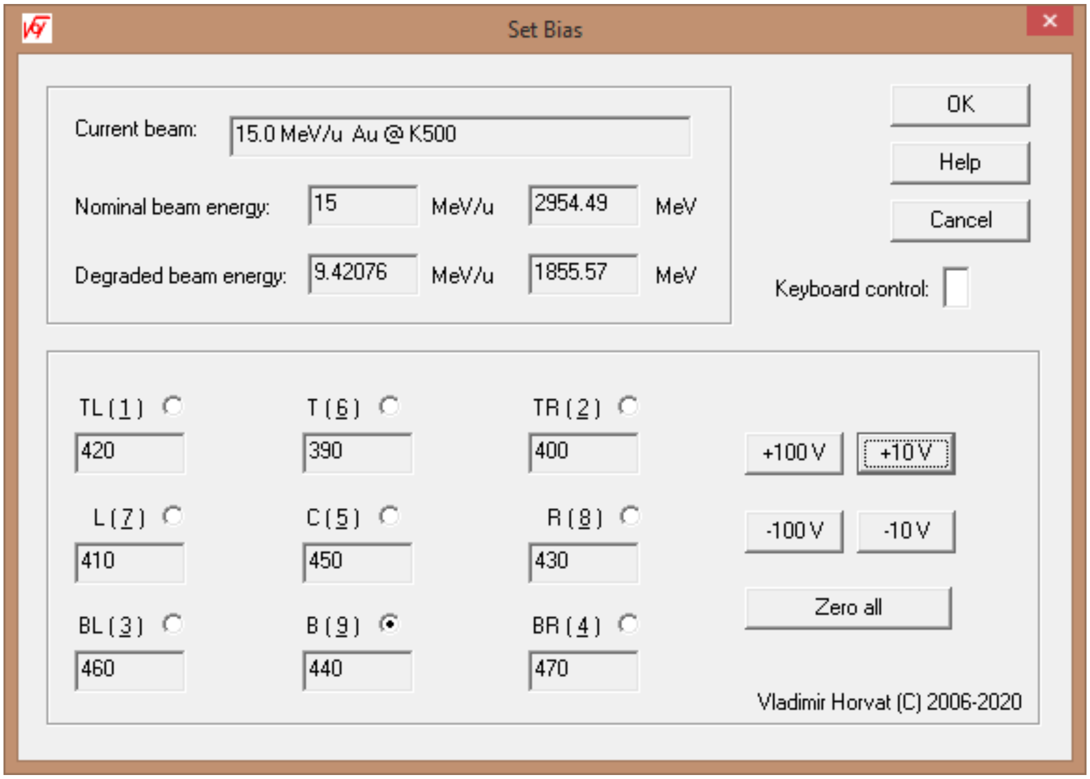
Set Bias

Current beam: 15.0 MeV/u Au @ K500

Nominal beam energy: 15 MeV/u 2954.49 MeV

Degraded beam energy: 9.42076 MeV/u 1855.57 MeV

Keyboard control: ☐

TL(1) ○ 420

T(6) ○ 390

TR(2) ○ 400

L(7) ○ 410

C(5) ○ 450

R(8) ○ 430

BL(3) ○ 460

B(9) ● 440

BR(4) ○ 470

Vladimir Horvat (C) 2006-2020

Fig. 1. New window for the control of nine detector power supplies. The default bias setting is determined programmatically based on the characteristics of the ion beam in use and the past performance of the detectors. Adjustments can be made on demand.

[1] http://www.srim.org/ .

[2] http://cyclotron.tamu.edu/vladimir/SeussW-Download.htm .

[3] http://www.ni.com .

K500 and K150 remote heat gun control system
April 1, 2019 – March 31, 2020

M. Kennas and B. Hyman

A control system was requested to allow customers in the K150 and K500 SEELine areas to remotely operate Leister MISTRAL-6 SYSTEM heat guns for the purpose of in-air heating of a component undergoing radiation testing. Previously the heat guns were restricted to local control only, meaning adjustments to the output of the heat guns would have to be made from inside the cave/vault.

General purpose remote operation controllers (Leister Model CSS) were ordered from Leister, the manufacturer of the heat gun. These controllers are designed for products throughout the Leister catalog, and therefore are not intended specifically for use with the MISTRAL-6 SYSTEM. As such, the units were adapted and reprogrammed in order to adequately control the heat gun. A single controller unit can control either the temperature output or the fan speed of the heat gun, but not both simultaneously. Therefore, two units are necessary for an individual heat gun. The controller units have 16 input/output ports on their rear face. Connections made between these ports can be considered as exposed circuitry, as such an enclosure is required. The enclosure manufacturing services of Protocase were selected for fabrication of two custom-designed enclosures for the control units (one enclosure box per SEE area). Pictured in Fig. 1 is the front face of the fully assembled enclosure. Communication between the controllers and the heat gun is made through a single RJ45 cable patched from the data room to the cave/vault.

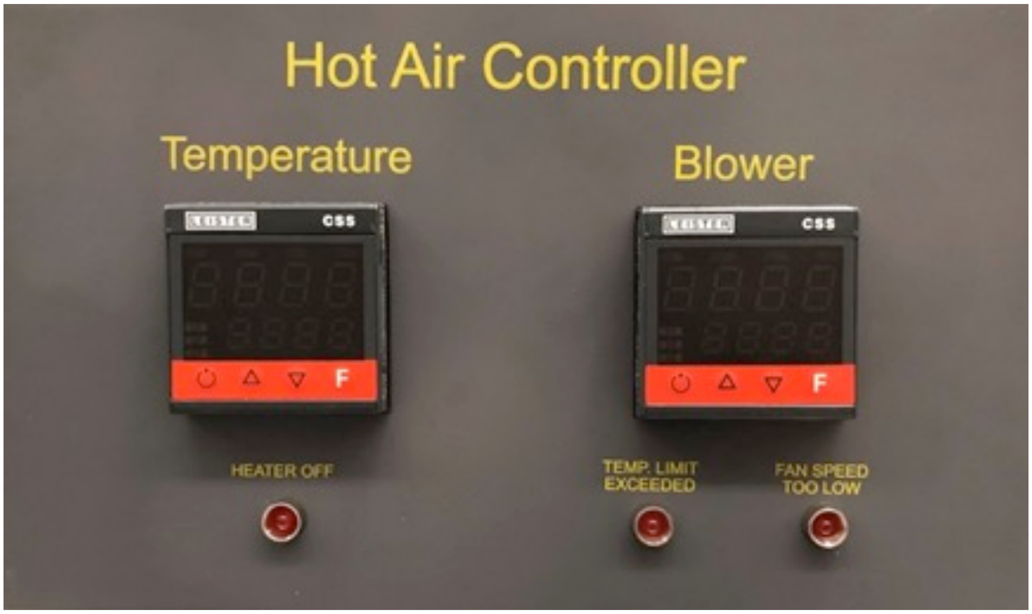

Fig. 1. Front face of a control box. Status LEDs are provided to indicate various fault states of the heat gun operation.

As the CSS controllers are PID (proportional, integral, derivative) units, they can monitor an external component's temperature via thermocouple signal and adjust heating power and fan speed of the heat gun in real time to maintain a set temperature of the component being heated. Thermocouple patches from the cave/vault to data rooms were installed in the K500 SEE area (2x K-type, 1x T-type, 1x J-type). For the K150 SEE area, a thermocouple signal transmitter was installed to the K150 area heat gun. This transmitter takes a local thermocouple signal (K, T, J, E, R, S, B, N, or C-type) and sends a proportional output current signal to the controllers. This signal connection to the controllers has been incorporated to the already present RJ45 connection between the controllers and heat gun. The power supply for the thermocouple signal transmitter is also incorporated into the RJ45 wire, as the CSS controllers have a built-in 24V DC power supply that can power the transmitter.

Temperature testing to verify accurate thermocouple reading between the systems was performed. A test part was heated to four temperatures and comparisons were made between the readouts of a dedicated thermocouple reader (DTR), IR thermometer (IRT), the K500 box, and the K150 box. The results of the testing are shown in Table I. It should be noted that the temperature set point (SP) was set using the K150 box, which was actively controlling the heat gun that was heating the test part. As a result, the K150 box value should closely match the SP. The IR thermometer readings were taken by pointing an IR thermometer at a piece of painter's tape stuck in the same location that the thermocouples of the K150 box and the K500 box were attached. The results indicate adequate uniformity of the temperatures reported, showing that both boxes can read temperatures similarly despite their different means of signal transmittance. Additionally, the results show that the set points of the boxes are accurate (within 5%) to the real temperature of the test part ('real temperature' according to the dedicated thermocouple reader).

Table I. Temperature testing of the K150 and K500 boxes. All values in °C.

SP	K150 BOX	K500 BOX	IRT	DTR
65	65	64	63	65
80	81	78	78	80
95	95	92	92	94
110	111	107	105	107

Once basic functionality programming was completed, safety systems were then programmed into the control system. In order to protect the part being heated from overheating, an upper temperature limit can be set by the customer. When the thermocouple reports this temperature has been reached, the heating element of the heat gun is automatically disabled until the temperature falls below this upper limit. This system is unavailable in manual heat gun control, as manual control does not take any input signal from a thermocouple. The heating element requires constant blowing to protect itself from overheating and is protected by locking the user out of lowering the fan speed excessively. If the user attempts to lower the blower too far, the heating element is automatically disabled until the fan speed is raised above the minimum threshold. This system can be bypassed if necessary, should the customer request low temperature and low blower speed. In the event that the signal between the controllers and heat gun is disrupted, the heating element automatically disables until the signal is reestablished. If the thermocouple disconnects from the part being monitored, or if the thermocouple 'burns out,' there is either a fault signal (K500 box) or excessive temperature (K150 box) read by the controllers, and the heating element is automatically shut off. The controller enclosure is fused and is grounded when plugged into 120VAC wall power.

Work is complete and the controller systems are currently active in the K500 and K150 areas for customer use.

Diamond detector telescopes for cyclotron beam identification

B.T. Roeder

This year, we have started a new development project to use diamond detectors for the identification of beams from the K500 and K150 cyclotrons. Diamond detectors have many advantages over traditional silicon detectors in that they are more radiation resilient, are low noise, and have intrinsically low leakage current. However, these detectors can only be made to cover relatively small area (typically less than 25 mm^2), and they also produce less signal than similar silicon detectors.

In the past, single crystal diamond detectors (scCVD) have mainly been used for fast timing applications such as high-resolution time-of-flight measurements [1]. Recently, with the wider availability of so-called "electronic-grade" single crystal diamond detectors, spectroscopic applications with high energy resolution have become possible. With this improved resolution, it is envisioned that two diamond detectors could be combined into a ΔE-E telescope configuration and employed to identify beams from the cyclotrons according to their energy loss. These diamond detector telescopes could then replace existing silicon telescopes currently used for beam identification at MARS [2] and elsewhere. They could also allow for beam identification at higher count rates, which is often not possible with silicon detectors without significantly damaging them

We have been developing a prototype diamond detector telescope for the Cyclotron Institute with Applied Diamond Inc. in Wilmington, Delaware, USA. The resulting detector has been received and is shown in Fig. 1. The detector is composed of a ΔE detector of 50 μm diamond and an E detector 500 μm diamond. Both detectors are scCVD, have 16 mm^2 active area, and Cr-Au pad metallization.

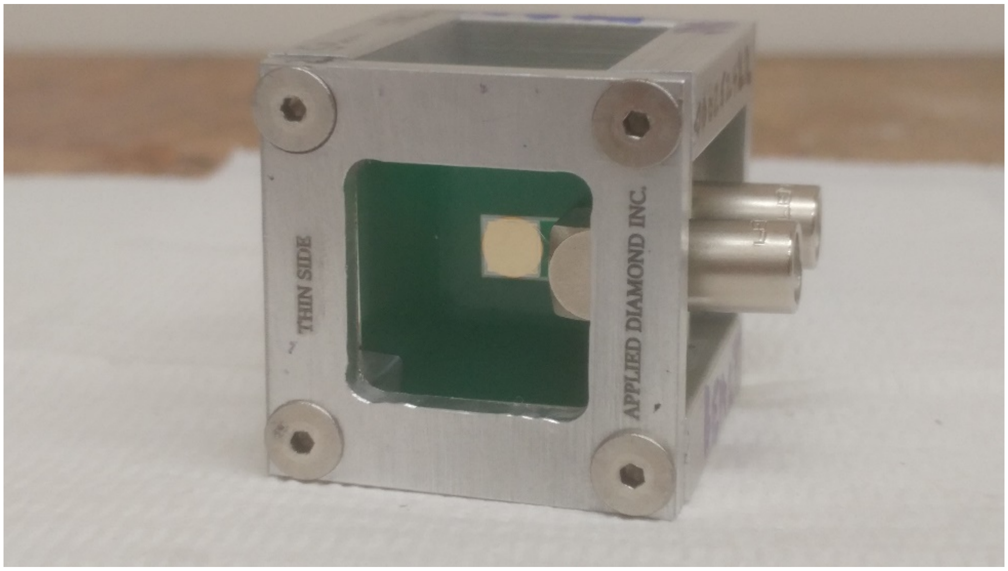

Fig. 1. The diamond telescope assembly, produced by Applied Diamond Inc. The entire assembly is about 1 in^3 in volume. See text for further explanation.

The detector was tested with a ^{228}Th alpha source to measure the resolution of the individual detectors in the telescope. To obtain the best resolution, the combination of an Ortec 142A charge-sensitive preamplifier and a CAEN DT-5780 desktop digitizer was employed. Special care was also taken to reduce electronic noise by minimizing the cable lengths, especially between the vacuum flange and the preamplifier input. A typical spectrum from the diamond detector tests with the ^{228}Th source is shown in Fig. 2. A peak resolution of better than 80 keV FWHM, or about 1.5%, was obtained.

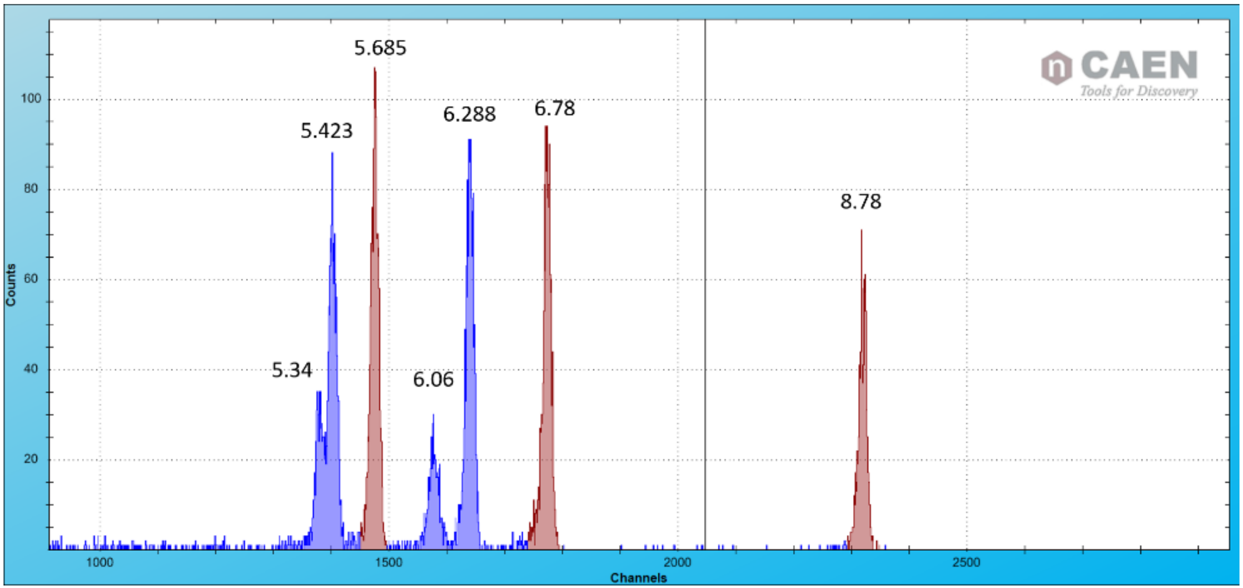

Fig. 2. ^{228}Th alpha source spectrum obtained with the 50μm thick diamond detector. The resolution obtained was about 1.5% FWHM. Peak labels shown are the alpha particle energies in MeV. See text for further explanation.

In the coming year, this diamond telescope will be tested with beams from the K150 and K500 cyclotrons. As the Ortec 142A preamps saturate for energy deposits above 200 MeV, lower gain, higher range CAEN model 1422A preamps have been purchased for measuring higher mass and higher energy beams. Once tested, the diamond telescope will have applications in verifying the beam purity for the SEE line, identifying the re-accelerated beams for the Light Ion Guide, and in tuning rare isotope beams with MARS.

[1] S. Michimasa *et al.*, Nucl. Instrum. Methods Phys. Res. **B317**, 710 (2013).
[2] R.E. Tribble, R.H. Burch, and C.A. Gagliardi, Nucl. Instrum. Methods Phys. Res. **A285**, 441 (1989).

MARS Status Report for 2019-2020: Tuning of new rare isotope beams ^{12}B, ^{11}Be, ^{10}Be, ^{13}B, ^{23}Ne, and ^{7}Be

B.T. Roeder and A. Saastamoinen

This year, we continued the program of providing rare isotope beams (RIBs) for the physics program at the Cyclotron Institute at Texas A&M University with the Momentum Achromat Recoil Separator (MARS) [1]. The MARS beam line was utilized in 20 separate experimental runs for RIB development and various experiments. The beams that had been developed in previous years that were employed in physics experiments this year are as follows. A ^{42}Ti beam, made with the ^{40}Ca+^{4}He reaction at 32 MeV/u, was provided once again to Dr. Hardy's research group for their continuing studies of super-allowed β-decay. ^{14}O was prepared for experiments with Dr. Rogachev's research group in collaboration with L. Sobotka's group from Washington University in St. Louis for experiments with the TexAT active target. Also, a degraded ^{8}B beam was prepared for the CENTAUR collaboration for Prof. Scott Marley from Louisiana State University. Finally, a ^{27}P beam was made with the p(^{28}Si,^{27}P)2n reaction with ^{28}Si beam at 40 MeV/u for a measurement of ^{27}P β-p decay with Astrobox2.

Six new RIBs were developed this year: ^{12}B, ^{11}Be, ^{10}Be, ^{13}B, ^{23}Ne and a low energy ^{7}Be beam. These new MARS tunes are described in the following paragraphs.

The ^{12}B, ^{11}Be and ^{10}Be RIBs were requested by Dr. Christian's group to measure (d,^{3}He) transfer reactions with TexAT. The (d,^{3}He) reactions in question have relatively high Q-values and thus secondary beam energies greater than 20 MeV/u were required. All three of these RIBs were produced with a ^{13}C^{4+} beam at 30 MeV/u from the K500 cyclotron bombarding a 1mm thick ^{9}Be target. Primary beam intensities up to 400 enA (electrical) were available. For the case of ^{12}B, with the MARS momentum slits at ± 1.0cm, a production rate of 5240 eV/nC was obtained. About 2.6% of the total secondary beam was from ^{10}Be and ^{7}Li contamination, both of which could be reduced by closing the focal plane slits. The ^{12}B beam energy was 20.9 MeV/u. With the full intensity of the primary beam, a rate of about 2×10^{6} p/s of ^{12}B was measured. A spectrum showing the final tune for ^{12}B is shown in figure 1. For the case of ^{11}Be, with the MARS momentum slits at ± 1.0cm, a production rate of 191.7 eV/nC was obtained. About 10% of the total secondary beam was from ^{8}Li contamination. The ^{11}Be beam energy was 22.9 MeV/u. With the full intensity of the primary beam, a rate of about 7.7×10^{4} p/s of ^{11}Be was measured. For the case of ^{10}Be, with the MARS momentum slits at ± 1.0cm, a production rate of 600 eV/nC was obtained. About 4% of the total secondary beam was from ^{11}Be contamination, which could be reduced by closing the focal plane slits. The ^{10}Be beam energy was 21.6 MeV/u. With the full intensity of the primary beam, a rate of about 2.4×10^{5} p/s of ^{10}Be was measured. The ^{12}B experiment with TexAT has already been completed and the measurements with ^{11}Be and ^{10}Be are planned for next year.

The ^{13}B beam was also requested by Dr. Christian's group for a future (d,^{3}He) transfer reaction experiment with TexAT. It was prepared in a similar way as the previous three RIBs. ^{13}B was produced with ^{15}N^{5+} beam at 30 MeV/u from the K500 cyclotron bombarding a 1mm thick ^{9}Be target. Primary beam intensities up to 420 enA (electrical) were available for the production test run. With the MARS momentum slits at ± 1.5 cm, a production rate of 100 eV/nC was obtained. About 20% of the total secondary beam was from contaminants, mostly from ^{8}Li and lower mass particles. The ^{13}B beam energy was 19.7 MeV/u. With the full intensity of the primary beam, a rate of about 4.2×10^4 p/s of ^{13}B was measured. The ^{13}B experiment is also planned for the coming year.

The ^{23}Ne beam was requested by Dr. Melconian's group for a β-decay measurement with the TAMU tape drive. This experiment will be conducted in collaboration with Prof. G. Ron from the Hebrew University of Jerusalem. ^{23}Ne was produced with ^{22}Ne^{6+} beam at 24.8 MeV/u from the K500 cyclotron bombarding the MARS gas production target, filled with deuterium gas at a pressure of 1.5 atm and cooled with liquid nitrogen. Primary beam intensities up to 100 enA (electrical) were available for the production test run. With the MARS momentum slits at ± 0.5 cm, a fantastic production rate of 6500 eV/nC was obtained. About 5.8% of the total secondary beam was from contaminants, mostly from ^{21}F. The ^{23}Ne beam energy was 20.9 MeV/u. With the full intensity of the primary beam, a rate of about 7.8×10^5 p/s of ^{23}Ne was measured. A spectrum showing the final tune for ^{23}Ne is shown in Fig. 1. The ^{23}Ne experiment is planned for the coming year, depending on the availability of the collaborators.

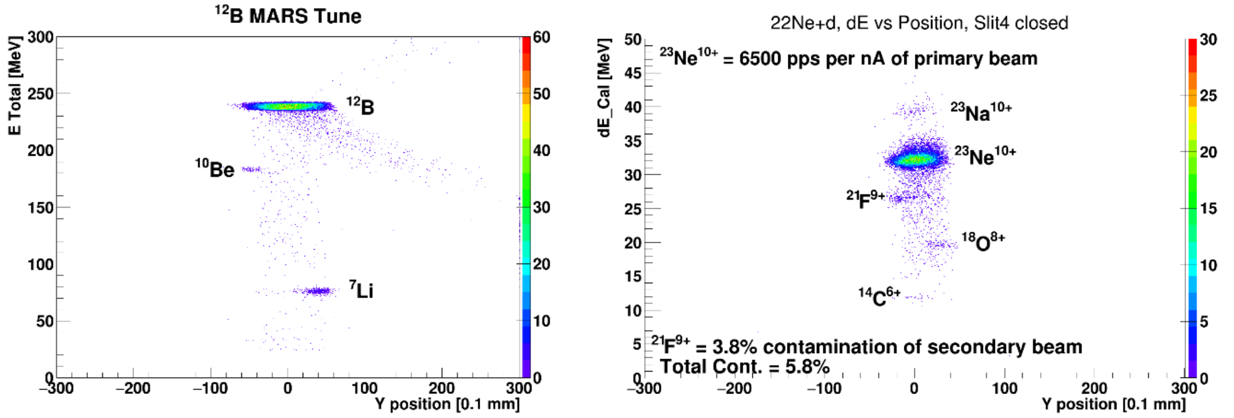

Fig. 1. Spectra showing the final MARS tunes for the new RIBs 12B (left panel) and 23Ne (right panel). See text for further explanation.

Finally, a low energy ^{7}Be beam was requested by Dr. Rogachev's group to measure reactions related to nuclear astrophysics with the new TexCAM detector. To reach the beam energies relevant to astrophysics, the ^{7}Be beam energy needed to have 10 MeV total energy or less. This low energy secondary beam was produced with ^{7}Li^{1+} beam at 3.0 MeV/u from the K150 cyclotron bombarding the MARS gas production target, which was filled with H_2 gas at a pressure of 100 torr and cooled with liquid nitrogen. With the MARS momentum slits at ± 1.0 cm, a production rate of 3661 eV/nC was obtained with no contamination. Due to the low beam energy, the focus was extremely poor and could not be improved except by closing the focal plane slits. With the focal plane slits (slit #4) closed to ± 1.0 cm, the production rate was reduced to 2350 eV/nC. The final ^{7}Be beam energy was 8 MeV total energy. The full intensity of the ^{7}Li primary beam at 3.0 MeV/u has yet to be determined and may be limited by the relatively low energy. However, an intensity of 100 enA on target should be achievable, providing about 2.4×10^5 p/s of ^{7}Be for the measurement. The ^{7}Be experiment with TexCAM is also planned for the coming year.

As part of a continuing study to produce nuclei near the proton dripline for β-decay measurements, a beam of ^{54}Fe at 36 MeV/u and ^{40}Ca at 40 MeV/u were fragmented on Be, Al and Ni targets and measured with a silicon ΔE vs. E telescope. These measurements were conducted as part of the Research Experience for Undergraduates (REU) and undergraduate students participated. The results of these experiments are summarized in a separate report [2].

A summary of the new rare isotope beams produced this year with MARS is given in Table I.

Table I. Summary of New MARS RIBs for 2019-2020.

RIB beam	**Reaction**	**Primary Beam**	**Purity**	**Intensity on Target**
^{12}B*	^{9}Be(^{13}C,^{12}B)X	^{13}C at 30 MeV/u	~97.4%	2×10^{6} p/s
^{11}Be*	^{9}Be(^{13}C,^{11}Be)X	^{13}C at 30 MeV/u	~90%	7.7×10^{4} p/s
^{10}Be	^{9}Be(^{13}C,^{10}Be)X	^{13}C at 30 MeV/u	~96%	2.4×10^{5} p/s
^{7}Be*, (1.1 MeV/u)	p(^{7}Li,^{7}Be)n	^{7}Li at 3.0 MeV/u	~100%	2.4×10^{5} p/s
^{13}B	^{9}Be(^{15}N,^{13}B)X	^{15}N at 30 MeV/u	~80%	4.2×10^{4} p/s
^{23}Ne	d(^{22}Ne,^{23}Ne)p	^{22}Ne at 24.8 MeV/u	~94%	7.8×10^{5} p/s

[1] R.E. Tribble, R.H. Burch, and C.A. Gagliardi, Nucl. Instrum. Methods Phys. Res. **A285**, 441 (1989).

[2] B.T. Roeder *et al.*, *Progress in Research*, Cyclotron Institute, Texas A&M University (2019-2020), p. IV-36, http://cyclotron.tamu.edu/progress-reports/2019-2020/SECTION IV.html.

The 2019 REU experiment: Rare isotope beam production from the ^{54}Fe+^{58}Ni and ^{40}Ca+^{58}Ni reactions with MARS

B.T. Roeder, I. Richardson,[1] M. Youngs, and Summer 2019 REU students
[1]*Old Dominion University, Norfolk, Virginia 23529*

During our Research Experience for Undergraduates (REU) program for summer 2019, a dedicated experiment for the undergraduate students was conducted using the Cyclotron Institute facilities. The experiment was designed to give the students some “hands-on” experience with the setting up and execution of a real nuclear physics experiment. The REU students received one day of introductory lectures prior to their participation in the experiment, followed by two days of experiment. During the experiment, the students aided in debugging the detector electronics, tuning rare isotope beam through the MARS spectrometer [1], and analyzing the online data as it was collected. In addition, the REU student directly associated with the project, I. Richardson, participated in the planning of the experiment by performing simulations prior to the experiment. The student also analyzed the data in detail following the experiment and reported the results in a poster at the Fall 2019 meeting of the Department of Nuclear Physics of the American Physical Society.

Leading up to the experiment, I. Richardson participated in the ^{54}Fe+^{58}Ni beam production experiment with the Momentum Acromat Recoil Separator (MARS) [1]. For that experiment, a ^{54}Fe^{18+} beam at 36 MeV/u from the K500 cyclotron impinged on a natural nickel target 50 μm thick. Analysis of this data for production rates is ongoing.

Next, I. Richardson conducted simulations for the ^{40}Ca+^{58}Ni experiment with the model of the MARS in the program LISE++ [2]. He was instructed to study the reaction ^{40}Ca+Ni for the purpose of investigating what isotopes could be produced and separated near the proton dripline in the region near mass A=40, such as ^{35}Ca. To maximize production of these isotopes, he performed simulations to optimize the predicted beam energy, intensity, target thickness, and whether or not a stripper foil following the target could improve the production. Following extensive calculations, it was determined that ^{40}Ca at 40 MeV/u on a nickel target 100 μm would give the best results based on the beam intensities available at the Cyclotron Institute. Reactions for ^{40}Ca on ^{9}Be and ^{27}Al targets were also simulated for comparison.

The ^{40}Ca+Ni and ^{40}Ca+Be experiment was conducted over two days with one day for each target. For the ^{40}Ca+Ni, a 40 MeV/u ^{40}Ca^{14+} beam from the K500 impinged on a 100 μm natural nickel foil at the entrance of MARS [1]. About 50 electrical-nA of beam intensity was available for most of the measurement. To investigate the nuclei produced near the proton dripline, MARS was tuned for magnetic rigidities consistent with the production of ^{35}Ca. This allowed a search for isotopes near the dripline for all elements Ca and lighter. The results for a data run taken for about 11 hours are shown in Fig. 1. To remove background due to scattered primary beam, the particle identification plot ΔE vs. Y-position shown was gated with a large gate in the ΔE versus E spectrum. This ensures that only particles with the proper predicted energy losses are taken into account for the identification. As shown, isotopes with neutron (N) number vs. proton number (Z) in the N=Z-5 line, such as ^{35}Ca and ^{31}Ar, were clearly populated. A production rate of about 80 counts/hour for ^{35}Ca was observed. Lighter “even-Z” isotopes with N=Z-4 such as ^{36}Ca, ^{32}Ar, ^{28}S and ^{26}P were also observed with production rates about 10 times higher than those for the N=Z-4 nuclei.

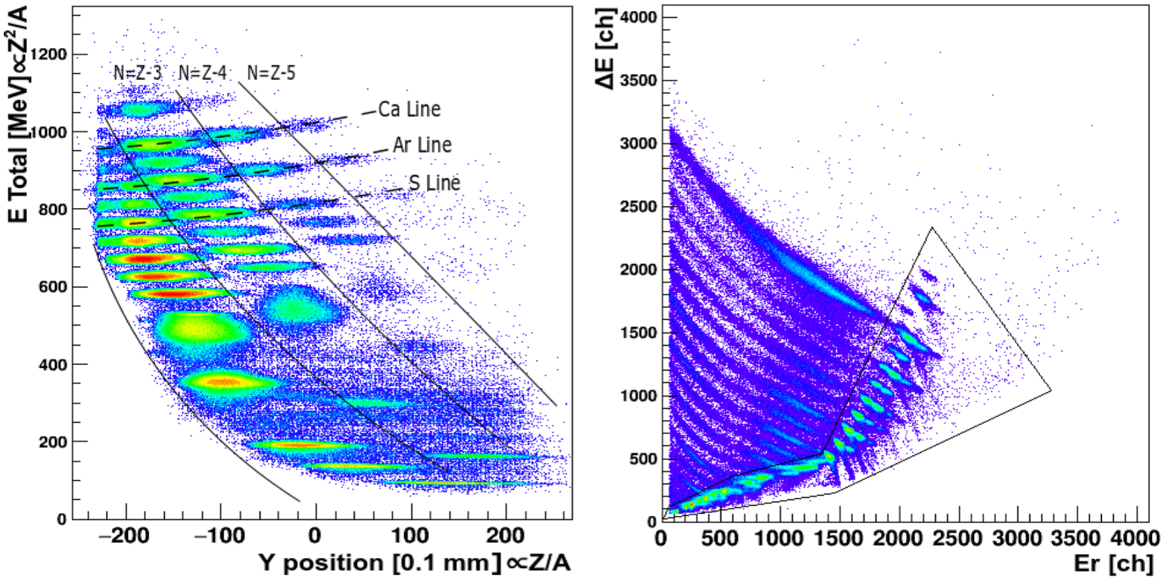

Fig. 1. Particle identification plots for the ^{40}Ca+Ni data. The data shown represent about 11 hours of beam on target. N=Z-4 and a few N=Z-5 isotopes were populated. For the Z-5 nuclei, ^{35}Ca, ^{31}Ar, and ^{27}S were produced. See text for explanation.

For the ^{40}Ca+Be target data, the same ^{40}Ca beam at 40 MeV/u from the K500 cyclotron impinged on a Be foil 456 μm thick. The reaction was measured for about 3 hours. In that case, about 10 counts/hr consistent with N=Z-5 isotopes were observed. This result was consistent with comparisons of the Ni vs. Be targets from previous beams [4].

In conclusion, N=Z-4 and N=Z-5 nuclei in the mass region of A < 40 have been produced and observed using a beam, in this case ^{40}Ca at 40 MeV/u, available at the Cyclotron Institute. However, contrary to the predictions of LISE++ [2,3], more exotic isotopes closer to the proton dripline were produced with the Ni target as opposed to the Be target, contradicting what was predicted by the model. This is part of an on-going study that has shown that using nickel as a production target produces nuclei further from stability and removes more particles from the primary beam than a beryllium target. Analysis of the data to determine the final production rates for the dripline nuclei is ongoing.

[1] R.E. Tribble, R.H. Burch, and C.A. Gagliardi, Nucl. Instrum. Methods Phys. Res. **A285**, 441 (1989).

[2] B.T. Roeder *et al.*, *Progress in Research*, Cyclotron Institute, Texas A&M University (2013-2014), p. IV-40, http://cyclotron.tamu.edu/progress-reports/2013-2014/SECTION IV.html.

[3] O.B. Tarasov and D. Bazin, Nucl. Instrum. Methods Phys. Res. **B266**, 4657 (2008).

[4] B.T. Roeder *et al.*, *Progress in Research*, Cyclotron Institute, Texas A&M University (2017-2018), p. IV-70, http://cyclotron.tamu.edu/progress-reports/2017-2018/SECTION IV.html.

Efficiency calibration of a lithium-drifted silicon detector for photon energies between 11 and 90 keV

V. Horvat and J.C. Hardy

We have used a lithium-drifted silicon detector [Si(Li)] in our measurement of the *K*-shell internal conversion coefficient α_K for the 30.8 keV *M*4 transition in ^{93}Nb, in which we recorded emission spectra of *K* x rays and γ rays. Since the decay scheme involved only a single transition that could convert in the atomic *K* shell, α_K was determined based on the expression

$$\alpha_K = \frac{N_K}{N_\gamma} \cdot \frac{\epsilon_\gamma}{\epsilon_K} \cdot \frac{1}{\omega_K} \tag{1}$$

where ω_K is the niobium *K*-shell fluorescence yield; N_K and $N\gamma$ are the total numbers of observed *K* x rays and γ rays, respectively; and $\epsilon_\gamma / \epsilon_K$ is the detector efficiency for the γ rays relative to its efficiency for the *K* x rays.

Absolute efficiency of our silicon detector was measured at the distance of 10.2 mm using a ^{109}Cd source of known reference activity. For the 22.61 keV *K* x rays of silver and the 88.03 keV γ rays of ^{108m}Ag emitted from the source, the absolute efficiencies ϵ_{23} and ϵ_{88} of the detector were found based on the measured numbers of counts in the corresponding peaks, known live time of the acquisition and deduced activity of the source at the time of the measurement. The reference data we used to deduce the expected number of *K* x rays and γ rays per ^{109}Cd decay were the same as those used in Ref.[1]. Another measurement was made with the same source at the source-to-detector distance of 0.8 mm, from which we determined the corresponding absolute efficiencies ϵ_{23}' and ϵ_{88}'

In addition, a source of ^{241}Am, was used to determine the ratio of efficiencies $\epsilon_{12} / \epsilon_{60}$ for the 11.89 keV neptunium *Ll* x rays and the ^{237}Np 59.54 keV γ rays. Unfortunately, the ^{241}Am source had a considerable thickness and so we had to correct the measured value of $\epsilon_{12} / \epsilon_{60}$ for self-absorption. To that end we kept the source center at the same position relative to the detector, but varied the source orientation angle θ between -60° and +60°. From the recorded spectra we extracted the areas of the 11.89 keV and 59.54 keV peaks. Their ratio is expected to depend on θ according to $\exp[-x\Delta\mu/\cos\theta]$, where $\Delta\mu$ is the difference between the known [2] absorption coefficients in americium at photon energies of 11.89 keV and 59.54 keV, and *x* is the source thickness. By least-squares fitting the data we determined *x* to be 263 μg/cm^2, which corresponds to a self-absorption correction factor of 1.032(2). The same source thickness was used to determine the relative self-absorption correction factors for the remaining peaks in the spectra, based on the values of the absorption coefficients at their corresponding energies [2].

In the next step, ϵ_{23}, ϵ_{88}, $\epsilon_{23}'/\epsilon_{23}$, and $\epsilon_{12} / \epsilon_{60}$ were calculated using CYLTRAN Monte Carlo electron-and-photon transport code [3]. The geometric data we input to the code specified the space occupied by all relevant materials comprising and surrounding the source and the detector. Initially, geometric modeling of the detector was based on the manufacturer's specifications. However, these led to calculated efficiencies that were much larger than those determined experimentally. This is not surprising and can be attributed principally to aging of the detector [4], which leads to a gradual reduction in the active volume of the cylindrical silicon crystal. We modeled this effect by introducing d_F, the thickness of the silicon dead layer in the front of the active volume, d_B, the dead-layer thickness behind the active volume, and r, the radius of the active volume, which was required to be less than the manufacturer-specified radius of the complete silicon crystal. Likewise, we set the length of the active volume equal to the manufacturer-specified length of the silicon crystal diminished by the sum of d_F and d_B. Values of the parameters d_F, d_B, and r were adjusted in order to produce a match between the calculated and measured values of ϵ_{23}, ϵ_{88}, $\epsilon_{23}'/\epsilon_{23}$, and $\epsilon_{12}/\epsilon_{60}$. In the process, we also elected to adjust the distance D between the front active surface of the silicon crystal and the front of the detector cap, which was not precisely specified. The remaining geometric parameters of the detector were deemed reasonable and/or not critical in efficiency calculations and therefore were accepted without modifications. A list including the accepted and the adjusted parameters is given in Table I, and the detector geometry is illustrated in Fig. 1.

Ultimately, the parameters, as listed in Table I, were used to calculate absolute efficiencies for niobium K x rays (ϵ_K) and the 30.76 keV γ ray (ϵ_γ) for the actual position and size of the ^{93m}Nb source, as well as their relative efficiency ($\epsilon_\gamma/\epsilon_K$) featured in Eq. 1. Uncertainty of $\epsilon_\gamma/\epsilon_K$ was assessed by varying d_F, d_B, D, and r individually and simultaneously, and monitoring the effect of these variations on the calculated value of $\epsilon_\gamma/\epsilon_K$. Variations of the parameters were limited by the uncertainties of the measured values of ϵ_{23}, ϵ_{88}, $\epsilon_{23}'/\epsilon_{23}$, and $\epsilon_{12}/\epsilon_{60}$.

Table I. Parameters of the Si(Li) detector geometry.

Quantity	Value
Accepted:	
Be window thickness	2.54 μm
Be window radius	6.95 mm
Au layer thickness	200 Å
Si crystal length	5.5 mm
Si crystal radius	3 mm
Al collimator inner radius	3 mm
Al collimator length	2.5 mm
Al detector cap outer radius	3.63 cm
Al detector cap thickness	0.13 mm
Adjusted:	
Si front dead layer thickness (d_F)	0.069 mm
Si back dead layer thickness (d_B)	0.534 mm
Active Si radius (r)	2.634 mm
Crystal to detector front distance (D)	8.602 mm

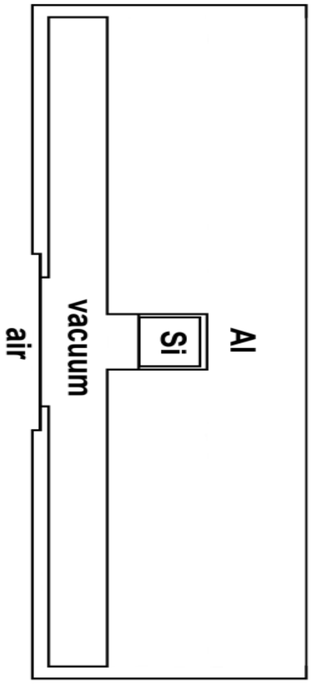

Fig. 1. Model of the Si(Li) detector structure.

In addition to the calibration peaks at 11.89 and 59.54 keV, the spectra measured with the ^{241}Am source contained additional peaks and peak structures at energies of 13.90 keV (Np $L\alpha$), 17.81 keV (Np $L\beta,\eta$), 20.82 keV (Np $L\gamma$), 26.34 keV (^{237}Np γ_{26}), 33.20 keV (^{237}Np γ_{33}), and 43.42 keV (^{237}Np γ_{43}). They were used to validate the detector's relative efficiencies as calculated with the parameters presented in Table I. The results are shown in Fig. 2. All measured efficiencies included correction for self-absorption. The emission probabilities per ^{241}Am decay were taken from Ref. [5].

The most critical geometric parameters of our Si(Li) detector were determined from measurements with well-centered sources of ^{109}Cd and ^{241}Am, which were shaped like thin discs with 3-mm diameters. Hence the source diameters were considerably smaller than the diameter of the active silicon crystal and the source-to-crystal distances used. Consequently, our source measurements were rather insensitive to the geometric parameters of the detector's supporting structure.

This might not be the case for our ^{93m}Nb source, the diameter of which was as large as 17 mm. So, even though CYLTRAN Monte Carlo code takes account of the larger source diameter, we needed to verify that our geometrical model properly accounted for the detection efficiency for source components that were up to at least 8.5 mm off axis. To test this we measured a series of spectra with our almost point-like sources placed horizontally off-axis by as much as 24 mm on either side of the central axis.

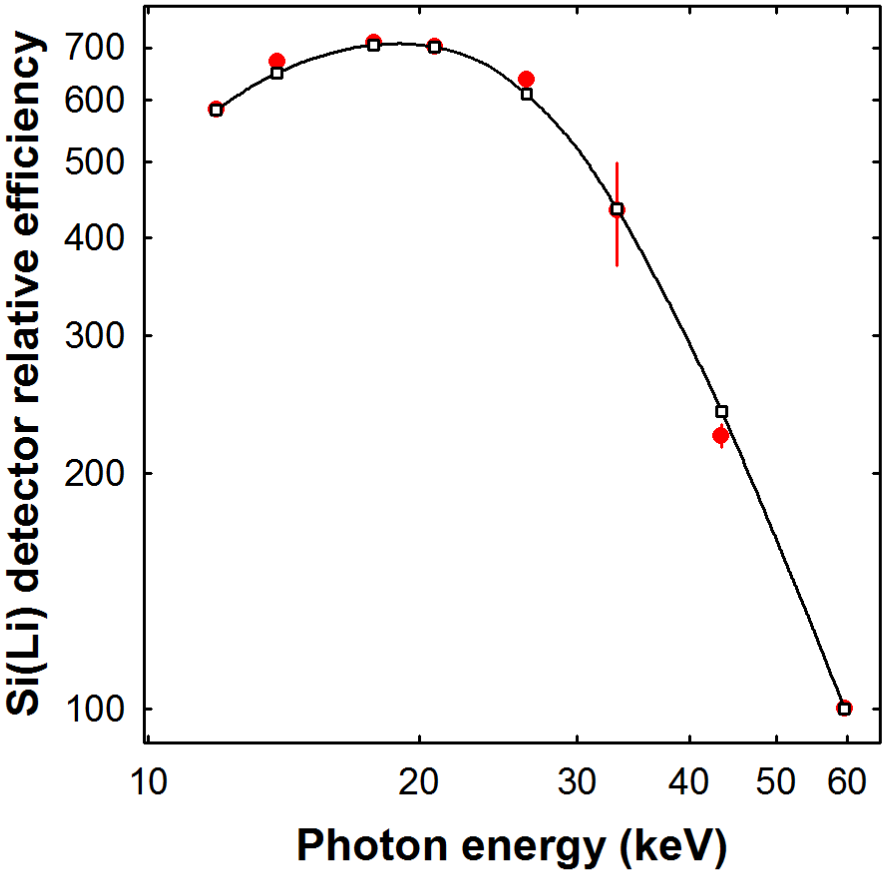

Fig. 2. Measured and calculated efficiencies for our Si(Li) detector. The red solid circles represent the relative efficiencies measured using the ^{241}Am source. The black hollow squares show scaled results of the calculations with the CYLTRAN Monte Carlo code. The black line, which connects the calculated values, is to guide the eye.

Measurements of silver *K* x rays from the ^{109}Cd source were made at a source-to-detector distance of 5.0 mm and horizontal displacements ranging from -24 to 24 mm in steps of 3 mm. The same displacement steps within the same range were also made with the ^{241}Am source but in its case the source-to-detector distance was 15.9 mm and we analyzed all major peaks in the spectrum. Both sets of results were compared to CYLTRAN calculations and found to be in satisfactory agreement, which confirms that our geometrical model is valid for Monte Carlo analysis of the 17 mm diameter ^{93m}Nb source. An example of the measured and calculated counting-rate dependence on horizontal displacement is shown in Fig. 3. for ^{237}Np γ_{26}.

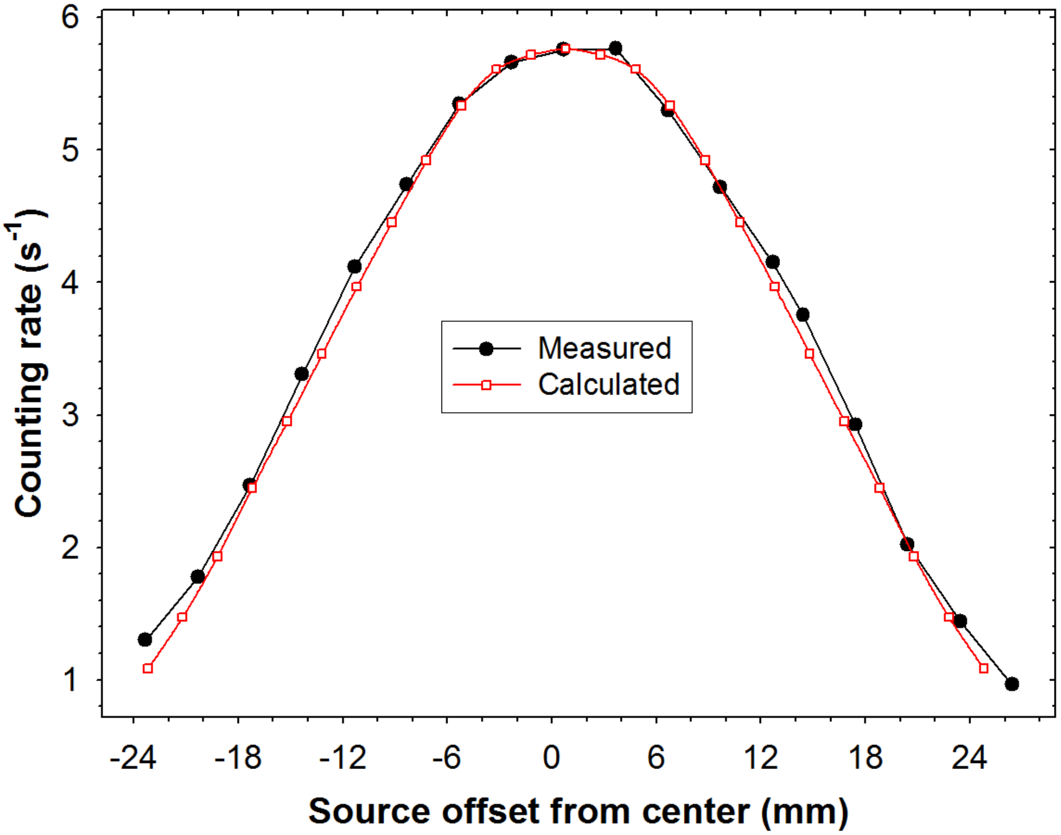

Fig. 3. Measured and calculated counting-rate dependence on horizontal displacement of the ^{241}Am source for the ^{237}Np 26.34 keV γ ray.

[1] N. Nica, J. C. Hardy, V.E. Iacob, M. Bencomo, V. Horvat, H.I. Park, M. Maguire, S. Miller, and M. B. Trzhaskovskaya, Phys. Rev. C **89**, 014303 (2014).

[2] M.J. Berger, J.H. Hubbell, S.M. Seltzer, J. Chang, J.S. Coursey, R. Sukumar, D.S. Zucker, and K. Olsen, "XCOM: Online Photon Cross Section Database (version 1.5)". Available online at http://physics.nist.gov/xcom.

[3] J.A. Halbleib and T.A. Mehlhorn, Nucl. Sci. Eng. **92**, 338 (1986); J.A. Halbleib, R.P. Kensek, T.A. Mehlhorn, G.D. Valdez, S.M. Seltzer, and M.J. Berger, CYLTRAN 3.0, Sandia National Laboratories, Albuquerque, NM, Report SAND91-1634 (1992).

[4] H.H. Hansen, E. de Roost, W. Van der Eijk, and R. Vaninbroukx, Z. Phys. **269**, 155 (1974).

[5] V.P. Chechev and N.K. Kuzmenko, Appl. Radiat. Isot. **68**, 1578 (2010).

^{60}Fe project: barium fluoride detector 19 pack characterization

M. Sorensen, A. Abbott, A.B. McIntosh, E. Bennet, A. Couture, J. Gauthier, K. Hagel, S. Ota,
A. Simon, and S.J. Yennello

^{60}Fe is seen in a variety of places on earth and in space even though it only has a half-life of 2.64 million years, quite small compared to the life span of the solar system[1-3]. ^{60}Fe must thus be produced recently in the universe. The clear electromagnetic signature associated with ^{60}Fe can be used to help model the stellar evolution of star if enough knowledge about its nucleosynthesis is learned[4]. When ^{60}Fe is initially produced by neutron capture on ^{59}Fe it is produced in an excited state; which can re-emit the neutron or deexcite via gamma ray emission. The photon strength function describes the bulk quantum mechanical component of photon emission probabilities and thus it is important in describing this reaction. For some nuclei, experiments have shown an enhancement in the photon strength function at very low energy; this feature is commonly referred to as an up-bend. This up-bend has large potential ramifications for r-process nucleosynthesis. Experiments have shown an up-bend in the ^{56}Fe and ^{57}Fe nuclei[6], so the observation of its presence in ^{60}Fe would illustrate that this feature may be more widespread. Learning how the photon strength function varies across the chart of nuclides would also aid in modeling the neutron economy of advanced reactors.

A test run was conducted on November 1st of 2019 to begin testing the equipment to be used for the ^{60}Fe photon strength function experimental set up. 7.5 MeV/u ^{57}Fe was impinged on a CD_2 target to do a ^{57}Fe(d,p)^{58}Fe reaction . The free protons produced in this reaction in the angular range of approximately 120 to 150 degrees were detected by an annular silicon detector. Gamma rays produced from excited states in ^{58}Fe were detected using a hexangular arrangement of 19 BaF_2 detectors. A parallel plate avalanche counter was also employed to measure the ^{58}Fe residue produced in the reaction and for beam tuning purposes. This report shall focus on the performance of the 19 pack of BaF_2 detectors.

Gamma rays can undergo Compton scattering or pair production, which can spread their energy out over multiple detectors, or cause some energy to go unmeasured. The energy of the of the gamma rays detected, and the gamma ray multiplicity associated with the event are important observables for extracting the photon strength function. To attempt to correct for this problem neighboring detectors that fired next to each other in the same event are added together. Code to do this was adapted from the DANCE project at Los Alamos Lab. The effect of this is shown from the comparison made in Fig. 1. The gamma ray spectrum is shown for individual BaF2 crystals' recorded energies within a 100ns of the silicon trigger (blue) with the yield normalized to one. On top of this spectrum is the gamma spectrum when these same crystals are "clustered" together (red), again normalized to one. When contiguous neighboring crystals are added together the 810 keV corresponding to the first excited state to the ground state transition in ^{58}Fe becomes more prominent. This enhancement suggests that the clustering method is successfully reconstructing gamma rays. In addition, there is a clear enhancement in the yield at higher gamma ray energy and a reduction in the relative yield of the 511 keV region as pair produced annihilation photons are added back to reconstruct their higher energy gamma ray progenitors. The low energy Comptons at around 200 keV are also reduced in intensity under the clustering method regime.

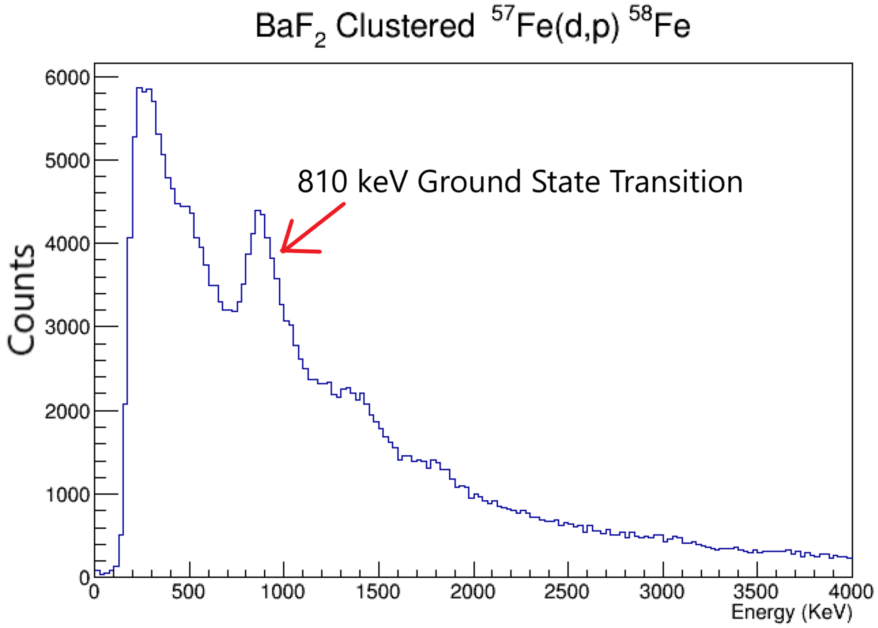

Fig. 1. In blue is the energy of any individual crystal that triggered within 100ns of the silicon detector triggering. Plotted in red is the clustered gamma spectrum, instead of taking the individual crystal energies contiguous crystals that triggered have their energies added together. Both spectra are normalized to one.

The other key observable in the experiment is the excitation energy calculated for the residue. This information is calculated from the backward silicon detector's measurement of the protons emitted in the reaction. Using the proton's energy and the know kinematics of the reaction the excitation energy is calculated [8]. For the purposes of the photon strength function analysis if the total gamma energy calculated is not sufficiently close to the excitation energy calculated the event is thrown away. The excitation energy detected in the silicon detector is plotted against the sum of the energy detected in the BaF2 detectors in Fig. 2. From this figure it is obvious that in most of the events there is incomplete collection of the gamma energy. This is unsurprising because in this test run only 19 BaF2 detectors were used, much less than the proposed 128 BaF2 detectors for the final setup. The events where there is more energy collected in the pack than excitation energy comes from cosmic contamination and the presence of carbon fusion events.

The 19-Pack performance is a good step in the direction of the final experimental setup. A clustering routine from DANCE has been successfully utilized to reconstruct gamma rays. Clearly there is still room for improvement, especially in acquiring greater solid angle coverage and to select out fusion events. In a future test run a 37 Pack of BaF2 will be used in addition to the 19 Pack to improve coverage. Further test plans involve the use of a TOF measurement of the residues to gate out the fusion contamination.

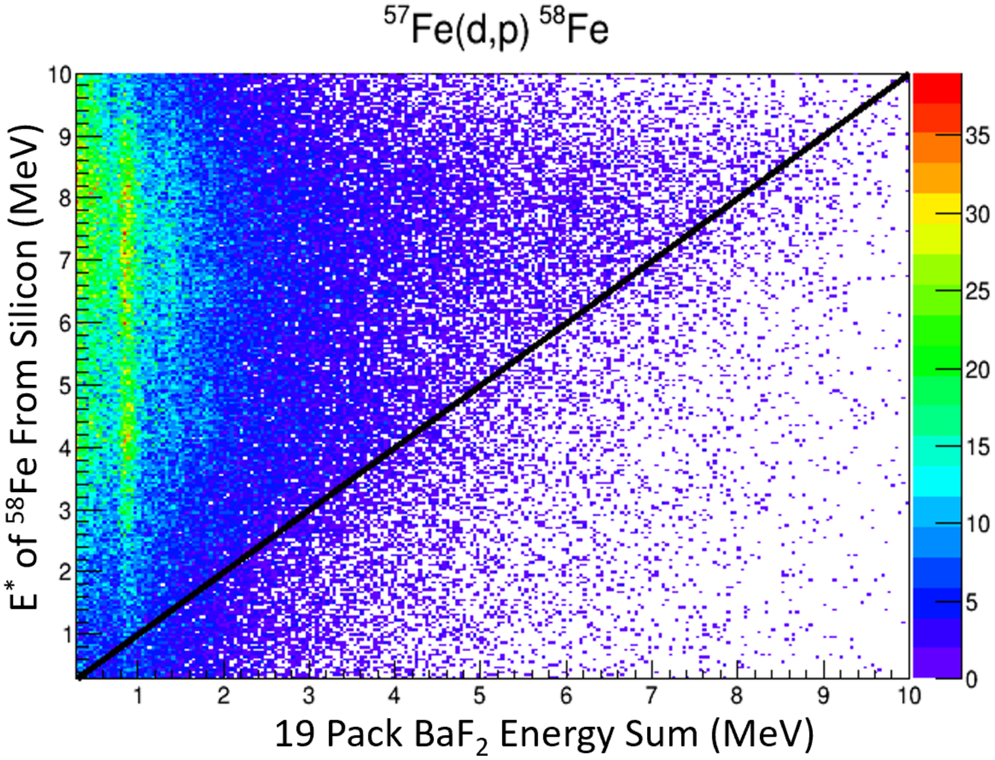

Fig. 2. The excitation energy of the ^{58}Fe residue calculated from the proton detected in the annular silicon detector is plotted against the sum of all the energies collected in the 19 Pack of BaF$_2$ detectors. The diagonal black line is the y=x line, which points out potentially complete events.

[1] A. Wallner, J. Feige, and N. Kinoshita *et al*., Nature **532**, 69. (2016).

[2] D. Koll *et al*., Phys. Rev. Lett. **123**, 072701 (2019).

[3] L. Fimiani *et al*., Phys. Rev. Lett. **116**, 151104 (2016).

[4] W. Wang *et al.*, A&A, **469**, 1005 (2007).

[5] S. Goriely, Phys. Lett. B **436**, 10 (1998).

[6] M. Arnould, S. Goriely, and K. Takahashi, Phys. Rep. **450**, 97 (2007).

[7] A. Voinov *et al.*, Phys. Rev. Lett. **93**, 142504 (2004).

[8] A. Abbott *et al., Progress in Research*, Cyclotron Institute, Texas A&M University (2019-2020), p. IV-66.

^{60}Fe project: barium fluoride detector recoupling

M. Sorensen, J. Gauthier, A. Abbott, A.B. McIntosh, E. Bennet, A. Couture, K. Hagel, S. Ota,
A. Simon, and S.J. Yennello

Over the past year further re-coupling of the TAMU-ORNL BaF2 array detectors [1] were done to improve their performance. BaF2 detectors consist of two components: the BaF_2 crystal and the photomultiplier tube (PMT). These components are typically coupled using viscous silicone oil that matches the crystal's index of refraction and is transparent to UV light then wrapped with Teflon to reflect the light towards the quartz PMT window. The crystal and the PMT are then optically sealed with electrical tape to keep out ambient light. Unfortunately, we observed that over time the coupling of the crystal and the PMT degrades as silicon oil slowly leaks out from the interface. This loss of silicone oil causes a reduction in the light that enters the PMT. The loss of light has two effects, one is a degradation in the energy resolution due to lower information carrier statistics, and the second is the reduction of particle identification due to the UV fast light component of BaF_2 crystal photo response being more vulnerable to the loss of the silicon oil coupling. The loss of particle separation is a problem for BaF_2 detectors due to the presence of alpha emitting Radium isotopes mixed in with the Barium. If unidentified this alpha background would adversely affect the gamma ray spectra these detectors produce.

During the course of the November 1st 2019 test beam run a number of barium fluoride detectors showed signs of degradation in their particle separation (see Fig. 1). Some of these troubled detectors were selected for recoupling. In an effort to delay the degradation of the silicone oil coupling an alternate recoupling procedure was developed. In this procedure a thick layer of RTV (Room-Temperature-Vulcanization) was placed around the contact between the PMT window and the crystal in attempt to keep the silicone oil from leaking into the surrounding Teflon. For this report, we will focus on two detectors, AM16 and AM20, which were the first two recoupled with the RTV barrier. In order to quantify the separation, the fast integral was divided by the total integral and plotted against the total

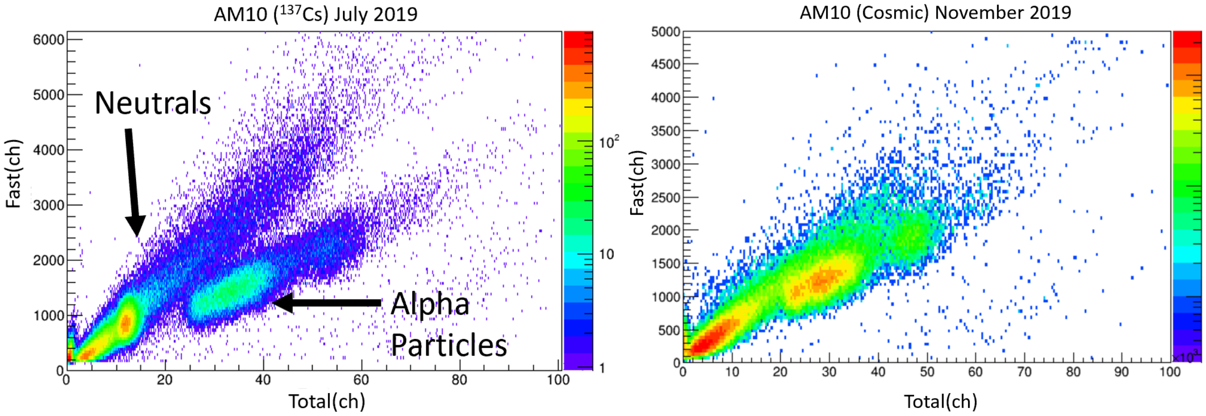

Fig. 1. Yield as a function of fast component of light output and total output. Both spectra are for detector AM10. Left) run with a ^{137}Cs source just after re-coupling in July 2019. A clear separation is seen between the alpha particles and the gamma rays. Right) cosmic spectra taken 5 months later. A clear degradation is seen in the particle identification.

integral. The total channel region above where the alpha particles first appear was chosen to project the fast/total over.

As shown in Fig. 2a, detector AM16 appeared quite stable between the first two cosmic tests of its recoupling. In the last test, there appears to have a slight shift in the gamma peak. However, the BaF_2 detectors in these tests were not thermally stabilized, so it is possible this discrepancy is a thermal effect. As clearly seen in Fig. 2b, detector AM20 underwent a rapid decline in the separation between alpha particles and gamma rays, more than likely the recoupling was not stable in this case. Other detectors were also tested; some clearly need recoupling while others may be stable with a more thorough testing

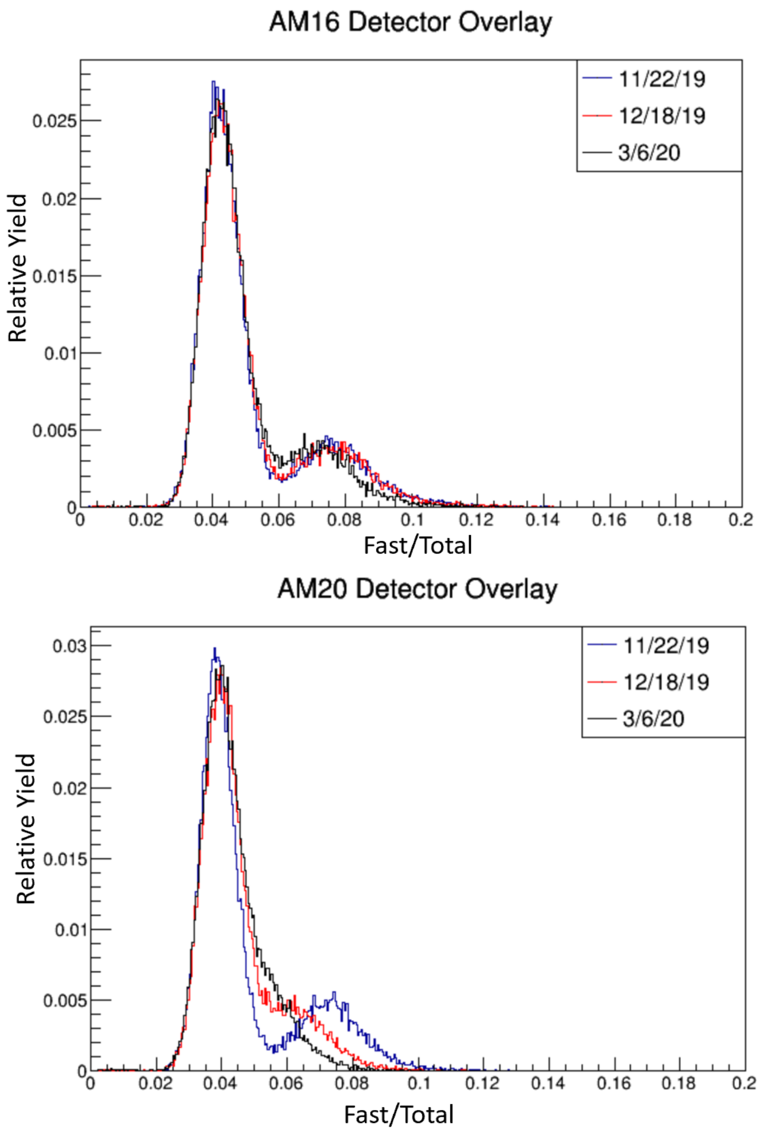

Fig. 2. a) Fast/Total projections for AM16 at different times, area normalized to one. These projections were taken starting from a total channel region of the lowest energy alpha particle seen in the first test. b) Same as panel a but for detector AM20. A clear degradation in the separation of alpha particles (left peak) and cosmic rays (right peak) were seen.

procedure. A possible reason for the failures in the barrier could be the messy nature of the barrier application around the crystal-PMT junction. A potential solution could be a Teflon ring around the interface to hold the silicon rubber in place while it is applied. Another issue with the barrier is that the RTV could react with the silicon oil, so if the RTV penetrates inside the junction before it dries up it could impair the effectiveness of the oil, thus creating a bad coupling within the most external area of the crystal-PMT junction. If this effect is not negligible, the RTV barrier technique might not be efficient but a solid, static sealing (Teflon) ring could still help to prevent the oil from leaking out.

Detectors will be tested again with active cooling to stabilize the temperature. If the changes in resolution observed can be explained by temperature variations, the coupling procedure may be working better that it seems at present. In the event that a noticeable increase in particle separation stability is not found between the barrier method and the conventional method, a return to the conventional method will be implemented for those detectors showing poor particle identification.

[1] J. Gauthier *et al.*, *Progress in Research*, Cyclotron Institute, Texas A&M University (2018-2019), p. IV-58.

Cyclotron effect on S3 annular silicon detector resolution

A. Abbott, M. Sorensen, A.B. McIntosh, and S.J. Yennello

A Micron S3 annular silicon detector is used as a part of the experimental setup being designed to measure the photon strength function for ^{60}Fe [1]. One surface of the detector is segmented into 24 rings and the other surface is segmented into 32 sectors (“pies”), providing angular resolution. From the measured proton energy and angle, the excitation energy of the ^{60}Fe nucleus, an essential quantity for determining the photon strength function, can be calculated. The resolution of our calculated excitation energy is dependent, in part, upon the energy resolution of the silicon detector, so a test was performed to investigate how the resolution was affected by interference caused by running the cyclotron. In this test we changed various settings that are present during beam production and took source data of ^{228}Th with the silicon. As a result of this run, we have determined that our excitation energy resolution is not being limited by the resolution of our detector.

The test run was performed on the end of the MARS spectrometer with a beam of ^{40}Ar at 15 MeV/u produced by the K150 cyclotron. We used a 492 um S3 annular silicon detector (wafer 2790-01) reverse biased to -70 V with a ^{228}Th source covered with a 1.4 um Mylar foil placed 2 cm away from the center of the detector. We took six 30 minute runs where certain parameters (magnet settings, RF settings, valve positions) were changed and the source spectrum was collected. The settings for each of these runs are given in Table I. The ^{228}Th spectrum was collected (Fig. 1) and energy loss corrections were done based on the Mylar foil thickness, silicon dead layer thickness, and aluminum contact thickness for each ring. The resulting spectra were fit and the resolution of the rings were obtained and plotted as a function of the ring number.

Table I. Cyclotron and beam settings for each run.

Run Number	**Settings**
16	Cyclotron RF was on. The beam line valves were closed. The MARS magnets were turned off and the velocity filter E field was on.
17	Cyclotron RF was on. The beam line valves were opened. The MARS magnets were turned off and the velocity filter E field was on.
18	Cyclotron RF was on. The beam line valves were opened. The MARS magnets were turned on and the velocity filter E field was on.
19	Cyclotron RF was on. The beam line valves were opened. The MARS magnets were turned on and the velocity filter E field was on. The ^{40}Ar beam was directed to the slits of the MARS coffin.
20	Cyclotron RF was on. The beam line valves were closed. The MARS magnets were turned on and the velocity filter E field was on.
21	Cyclotron RF was off. The beam line valves were closed. The MARS magnets were turned off and the velocity filter E field was off.

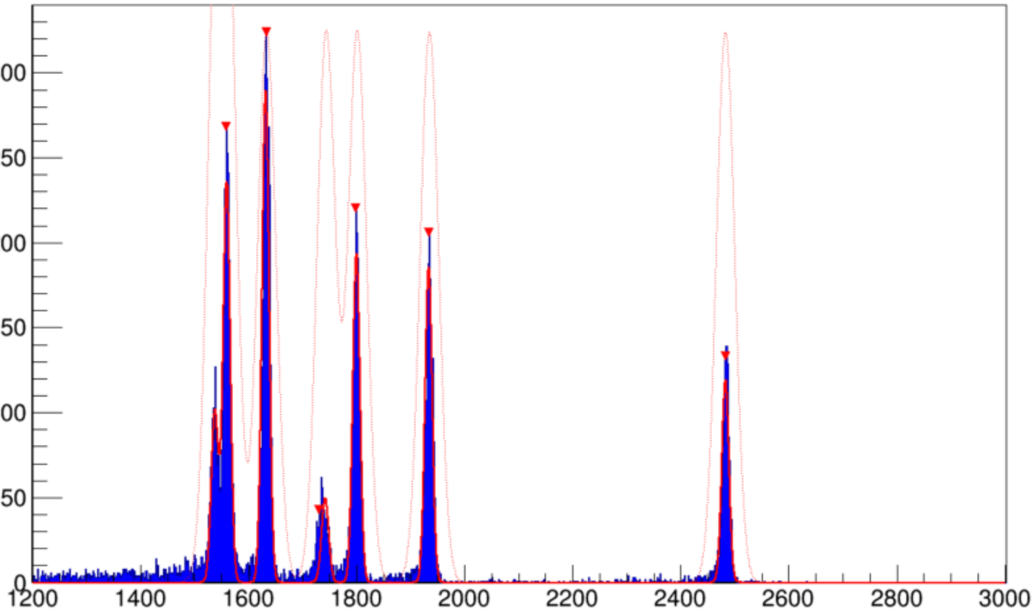

Fig. 1. ^{228}Th spectrum (blue) from ring 0, run 19. The dotted red lines indicate the initial guess fit and the solid red lines are the true fit. The red arrows are placed by the TSpectrum peak finder which give accurate guess parameters.

The resolution (FWHM) of each of the silicon rings for two particular runs are shown in Fig. 2. Runs 19 and 21 were chosen as they consisted of having either all of the settings either on or off.

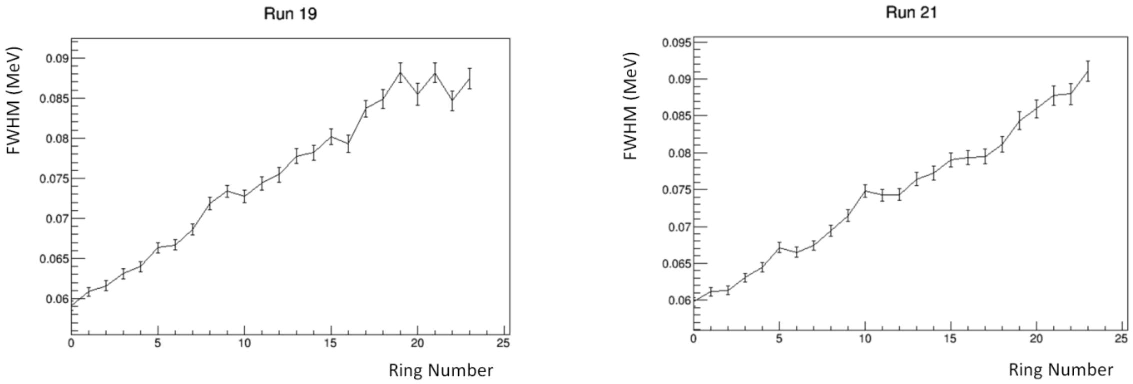

Fig. 2. The resolution of each ring is shown for two separate runs. Run 19 had all settings on and run 21 had all settings off. The resolution is relatively consistent between runs.

Although there is some variation in the resolution of the rings between the runs, they remain relatively consistent and the resolution for all rings remain below 100 keV FWHM. The increasing resolution as a function of ring number is understood to be due to the angular coverage of the rings. What is labeled as ring 0 is the innermost ring which covers the narrowest angular range while the outermost ring, labeled ring 23, covers the largest angular range which results in a reduction of the resolution. A well-collimated source would be expected to decrease this effect. Fig. 3 shows the resolution of ring 0 as a function of run number and it is apparent that there is little fluctuation in the resolution when changing different cyclotron and beamline parameters.

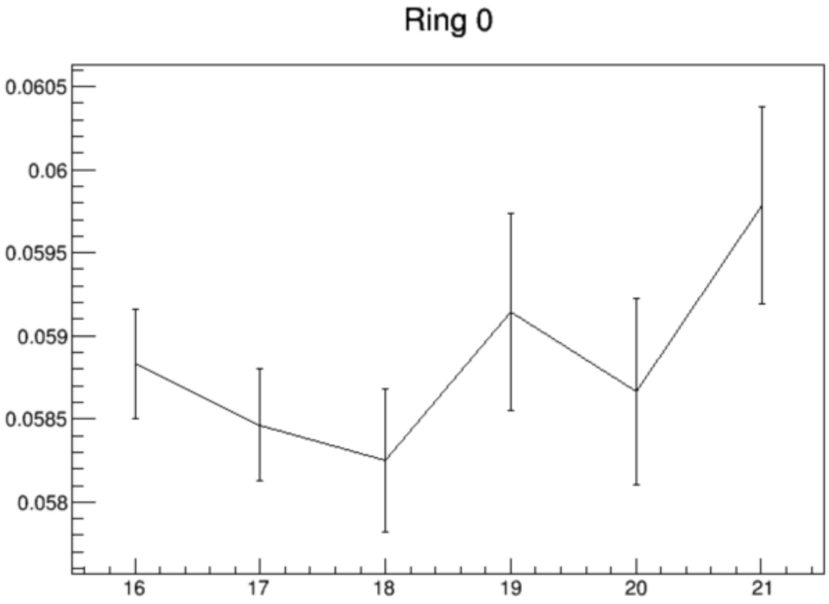

Fig. 3. Ring 0 resolution as a function of run number.

In order to see the effect of the resolution of the silicon detector on the resolution of the excitation energy of the residue, a simulation was written. This simulation takes into effect the beam spot size, silicon resolution, dead layer thickness, and target thickness. Using a worst case scenario beam spot radius of 5 mm, a dead layer thickness of 800 um, a target thickness of 0.905 mg/cm^3, and a silicon resolution of 100 keV (FWHM), the plot of the separation of the excitation energies is produced and shown below and labeled Fig. 4. With a silicon energy resolution of 100 keV (FWHM) we obtain an excitation energy resolution of approximately 600 keV (FWHM).

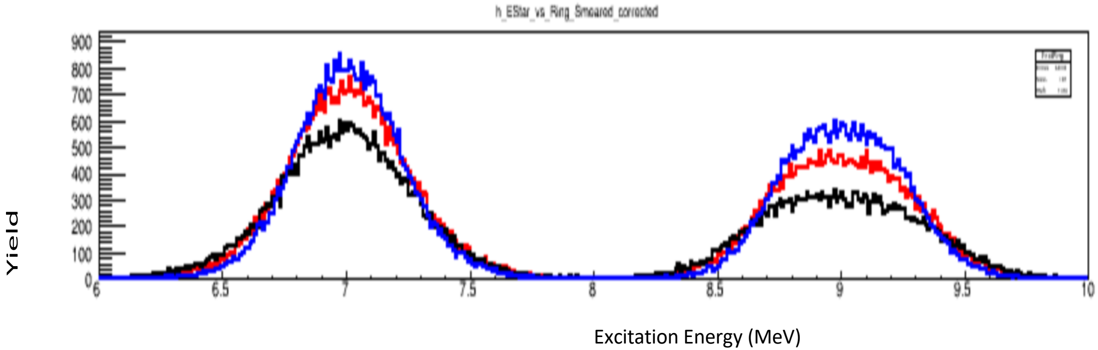

Fig. 4. Simulated ^{58}Fe residue excitation energy widths.

[1] A. Abbott *et al.*, *Progress in Research*, Cyclotron Institute, Texas A&M University (2019-2020), p. IV-66.

Measurement of target thicknesses

M.A. McCarthy and L.A. McIntosh

Several thin CD_2 targets have been obtained in order to measure the photon strength function of ^{60}Fe using the ^{59}Fe(d,p)^{60}Fe reaction [1,2]. The thicknesses of the targets are labeled based upon the production process; however, the precise knowledge of the target thickness improves the quality of the measurement. Therefore, the target thicknesses are being measured using energy loss with an alpha source. The alpha particles lose energy as they pass through the target, and the amount of energy lost is dependent on the thickness of the target. The energy loss in the target was measured when the targets were at 0^o and 45^o relative to the line between the source and the silicon detector. The experimental set up is shown in Fig. 1. Thorium-228 was used as the alpha source.

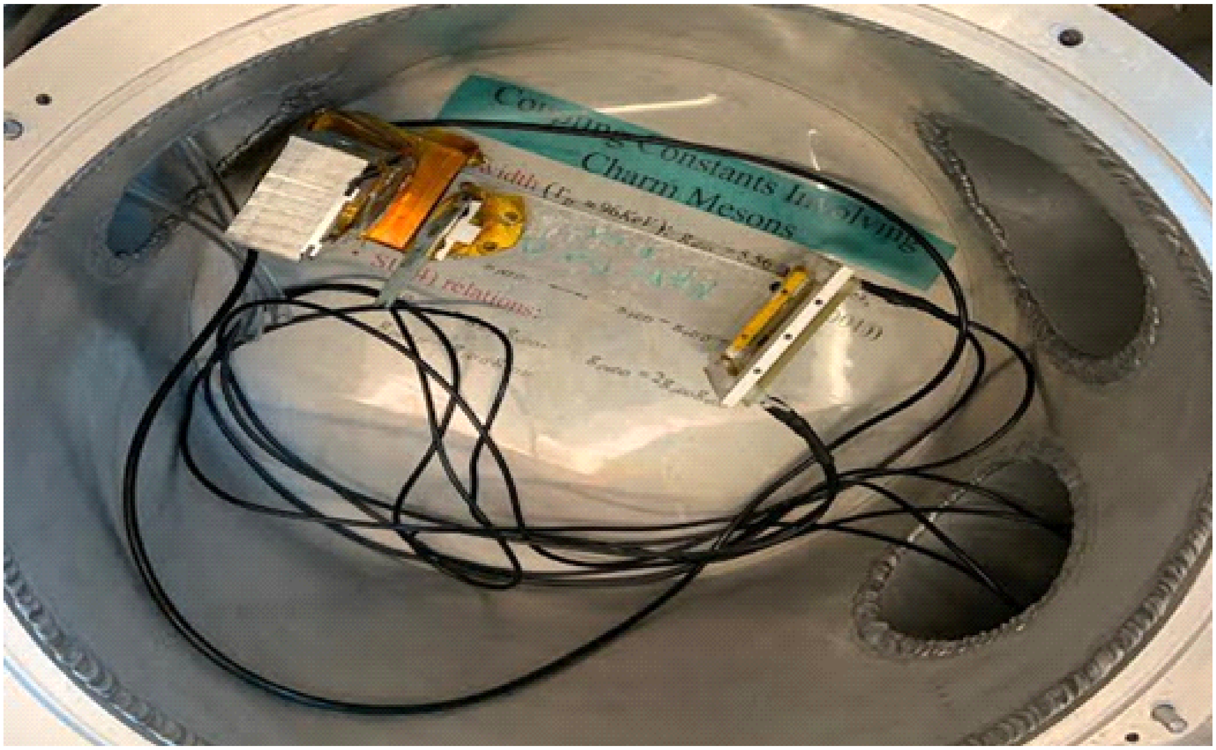

Fig. 1. Experimental setup. A quadrant Si detector was used to detect the alpha energies. A target at 0° refers to when the target is perpendicular to the direction of travel of the alpha particles.

Almost the full complement of targets has been measured in this way. Runs without a target were done in between the target runs to ensure the calibrations were consistent from one run to the next. Each of these runs has now been calibrated. Fig. 2 shows one such calibrated run, thorium-228 source on the silicon detector. The peaks should range from 5.685 MeV to 8.785 MeV.

The calibrated measured peak energies from the thorium-228 source were compared to calculations of energy loss using CycSrim calculations, which are based upon the Stopping Range of Ions

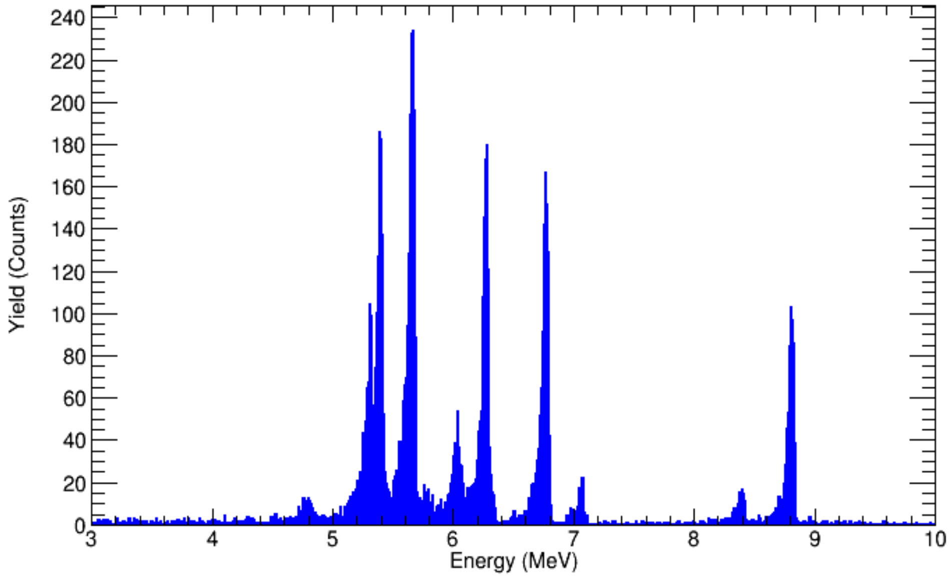

Fig. 2. Calibrated spectrum of ^{228}Th source used for target thickness measurements.

in Matter (SRIM). The percent difference between the measured energy of the alpha particle and the expected energy, based upon SRIM, is shown in Fig. 3 below for two different assumptions of the thickness for one representative target. Analysis of this data is ongoing.

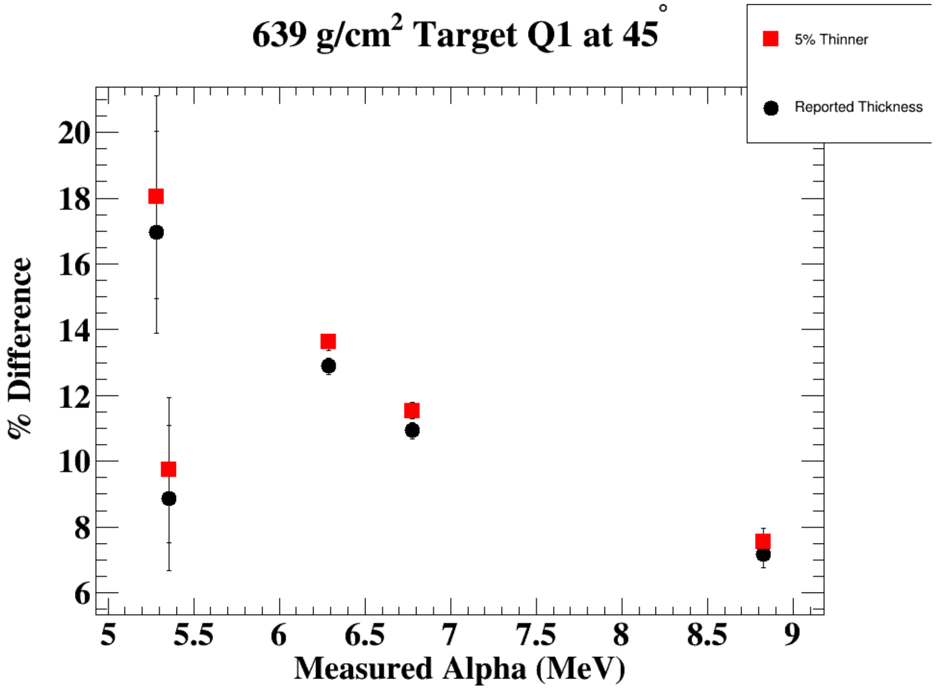

Fig. 3. A 639 g/cm^2 target at 45°. This shows the percent difference between the measured and calculated alpha energy (MeV). This was also done to a 5% thinner target than was reported.

[1] A.B. M 018-2019), p. II-1

[2] A.B. McIntosh *et al.*, *Progress in Research*, Cyclotron Institute, Texas A&M University (2018-2019), p. II-21.

PIGE (Particle Induced Gamma Ray Emission) standards testing

A. Watts, M. McCarthy, J. Gauthier, and S.J. Yennello

Particle Induced Gamma Ray Emission (PIGE) is an Ion Beam Analysis (IBA) technique used to study a composition of a sample. This technique allows for multi-elemental, quick analysis, and minimal sample preparation [1]. PIGE has been implemented at Texas A&M University's Cyclotron Institute.

A target nucleus is excited with an ion beam and upon de-excitation characteristic gamma-rays are emitted. PIGE is used for low Z elements, from lithium to aluminum. The PIGE technique has been used to identify per- and polyfluoroalkyl substances (PFAS). PFAS are a group of man-made chemicals found in consumer products that are nonstick, grease- and water-resistant, and in personal care products such as cosmetics [2]. PFAS are of interest since studies have shown these chemicals are linked to health and environmental concerns [2].

During the November 2018 run, it has been observed that the irradiation degrades the standards, lowering the fluorine concentration over time and making them unusable. We thus started the project of making our own standards [3]. Several batches of standards, made over the past few semesters, have been tested in March 2020 and were used to generate a calibration curve. These standards, made at CVE lab building, were prepared with PFOA (perfluorooctanoic acid) with successive dilutions of methanol and water. The standards were dyed with food coloring and pipetted onto a piece of filter paper. The standards have a range of concentrations from 0 – 12k ppm of F (fluorine). The K150 cyclotron was used to bombard the standards with a 3.6 MeV proton beam. The gamma-rays were detected by a CdTe detector which was placed about 45° from the direction of the beam. The decay of ^{19}F nucleus has two characteristic gamma-rays, 110 keV and 197 keV. The total amount of F counts in the two peaks were integrated and normalized. Fig. 1 shows the calibration curve for the organic standards tested during the run. The purpose of this curve is to be used to determine the concentration of fluorine in consumer products.

The F concentrations in standards that were tested during this run need a correction factor for the current that was measured with the Faraday cup (FC). The FC was moved into the beam path for beam current measurements between each run and removed by a stepper motor before the run to prevent background counts from the FC material. To make precise beam intensity measurements an electron suppression negative voltage needs to be applied to the front ring of the cup to repeal back the electrons kicked off by the beam inside the FC but in our case, this voltage was generating a high negative current at the reading output instead of the low positive current that we were expecting. It is hypothesized that the fast electrons coming from the window and the air most likely induced a high negative current when the suppression voltage was applied. Without the voltage, the kicked off electron from the FC were not repealed back in the cup and were thus most likely compensating for the extra fast electrons from the window, providing a more or less correct positive current readout. To test if this hypothesis is correct, a measurement would need to be taken with the same beam, H+, with the cup inside the chamber under vacuum so the electron suppression voltage can be applied efficiently without the contribution of external fast electrons. Another measurement would then need to be taken where the FC originally was during the run (behind the target). With those two measurements, a correction factor can be calculated, which then can be applied to the current measurements that was read during the run, allowing us to extract more accurate concentration values.

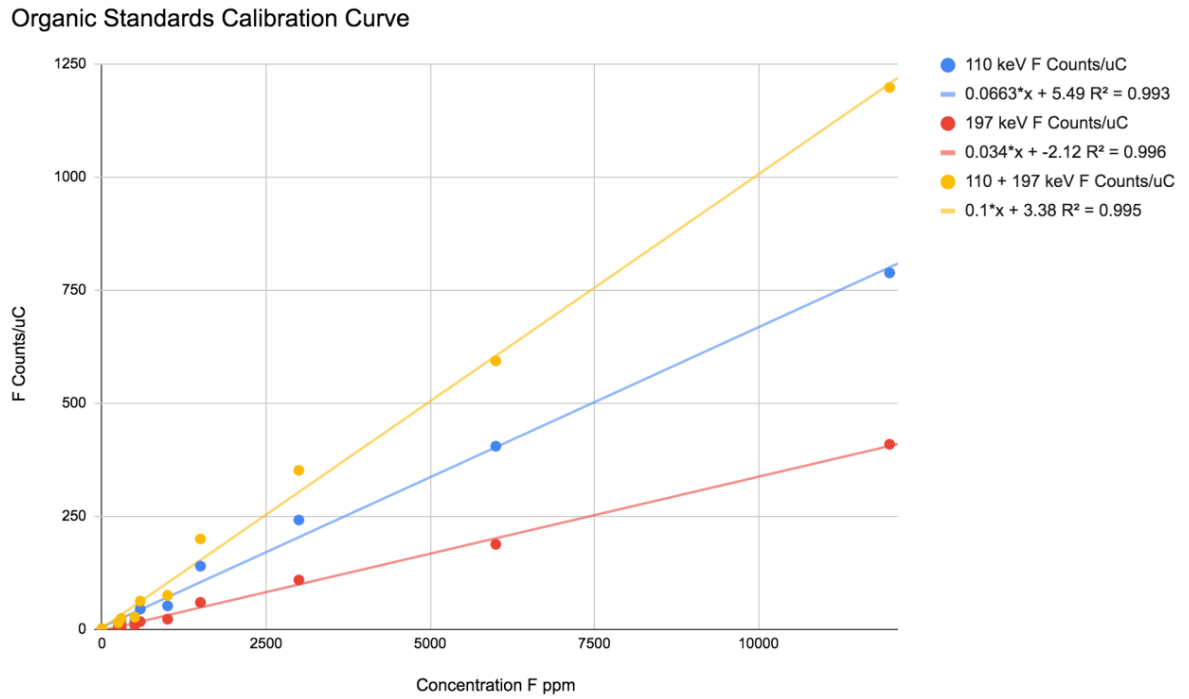

Fig. 1. Organic Standards Calibration Curve with standards ranging from 0 -12k ppm of F.

[1] A. Rodriguez Manso *et al.*, AIP Conference Proceedings **2160**, 050023 (2019).

[2] Laurel A. Schaider *et al.*, Environ. Sci. Technol. Lett., **4(3)**, 105 (2017).

[3] M. McCarthy *et al.*, *Progress in Research*, Cyclotron Institute, Texas A&M University (2018-2019), p. IV-61.

PPAC counting rate characterization

A.B. McIntosh, A. Abbott, M. Sorensen, J. Gauthier, H. Hagel, and S. Ota

Parallel Plate Avalanche Counters (PPAC) are widely used in nuclear physics to measure the presence of an ionizing particle and provide an accurate timing signal. It is widely rumored that these detectors are capable of handling a rate of up to one million particles per second. However, achieving this high counting rate is not trivial. In this report, we investigate the performance of a PPAC using a beam of ^{57}Fe @ 7.5 MeV/u.

The PPAC was fabricated at Michigan State University's National Superconducting Cyclotron Laboratory and subsequently refurbished there by John Yurkon. The detector has a 10cm x 10cm square active area. Aluminized mylar foils contain the detection gas (isobutane). A central anode foil (gold coated mylar) is positively biased to collect electrons. Adjacent foils with strip segmentation of the gold coating collect cations; these are 3mm from the anode foil. The gas-containing foils are 6mm from the strip foils when there is no bowing of the windows. Typical gas pressure of isobutane is 6 Torr, and bias voltages are typically between +500V and +600V.

Direct beam of ^{57}Fe from the TAMU K150 cyclotron was focused onto phosphor target approximately 30 cm downstream of the standard MARS detector focal point. The PPAC was positioned approximately 90 cm farther downstream. During the experiment, the phosphor used for focusing was replaced with a 709 ug/cm^2 CD_2 foil. The rate measured by the PPAC was studied as a function of the PPAC gas pressure, the PPAC bias voltage and the beam intensity.

The beam intensity was measured on FC02, a Faraday cup immediately at the exit of the cyclotron; this is not electron suppressed. It should be noted that due to drifts in the beamline optics magnets, this beam current can drift relative to the beam current at the PPAC position. For measurements taken sufficiently close in time, direct rate comparisons can be made.

The gas pressure is controlled with a gas-handling system (GHS) which utilizes an MKS520 controller. A pressure gauge just after the controller matches the set pressure on the MKS setting dial. A precision analog relative pressure gauge measures the pressure on the output line of the PPAC just before re-entering the GHS en route to the output line vacuum pump. The pressures reported in all figures correspond to the set pressure from the MKS controller. The reading on precision analog gauge is typically 0.6 Torr lower. The gas flow rate was varied from 15 to 50 cc/min and did not have a discernible impact on the measured event rates reported below.

The anode output of the detector was amplified with a fast timing pickoff (Spielier-type), which was then amplified with a fast amplifier (Ortec FTA 820) and then discriminated with a Tennelec constant fraction discriminator (TC-454) with an external cable delay of ~0.5ns. The bypass output of the fast timing pickoff went to a standard preamplifier ("hex-amp"), followed by a shaping amplifier (Caen N568B) which was sent to an oscilloscope for monitoring sparking in the PPAC.

Fig. 1 shows the measured PPAC rate as a function of beam current on FC02 with 8 Torr of isobutane in the detector with 580 V, 590 V, and 610 V applied to the anode. As beam current was raised, the measured counting rate rose, and then saturated. At rates below saturation, the counting rates agree within experimental uncertainty. The counting rate at saturation is higher for higher voltages. The lower two curves were stopped when saturation became evident. The higher curve was terminated when a single spark event was observed on the oscilloscope.

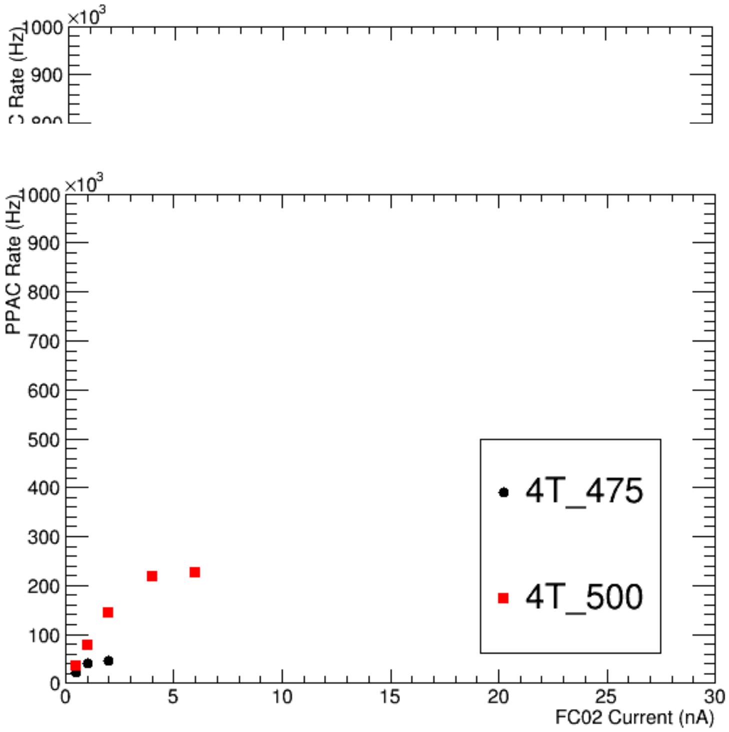

Fig. 2. Measured rate vs beam current, 4 Torr.

Fig. 2 shows the measured PPAC rate as a function of the beam current on FC02 with 4 Torr of isobutane at voltages of 475V and 500V on the cathode. These curves clearly saturate at a lower rate than at 8 Torr. A curve at 515V was attempted but stopped early on at the occurrence of a single spark event. It is not surprising that at lower pressure, a lower voltage is needed to induce sparking.

Higher voltages were explored at 8 Torr, allowing for some occasional sparking. Fig. 3 shows the measured rate as a function of beam current using 8 Torr with voltages of 620V, 630V, and 640V. The horizontal axis cannot be compared directly to Fig. 1 due to slight changes in the beam optics which affect the transmission efficiency from the cyclotron to the detector. Still, it is clear that as the voltage is increased, the saturation rate rises. For this detector 860,000 counts per second was the highest measured rate. However, the actual rate on the detector must have been higher because some saturation is already present. Worse, the sparking at this pressure, voltage and beam rate, is steadily damaging the detector. These highest voltages are not sustainable on the time scale of even an hour, at least not with a beam of ^{57}Fe @ 7.5 MeV/u with an intensity of 100,000 particles per second spread out within a 1cm radius on the PPAC.

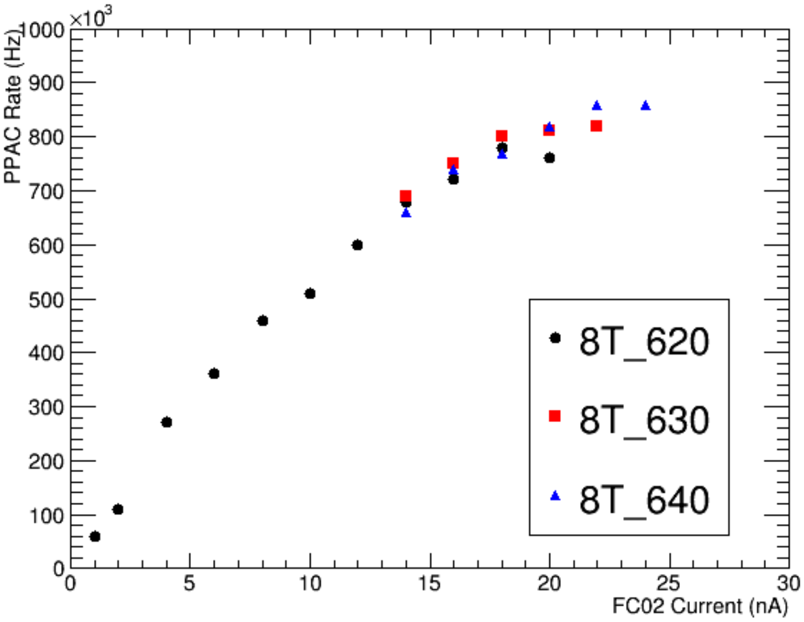

Fig. 3. Measured rate vs beam current, 8 Torr, high voltage.

Sparking appears to come in bursts. At a particular voltage, a spark occurs on average once a minute for ten or fifteen minutes, and then for several tens of minutes only occurs closer to once every ten minutes.

After significant sparking, the detector reaches a lower saturation rate. Fig. 4 shows the measured rate as a function of the FC02 current for 8 Torr and 610V. After only minimal sparking damage (circles), the rate continues to climb, only beginning to saturate above 600kHz. After moderate sparking damage (squares), the performance is poorer, strongly saturating around 550kHz. After significant sparking damage, the voltage and/or beam intensity must be reduced to avoid constant sparking.

In Fig. 5, the saturation rate is shown as a function of the applied bias voltage. Data is shown for four different pressures from 4 Torr to 8 Torr. In general, higher voltage achieves a higher saturation rate. Higher pressure is needed to allow higher voltage to be applied. It is possible that at pressures beyond 8 Torr, higher voltage could be applied and allow the detector to measure more than 1,000,000 counts per

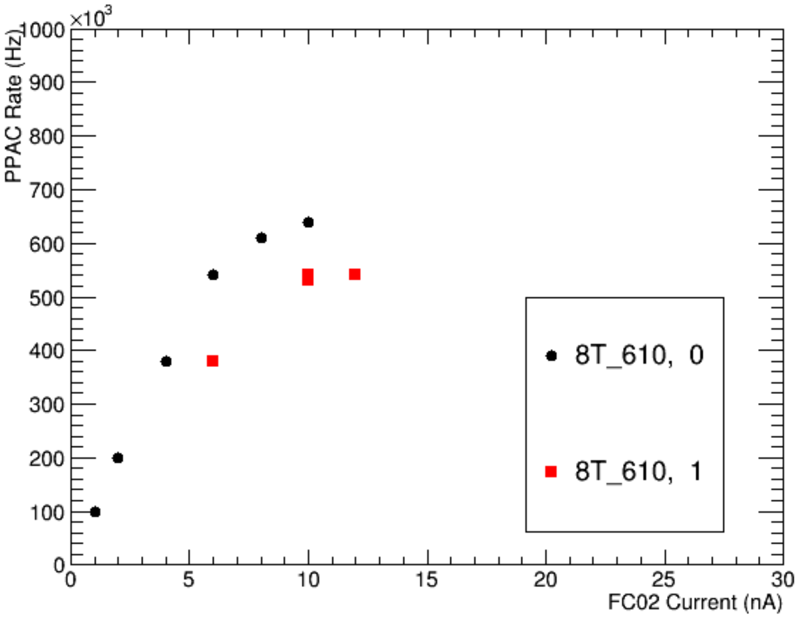

Fig. 4. Measured rate vs beam current, 8 Torr, moderate voltage. Damage evident. The 0 label refers to the earlier run, and the 1 to the later run.

second. Again, we note that such performance is not sustainable even on the timescale of an hour, as a few sparks cause damage, allowing (on average) more frequent sparking, and causing ever more rapid damage. It is certainly possible that having the ionizing radiation spread out evenly over the detector rather than concentrated within a 1cm radius would allow longer term survival of the detector; this is beyond the scope of this study.

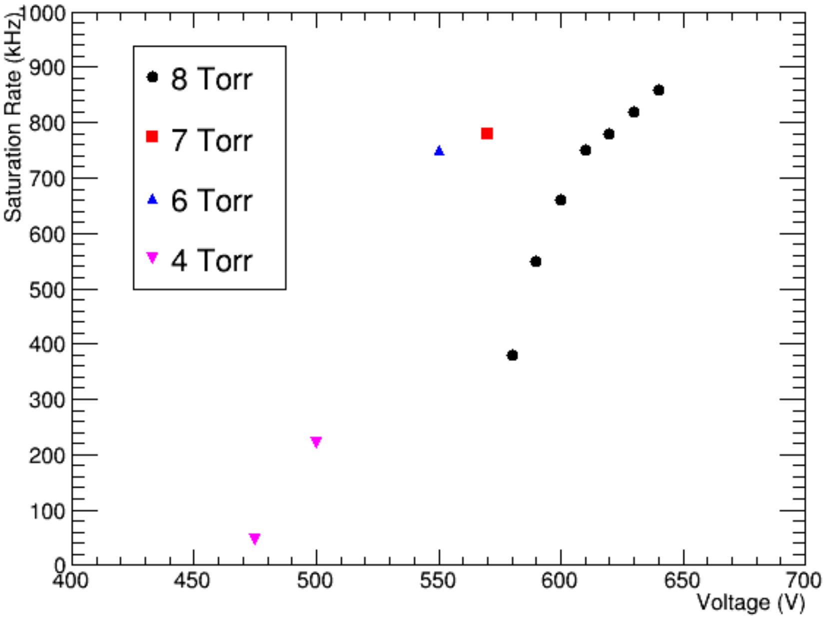

Fig. 5. Measured rate at saturation vs detector voltage.

Production of astatine-211 at the Cyclotron Institute

L.A. McIntosh, G.C. Tabacaru, J.D. Burns, E.E. Tereshatov, K.N. Lofton, M.A. McCarthy,
G. Avila, and S.J. Yennello

Astatine-211 shows promise for cancer treatments when connected to a targeting agent such as a monoclonal antibody, especially for non-localized cancers [1]. With the advent of such targeting agents, the major impediment to its use in clinical trials remains the availability of production and reliable separation chemistry [2]. We have produced ^{211}At at the Cyclotron Institute using the (α,2n) reaction at 28.8 MeV on a ^{209}Bi target. In the past, astatine-211 has been successfully produced in small quantities at the CI [3-5]. However, the dry distillation method used to separate out the astatine-211 from the target was laborious and not very efficient [5]. In the past year, a new team has been assembled, and novel chemistry is being used for the separation.

Successful production, recovery, and experimentation of ^{211}At were achieved at the CI using this new team. Two irradiations have been conducted, producing approximately 24 ± 2 mCi and 40 ±4 mCi of ^{211}At on December 12, 2019 and March 3, 2020, respectively. The average beam current of the 28.8 MeV α-particle beam was 5.3 μA (4.0–8.7 μA) for 8 h during the first campaign and 6.3 μA (5.5–7.0 μA) for 9 h during the second campaign. The targets were transferred to Radiochemical Lab 118 within the Cyclotron Institute, where a portion (roughly 30% in December 2019 and 46% in March 2020) of the target was dissolved in HNO_3 and experiments into a number of new separation systems were carried out. For the first campaign a series of solvent extraction system were studied, with the goal of direct extraction of ^{211}At out of HNO_3, and a promising system was identified to produce a rapid and efficient separation. In the second campaign, the promising system was adapted into extraction chromatography separation system and was shown to have an ^{211}At recovery yield of $\geq$ 95% with a decontamination factor from Bi of $\geq$ 100,000 by direct loading of the dissolved target on the column. These results are promising from both the practical side of being able to make and purify ^{211}At, but also for the scientific standpoint of discovering and understanding the unique chemistry of ^{211}At.

Improvements were made between the December and March runs, including the introduction of a sealed dissolution container, scrubber, and charcoal filter, which reduced the amount of astatine-211 detected by the Continuous Air Monitor, or iCAM (an alpha and beta particle detector and monitor) connected to the exhaust of the biosafety cabinet, where the target dissolution was performed. Air is drawn through the instrument by means of an external pump, and airborne particulate material is deposited on a filter. The filter is monitored by a Canberra PIPS ion-implanted silicon radiation detector, which allows simultaneous measurement of energy of both alpha and beta particles deposited on the filter. Data is recorded every 15 seconds.

The counts in the appropriate alpha energy range for astatine-211 were integrated in 10-minute increments before, during, and after the target dissolution and separation chemistry. Alpha particles of the appropriate energy are shown in Fig. 1 (December 2019 run) to increase at the time of target dissolution, and then drop off, congruent with astatine-211's short half-life ($t_{1/2}$=7.2 hours). In the March

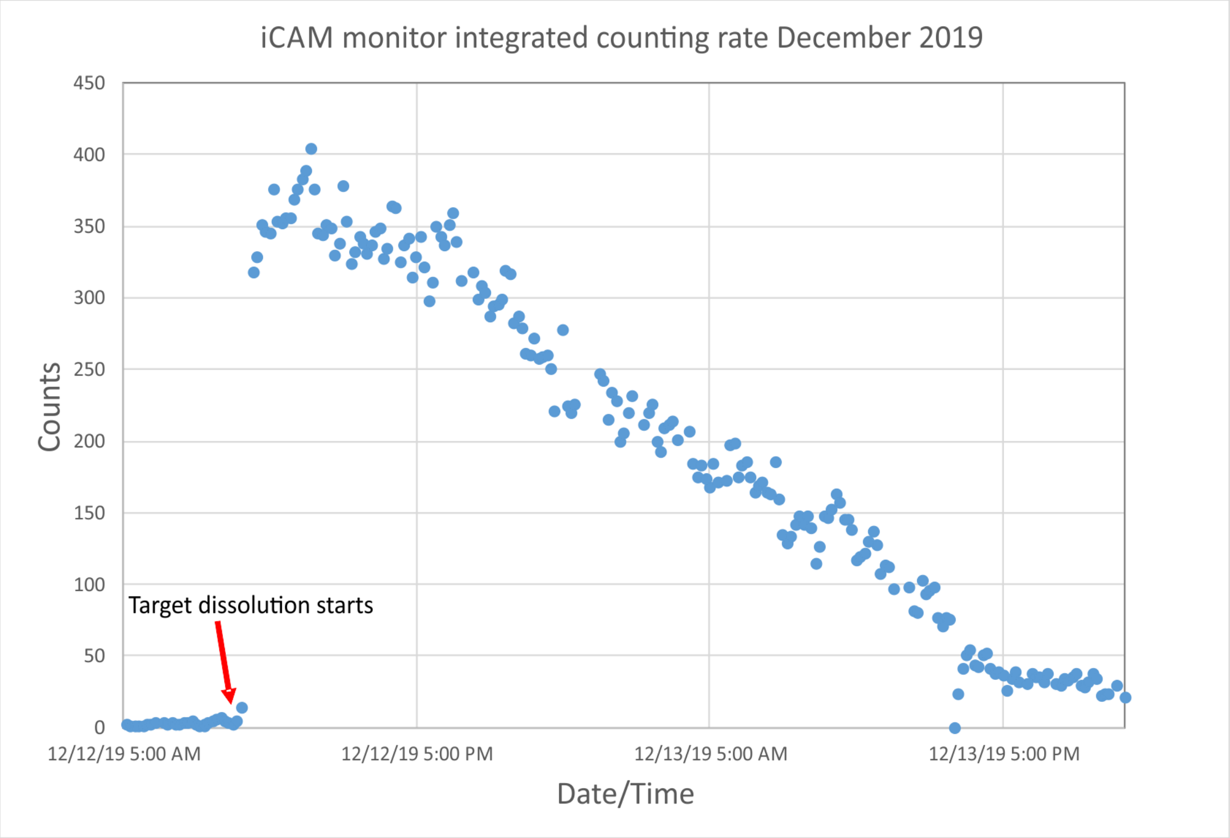

Fig. 1. Integrated iCAM Count Curve for December 12-13 dissolution of bismuth target with produced astatine-211.

run, shown in Fig. 2, the graph has a similar shape, but does not reach the same height of counts, indicating less astatine-211 was volatilized. The March 3-4 runs peaked at 82 counts, while the December 12-13 runs peaked around 375 counts.

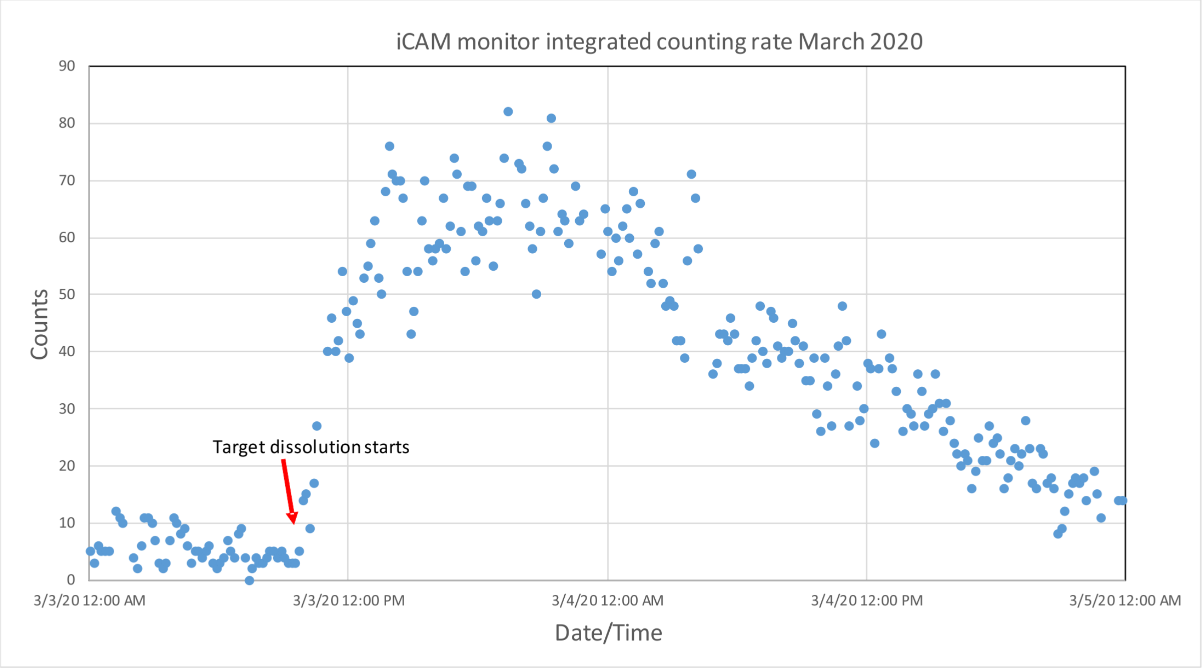

Fig. 2. Integrated iCAM Count Curve for March 3-4 dissolution of target with produced astatine-211.

A High Purity Germanium (HPGe) detector was used to measure the hundreds of liquid samples that were produced during the separation chemistry. A spectrum of one of our samples containing astatine-211 is shown in Fig. 3. Below 100 keV, there are many x-rays. The characteristic γ-ray of ^{211}At is pointed out at 687 keV. The two γ-rays of 211Po are also labeled at 569 and 897 keV. The other two γ-rays belong to unknown radiochemical species, which are separated out by the separation chemistry, but merit further investigation.

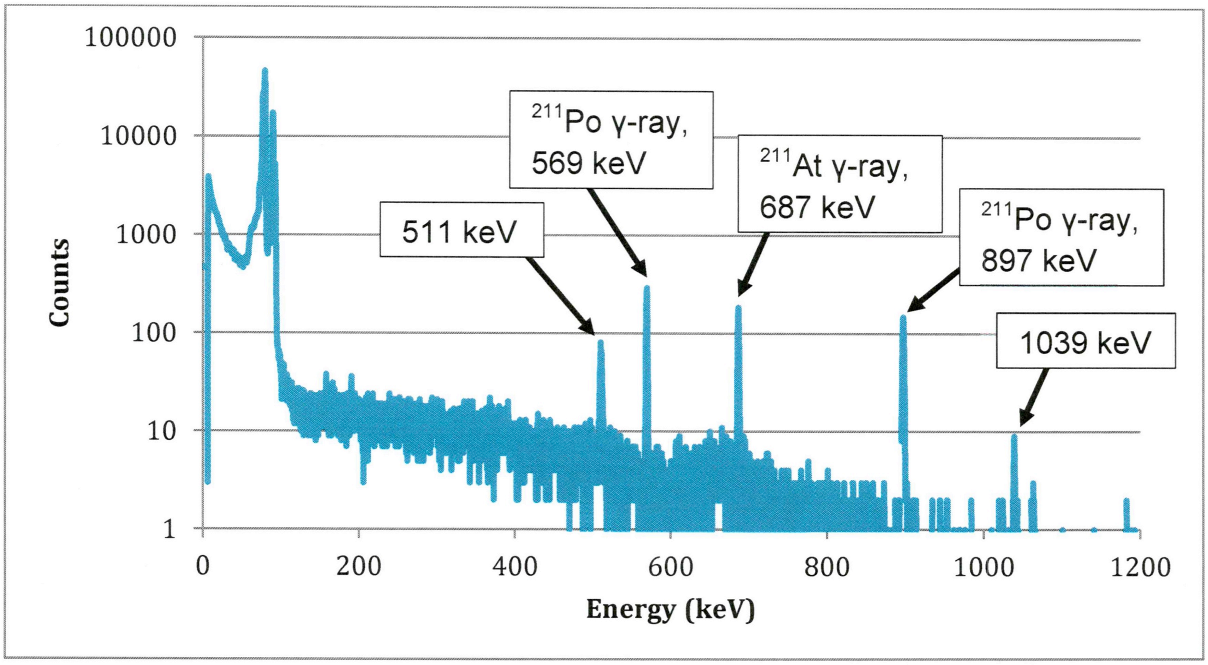

Fig. 3. HPGe spectrum of an aliquot of target dissolved solution, containing the characteristic gamma-rays from astatine-211 and its decay daughter polonium-211. The gamma-rays at 511 and 1039 keV merit further investigation.

[1] J. Elgqvist, S. Frost, J. Pouget, and P. Albertsson, Frontiers in Oncology **3**, 1 (2014).

[2] M.R. Zalutsky and M. Pruszynski, Curr. Radiopharm. **4**, 177 (2011).

[3] G.J. Kim *et al.*, *Progress in Research*, Cyclotron Institute, Texas A&M University (2016-2017), p. IV-5-8.

[4] G.J. Kim *et al.*, *Progress in Research*, Cyclotron Institute, Texas A&M University (2017-2018), p. IV-5-7.

[5] T.M. Martin, Ph.D. Thesis, Texas A&M University, 2017.

sCVD diamond detectors for the use in heavy-ion reactions

Z. Tobin, K. Hagel, A. Hannaman, A. Hood, A.B. McIntosh, R. Wada, A. Wakhle, and S.J. Yennello

Single-crystalline diamond detectors formed by chemical vapor deposition (sCVD) have received significant interest in high-energy nuclear physics as charged particle and neutron detectors due to high radiation hardness, fast response time, and good energy resolution (sub 1% for 5.5 MeV alpha particles) [1,2]. Near 100% charge collection has also been observed with these detectors [3]. These interesting physical properties make sCVD diamond detectors a good candidate for the use in low energy, heavy-ion reactions, particularly with high rates of incident radiation. ΔE-E telescope detectors are commonly implemented in heavy-ion reactions for the purpose of particle identification (PID). Cesaroni et al. have shown alpha particle identification using a prototype diamond telescope with an ^{241}Am source [4]. However, PID capabilities for diamond telescopes with $Z > 2$ have not been well established. It is the purpose of this work to investigate PID for $Z > 2$ with diamond telescope detectors in heavy-ion reactions.

To examine the suitability of these detectors in heavy-ion reactions, we have procured a Knopf B12 sCVD detector and a telescope detector with two sCVD diamond sensors from CIVIDEC Instrumentation GmbH. The B12 is 500 μm thick, with a sensitive area of 4.5 x 4.5 mm^2. The telescope detector has the following configuration: the transmission sensor (ΔE) is 20 μm thick and the stopping sensor (E) is 500 μm thick. Both sensors are 4 mm in diameter [5].

We investigated the performance of the Knopf B12 detector using CIVIDEC's Cx spectroscopic shaping amplifier by collecting ^{228}Th source and direct beam data. The energy resolution was approximately 1% for the 8.79 MeV alpha peak with the ^{228}Th source. We used a cocktail beam of ^{4}He, ^{12}C, and ^{16}O at 2.5 MeV/u in order to examine the detector's response to higher energy particles. Regardless of the particle identity, the response was linear with the energy deposited into the sensor (see discussion below on pulse height defect). We ran this beam at rates ranging from 10^3 to 10^8 pps (as determined on the Faraday cup) to observe the degradation of the detector's performance. We found that after an hour of an average of 10^7 pps on the detector, the energy resolution degraded by approximately 0.3 percentage points.

In a later experiment, the diamond telescope was tested for heavy-ion PID. With the telescope detector located at approximately 8 degrees from the beam axis, we ran a ^{20}Ne beam on ^{12}C target at 20 MeV/u. The signals were processed using two, single-channel model 1984 Canberra preamplifiers with Tennelec spectroscopic shaping amplifiers. In ^{228}Th source tests, the energy resolution on both sensors was near 1%.

Fig. 1 presents the ΔE vs E spectrum collected from this reaction. The spectrum shows clear elemental resolution, as well as isotopic resolution. Isotopic resolution was obtained for nuclei with Z less than or equal to magnesium. Isotopic resolution may also be present in the band for aluminum; however, it is difficult to identify any Al isotopes in this case due to the low number of counts in this region. The red circle on the left plot indicates the suspected peak for the elastically scattered beam (^{20}Ne). The energy calibration using the ^{228}Th source underestimates the location of this peak at 300 MeV with a linear fit. Using a calibration based on LISE calculations for punch-throughs, the location is now at

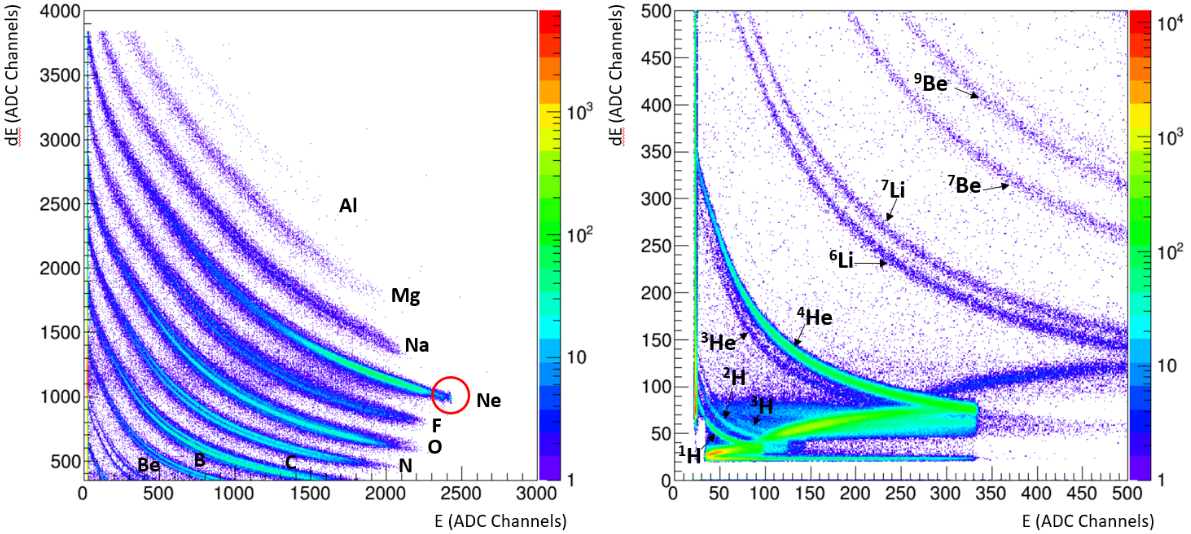

Fig. 1. dE vs E spectrum zoomed in at different locations. Left: The bands shown are identified as Be up to Al. Shown in the circle is Ne elastic peak (See text for further details). Right: Protons up to Be, the various isotopes of the lighter nuclei produced in this reaction are labelled as well.

approximately 350 MeV. However, the thicknesses of the sensors may not be exactly what is reported by the manufacturer, which may account for this. Additionally, these detectors have been reported to suffer significantly more from pulse height defects than Si detectors for high energy heavy ions [6]. This, of course, means that the detector response is not as linear as what we have observed with the lower energy beam on the B12 detector. Further analysis needs to be done in order to examine the effects of pulse-height defect in greater detail.

[1] L. Bani *et al.*, JINST, **13**, C01029 (2018).
[2] M. Pomorski *et al.*, Phys. Status Solidi. **202**, 2199 (2005).
[3] E. Berdermann *et al.*, Diam. Relat. Mater. **17**, 1159 (2008).
[4] S. Cesaroni *et al.*, Nucl. Instrum. Methods Phys. Res. **A947**, 162744 (2019).
[5] CIVIDEC Instrumentation GmbH, www.cividec.at, Austria
[6] O. Beliuskina *et al.*, Eur. Phys. J. A **53**, 12223 (2017).

Silicon characterization in preparation for measurement of ^{60}Fe photon strength function

A. Abbott,[1] M. Sorensen,[1] A.B. McIntosh,[1] E. Bennett,[1] A. Couture,[2] J. Gauthier,[1] K. Hagel,[1] S. Ota,[1] A. Simon,[3] and S.J. Yennello[1]
[1]*Cyclotron Institute, Texas A&M University, College Station, Texas 77843*
[2]*Los Alamos National Laboratory, Los Alamos, New Mexico 87545*
[3]*University of Notre Dame, Notre Dame, Indiana 46556*

^{60}Fe is a neutron-rich isotope of iron produced at a branch point in slow neutron capture (s-process) nucleosynthesis that holds astrophysical importance through the detection of its gamma rays in the interstellar medium. Despite its 2.5 million year half-life, it has been measured deep in the ocean crust [1], in Antarctic snow [2] and on the moon [3] indicating that this isotope is being actively produced in the nearby universe. The photon strength function (PSF) describes how probable the emission of a gamma ray would be from an excited state in a nucleus and is important for calculating neutron capture cross-sections [4]. By determining the PSF, we can place constraints on astrophysical models used to calculate the production and abundances of these neutron-rich isotopes produced in nucleosynthesis. An experiment has been proposed to measure the PSF for ^{60}Fe and testing of the experimental setup has begun.

For the measurement of the PSF we will use a beam of ^{59}Fe at 7.5 MeV/u separated using MARS and impinge it on a CD_2 target to produce ^{60}Fe in an excited state through a (d,pγ) reaction allowing us to mirror the direct neutron capture reaction. For the purpose of testing our experimental design and detector response, two test runs have been performed using a beam of ^{57}Fe at 7.5 MeV/u resulting in the ^{57}Fe(d,p)^{58}Fe reaction. In the first test run, an S3 annular silicon detector (wafer 2790-01), a CD_2 target, a PPAC and four BaF_2 detectors were used. The second test run added another 15 BaF_2 to the setup. A schematic of the second test run is shown in Fig. 1. For the purpose of this annual report, the performance of the silicon detector will be the focus.

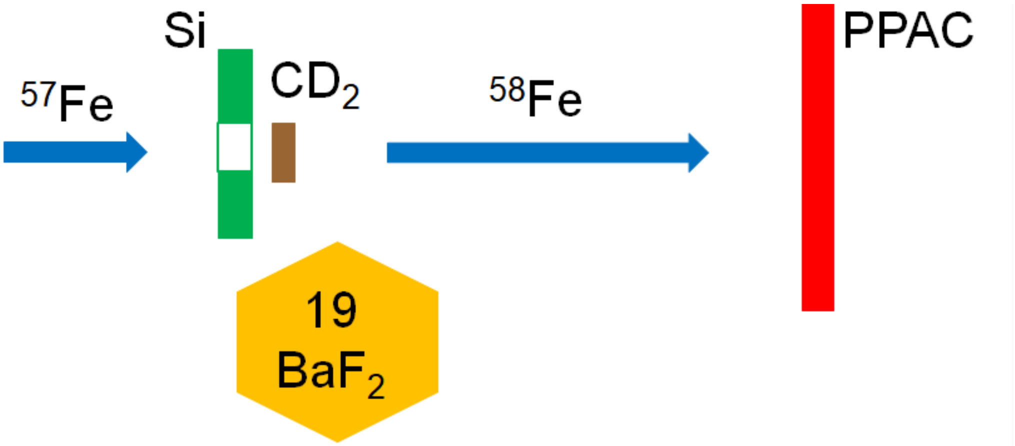

Fig. 1. Schematic of the test run setup.

The Micron S3 annular silicon detector serves to detect and measure the energy of the emitted proton from the (d,p) reaction. The 24 rings and 32 segments on the detector give position sensitivity which is used to calculate the excitation energy of the resulting ^{58}Fe nucleus. The detector covers the angular range of approximately 120-150 degrees. Fig. 2 shows the measured proton energies as a function of the angle of the emitted particle. The bands in the plot indicate specific states populated in the (d,p) reaction. This is then used to calculate the excitation energy of the nucleus as a function of the emitted proton angle which is shown in Fig. 3. This calculation currently only includes corrections due to the beam spot position on the target.

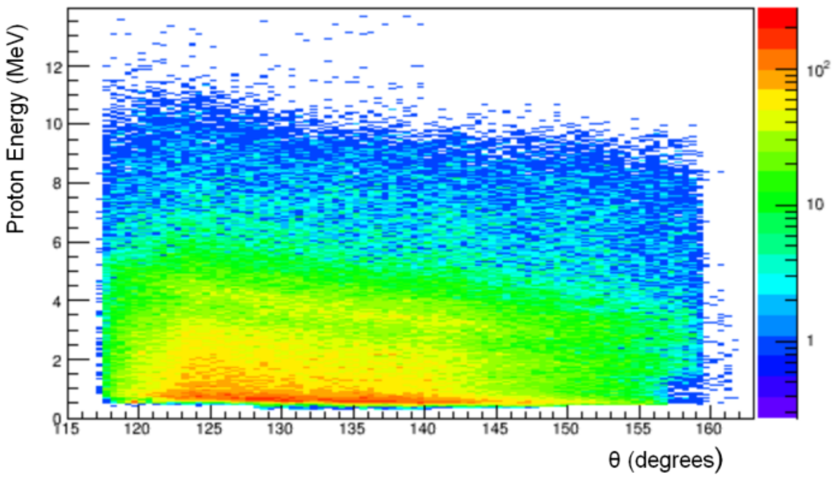

Fig. 2. Measured proton energy as a function of theta. The band indicates a particular excited state in ^{58}Fe.

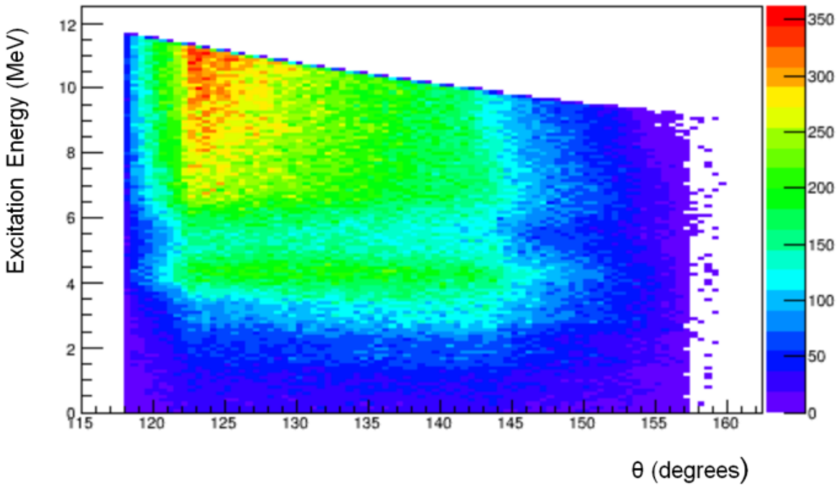

Fig. 3. Excitation energy of ^{58}Fe as a function of emitted proton angle.

We can take a projection of Fig. 3 and apply a multiplicity one and segment gate condition whereby we require only a single event to have occurred and take the ring spectra with respect to one particular segment that fired. This is plotted in Fig. 4. By doing so, hints of known states in ^{58}Fe are observed at 810 keV and 1674 keV, the first and second excited states. Corrections to the energy loss through the target are the next step in the analysis and are expected to improve the measured proton energies.

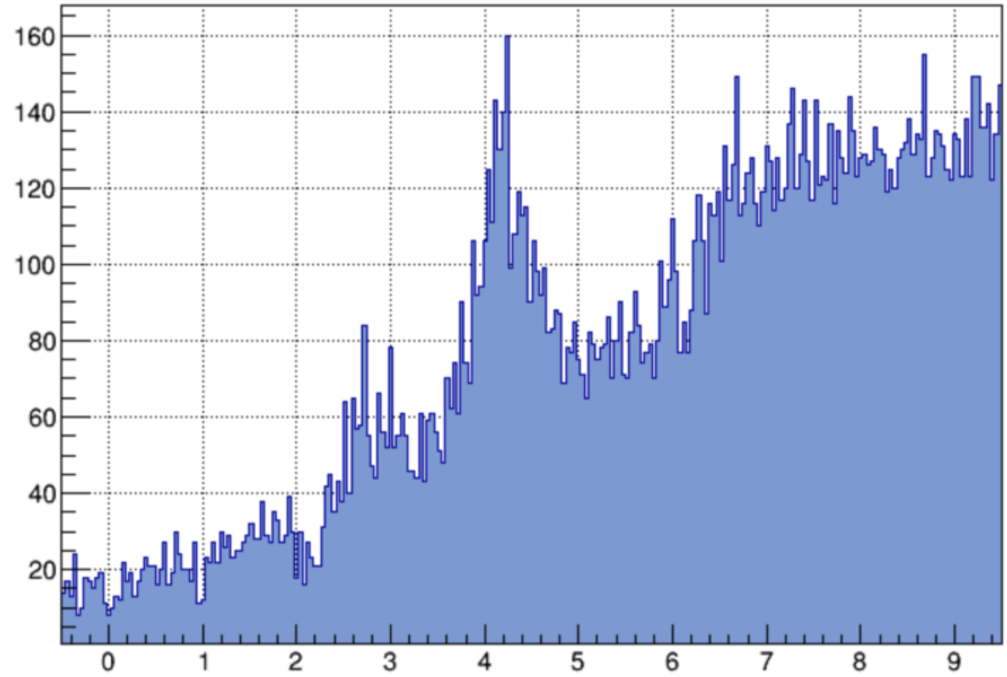

Fig. 4. Plot of the yield of calculated 58Fe residue excitation energy from the measured proton energy. Peaks in the 800 keV and 1600 keV range indicate the location of the first and second excited states of the nucleus.

[1] A.Wallner, J. Feige, N. Kinoshita *et al.*, Nature **532**, 69 (2016).
[2] D. Koll *et al.*, Phys. Rev. Lett. **123**, 072701 (2019).
[3] L. Fimiani *et al.*, Phys. Rev. Lett. **116**, 151104 (2016).
[4] M. Guttormsen *et al.*, PoS the 26th International Nuclear Physics Conference, 062 (2016).

Summed trigger analysis method for resistive dual-axis duo lateral position sensitive silicon detectors

A. Hannaman, M.W. Aslin, M.D. Youngs, A.B. McIntosh, K. Hagel, L.A. McIntosh,
R. Wada, and S.J. Yennello

Recently, the telescope detectors of FAUST have been upgraded with position sensitive silicon detectors that measure the position of incident particles through resistive charge splitting [1-3]. The Dual-Axis Duo-Lateral detector (DADL) provides excellent angular resolution while reducing the number of electronics channels necessitated if using double sided strip silicon detectors of similar resolution. However, conventional electronics yield position and energy non-linearities. This work presents a new waveform analysis method that significantly reduces these distortions.

The DADL detectors are 300 µm thick silicon diodes fabricated by Micron Semiconductor, each with a 20 mm x 20 mm active area as shown in Fig. 1(a) [4]. Vertical position information is obtained by measuring charge obtained at the contacts F1 (bottom) and F2 (top). Horizontal position information is obtained by measuring charge obtained at the contacts B1 (left) and B2 (right). The detector is reverse biased by applying -40 V to the front p-type face (F1 and F2). Ionizing radiation excites electrons that are attracted to the back face of the detector and the holes are attracted to the front face of the detector. These charge carriers then split due to the resistivity of each face and are collected on the contacts. Conductive strips are embedded on each face of the detector to promote the spreading of charge for complete charge collection at each contact. The measured charge on each contact is used to calculate the local position coordinates $X = c_x * (Q_{Right} - Q_{Left})/(Q_{Right} + Q_{Left})$ and $Y = c_y * (Q_{Top} - Q_{Bottom})/(Q_{Top} + Q_{Bottom})$. The total charge collected on a single face is proportional to the energy deposited in the detector $E = E_F \propto Q_{Bottom} + Q_{Top}$.

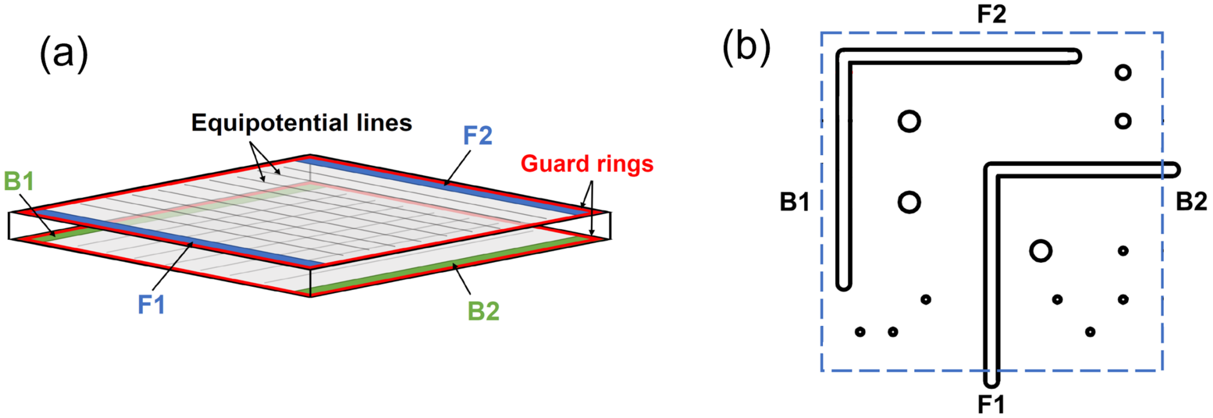

Fig. 1. (a) Schematic of a DADL detector. Charge is collected on the contacts F1 and F2 on the front face and B1 and B2 on the back face. The equipotential conductive lines help facilitate charge movement and the guard rings help to prevent charge bleeding. (b) Schematic of the brass mask with precision holes and slots. The dashed blue line marks the approximate position of the DADL detector behind the mask.

To test the performance characteristics of the DADL detector, a physical mask with precision slots and holes was constructed of 0.25-inch-thick brass whose dimensions are depicted in Fig. 1(b). This mask was placed 0.5 inches in front of the DADL detector to block incident radiation. A beam of 7.22 MeV/nucleon alpha particles was impinged on this detector configuration. The signals from the four contacts were sent to ZeptoSystems 45mV/MeV charge-sensitive preamplifiers and the resulting signals were digitized using a Struck SIS3316 waveform digitizer using 4 ns bins over 32 μs.

All waveforms from the four contacts from a single event are shown in Fig. 2(a). Waveform F1 clearly shows anomalous features, where it continues to rise over the entire range displayed. Additionally, the waveform does not have a fast-initial rise as expected, but instead dips below the baseline before rising as seen in Fig. 2(b). The inconsistent trigger timing that results from the range of observed waveform shapes ultimately leads to the distortions subsequently discussed. To approximate charge values like those obtained using conventional shaping electronics, each waveform was integrated for 0.25 us once the waveform reached a threshold of 300 channels above baseline as depicted in Fig. 2(c). This individual trigger analysis method gives position reconstruction that has severe pin-cushioning distortions as shown in Fig. 2(d). These distortions have been observed in previous experiments; however, the distortion is noticeably more severe in this work due to the short integration window and lack of shaping electronics [5].

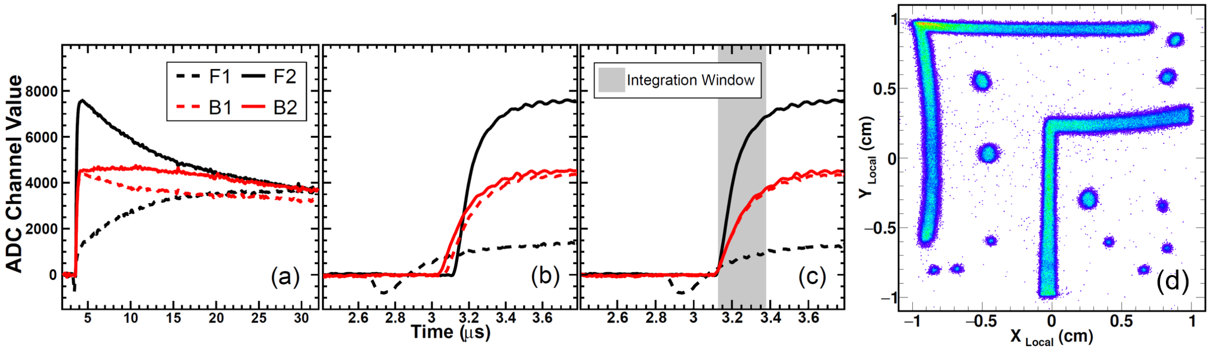

Fig. 2. Individual trigger analysis method. (a): Full 32 us length of baseline-corrected waveforms. (b): Same as (a) with time range to show initial rise. (c): Waveforms shifted so each reaches threshold at same time for demonstration purposes. Each waveform is integrated for 0.25 us (gray box). (d): Position plot using individual trigger method.

A new analysis method was developed that makes use of the fact that the distortions in the sum waveform of F1 + F2 (B1 + B2) are less severe than those seen in F1 and F2 (B1 and B2). To obtain the sum waveform, the individual waveforms needed to have the same absolute timing. The waveform digitizer records a time stamp of when each waveform is triggered. Each waveform was shifted in time by their respective differences in time stamps to that of F2 (arbitrarily chosen as reference) as shown in Fig. 3(b). The time-corrected waveforms for each face were then summed (F1+F2 and B1+B2), giving total energy signals as shown in Fig. 3(c). The integration start time for the individual waveforms (i.e. F1 and F2) was found by delaying the time that the respective summed waveform (i.e. F1+F2) reaches threshold by 0.6 us. The summed trigger analysis method yields considerable improvement in position reconstruction as seen in Fig. 3(d). Notice that the curvature and inconsistent strip widths seen using the individual trigger method are markedly improved.

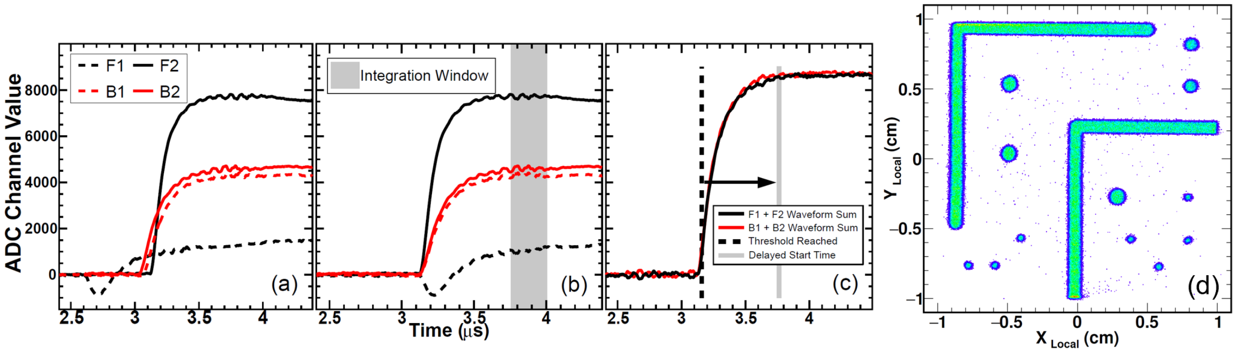

Fig. 3. Summed trigger analysis method. (a): Analogous to Fig. 2(b). (b): Waveforms have been shifted in time based on the 3316 digitizer time stamp relative to F2. (c): Sum of time shifted front (black) and back (red) waveforms. The time that the summed waveform reaches threshold (dashed line) is delayed by 0.6 us (gray line) and is used as the integration start time in panel (b). (d): Position plot using summed trigger method.

The improved linearity in position reconstruction using the summed trigger analysis method can be understood by a previous study that modelled DADL-type detectors [6]. In this work, it was found that there exist position dependent capacitively induced currents, which are the source of the inconsistent pulse shapes. As a result, there is an effective "settling time" that depends on the capacitance of the detector and the resistance relevant for any given position. By delaying the integration window past this settling time and measuring the charge for all contacts over the same time interval, these distortions are largely avoided.

[1] L.A. Heilborn, PhD thesis, Texas A&M University, 2018; http://hdl.handle.net/1969.1/174435.

[2] L.A. McIntosh *et al.,* Nucl. Instrum. Methods Phys. Res. **A** (Submitted).

[3] S.N. Soisson *et al.,* Nucl. Instrum. Methods Phys. Res., Sect. **A613**, 240 (2010).

YAP counting rate characterization

A.B. McIntosh and A. Abbott

Yttrium Aluminum Perovskite (YAP) scintillators are used in nuclear physics for their fast time response, and radiation hardness. They provide some pulse-shape discrimination and energy measurement. We are interested to use YAP coupled to a photomultiplier tube (PMT) as a zero-degree residue timing detector in an experiment to measure the photon strength function of ^{60}Fe and ^{58}Fe with (d,p) reactions. The YAP will see the full beam rate. For the ^{60}Fe measurement (secondary ^{59}Fe beam), we expect a rate of 2E5 particles per second. For the ^{58}Fe measurement (stable ^{57}Fe beam) the accelerator can easily provide 1E7 pps. We would like to use as much as possible, and at least 1E6 pps.

This report describes the testing of a single YAP crystal 1mm thick, ≈19 mm in diameter. The crystal was coupled with BC-630 optical grease to a Hamamatsu 1355 PMT. Voltage was supplied to the phototube electrodes with three active bases which utilize transistors to maintain the voltage on late-stage dynodes during high-rate operation. Active base #57 has a resistance from cathode to ground of 17 MOhm. Active bases #2 and #8 have 1 MOhm from cathode to ground. Each base is tested at a variety of cathode voltages. The ^{84}Kr @ 7.5 MeV/u beam was produced with the K150 cyclotron, and the beam intensity was varied. A plastic scintillator positioned away from the focal point was used to measure the relative beam rate without rate-saturating the plastic scintillator. The rate on the YAP for each beam intensity was measured.

Fig. 1 shows the rate measured on the YAP as a function of the rate measured on the plastic scintillator for five cathode voltages using base #8. For all settings, the YAP rate rises in proportion to the

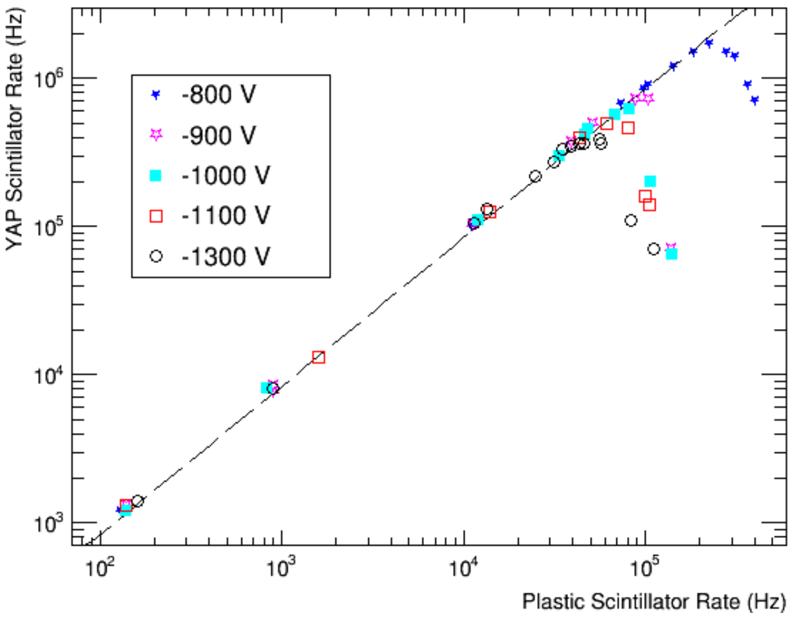

Fig. 1. Measured rate on YAP+PMT with low-resistance active base as a function of an independent detector rate proportional to the beam intensity. Lower voltage allows higher rate. The dashed line (a linear fit to the -800 V data with a y-intercept of zero) serves to guide the eye.

plastic rate until a maximum is reached, beyond which the YAP rate drops rapidly. A line with offset of 0 channels is plotted to guide the eye. For the highest cathode voltage (-1300 V), rate-saturation is reached earliest. As the cathode voltage is lowered, a higher rate is obtained before rate-saturation. At the lowest voltage (-800 V) a maximum rate of 1.7E6 pps was observed. Naturally, the pulses from the PMT become smaller as the voltage is lowered, but the rise time and fall time of the signals remain constant. At -700 V, signals from the anode were not observed.

The maximum rate observed on the YAP is plotted in Fig. 2 as a function of the cathode voltage for all three bases. For base #8, the rise in the rate with lower voltage is clear. This trend is perhaps reasonable considering that the base can only supply a certain current through the dynode chain and through the anode coupled with the fact that at lower voltage there is lower gain and thus lower current. For base #2, data was only collected at the lowest two voltages. The rates measured for #2 are similar to the rate measured for #8. The difference between #2 and #8 might be due to a difference in gain, but data at additional voltages would be needed to investigate this. Base #57 has a much lower saturation rate and does not significantly depend on the voltage in the range measured. The higher resistance in this base results in a lower current from the bias supply to the dynodes and thus the dynodes fail to maintain voltage at a moderate rate.

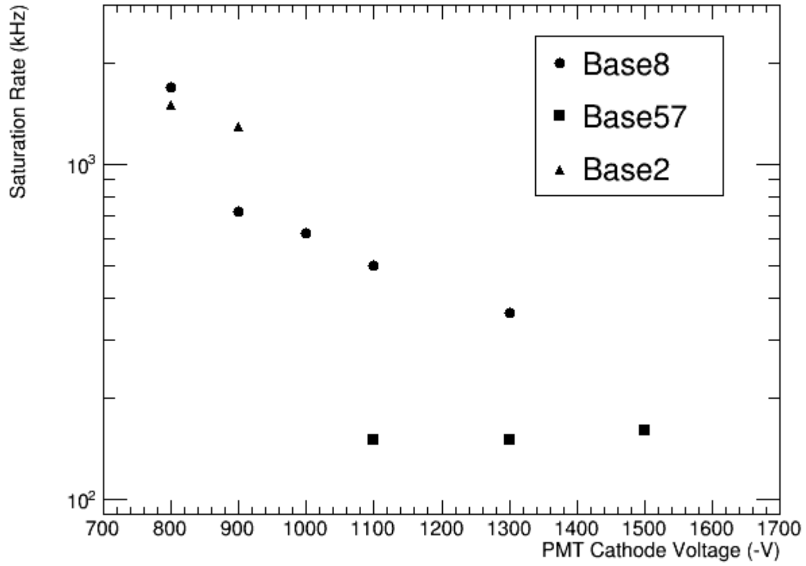

Fig. 2. Rate at which the YAP+PMT saturates as a function of voltage. Low resistance bases (#8 and #2, 1MOhm) achieve significantly higher rates than the higher resistance base (#57, 17MOhm).

The YAP itself shows no indication of degradation of performance at high rate. The low-resistance bases performed better than the high resistance base. (This is in agreement with the work of Ren et al. [1], but those authors use bases with much higher resistance, and thus get lower saturation rates.) Best performance, in terms of rate-saturation, was obtained at the lowest possible cathode voltage.

[1] P.P. Ren *et al.*, Nucl. Sci. Tech. **28**, 145 (2017).

Temperature and pressure monitoring for the AstroBox2 detector

A. Saastamoinen

Gas gain, especially in the exponential regime of a Micromegas, can be very sensitive to various changes in the detection medium such as gas impurity levels and gas density changes due to either pressure or temperature fluctuations. We have implemented multiple independent ways to track possible gain drift and to monitor the stability of the detector: (1) an α-source on an active side pad of the detector, (2) a separate chamber for a ~1 cm^2 Micromegas detector using ^{55}Fe X-ray source at the gas exhaust, (3) a pulser in the AstroBox electronics, and (4) possible strong decay branches of the species under study and devised methods for correcting these fluctuations [1].

Temperature related fluctuations are very evident in laboratory spaces without proper environmental controls such as in the high-bay area. Inside the experimental caves which are closed for the beam time, the temperature stabilizes relatively quickly during beam tuning and the remaining fluctuations are monitored during data taking. In the past these fluctuations during the beam time have washed out into the intrinsic detector resolution. However, during the latest runs in 2017 and 2019 we have observed quite strong fluctuations in the signal amplitudes of the sources used for monitoring as well as in the real data, all correlated with daily outside temperature variations. This is likely due to fact that there was an upgrade into the building air conditioning in general improving the cooling also inside the caves. On the other hand, some of the external cooling water circuit connected to the cave air handler heat exchanger are likely not well insulated outside the building enhancing the coupling to the outside air temperature.

Thus far we can only show the correlation between the daily weather data and that the signals track the changes outside the building but we have lacked actual temperature measurement other than a household thermometer and the temperature logging of the gas controller. However, the controller is heated by manufacturer's design to ensure steady mass flow through the controller but the gas lines and the detector are in the ambient room temperature.

To improve understanding of the origin of the drifting of the signals beyond just qualitative level and perhaps even to quantify the connection between actual gas temperature inside the detector setup we have designed and built a simple readout circuit to measure temperature with high precision thermistors (Omega instruments 44004, R = 2252 Ohm at 25C) and record the temperature event-by-event basis into the data stream. Fig. 1. shows the schematic of the circuit which is a very basic resistance readout powered with +6V NIM voltage from a preamplifier power supply. The thermistors are mounted into end of shielded 50 Ohm coaxial cables while the auxiliary resistors are housed inside a metal box. The box receives external NIM power via shielded cable and connects the ADC readout cables for each thermistor. The configuration in Fig. 1. allows recording of temperature from -10C to +100C, covering most of usable range of a 44004 thermistor as well as all realistic temperatures in the lab and in the setup. In addition, an old MKS 122 baratron was added into the detector setup for testing purposes to measure the actual pressure inside the detection volume (the MKS piPC99 gas controller pressure measurement is inside the unit itself). The output of the MKS 122 at 10V corresponds to 1000 torr pressure, allowing direct recording of pressure with an ADC capable of reading DC voltages (e.g. mesytec MADC32 as in this case).

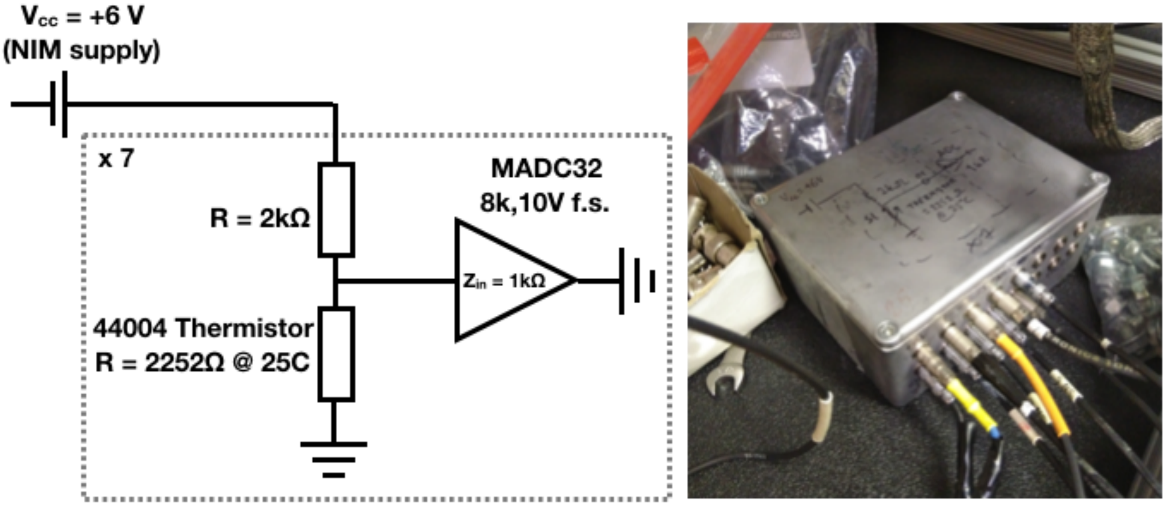

Fig. 1. Left: Schematic of a simple temperature measurement circuit to read thermistors resistances (therefore temperatures) from all over the detector setup and to record the values into the data stream event-by-event basis. Right: a photo of the metal box housing the readout circuit and connectors to connect external NIM power, thermistors and the cables to ADC. See text for details.

Fig. 2. shows an example of alpha source data and temperature reading from inside AstroBox2 detector collected of about two days test period in the high-bay lab. It is evident that the signals from a mixed ^{239}Pu, ^{241}Am, ^{244}Cm source do track the fluctuations in the gas temperature. In addition to the thermistor inside gas volume, pressure from the detector as well as temperature data from various parts of the setup and the room were recorded. In offline analysis these readings can be correlated roughly (to about few seconds) with the MKS piPC99 gas controller logs by using the controller timestamps and the

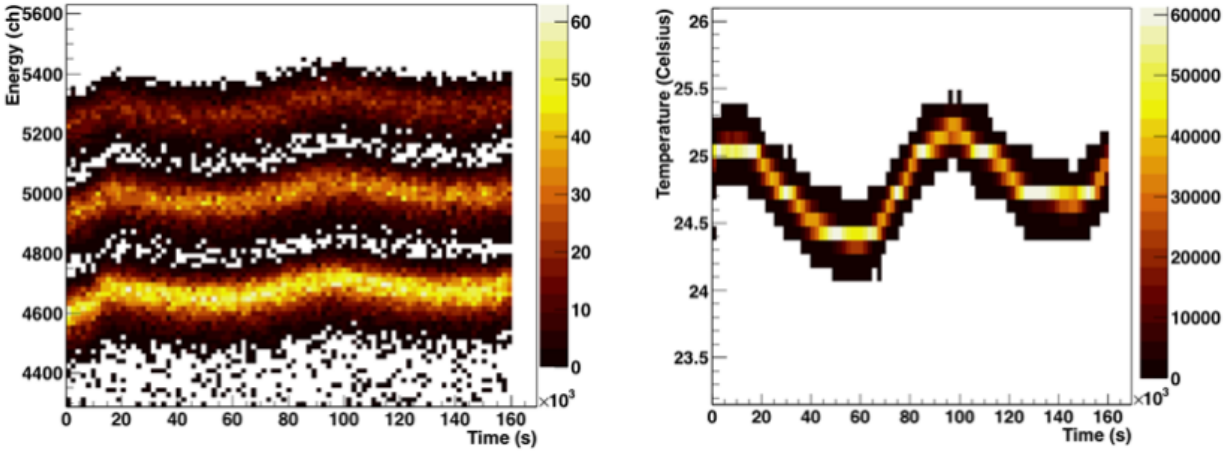

Fig. 2. Left: Signals from mixed ^{239}Pu, ^{241}Am, ^{244}Cm source versus setup timestamp since beginning of data collection (not real-time clock). Right: Calibrated Omega instruments 44004 thermistor reading from inside AstroBox2 chamber during the same time period as source data on left.

event real-time timestamps (reconstructed from the datafile opening unix timestamps and the clock time stamping each event in the data stream). Further testing and analysis of these environmental data and influence on the detector performance will resume once the situation with the ongoing pandemic allows.

[1] A. Saastamoinen *et al.*, Nucl. Instrum. Methods Phys. Res. **B463**, 251 (2020).

A novel approach to medical radioisotope production of ^{99}Mo using inverse kinematics

M.R.D. Rodrigues,[1] G.A. Souliotis,[2] A. Bonasera,[1,3] V.E. Iacob,[1] N. Nica,[1] B. Roeder,[1]
G. Tabacaru,[1] D. Scriven,[1] and J. Mabiala[4]
[1]*Cyclotron Institute, Texas A&M University, College Station, Texas*,
[2]*Laboratory of Physical Chemistry, National and Kapodistrian University of Athens, Greece*,
[3]*Laboratori Nazionali del Sud, INFN, Italy*,
[4]*Prairie View A&M University, Prairie View, Texas*.

A novel method for the production of important medical radioisotopes has been developed. The approach is based on performing the nuclear reaction in inverse kinematics, namely sending a heavy-ion beam of appropriate energy on a light target (e.g. ^{1}H, d, ^{3,4}He) and collecting the isotope of interest. A successful test of this concept was performed at Cyclotron Institute, Texas A&M University with the production of the theranostic radionuclide ^{67}Cu ($T_{1/2}$ = 62 h) through the reaction of a ^{70}Zn beam at 15 MeV/nucleon with a hydrogen gas target [1]. The ^{67}Cu radionuclide alongside other coproduced isotopes, was collected after the gas target on an aluminum catcher foil, them their γ-activity was measured off-line. Moreover, along with the production of the radionuclide of interest in inverse kinematics, additional radioisotopes can be generated by using the forward-focused neutrons from the reaction and allowing them to interact with a secondary target. The main requirement to obtain activities appropriate for preclinical studies is the development of high-intensity heavy-ion primary beams.

Pursuing the investigation of an alternative production method in inverse kinematics for isotopes that are important in nuclear medicine and are in high demand worldwide, where the production in reactors is not enough to supply the demand, the well-known ^{99}Mo/^{99m}Tc generator system [2] was the next goal. The ^{99m}Tc as a 140 keV γ-ray emitter (I_γ = 89%) with a half-life of $T_{1/2}$ = 6.01 h, is considered to be an ideal radiotracer and it is estimated to be used in approximately 85% of all nuclear medicine diagnostic scans worldwide [3]. The ^{99m}Tc is produced via β-decay of ^{99}Mo ($T_{1/2}$ = 65.94 h).

The ^{99}Mo was produced with a primary beam of ^{100}Mo accelerated by the K500 to an energy of 12 MeV/nucleon impinging on ^{4}He gas cell-target. The experiment took place at MARS recoil separator. The cryogenic gas-cell target has a length of 10 cm and has at the entrance and exit 4 μm thick, 19.0 mm diameter Havar windows. The target temperature was kept at T = 77 K during all the irradiations. The gas-cell target, the aluminum catcher foils and a Faraday cup to monitor the beam current, were set up in the MARS target chamber. A 127 μm thick aluminum catcher foil was mounted in a target frame with a 12.7 mm diameter hole and positioned after the gas-cell target. In order to measure the neutron yield produced during the irradiation, ten neutron detectors were positioned around the chamber. Three aluminum catcher foils were irradiated. The foils 1, 2, and 3 were irradiated for 12h, 13h, and 8h, with average current beam of 6 nA, 19 nA, and 16 nA and gas-cell pressures of 102, 213, and 1008 Torr, respectively. After 2.5 h of the end of irradiation, γ decay spectra of the foils were measured with HPGe detectors. Fig. 1 presents for instance a partial γ decay spectrum for foil 3. The foil was positioned at 50 mm from the detector and the spectrum was acquired for 16 h. The peaks associated with ^{99}Mo and the most intense impurities are indicated.

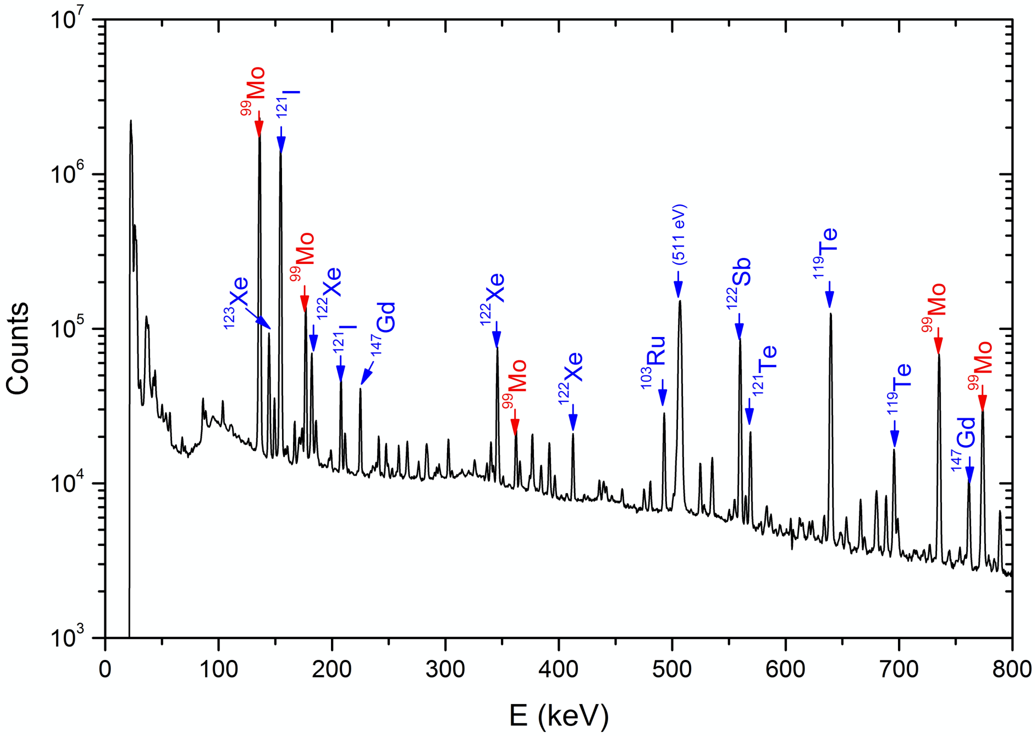

Fig. 1. Experimental γ decay spectra from foil 3.

As seen in Fig. 1, prominent γ peaks associated to the β-decay of ^{99}Mo and dominated by 140.5 keV (89.4% relative intensity) indicate that the reaction used has a good production of ^{99}Mo. The analysis is underway. The activity of ^{99}Mo and the impurities will be determined. The analysis of the neutron production will also be completed.

In addition to the ^{99}Mo production study from the ^{100}Mo + α reaction, a preliminary test was performed with the Ru isotopes production using MARS to separate the particle of interest. The MARS was tuned to optimize the focus of ^{100,99}Ru. The acquisition was done with an ΔE- E (55 and 500 μm) silicon detector telescope and the neutron detectors were put in coincidence with the MARS acquisition.

[1] G.A. Souliotis, M.R.D. Rodrigues, K. Wang, V. Iacob, N. Nica, B. Roeder, G. Tabacaru, M. Yu, P. Zanotti-Fregonara, and A. Bonasera, Appl. Radiat. Isot. **149**, 89 (2019).

[2] B. Wolterbeek *et al.*, J. Radioanal. Nucl. Chem. **302**, 773 (2014).

[3] OECD/NEA (2019), The Supply of Medical Isotopes: An Economic Diagnosis and Possible Solutions, OECD Publishing, Paris, https://doi.org/10.1787/9b326195-en.

A windowless supersonic gas jet target for basic research and applications at the Cyclotron Institute

M.R.D. Rodrigues[1] and A. Bonasera[1,2]
[1]*Cyclotron Institute, Texas A&M University, College Station, Texas*,
[2]*Laboratori Nazionali del Sud, INFN, Italy.*

The goal of the present project is to develop a portable supersonic gas jet target with cooling system. The target will be applied for Nuclear Physics studies at Cyclotron Institute and for plasma-laser experiments. The gas target system will be composed of a gas pulse valve, a nozzle, a skimmer and a catcher, with two differential pumping stages in a flow-through design feed from a compressed gas bottle. The valve will be cooled with a cooper jacket and the temperature will be controlled.

The target will be used in the development of research by our group: Medical radioisotope production using inverse kinematics, alpha cluster phenomenon on light and medium nuclei and plasma studies. The Medical radioisotope production using inverse kinematics research line pursues the investigation of an alternative production method for important isotopes for nuclear medicine in high demand worldwide, where the production in reactors are not enough to supply the demand. The production test of the radionuclide ^{67}Cu ($t_{1/2}$ =62h) with a beam of ^{70}Zn at 15MeV/nucleon produced by the K500 superconducting cyclotron on a hydrogen cell-target was already performed with success [1]. The well-known ^{99}Mo/^{99m}Tc generator system [2] was recently tested with a beam of ^{100}Mo at 12 MeV/nucleon on ^{4}He gas cell-target. In the short term, the next candidates for these studies are ^{47}Sc production, $^{44}\text{Ca} + \alpha \rightarrow {}^{47}\text{Sc} + p$, and an alternative production of ^{67}Cu, $^{70}\text{Zn}+d \rightarrow {}^{67}\text{Cu} + \alpha + n$. Note that, in the present experimental set-up the main source of radio impurities came from the interactions with the gas-cell windows. The implementation of a windowless supersonic gas jet target would improve considerably this problem besides the advantage of the high-density gas important for low cross section measurements.

Another project is the study of the experimental evolution of the a -cluster phenomenon on light and medium mass nuclei through (^{6}Li,d) transfer reactions. Data of the $^{12,13}\text{C}(^{6}\text{Li},d)^{16,17}\text{O}$ [3] and $^{9}\text{Be}(^{6}\text{Li},d)\,^{13}\text{C}$ reactions were measured in São Paulo. The a -d angular correlations applied to the reaction $^{12}\text{C}(^{6}\text{Li},d)^{16}\text{O} \rightarrow \alpha + {}^{12}\text{C}$ with $q_d = 0^o$ were performed at the Tandem- MAGNEX Large-Acceptance Spectrometer facility at LNS, INFN, Catania, Italy. The proposal is to perform measurements at TAMU using MDM spectrometer in inverse kinematics with the supersonic gas jet target. Applying ^{4}He and H_2 gas as target to study cluster phenomenon on light nuclei of C, O, N, F, and Ne where exist few experimental information on high exited stated near the clusters threshold.

Other studies, similar to the laser experiments at UT using the PW laser facility [4], will be performed using high intensity low energy ions from the Cyclotron ECR ion source. A systematic investigation of the beam range in a gas prepared near the critical point of the liquid-gas (LG) phase transition will be one of the applications of the gas-jet target.

In addition, the supersonic gas target can be a very important resource for the Cyclotron Institute Laboratory research program, in particular, for Astrophysics and exotic beam experiments where low background environment and high resolution are essential.

In order to have efficiency in low cross-section reactions induced by limited beam intensities and achieve high resolution measurements, the target should present: an optimized balance of target nucleus number density and thickness to maximize count rates but minimize reaction product energy loss and straggling, target size close to the beam spot and be chemically pure.

For light target isotopes, necessary in inverse kinematics, these properties are difficult to be produced. Solid targets, usually plastic thin-foils, degrades with exposure to beam and introduces unwanted contaminants. Gas targets with windows also introduces unwanted contaminations, besides the energy loss and the straggling. In addition, if the gas is static there are the degradation and the non-uniform heating due to interaction with beam. A supersonic gas jet target provides a spatially well-defined high density target using high purity gas, allowing a better efficiency production and a high resolution measurement. Other advantage of the target being well-defined spatially is the possibility of set up silicon detectors, γ-ray detectors, and heavy ion detectors to measure reaction products in the region around the jet. In addition, a cluster jet target has a high uniformity at long distance of the nozzle.

The present project has the aim to develop a supersonic gas jet target with cooling system that can be used as a supersonic gas jet target or a cluster jet target according with the experiment requirement. The portability of the gas jet target is also important in order to allow its use in different experimental lines of the Laboratory or used for plasma-laser experiments.

The main components for design a supersonic gas jet system are: the valve, the nozzle, the gas beam catcher and the vacuum pumping requirements. In particular, for experiments where cluster jet is required the cooling system is essential. In some situations, when cluster gas beams are used, the gas beam skimmer is also extremely important when low pressure is desired in the gas target chamber.

In the present project the system will use the Cryogenic Copper (Ni \Ti. Ni. plated) HRR, Even-Lavie valve [5] with the respective electronic driver. Initially the Trumpet shape, ~125μØ hole (43° cone) nozzle will be tested and afterwards, different shape and diameter nozzles will be produced locally and tested. The valve will be cooled with a cooper jacket and the temperature will be measured and controlled with the 325 Temperature Controller and DT-670 Silicon Diode from Lakeshore Cryotronics together with two resistors heaters. A flow-through design will be used, where the pulse valve will be feed from a compressed gas bottle. Pressure diagnosis, needle and relieve valves will be used in the gas line for control and safety purposes. The precooled gas is expanded through the nozzle. A skimmer transfers the central part of the beam into the first differential pumping stage, a second skimmer serves as collimator which limits the divergence of the beam. The cluster beam arrives in the scattering region and afterwards the beam is absorber in the catcher in a second differentially pumped stage. The distance and shape of the skimmer and the catcher need to be tested for each experiment requirement.

[1] G.A. Souliotis, M.R.D. Rodrigues, K. Wang, V. Iacob, N. Nica, B. Roeder, G. Tabacaru, M. Yu, P. Zanotti-Fregonara, and A. Bonasera, Appl. Radiat. Isot. **149**, 89 (2019).
[2] B. Wolterbeek *et al.,* J. Radioanal. Nucl. Chem. **302**, 773 (2014).
[3] M.R.D. Rodrigues *et al.*, Phys. Rev. C **89**, 024306 (2014).
[4] G. Zhang *et al.*, Phys. Lett. A **381**, 1682 (2017).
[5] U. Even, Eur. Phys. J. TI **2**, 17 (2015).

Extraction and separation of iridium(IV) and rhodium(III) from hydrochloric acid media by a quaternary ammonium-based hydrophobic eutectic solvent

V. Zakusilova,[1,2] G. Zante,[1,3] E.E. Tereshatov,[2] C.M. Folden III,[2,4] and M. Boltoeva[1]
[1]*Université de Strasbourg, CNRS, IPHC, UMR 7178, F-67000 Strasbourg, France*
[2]*Cyclotron Institute, Texas A&M University, College Station, Texas 77843*
[3]*ADEME, 20 Avenue du Grésillé, 49004 Angers Cédex 01, France*
[4]*Department of Chemistry, Texas A&M University, College Station, Texas 77843*

The main goal of green chemistry is to reduce the hazardous environmental impact of solvents used in chemical production, including extraction and separation of analytes [1]. Over the past twenty years, a new type of solvents called eutectic solvents were actively being developed. Alternative solvents should be more environmentally friendly, less toxic and non-flammable compared to conventional molecular solvents. Ideally, they should also be less expensive, easy to prepare and biodegradable. Moreover, eutectic solvents can be recycled owing to their low vapor pressure. For these reasons, they are also called “green solvents” [2].

To date, the majority of published investigations are devoted to the utilization of hydrophilic eutectic solvents. In contrast, hydrophobic eutectic solvents have attracted attention only recently due to their effective extraction of metal ions from aqueous solutions [3-5].

Currently, the demand for platinum group metals (PGMs) is increasing due to the shift in the global energy sector towards low-carbon-emission technologies and renewable energy sources [6]. In addition, mining of these metals and their application in a number of industries leads to significant pollution of the environment, endangering people’s health [7]. Thus, their recycling is crucial from both the ecological and economical points of view. The focus of our work is to find a greener way to extract two PGMs, namely iridium (Ir) and rhodium (Rh), from HCl solutions. These metals’ similar chemical behavior and the existence of multiple metallic species in chloride solutions make their separation a challenging task.

We studied the extraction performance of a hydrophobic eutectic solvent composed of a quaternary ammonium salt and a fatty acid, namely tetraheptylammonium chloride and decanoic acid (C10:0) in a 1:2 molar ratio; this ratio was chosen based on literature data [3]. This is the first time that this eutectic solvent has been used for extraction and separation of PGMs. The effects of the main experimental factors (HCl concentration and initial metal concentration in the aqueous phase) on the extraction behavior of Ir(IV) and Rh(III) have been investigated. Concentrations of metals in the aqueous phase before and after extraction were analyzed by inductively coupled plasma mass spectrometry (ICP-MS).

Solvent extraction trials were performed by mixing 0.1 g of the synthesized eutectic solvent with 1.5 mL of an aqueous phase (volume ratio of aqueous to organic phase, $V_{aq}/V_{org} = 13.4$). This choice was made based on the significant extraction of Ir(IV) with a distribution ratio (D) value around 10 under such experimental conditions. In the described experiment the initial metal concentration for Ir(IV) was 5.2×10^{-4} M in 0.4 M HCl solution [initial metal concentrations for ultraviolet-visible (UV-Vis) analysis (discussed below) and acidity dependency test were different].

The extraction equilibrium for both metals is reached within 1 min of shaking. However, to simplify technical conditions of the performed experiments and minimize any discrepancies associated with short time of phase contact, in all solvent extraction experiments the shaking time was extended to 30 min.

The highest D values represented in Fig. 1 were obtained at 0.04 M HCl, reaching ~60 and ~10 for Ir(IV) and Rh(III), respectively. High D values for Ir(IV) and low D values for Rh(III) indicate that the preceding eutectic solvent is efficient for Ir(IV)/Rh(III) separation. The highest Ir(IV) and Rh(III) separation factor K_{sep} (which is a ratio of corresponding D values) at a level of ~20 was obtained at ~0.4 M HCl as shown in Fig. 2.

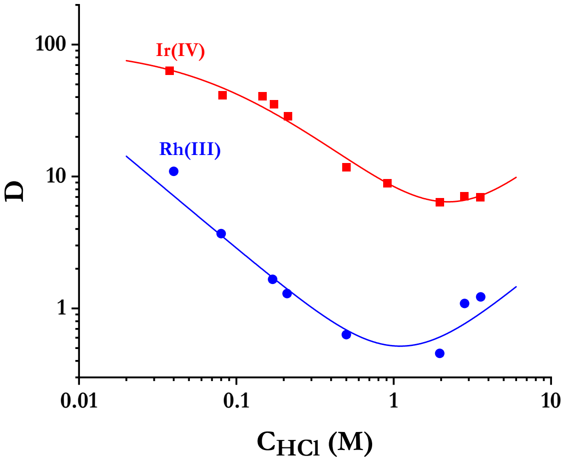

Fig. 1. Distribution ratio variation for Ir(IV) and Rh(III) as a function of the initial HCl concentration in the aqueous phase. $[Ir]_{init,aq} = 5.2\times10^{-5}$ M, $[Rh]_{init,aq} = 9.7\times10^{-5}$ M, $V_{aq}/V_{org} = 13.4$. The lines are drawn to guide the eye.

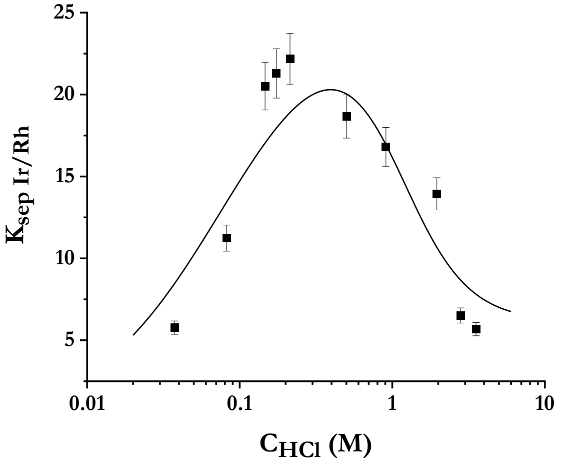

Fig. 2 Separation factor of Ir(IV) and Rh(III) as a function of the initial HCl concentration in the aqueous phase. $[Ir]_{init, aq} = 5.2\times10^{-5}$ M, $[Rh]_{init, aq} = 9.7\times10^{-5}$ M. $V_{aq}/V_{org} = 13.4$. The line is drawn to guide the eye.

Results of UV-Vis spectroscopy displayed in Fig. 3 provide insight on the Ir(IV) speciation in HCl solutions. Observation of distinct characteristic peaks for $[IrCl_6]^{2-}$ complexes at 433 nm and 488 nm leads to the conclusion that the major extracted species is a doubly charged complex $[IrCl_6]^{2-}$ in the entire HCl concentration range.

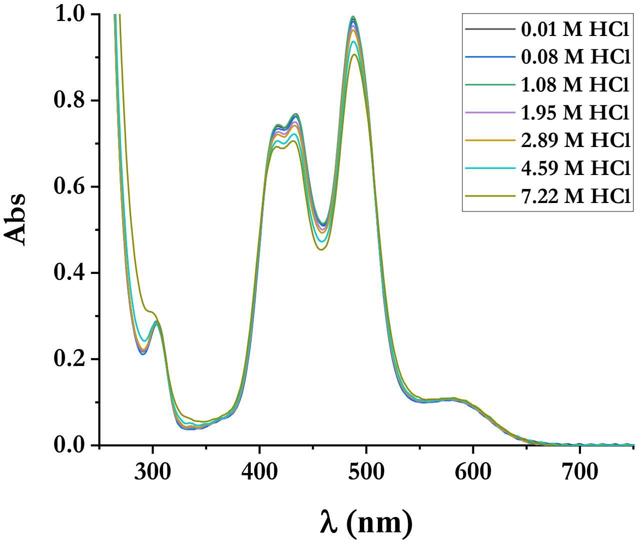

Fig. 3. Selected experimental UV-Vis absorption spectra of $[IrCl_6]^{2-}$ complexes at different HCl concentrations. $[IrCl_6]^{2-} = 2.6 \cdot 10^{-4}$ M.

The impact of the metal loading on the extraction yield is shown in Fig. 4. The results indicate that while the initial Ir(IV) concentration in the aqueous phase increases, D values decrease. This is most

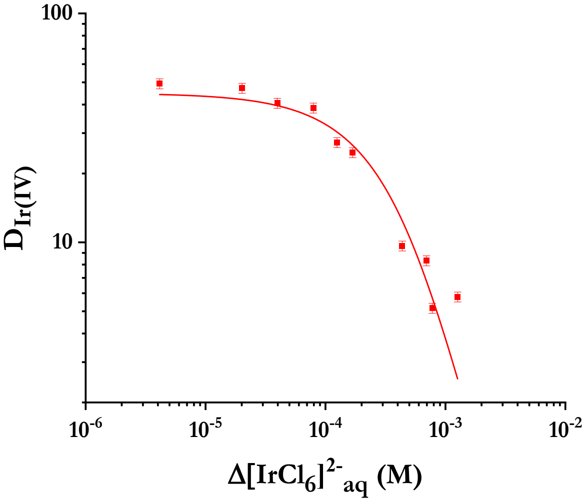

Fig. 4. Distribution ratio variation for Ir(IV) as a function of complex concentration difference in the aqueous phase before and after extraction.

likely due to the limited capacity of the organic phase. The most efficient extraction (D_{Ir}~50) was observed for 5.2×10^{-6} M Ir(IV) solution at 0.12 M HCl.

We developed a mathematical model to fit the experimental data illustrated in Fig. 4. This model is based on the comparison of two possible mechanisms of Ir(IV) extraction: ion pair formation (the corresponding extraction constant is K_{ip}) and ion exchange (the corresponding extraction constant is K_{ie}).

A high value of $R^2=0.864$ shows a good quality of the fit and confirms that the major extracted species is a doubly charged complex $[IrCl_6]^{2-}$. Results of this independent method are in good agreement with those obtained by UV-Vis analysis.

The comparison of the extraction constants (K_{ip} and K_{ie}) from the developed mathematical model testifies that the predominant mechanism of extraction is ion pair formation between $[IrCl_6]^{2-}$ and $[N_{7777}]^+$, while ion exchange is a negligible process:
$K_{ip} = (1.1 \pm 0.4)\times10^8$ and $K_{ie} = (1.8 \pm 0.4)\times10^{-5}$. The mathematical model also allowed us to estimate the conditional constant of the eutectic solubility product: $K_{sp} = (3.6 \pm 0.9)\times10^{-7}$.

A publication based on these results is in the late stages of preparation.

[1] M. Francisco *et al.*, Angew. Chem. Int. Ed. **52**, 3074 (2013). doi: 10.1002/anie.201207548

[2] B. Tang *et al.*, J. Sep. Sci. **38**, 1053 (2015). doi: 10.1002/jssc.201401347

[3] D.J.G.P. van Osch *et al.*, Green Chem. **17**, 4518 (2015). doi: 10.1039/c5gc01451d

[4] D.J.G.P. van Osch *et al.*, Chem. Commun. **52**, 11987 (2016). doi: 10.1039/c6cc06105b

[5] E.E. Tereshatov *et al.*, Green Chem. **18**, 4616 (2016). doi: 10.1039/c5gc03080c

[6] L. Grandell *et al.*, Renew. Energy **95**, 53 (2016). doi: 10.1016/j.renene.2016.03.102

[7] S.J.L. Linde *et al.*, Chem. Res. Toxicol. **30**, 1778 (2017). doi: 10.1021/acs.chemrestox.7b00184

Separating super-grade plutonium for forensic analysis

K.J. Glennon,[1,2,3] E.M. Bond,[3] T.A. Bredeweg,[3] S.S. Chirayath,[4,5] and C.M. Folden III[1,2]
[1]*Department of Chemistry, Texas A&M University, College Station, Texas 77843*
[2]*Cyclotron Institute, Texas A&M University, College Station, Texas 77843*
[3]*Nuclear and Radiochemistry, Los Alamos National Laboratory, Los Alamos, New Mexico 87545*
[4]*Center for Nuclear and Security Science and Policy Initiatives, Texas A&M University, College Station, Texas 77843*
[5]*Department of Nuclear Engineering, Texas A&M University, College Station, Texas 77843*

Discriminating the origin of special nuclear material (SNM) such as Pu and ^{233,235}U is of key importance in the field of pre-detonation nuclear forensics. Discriminating the irradiation conditions under which proliferated Pu material was produced can help lead intelligence officials to the source of such proliferated material. One Pu discrimination technique previously investigated by our group is a maximum likelihood methodology which compares a set of measured fission product (FP) isotope ratios in unidentified Pu material to a set of simulated FP isotope ratios produced under a variety of reactor conditions [1,2]. The use of FP isotope ratios in addition to Pu isotope ratios allows this discrimination approach to distinguish between many reactor types over a large range of fuel burnups without considering assumptions about the material's origin. Our previous study suggested that at least 5 g of PUREX separated Pu would be necessary to contain a sufficient mass of the FPs for analysis [3].

Recently, four samples of super-grade Pu between 4 – 60 mg have been used to develop a chemical methodology to isolate and concentrate the FP elements of interest for maximum likelihood reactor-type discrimination. The four samples of Pu were dissolved in 8 M HNO_3 and loaded onto an anion exchange column to retain Pu^{IV} while U, Cs, Ba, and the rare-earth elements (REEs) eluted. The U was isolated into its own fraction at this step; the Cs, Ba, and REEs were further separated in concentrated HNO_3 using a cation exchange column to isolate the REEs. Cs and Ba were then isolated into their own fractions using a Sr specific extraction chromatography resin (SR Resin by Eichrom) in 1 and 0.1 M HNO_3. Fig. 1 describes the isolation of these elements into their own fractions with their reported yields. In general, the FP elements were recovered with excellent yields greater than 80%. This procedure was shown to recover quantities of FP elements as low as 10^{-10} g from the 60 mg sample of Pu. A previous characterization of irradiated UO_2 material [4] suggests that 5 g of PUREX separated weapons-grade Pu discharged at a burnup of 1 GWd/MTU would contain at least 10^{-10} g of most FPs of interest, indicating that this chemical methodology may be sufficient to isolate and measure FP isotope ratios in large samples of PUREX separated Pu.

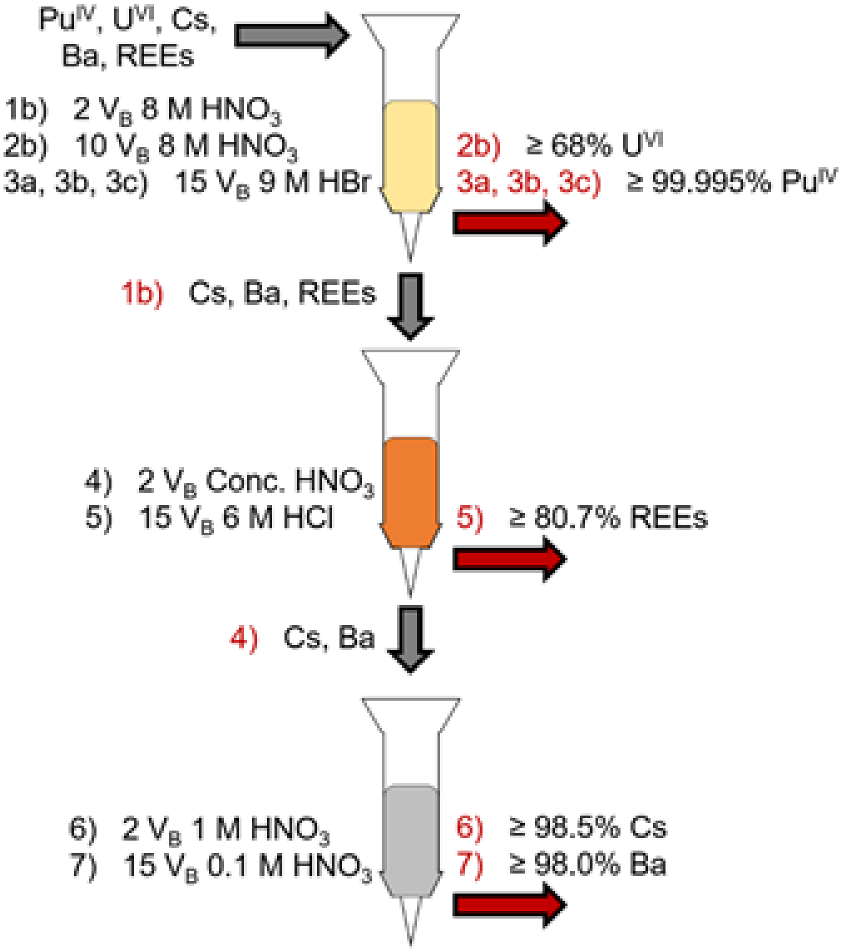

Fig. 1. Chromatography separations of the four Pu samples to isolate select FP elements. The first column used anion exchange resin (yellow), the second cation exchange resin (orange), and the third SR resin by Eichrom (gray).

[1] J.M. Osborn, K.J. Glennon, E.D. Kitcher, J.D. Burns, C.M. Folden III, and S.S. Chirayath, Nucl. Eng. Technol. **51**, 384 (2019). doi:10.1016/j.net.2018.11.003

[2] J.M. Osborn, E.D. Kitcher, J.D. Burns, C.M. Folden III, and S.S. Chirayath, Nucl. Technol. **201**, 1 (2018), doi:10.1080/00295450.2017.1401442

[3] K.J. Glennon, J.M. Osborn, J.D. Burns, E.D. Kitcher, S.S. Chirayath, and C.M. Folden III, J. Radioanal. Nucl. Chem. **320**, 405 (2019). doi:10.1007/s10967-019-06486-w

[4] J.M. Osborn, K.J. Glennon, E.D. Kitcher, J.D. Burns, C.M. Folden III, and S.S. Chirayath, Nucl. Eng. Technol. **50**, 820 (2019). doi:10.1016/j.net.2018.04.017

Development of the control system for TAMUTRAP: characterizing dampening effects in mass measurements of alkali ions

M. Nasser, G. Chubarian, V.E. Iacob, V.S. Kolhinen, D. McClain, D. Melconian, A. Ozmetin,
B. Schroeder, and P.D. Shidling

As reported last year [1], a number of software systems have been created for TAMUTRAP to improve flexibility and control of the beamlines, RFQ and Penning trap: the Scan Automation System (SAS), Python-Pulsing Software (P2S) and Time-Of-Flight Fitter and Integrator (TOFFI) have all contributed to the operation of TAMUTRAP's system and improved the mass measurements used to commission the Penning trap. Here we describe some improvements that have been developed as these control systems have evolved and new measurement techniques are pursued at TAMUTRAP.

One example of how the control software has required updating is to allow us to pursue a new (more sensitive) approach to mass measurements. The Ramsey method of oscillatory fields [2], described elsewhere in this report [3], has a more complex excitation pattern with a corresponding frequency scan exhibiting a different structure compared to the regular TOF-ICR technique. The Ramsey method has required SAS and P2S to be expanded to include the ability to add the extra excitations, and TOFFI had to be adapted to perform the fit to the more sinusoidal frequency scan.

Another example of how the control system has been upgraded to accommodate the developing TAMUTRAP program is the one-trap purification scheme, also described elsewhere in this report [4]. Although in this case the frequency scan is the regular TOF-ICR resonance curve (so TOFFI did not need alteration), again the excitation pattern is lengthier and more complicated, requiring SAS and P2S to be re-written to allow for this purification scheme.

Perhaps the most significant improvement, however, is the inclusion of dampening in the model used by TOFFI to fit the resonance scans taken at TAMUTRAP. The data plotted in the top panel of Fig. 1 exhibits a clear attenuation of the fringe pattern expected from a resonance scan. This is attributed to the finite vacuum from residual buffer-gas in the Penning trap from the RFQ (which in this case was operated at an atypically high pressure). As can be seen from the fit in Fig. 1, the reduced χ^2 is dramatically reduced when including the dampening term compared to when it is neglected. It is worth noting that since we adopt the PDG approach of scaling measurement uncertainties by $\sqrt{\chi^2/\mathrm{dof}}$, this has led to mass measurements which are as much as 4× more precise. The model of dampening implemented into TOFFI suggests a linear relationship between the pressure in the trap and the dampening parameter, γ. We have confirmed this with resonance scans at pressures of $(1–7)\times10^{-7}$ mbar and, as the bottom plot of Fig. 1 shows, we do indeed see a linear dependence.

As we develop more and more offline techniques to improve control and efficiency of the TAMUTRAP facility (beamlines, RFQ and Penning trap), the control system is being developed to allow for all upgrades. Near-term goals are to better quantify the dampening parameter, and a more complete automated logging of parameters and settings when frequency scans are performed.

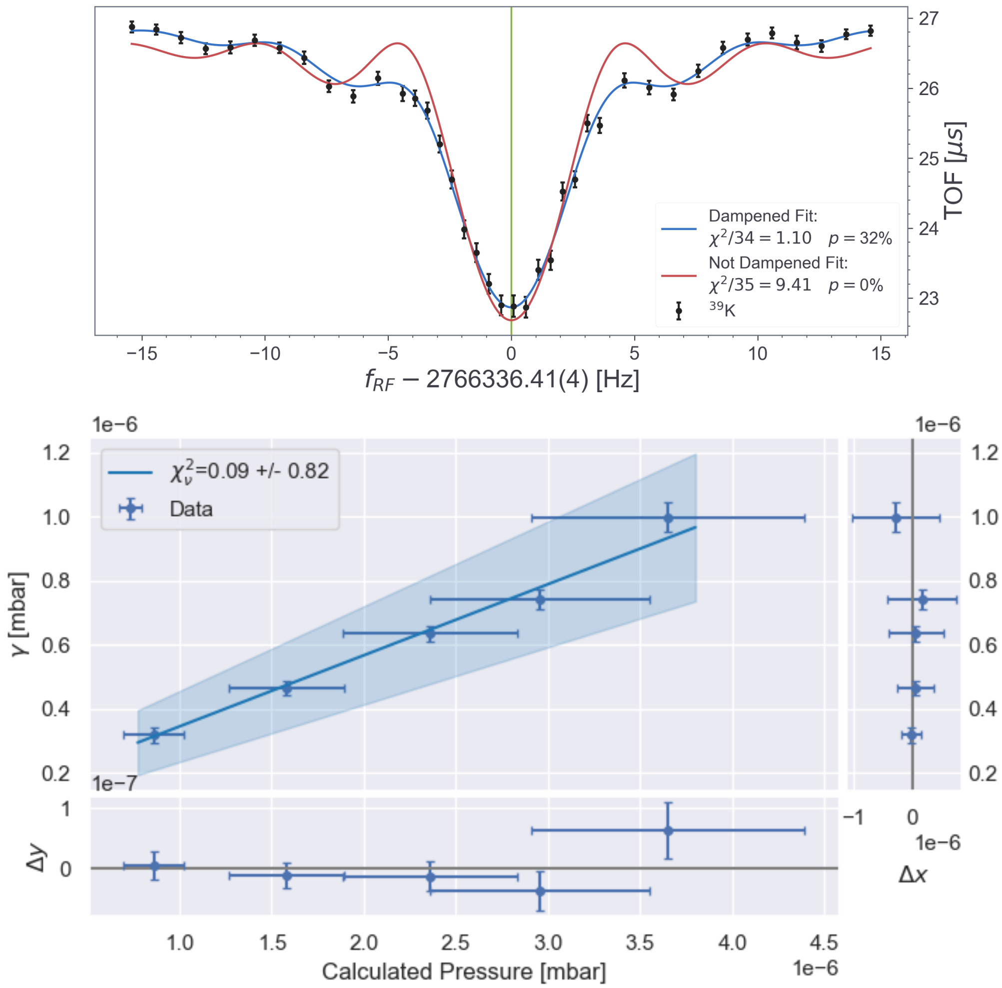

Fig. 1. Top panel: fits to a ^{39}K resonance scan with and without dampening included when the pressure in the trap was 3.7×10^{-7} mbar. Bottom panel: the fit dampening parameter, γ, as a function of pressure in the trap, showing the expected linear relationship.

[1] M. Nasser *et al.*, *Progress in Research*, Cyclotron Institute, Texas A&M University (2018-2019) p. IV-44.

[2] S. George *et al.*, Phys. Rev. Lett. **98**, 162501 (2007).

[3] V.S. Kolhinen *et al.*, *Progress in Research*, Cyclotron Institute, Texas A&M University (2019-2020) p. IV-90.

[4] V.S. Kolhinen *et al.*, *Progress in Research*, Cyclotron Institute, Texas A&M University (2019-2020) p. IV-98.

Implementing a Ramsey-type excitation to TAMUTRAP

V.S. Kolhinen, V.E. Iacob, D. McClain, D. Melconian, M. Nasser, A. Ozmetin,
B. Schroeder, and P.D. Shidling

We have implemented a Ramsey-type excitation [1] Time-of-Flight Ion-Cyclotron-Resonance (TOF-ICR) scheme to TAMUTRAP-Penning trap [2,3]. In principle, it works in the same way as a conventional single fringe excitation [4] pattern where one measures the flight time of ions from the Penning trap to a microchannel plate detector (MCP) as a function of the quadrupole excitation frequency near the cyclotron frequency, $f_C=1/(2\pi)qB/m$.

In TOF-ICR method a small number of ions are injected into a Penning trap, cooled so that they remain in the center of the trap, and excited with a dipole excitation at magnetron frequency (f_-) for a certain period of time to increase the radius of the magnetron orbit. A subsequent quadrupole excitation at cyclotron frequency (f_C) is then applied for a certain time and amplitude to convert the low-frequency magnetron motion to the high-frequency reduced cyclotron motion. Due to the change in the rotation frequency the radial energy of ions increases which leads to a stronger axial acceleration of ions in the decreasing gradient of the magnetic field after they are extracted from the Penning trap. This results in shorter TOF of ions from the trap to an MCP detector.

In a conventional excitation scheme, one applies one continuous excitation pattern, while in a Ramsey-type excitation one uses two time-separated fringes. Fig. 1 shows the timing pattern for the one trap cycle in a Ramsey-type TOF measurement.

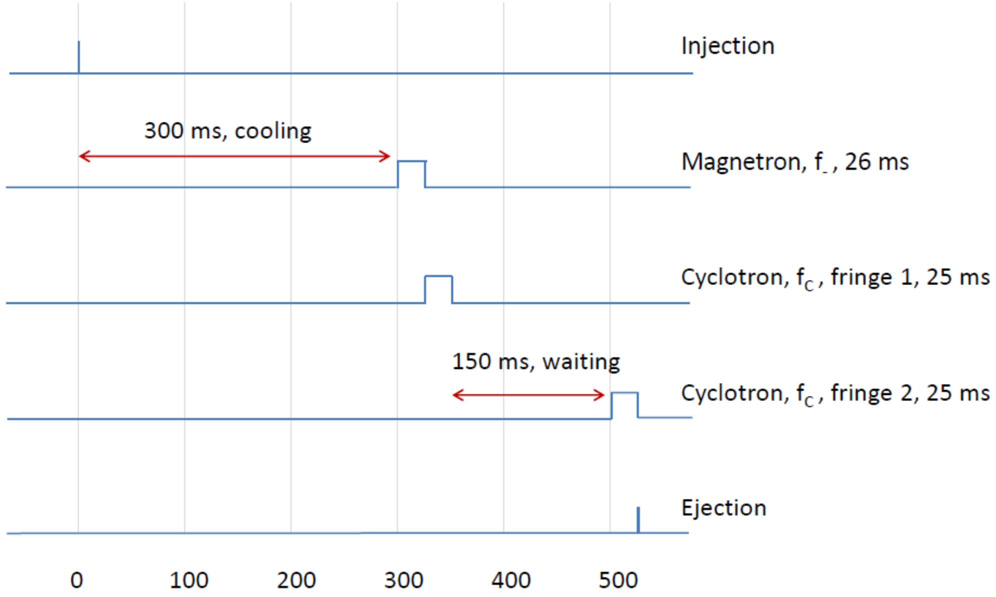

Fig. 1. Timing pattern used in a Ramsey-type excitation test at TAMUTRAP. The scale of the horizontal axis is ms.

A first step towards the implementation of Ramsey excitation was to increase the magnetron radius of the trapped ions. For this, a dipole excitation at the magnetron frequency, 155 Hz, RF amplitude: 5 Vpp (sinusoidal) was applied to one of the segments of the ring electrode for 26 ms (4 cycles in burst mode) using a DG1022 RIGOL function generator.

The cyclotron excitation was applied to two opposite segments of the ring electrode by using a Tektronics AFG3022B function generator in amplitude modulation mode with 95% depth. Another Rigol DG1022 generator was used to create a square wave amplitude modulation signal. This was run in the burst mode with a burst count of 1 with a 7 V amplitude and -2.5 V offset, with 2 separate triggers to create one modulation pulse per trigger. Table I shows the summary of RF generators and their settings, and Fig. 2 shows the resulting TOF pattern with using a 25-150-25 ms (On-Off-On) excitation pattern.

Table I. Summary of waveform generators used at TAMUTRAP for Ramsey excitation.

Model	Type	Motion	Amplitude	Mode	Other
Rigol DG1022	dipole	magnetron	5 V	burst/4	
Rigol DG1022	AM	modulation	7 V with a -2.5 V offset	burst/1	
Tektronics AFG3022B	quadrupole	cyclotron	adjusted	AM 95% depth	Ramsey excitation

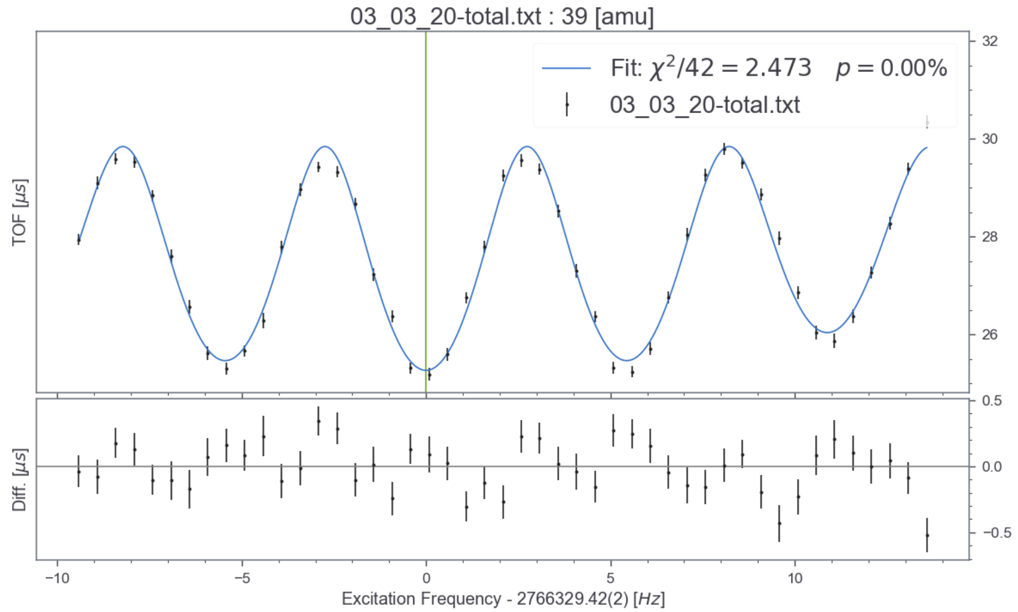

Fig. 2. TOF-ICR resonance curve of ^{39}K ions obtained with a 25-150-25 ms Ramsey excitation pattern.

[1] M. Kretzschmar, Int. J. Mass Spectrom. **264**, 122 (2007).

[2] P. Shidling *et al.*, Hyperfine Interact. **240**, 40 (2019).
[3] M. Mehlman *et al.*, Nucl. Instrum. Methods Phys. Res. **A712**, 11 (2010).

LSTAR: an isobar separator for the He-LIG system

G. Chubarian, V.S. Kolhinen, D. Melconian, P.D. Shidling, G.P.A. Berg,[1] M. Couder,[1]
M. Brodeur,[1] and M. Wiesher[1]
[1]*University of Notre Dame, Notre Dame, Indiana*

We have submitted a proposal to build “LSTAR”, a Light-ion guide Separator for Texas A&M’s Rare isotope beams. LSTAR is critically needed to purify the variety of exotic ions produced from the new K150 target station, He-LIG [1], being built to produced proton-rich isotopes for TAMUTRAP. Although the TAMUTRAP research program [2] is insensitive to contaminants – the coincident proton-β condition is extremely clean – a significantly impure beam from the He-LIG system will overload the gas-filled RFQ cooler/buncher. Without purification, we would not be able to efficiently transport RIB from He-LIG and load them in the Penning trap. In addition, experiments from other research programs could utilize the RIB produced by He-LIG with end stations on the 2nd floor high bay with LSTAR purifying the beams.

The basic requirements for LSTAR were determined quite early in the design process. Of the cases under consideration for TAMUTRAP (^{20,21}Mg, ^{24,25}Si, ^{28,29}S, ^{32,33}Ar, and ^{36,37}Ca), the greatest mass resolution necessary to remove isobaric contaminations are the heaviest cases. For example, ^{37}Ca and ^{37}K differ in mass by 0.033%; to separate these nuclides, LSTAR would need a mass resolution of $M/\Delta M > 3\,060$. Thus, our design specifications for LSTAR were quickly determined to be:

1. a mass resolution $M/\Delta M \geq 5\,000$ for A=6−50,
2. high acceptance and transmission (> 95%),
3. no energy compensation (meaning no electric dispersive elements),
4. purely electrostatic focusing and corrective elements (so that settings are independent of mass), and
5. the separator must fit in the existing space available in Cave 5 of the Cyclotron Institute.

The ion beam characteristics upon exiting the SPIG are well known based on the similar system at the University of Jyväskylä [3]. The predominantly q=+1 beam is expected to have a transverse emittance of < 3π mm-mrad and < ±1 eV energy spread. The LSTAR design must match these beam characteristics for optimal acceptance and transmission efficiency through the separator.

Many of the same design specifications may be found with the isobar separator built for the CARIBU facility at ANL [4]. We have therefore taken their separator design to guide our preliminary design for LSTAR, and are in the process of finalizing the configuration outlined in Fig. 1. The most significant difference from the CARIBU design is replacement of CARIBU’s two 60° bending magnets with LSTAR’s two 45° magnets operating with a dipole field of 0.45 T. This will reduce the mass resolution relative to CARIBU’s first-order mass resolution of $M/\Delta M$=22 400, but it allows us to transport the RIB 90° up through the roof planks to the TAMUTRAP facility. Our preliminary first-order calculation of LSTAR with 45° bending magnets indicates a mass resolving power of >6 000 which is already well within the design specifications. Nevertheless, we expect further optimizations to bring the resolving power up to $M/\Delta M \approx 10\,000$ once higher-order corrections have been applied.

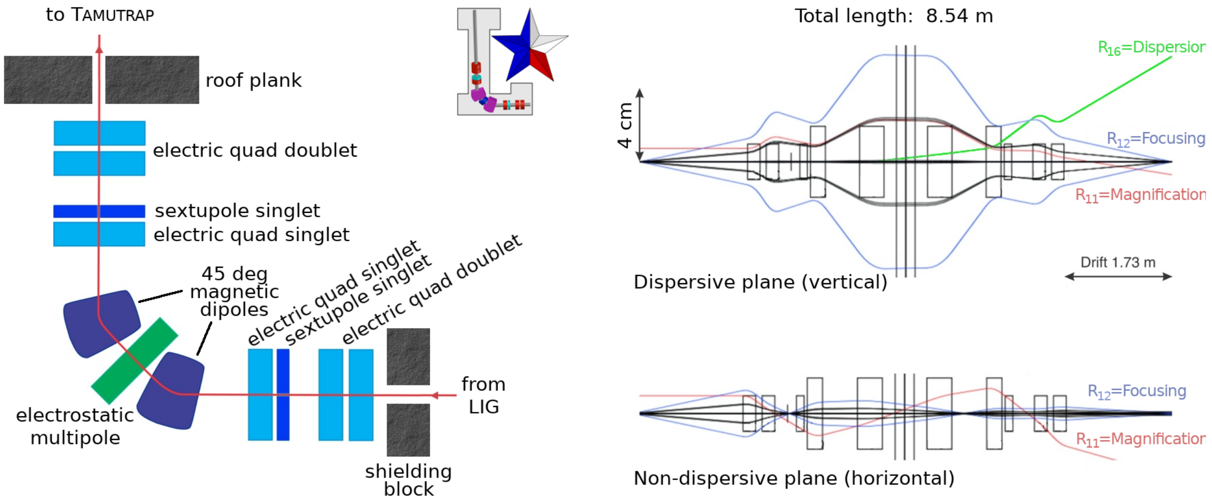

Fig. 1. Current design elements of LSTAR. The schematic layout of LSTAR is shown on the left. The system is symmetric about the electrostatic multipole and has 1.73-m long drifts at the front and the end to pass through the existing shielding blocks. On the right the preliminary ion-optics in both planes are shown. The system will be optimized as explained in the text.

To minimize higher-order aberrations, the LSTAR layout is symmetric about the central electrostatic multipole. Given the tight constraints of Cave 5, this was not a simple task. In order to achieve this, we are required to drill a new hole in the roof plank at a distance of 6.59 m from the gas cell. As of the writing of this report, we are awaiting the final location which will avoid the rebar in the plank; once that is determined, we will be able to optimize the mass resolving power. This can be accomplished by increasing, in the dispersive plane, the dispersion R16 and decreasing the magnification R_{11} while maintaining focusing $R_{12}=0$ at the end of the system. The first-order matrix elements R_{16}, R_{11} and R_{12} are shown in Fig. 1 along the central ray. The coloured lines of the functions of the matrix elements are scaled to distinguish them from the rays in black. The black rays are for a target size of ±0.5 mm and angles of ±6 mrad at the nominal energy of 50 keV. This optimization is time-expensive and sensitively dependent on the geometry, so can only be finalized after we learn exactly where the hole in the roof plank may be drilled.

Conservatively, the design of LSTAR fulfills all of the design specifications listed above. Based on our experience, we estimate that when the optimization is complete, the mass-resolving power of LSTAR will surpass the specification with $M/\Delta M \approx 10\,000$.

[1] P.D. Shidling *et al.*, *Progress in Research*, Cyclotron Institute, Texas A&M University (2019-2020), p. IV-95.

[2] P.D. Shidling *et al.*, Hyperfine Interacts. **240**, 40 (2019).

[3] P. Karvonen *et al.*, Nucl. Instrum. Methods Phys. Res. **B266**, 4794 (2008).

[4] C.N. Davids and D. Peterson, Nucl. Instrum. Methods Phys. Res. **B266**, 4449 (2008).

Production of radioactive ion beams for TAMUTRAP facility

P.D. Shidling, V.S. Kolhinen, G. Chubarian, V.E. Iacob, D. McClain, D. Melconian, M. Nasser,
A. Ozmetin, B. Schroeder, and G. Tabacaru

Last year, most of the time was dedicated to the investigation of an efficient way to produce proton-rich nuclei around 20 to 40 mass regions, which are of particular interest for the TAMUTRAP initial research program [1]. The TAMUTRAP facility can receive the low energy radioactive ion beams vertically either by light-ion guide (LIG) [2] or heavy-ion guide (HIG). The LIG technique is currently being implemented at the Cyclotron Institute as part of the institute's upgrade project. Currently, the K150 cyclotron is able to deliver a high-intensity beam of lighter ions (*p*, *d*, and α) as compared to heavier ions (>4 amu). The intensity of lighter ions is around 2-3 pμA. Due to this reason it was decided to proceed with light-ion guide method for producing RIB for TAMUTRAP.

In the light-ion guide technique, the reaction products from a nuclear reaction are thermalized in a very pure noble gas (He) where they stay as ions due to the high ionization potential of the stopping gas. Ions are flushed out of the ion guide via a differential pumping section where they are skimmed from the neutral gas with electric fields. The LIG technique for the proton-induced reaction is currently being commissioned at the Institute to produce and accelerate radioactive species mainly from (*p*, *n*) reactions for other research programs. For the TAMUTRAP program, the proton-rich nuclei of interest can only be produced via ^{3}He-induced nuclear reactions. The range of reaction products in helium for these reaction products is longer compared to those produced via proton-induced reactions. Therefore, a prototype of a new gas cell and low energy beamline, "^{3}He-LIG", was designed and built. To bring the beam to the TAMUTRAP facility, extraction from the new gas cell is in the direction opposite the existing LIG facility. Fig. 1 shows the design of the prototype ^{3}He-LIG system.

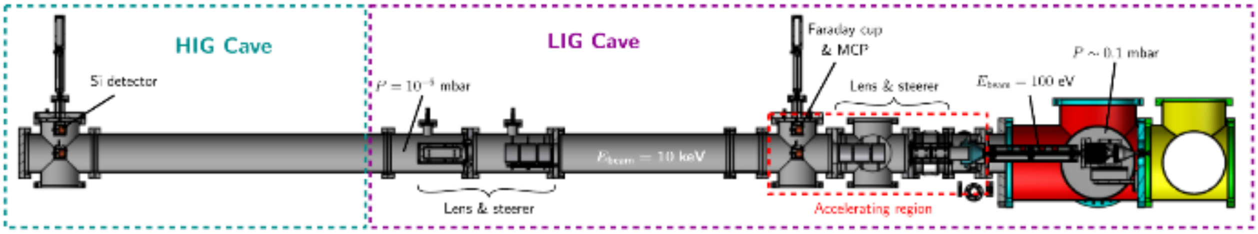

Fig. 1. The design of a new light ion guide towards the TAMUTRAP facility.

Two types of gas cells were designed and tested online: (a) the first design of gas cell uses the gas flow alone to extract the ions through an exit hole. (b) the second gas cell design includes an RF voltage structure gas cell, using a combination of gas flow, RF voltage, and DC potential gradient towards the exit hole of the gas cell. Both gas cells were tested online using a ^{3}He primary beam. In particular, ^{25}Si is of interest to the TAMUTRAP research program and so its production was extensively studied. The ^{3}He beam at 10 MeV/u was bombarded on $^{24(\mathrm{nat})}$Mg target for producing ^{25}Si. The reaction products were extracted from the gas cell by using electric fields and a helium gas jet via a sextupole ion guide (SPIG). Following the extraction, ions in charge state *q* were electrostatically accelerated to 10*q* keV of energy and guided further towards the detection system by using a combination of the Einzel lens and *x*-*y* steerers. The detection system consisted of a thin aluminum foil placed in front of a 500 μm-thick silicon detector. This detector was used to detect the charged particles (β, *p*, α) from the decay of the extracted RIB stopped in the aluminum foil. Several minor modifications were implemented between different runs in the extraction section of the beamline. These modifications improved the vacuum in the extraction section leading to an increase in the total rate (activity) of the silicon detector – an order of magnitude improvement. As one can clearly see in Fig. 2, the three most intense proton peaks which are emitted in the decay of ^{25}Si was observed in the silicon detector confirming the production of ^{25}Si isotope. Based on last year's theoretical and experimental investigation, the production rates of the nuclei of interest are tabulated in Table I.

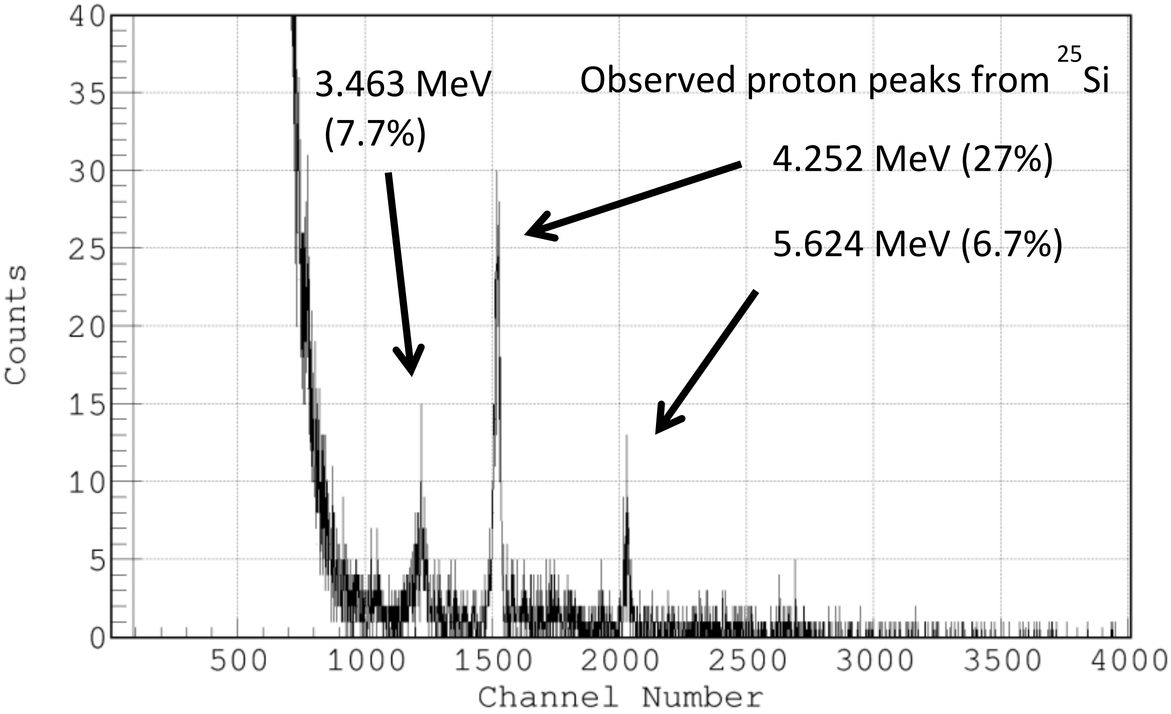

Fig. 2. Decay spectrum observed in the silicon detector. The three intense proton peaks which are emitted from the decay of ^{25}Si are clearly observed.

Table I. Estimated production rates of the T = 2 and T = 1/2 nuclei of interest for the TAMUTRAP research program. All nuclei are planned to be produced via ^{3}He induced fusion-evaporation reaction.

Nuclei T=1/2	Target	Rate at the target chamber	Nuclei T=2	Target	Rate at the target chamber
^{21}Mg	^{20}Ne	2.8×10^{5}	^{20}Mg	^{20}Ne	3.8×10^{3}
^{25}Si	^{24}Mg	1.5×10^{5}	^{24}Si	^{24}Mg	3.1×10^{3}
^{29}S	^{28}Si	0.8×10^{5}	^{28}S	^{28}Si	2.7×10^{3}
^{33}Ar	^{32}S	0.9×10^{5}	^{32}Ar	^{32}S	0.9×10^{3}
^{37}Ca	^{36}Ar	0.2×10^{5}	^{36}Ca	^{36}Ar	0.2×10^{3}

The results presented were obtained using the gas cell without the RF structure. The design including the RF structure has unfortunately so far been inconclusive. Online, we saw a greater overall current out of the RF-cell comparted to the 1st design, however the activity on the Si detector did not show proton peaks. This indicates the extraction time out of the larger RF-cell is presently too long to efficiently transport short-lived ions. It is worth noting that offline tests yielded a transmission efficiency of around 10%. We know of a number of improvements that may greatly improve the extraction time, and plan to perform a more detailed investigation in the near future.

An upgraded gas-only cell and improved low-energy beamline are currently being designed to further increase the extraction efficiency, and also to ensure the emittance of the beam out of He-LIG will match the acceptance of the LSTAR isobar separator currently being designed [3].

[1] P.D.Shidling *et al.*, Hyperfine Interact. **240**, 40 (2019).

[2] G. Tabacaru *et al.*, Rev. Sci. Instr. **83**, 02A905 (2012).

[3] G. Chubarian *et al.*, *Progress in Research*, Cyclotron Institute, Texas A&M University (2019-2020), p. IV-93.

TAMUTRAP as an isotopic separator

V.S. Kolhinen, G. Chubarian, V.E. Iacob, D. McClain, D. Melconian, M. Nasser, A. Ozmetin,
B. Schroeder, and P.D. Shidling

The TAMUTRAP facility consists of two main components: a radio frequency quadrupole (RFQ) Paul trap used to cool and bunch ions, and a cylindrical 180-mm diameter Penning trap [1,2]. This differs from several other trap facilities in that it has only one Penning trap designed for decay studies; other facilities have a purification Penning trap for isobaric and isotopic beam purification prior to a measurement trap dedicated to perform mass measurements. We have demonstrated that one can use a single trap to purify the beam and perform mass measurements.

A purification Penning trap is filled with helium buffer gas [3], usually $1x10^{-3}$ – $1x10^{-5}$ mbar, using a special gas-feeding system. The TAMUTRAP Penning trap does not have such a system, however helium gas used in RFQ cooler/buncher diffuses throughout the beamline, including into the Penning trap. A normal operating pressure for the RFQ is around $7x10^{-3}$ mbar leading to a vacuum of 3.7×10^{-7} mbar in the trap. However, if we increase the RFQ helium flow and operate it at $2.5x10^{-2}$ mbar, the gas pressure in the trap area increases reaching $1.3x10^{-6}$ mbar just before the superconducting solenoid housing the Penning trap, down to and $4.8x10^{-8}$ at the exit of the solenoid. The pressure at the centre of the trap can be then estimated to be an average of those two pressures.

We have carried out tests with natural rubidium released from an offline ion source located before the RFQ cooler/buncher. Natural rubidium consists of two main stable isotopes: ^{85}Rb and ^{87}Rb with natural abundances of 72.17% and 27.83%, respectively.

A bunched beam of ^{85,87}Rb ejected from the RFQ was captured in-flight into the Penning trap in the usual manner: the potential of the injection side of the trap was lowered to the level of the trap bottom (150 V) allowing them to enter. With the ejection side closed (300 V) ions are reflected back; trapping is accomplished by closing the injection side before the bunch beam escapes.

After capturing, the ions were allowed to collide with the buffer-gas atoms. Cooling occurs as energy is transferred to the lighter-mass helium atoms, and neutralization does not proceed due to the high ionization potential of helium. After cooling (in our case for 350 ms), the ions collected in the trap centre at the minimum of the axial electric potential well.

Fig. 1 show the timing pattern of our purification scheme, and Table I lists the other setting used. The first step in our one-trap purification scheme was to move all the trapped ions into a larger orbit than the 4-mm exit hole of the trap by applying a dipole excitation at the magnetron frequency (155 Hz, 20 V). This excitation is mass-independent and affects all ions confined in the trap, *i.e.* both ^{85}Rb^{+} and ^{87}Rb^{+}. Next a quadrupole excitation at the cyclotron frequency of a particular ion species, $f_C=1/(2\pi)qB/m$, selectivity re-centres ions of a particular mass m. Due to the lower pressure compared to typical purification traps, we needed to apply a relatively long (200 ms) and strong (20 V) quadrupole excitation in order to re-centre ions in our trap. After the purification process, a normal time-of-flight ion cyclotron resonance excitation [4] was applied for 200 ms to create frequency scans shown in Fig. 2.

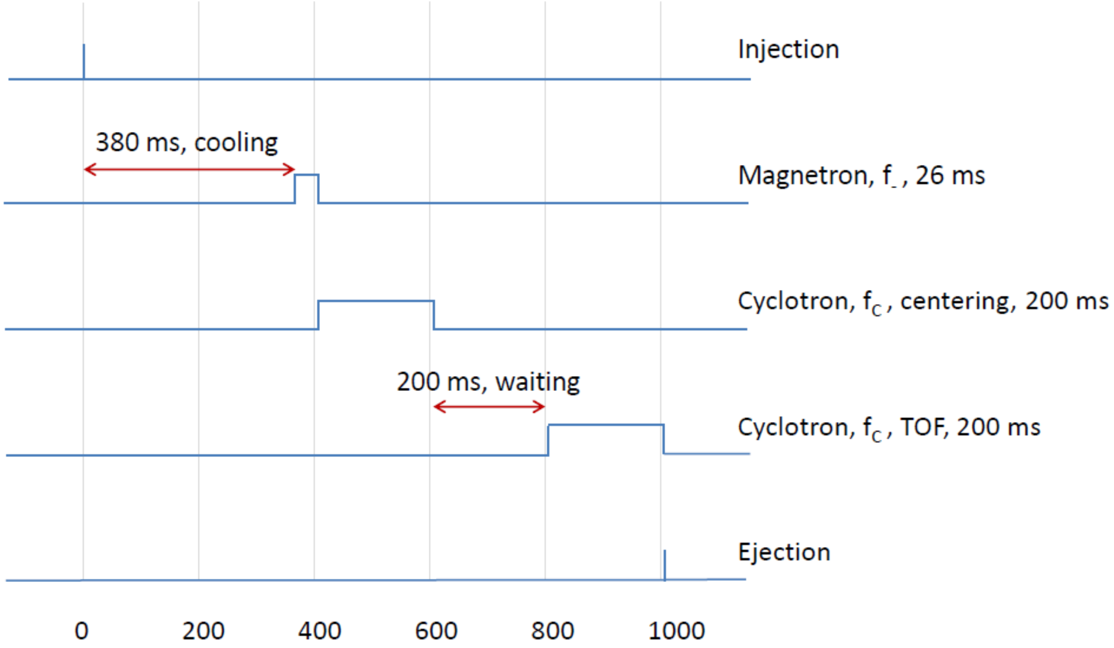

Fig. 1. Timing pattern used in the purification and subsequent TOF excitation for one-trap isotopic separation.

Table I. Summary of waveform generators used.

Generator	Motion	Amplitude	Mode	Other
Rigol DG1022	Dipole/magnetron	20 V	Burst/4	
Rigol DG1022	Quadrupole/cyclotron	20 V	Gated	centering
Tektronics AFG3022B	Quadrupole/cyclotron	adjusted	Gated, phase locking	TOF

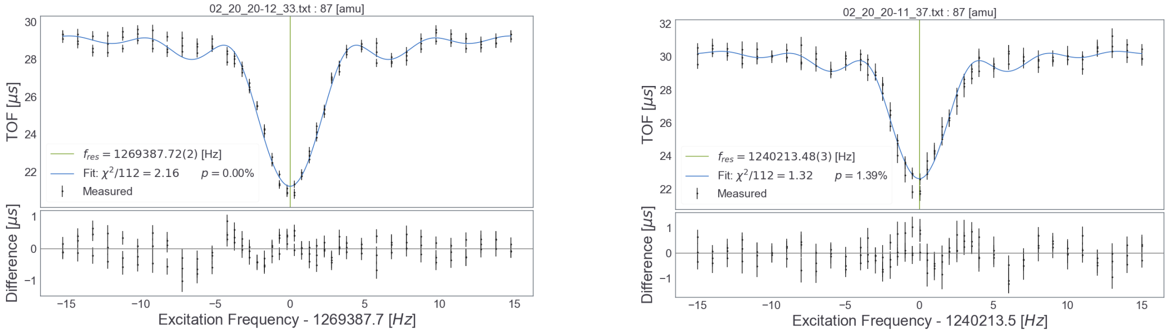

Fig. 2. Example of ^{85}Rb^{+} (left) and ^{87}Rb^{+} (right) frequency scans to determine their cyclotron frequencies.

Based on these resonance scans, we determined that our purification scheme is able to remove over 95% of the naturally abundant ^{87}Rb when cleaning for ^{85}Rb, and vice-versa.

[1] P. Shidling *et al.*, Hyperfine Interact. **240**, 40 (2019).
[2] M. Mehlman *et al.*, Nucl. Instrum. Methods Phys. Res. **A712**, 11 (2010).
[3] G. Savard *et al.*, Phys. Lett. A **158**, 247 (1991).
[4] M. Konig *et al.*, Int. J. Spectrom. **142**, 92 (1995).

Overview of the TAMUTRAP facility

V.S. Kolhinen, G. Chubarian, V.E. Iacob, D. McClain, D. Melconian, M. Nasser, A. Ozmetin,
B. Schroeder, and P.D. Shidling

The primary goal of the Texas A&M University Penning trap facility (TAMUTRAP) [1,2] is to search for a possible admixture of a scalar component to the predominantly *V-A* form of weak interaction by measuring the β-ν angular correlation parameter ($a_{\beta\nu}$), for T=2, super-allowed β-delayed proton emitters. The plan is to trap the radioactive ions in a Penning trap and observe the decaying particles. In order to achieve the precision necessary for a standard-model test, we have designed and commissioned a unique closed-endcap cylindrical Penning trap which is the world's largest. The TAMUTRAP facility has been commissioned using off-line ion sources and has demonstrated the ability to perform mass measurements. Fig. 1 shows a detailed overview of the TAMUTRAP beam line.

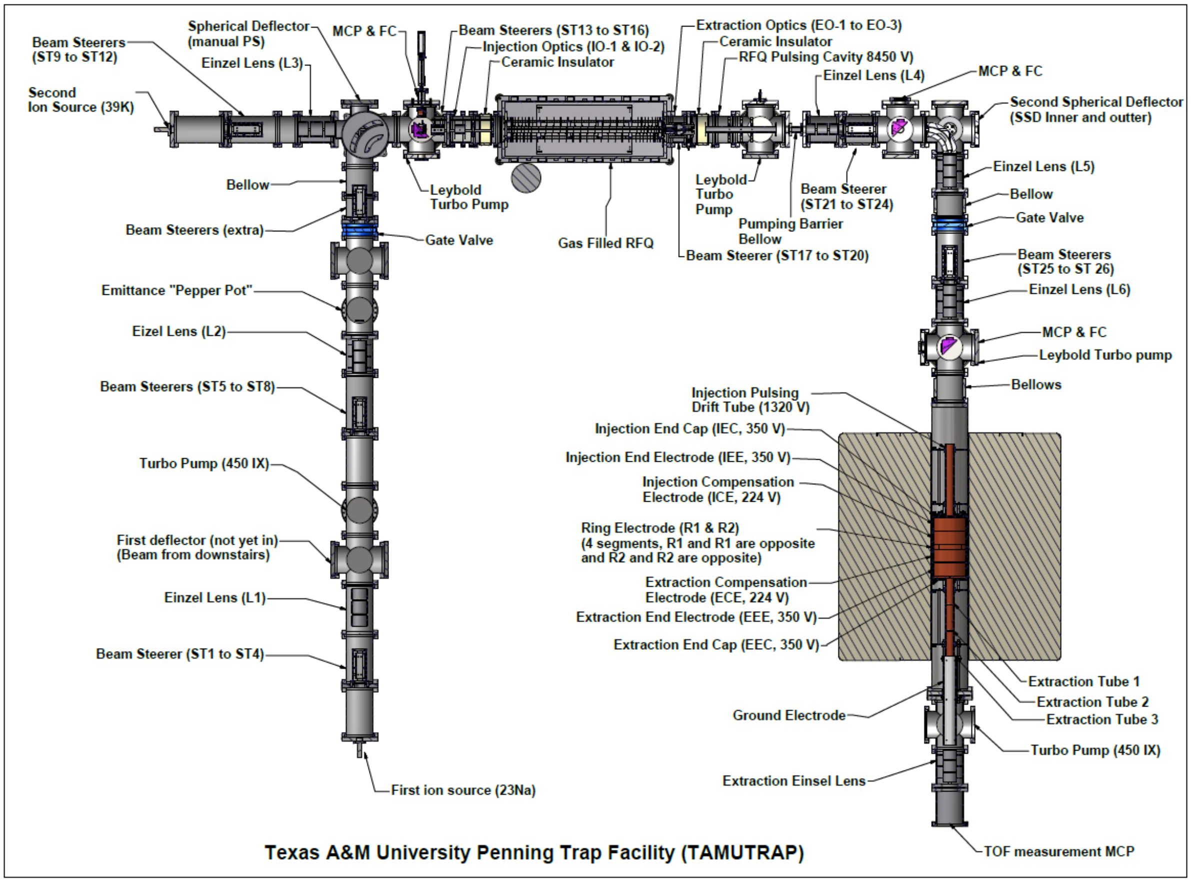

Fig. 1. Overview of the TAMUTRAP beamline.

The old 90-mm-diameter prototype Penning trap was replaced by the full 180-mm-diameter and 334.9-mm-long Penning trap, doubling the size of what was already the world's largest Penning trap. The new beamline and trap was inserted into our Agilent 7T210/ASR superconducting solenoid's bore from the extraction side and connected to the outer shell of the cryostat with adjustable non-magnetic supports that allow radial and axial adjustment of the tube compared to the solenoid. We transported beam from test ion sources in two separate locations by using ^{23}Na$^+$, ^{39}K$^+$, ^{85,87}Rb$^+$, and ^{133}Cs$^+$ ions and performed several mass measurements. Fig. 2 shows an example of a TOF ion-cyclotron resonance performed on ^{39}K$^+$ ions with a 200 ms excitation time. We have measured masses of each stable alkali isotope with ΔM/M≤60 part-per-billion precision, all in agreement with the literature values. A more detailed analysis process can be found in M. Nasser's report [3] of the TOF-fitting code which includes damping caused by the residual gas (mostly helium) in the Penning trap. We also improved the vacuum in the Penning trap by a factor of two by replacing the bellow after the RFQ with one having a smaller inner diameter.

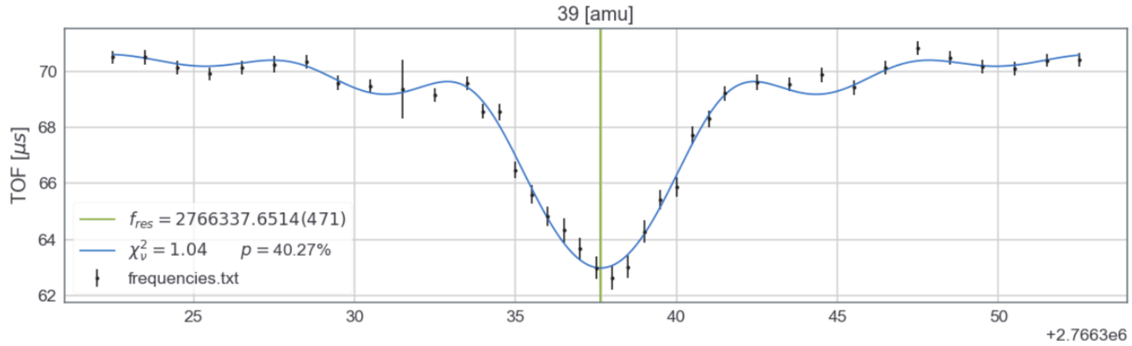

Fig. 2. An example of TOF-ICR frequency scan of 39K+ ions with 200 ms excitation time and fit to a model which includes dampening effects from a finite vacuum.

We have performed isobaric purification and subsequent mass measurements with a single Penning trap. The TOF-ICR resonances of ^{85}Rb$^+$, and ^{87}Rb$^+$ ions that were injected simultaneously in the Penning trap are shown in Ref. [4]. We have also implemented and tested a Ramsey-type excitation scheme for the Penning trap; see Ref. [5] which describes the waveform generator setting and timing pattern for the performed test run.


Output cable for HV

Inspect connection for Voltage.

10 turn potentiometer to adjust between 0 – 500 V with 0.1 V precision

Fig. 3. The control panel for the power supplies used for the Penning trap electrodes.

A new adjustment panel for the Penning trap 1 kV Spellman MPS power supplies have been built. Earlier the voltages were adjusted with coarse internal 1-turn potentiometers that had to be adjusted manually with a screw driver while standing on a ladder. In the present system, a 5 V control voltage has been fed through a Bourns 3590S-2-103L 10-turn, 2 Watt 10-kΩ linear potentiometer which allow adjusting the control input values between 0–5 V. This has been fed into the pin 5s of the 15-pin D-sub connectors of the power supplies allowing the output voltages of the power supplies to be adjusted easily and reproducibly between 0–500 V with a 0.05 V precision. Fig. 3 shows the photograph of the adjustment panel.

The injection electrode of the Penning trap has been modified to be able to pulse it between 0–10 kV instead of the original 0–1.5 kV. This allows us to transport 10 keV ions from the RFQ cooler/buncher to the Penning trap. However, there have been some discharge issues and we are currently working to better improve the shielding. Fig. 4, shows the Inventor illustration of the new design.

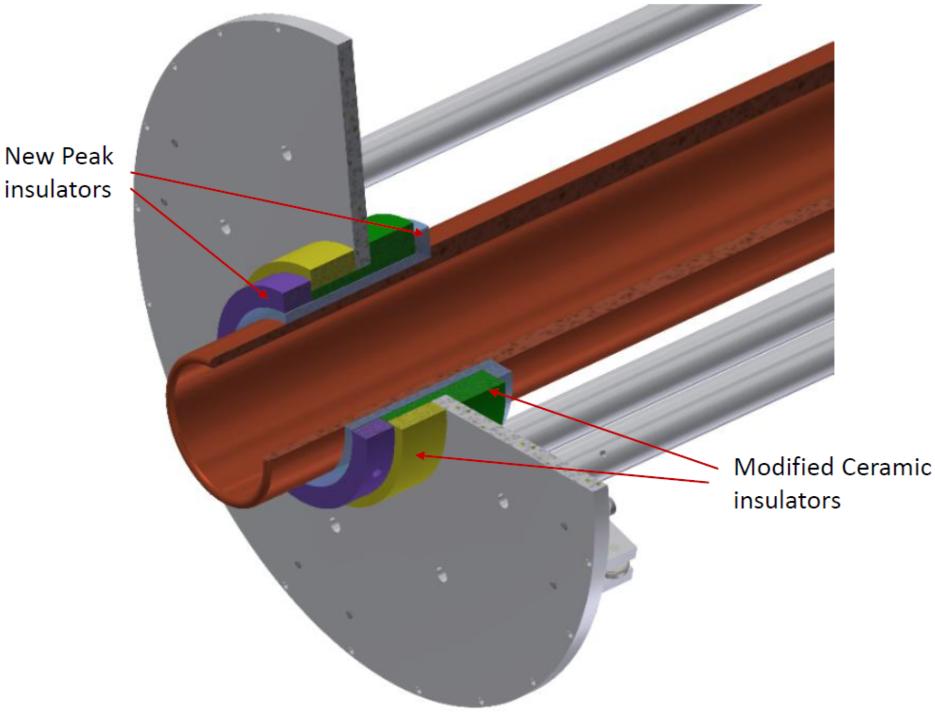

Fig. 4. Modified injection tube of the Penning trap.

We have also carried out test production runs for TAMUTRAP's radioactive ions of interest with a light ion guide technique with and without an RF structure inside the gas cell. Ref. [6] describes the test gas cell and achieved yields of the wanted radioactive ions. In parallel with developing the RIB production, we have started to design "LSTAR," the isobar separator needed to purify the radioactive beam and transport it to TAMUTRAP [7].

A new ion source, an electric discharge ion source is currently being developed to be used inside the light ion guide target chamber. We are also modifying our old surface ion sources used at the testing of the Penning trap. The main modification is the mounting of the source and the focusing lens immediately after the acceleration.

[1] P.D. Shidling *et al.*, Hyper. Interact. **240**, 40 (2019).

[2] M. Mehlman *et al.*, Nucl. Instrum. Methods Phys. Res. **A712**, 11 (2010).

[3] M. Nasser *et al.*, *Progress in Research*, Cyclotron Institute, Texas A&M University (2019-2020), p. IV-88.

[4] V.S. Kolhinen *et al.*, *Progress in Research*, Cyclotron Institute, Texas A&M University (2019-2020), p. IV-98.

[5] V.S. Kolhinen *et al.*, *Progress in Research*, Cyclotron Institute, Texas A&M University (2019-2020), p. IV-90.

[6] P.D Shidling *et al.*, *Progress in Research*, Cyclotron Institute, Texas A&M University (2019-2020), p. IV-95.

[7] G. Chubarian *et al.*, *Progress in Research*, Cyclotron Institute, Texas A&M University (2019-2020), p. IV-93.

Precision γ-ray branching ratio measurements for long-lived fission products of importance to nuclear-security

M. Bencomo,[1] K. Kolos,[1] J.A. Clark,[2] V.E. Iacob, D. Melconian, E. Norman,[3] H.I. Park, G. Savard,[2]
N.D. Scielzo,[1] and M.A. Stoyer[1]
[1]*Lawrence Livermore National Laboratory, Livermore, California,*
[2]*Argonne National Laboratory, Lemont, Illinois*
[3]*University of California Berkeley, Berkeley, California*

Continuing with our effort of precisely measuring the branching ratios for long-lived fission products we have collected and measured two radiopure ^{156}Eu samples. The samples were collected on thin (40 μg/cm^2) carbon-foil backings using a low-energy mass-separated beam of A = 156 fission products from CARIBU at Argonne National Laboratory. During collection, a HPGe detector was used to continuously monitor the implantation rate by detecting the characteristic γ rays emitted following the β decay of the shorter-lived fission products (Fig. 1). The first sample had measured activity of 375 Bq while the second one had an activity of 700 Bq. The implanted samples were then shipped to Texas A&M University for measurement of the subsequent decay.

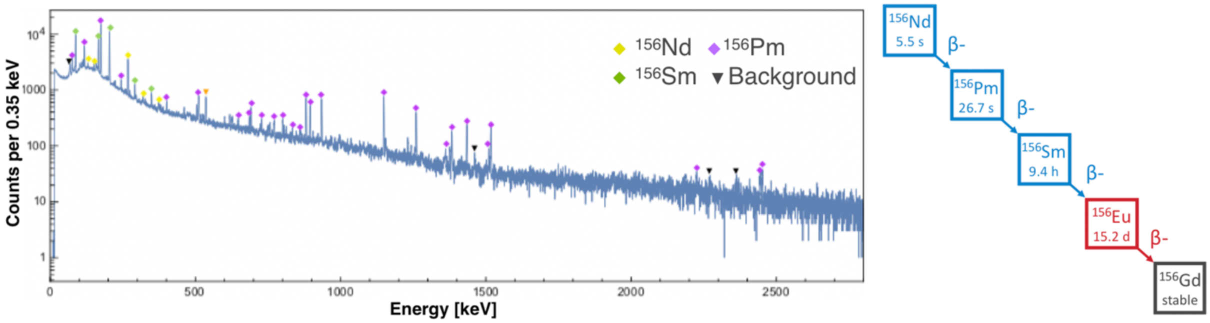

Fig. 1. γ spectrum from CARIBU during sample collection (January 2020). Most of the γ rays seen come from the A=156 decay chain.

As with previous experiments, the samples were placed in the center of a 4π proportional gas counter, with no internal windows, for β detection [1-3]. The γ rays were measured with a 0.2% absolute efficiency calibrated HPGe both with and without a coincident β particle at the nominal distance of 151 mm. This geometry has been discussed in previous reports and experiments [1, 5]. The measurement of both samples was done in 14 runs over the course of 2 weeks, where we collected over 120 hours of data for sample 1 and 220 hours for sample 2. These collection times yielded 2,091,588 and 8,096,150 coincidence events, respectively.

The analysis is currently underway. We have filtered the data to remove any noisy or faulty "cycles" encountered during the measurement. This filtering procedure reduces the total number of β singles by 3.5% (sample 1) and 5.3% (sample 2). This filter will also remove coincident events related to noisy/faulty runs by 3.5% and 18% (the large deficit in sample 2 is due to two runs where 43% and 25% of the data was noise). Further filtering of coincident events missing timing or energy information has also been done with the number of coincident events lost due to this being 0.34% for both samples. For the highest-intensity γ ray, which has an energy of 811 keV, there are over 30,000 counts for sample 1 and over 100,000 for sample 2 (Fig. 2). We have also identified a contaminant, ^{112}Ag, with a contribution of <0.3% to our total number of β particles detected.

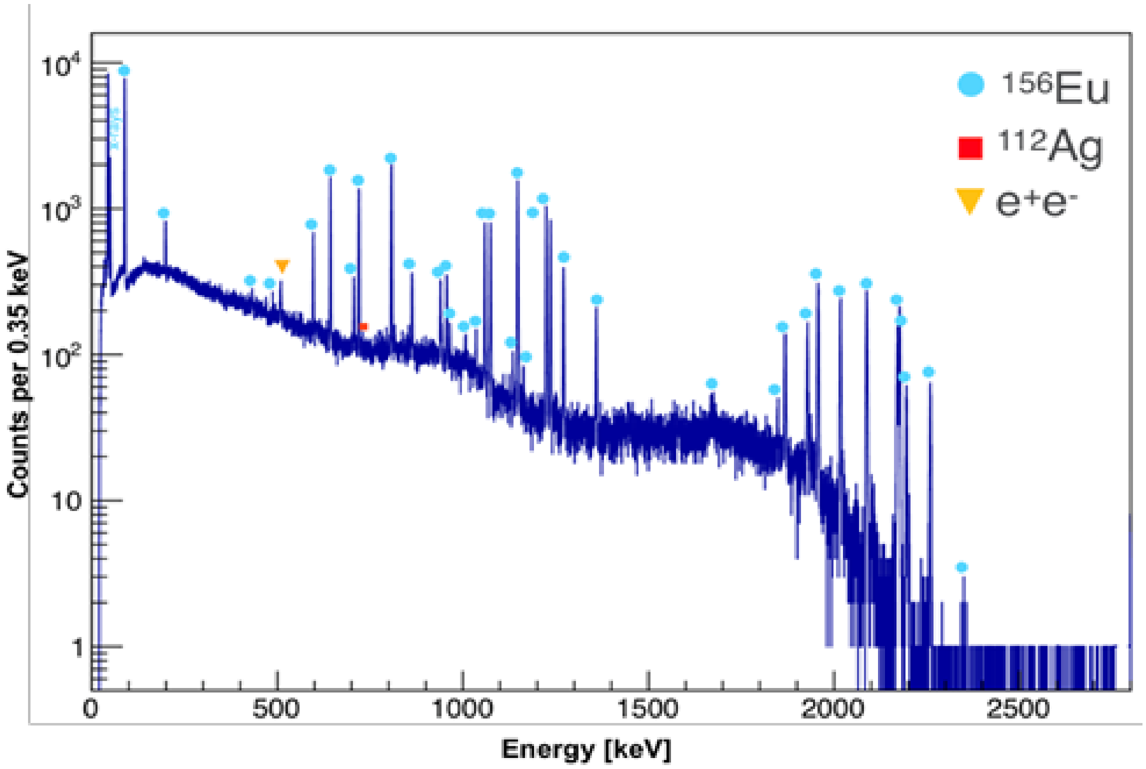

Fig. 2. Coincident γ-ray spectrum from the TAMU measurement (February 2020). The contaminant contribution is <0.3%.

Additionally, the efficiencies for all γ-ray energies, ranging from 89 to 2361 keV, have been calculated using the Cyltran Monte Carlo transport code [4] and the HPGe geometry [5]. This particular decay has close to 100 γ rays associated with it, most of which are not very intense. However, 85% of those γ rays are clearly identifiable in the measured γ spectrum, while for the rest we can set upper limits. Currently, there is work being done with the experimental data and GEANT4 simulations to obtain the efficiencies of the β detector, another crucial component to determine the branching ratios to high precision. We anticipate reaching a fractional precision of 1% for the highest-intensity transition in the decay of ^{156}Eu.

Furthermore, a proposal for "Improving decay data of the long-lived fission products ^{161}Tb and ^{111}Ag for nuclear medicine and national-security applications" has been approved by the ANL PAC for 6 days of beam collection. The scheduling for this experiment is pending, while we coordinate based on the availability of all collaborators involved.

This work was performed under the auspices of the US Department of Energy (DOE) by the Lawrence Livermore National Laboratory (LLNL) under Contract No. DE-AC52-07NA27344, DE-

AC02-06CH11357 (ANL), and DE-FG03-93ER40773 (TAMU), and the University of California under Contract No. DE-AC0376SF0098. This work was supported by the US DOE National Nuclear Security Administration through the Office of Nonproliferation Research and Development (NA-22) under the Funding Opportunity Announcement LAB 17-1763.

[1] K. Kolos *et al.*, *Progress in Research*, Cyclotron Institute, Texas A&M University (2016-2017), p. I-31.
[2] K. Kolos *et al.*, *Progress in Research*, Cyclotron Institute, Texas A&M University (2017-2018), p. I-30.
[3] K. Kolos *et al.*, *Progress in Research*, Cyclotron Institute, Texas A&M University (2018-2019), p. I-39.
[4] J.A. Halbleib *et al.*, Report No. SAND91-16734, Sandia National Labs, 1992.
[5] R.G. Helmer *et al.*, Nucl. Instrum. Methods Phys. Res. A**511**, 360 (2003).

A novel technique for the production of robust actinide targets

S. Dede,[1,2] G. Christian,[1,3] K. Manukyan,[2] and A. Aprahamian[2]
[1]*Cyclotron Institute, Texas A&M University, College Station, Texas 77843*
[2]*Department of Physics, University of Notre Dame, Notre Dame, Indiana 46556*
[3]*Department of Astronomy & Physics, Saint Mary's University, Halifax, NS B3H 3C3, Canada*

The success of accelerator experiments is highly influenced by the availability of targets with specific and well-defined properties. Actinide targets in particular are in high demand due to the importance they hold for stockpile stewardship as well as basic nuclear science. The main goal of this project is the development of revolutionary new approaches in the preparation of actinide targets that are isotopically pure, cost efficient, reliable, robust, and highly uniform with controlled thicknesses and dimensions. The actinides will be provided by the center of excellence in Actinide Research in the Engineering College at the University of Notre Dame.

The method used to produce these targets is electrospray deposition of chemically reactive layers that can be converted to actinide oxides by simple heat treatments. The target production setup is pictured in Fig. 1 and consists of the following components:

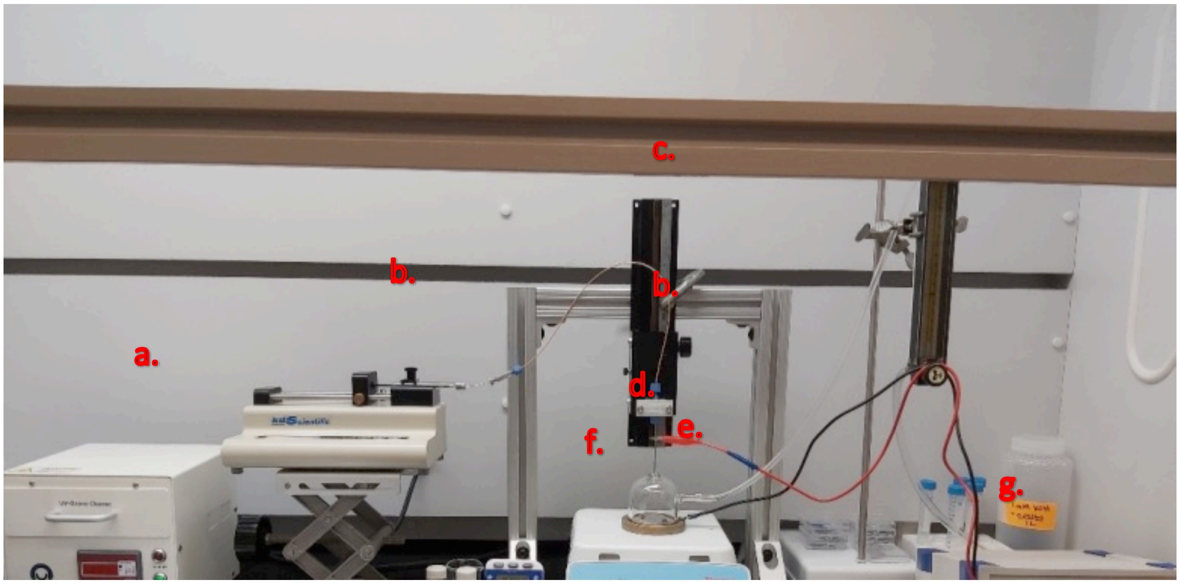

Fig. 1. The Electrospraying setup. The components are marked as follows; a) Ozone cleaner, for the preparation of my substrates before the spraying, b) Syringe pump – Syringe – Capillary nozzle, c) Distance regulator between the tip of the nozzle and the substrate, d) Pyrex dome, to control the environment of our electrospraying, e) Copper base, f) Hot plate, g) High voltage power supply, h) Nitrogen flow regulation

The project began by exploring the different combinations of parameters that will give the best possible targets. The first thing explored was the treatment of the aluminum substrates prior to the spraying. Here we discovered that nontreated substrates did not produce the desired result since instead of a uniform layer of material, droplets were forming on the substrate.

Using the same parameters for this set of targets (same distance between the nozzle and the substrate, flow rate of 25µl/h, voltage of 7.50 kV, nitrogen flow of 50 ml, spray time of 10 min and heat treatment time after spraying of 10 min), the substrate treatment was varied (parameters varied included plasma cleaning, ozone cleaning, sonication, ethanol cleaning, heat treatment and the combination of the above). Using microscope imaging, it was concluded that the best and most feasible treatment is a 30-minute heat treatment at 300ºC followed by a 20-minute ozone cleaning. Results from these substrate treating studies are shown in Figs 2.

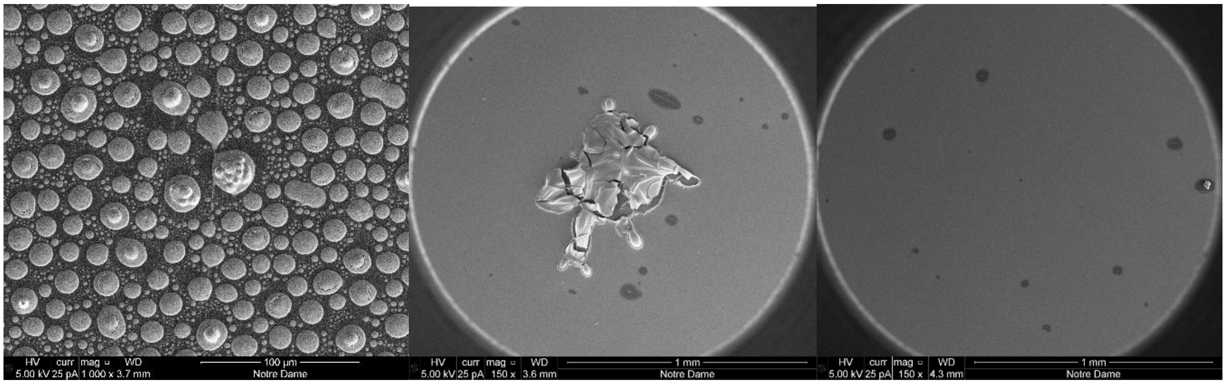

Fig. 2. (Left) Microscope image of a target produced after no substrate treatment. (Center) Microscope image of a target produced after 15 min plasma cleaning and 5 min ozone cleaning. (Right) Microscope image of a target produced after 30 min heat treatment and 20 min ozone cleaning.

Then next step of the project involved trying different flow rates, voltages, size of nozzles, distances between the nozzle and the substrate, temperature for the heat treatment of the target, time of spraying, time of the heat treatment of the target, as well as different temperatures on the hot plate. The preliminary results of these variations are shown in Figs. 3-4.

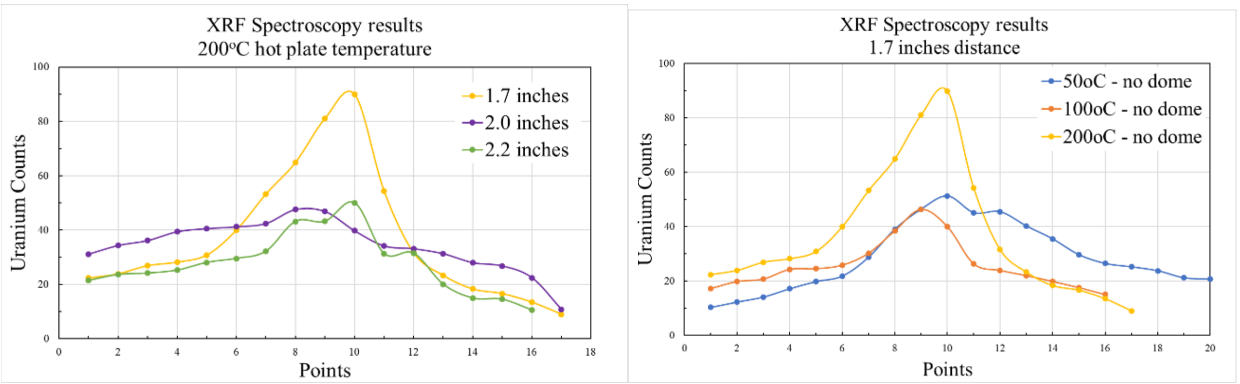

Fig. 3. (a) XRF results for targets with different distances between the nozzle and the substrate. (b) XRF results for targets with different temperatures on the hot plate.

Ideally, the curves in Figs. 3-4 would consist of straight lines, indicating that the amount of uranium is evenly distributed throughout the target. Instead, we have a higher concentration of uranium in the middle of the target. This means that the thickness variation across these targets is far greater than 15%, which is a high maximum for this kind of targets. Further conclusions that can be drawn from these tests are:

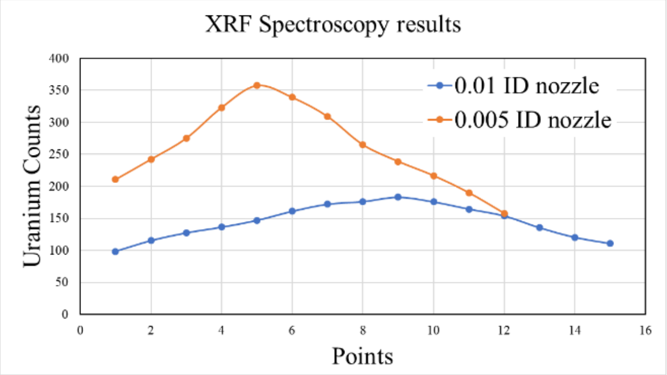

Fig. 4. XRF results for targets with different inner diameter (ID) nozzles.

a. Using the Pyrex dome while heat is applied by the hot plate creates a problem with the spraying. The solution is being evaporated at the tip of the nozzle, leading to clogging and non-uniform spraying.
b. The uniformity of the target improves with the increase of the distance between the tip of the nozzle and the substrate. The voltage applied has to increase as well in order for the electric field to remain unaffected by the change in distance.
c. The uniformity also improves when a nozzle with a smaller inner diameter is used.

Future work

More tests are essential in order to achieve the desired uniformity. Some of them being: using a new high voltage power supply which will allow applied voltage up to 20 kV, further increase of the distance between the tip of nozzle and the substrate, further increase of the temperature applied by the hot plate, as well as varying the flow rate and the time of spraying. Furthermore, we plan to investigate the deposition of different reactive solutions on self-supporting carbon substrates as well as the use of uranium oxide clusters in electro spraying deposition.

After the desired uniformity is accomplished, we plan to perform tests to determine the target's thickness and activity. These tests will be performed using a couple of different methods and microscopes like alpha spectroscopy, Rutherford Back Scattering (RBS) and X-Ray Fluorescence (XRF) measurements as well as a Focused Ion Beam (FIB) microscope and a Transmission Electron Microscope (TEM). Irradiation tests will also be performed in order to study our target's damage under a beam.

Finally, we have submitted a proposal at the Los Alamos National Lab (LANL), that requests for beam time to investigate the stability of the targets developed at Notre Dame. One aspect of the tests is to explore the interaction of neutrons with the various targets. This would involve the insertion of targets of varying thicknesses on both carbon and aluminum backings separately to understand the resulting γ-ray background in relation to the lines of interest from the uranium. Neutron beam time is requested in association with the DANCE detector (DANCE) [1],

The second aspect would ideally follow the first type of the test. The idea is to measure the average total kinetic energy (TKE) of correlated fission fragments of ^{238}U as a function of incident neutron energy with a twin Frisch-gridded ionization chamber (FGIC) at WNR [2].

[1] J.L. Ullmann, T. Kawano, T.A. Bredeweg, A. Couture, R.C. Haight, M. Jandel, J.M. O'Donnell, R.S. Rundberg, D.J. Vieira, J.B. Wilhelmy, J.A. Becker, A. Chyzh, C.Y. Wu, B. Baramsai, G.E. Mitchell, and M. Krtička, Phys. Rev. C **89**, 034603 (2014).

[2] D.L. Duke, F. Tovesson, A.B. Laptev, S. Mosby, F.J. Hambsch, T. Brys, and M. Vidali, Phys. Rev. C **94**, 054604 (2016).

Development of position and pulse shape discriminant neutron detector modules

D.P. Scriven,[1,2] G. Christian,[1,2,3] G.V. Rogachev,[1,2] C.E. Parker,[1] L. Sobotka,[4] S. Ahn,[1] S. Ota,[1]
E. Koshchiy,[1] A. Thomas,[4] E. Aboud,[3] and J. Bishop[1]
[1]*Cyclotron Institute, Texas A&M University, College Station, Texas 77843*
[2]*Department of Physics and Astronomy, Texas A&M University, College Station, Texas 77843*
[3]*Department of Astronomy and Physics, Saint Mary's University, Halifax Nova Scotia, B3H 3C3, Canada*
[4]*Departments of Chemistry and Physics, Washington University, St. Louis, Missouri 63130*

The detection of fast neutrons has many applications: fundamental physics, astrophysics, and stewardship science. In the last year, major strides have been made in the development of a fast neutron detector capable of precise energy measurement. In the 2018-2019 yearly report, we presented the results of both simulation as well as development guided by those simulations [1,2]. The simulations indicated that in order to get the energy resolutions of a few hundred keV, one needs to have position resolution of 2 cm or less with the assumed timing resolution. We since moved forward in the development with those crystals of the solid organic scintillator *p*-terphenyl to create *pseudo-bar* neutron detector modules.

A single pseudo-bar module is quite unique in its design. A module consists of six 2x2x2 cm^3 *p*-terphenyl scintillator crystals optically coupled together into a bar with Eljen Technology EJ-550 optical grease. The bar is wrapped in 3M™ Vikuiti™ Enhanced Specular Reflective Film (ESRF) on all four sides along the length. A wrapping of Teflon is then applied to mechanically secure the crystals and to bind the ESRF to the scintillator faces. A Hamamatsu R1450 photomultiplier tube (PMT) is placed at each end of the bar for light readout.

By looking at energy and timing measurements from the two PMTs (*left* and *right*) we can extract position information from the bar as is typically done. Shown in Fig. 1 (left) is the position separation parameter $ln(E_R/E_L)$ measured from the two PMTs as a function of energy. The separation parameter is the primary component used for crystal distinction. Each peak in the *y*-axis projected spectrum

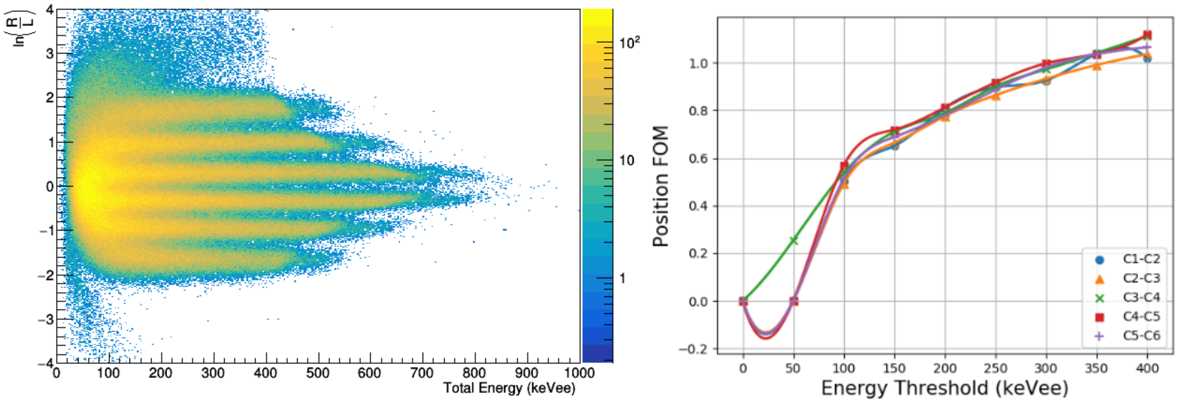

Fig. 1. Exposing the pseudo-bar to a ^{252}Cf source we show (left) the energy dependence on crystal distinguishability is shown here by plotting $ln(E_R/E_L)$ vs. E_{total}. At low energy it becomes more difficult to discriminate between crystals. (right) The FOM profiles for each neighboring pair of crystals. The FOM=0 points at low energy are present where no distinguishability exits.

corresponds to a single crystal in the pseudo-bar. We define a figure-of-merit (FOM) which allows us to quantify the discrimination between each peak,

$$FOM_{i,i+1} = \frac{\mu_{i+1} - \mu_i}{2.355(\sigma_i + \sigma_{i+1})} \tag{1}$$

Here, μ and σ are the mean and standard deviation from the Gaussian fit of each distribution. If labelling the crystals 1-6, the FOM is calculated for each pair of neighboring distributions. Looking at the 1D spectrum with cuts on energy of 50 keVee, the FOM is calculated for each bin, generating FOM profiles shown in Fig. 1 (right). These profiles give a detailed look at how distinguishable each peak is. Via its definition, a FOM=1 indicates the crossing point of the two Gaussians to be at the $2\sigma\sqrt{2\ln 2}$ level (>97%). This shows that position discrimination is capable above 300 keVee with high confidence.

In the presence of a neutron field, there nearly always exists a γ-ray field as well. Most neutron detectors are sensitive to both radiations. Some scintillators including *p*-terphenyl are capable of pulse shape discrimination (PSD) which allows for *n/γ* particle identification. We expose the pseudo-bar to a ^{252}Cf source to establish the quality of PSD in the pseudo-bar. The PSD quantity is calculated by taking two integrations of the scintillation pulse. The first integration is over the total waveform, and the second is over the tail. PSD is the ratio of the tail integration over the total integration.

In order to quantify the PSD, one again establishes a FOM. The FOM takes the same form as Eq.(1), were *i* and *i*+1 become γ and *n* respectively. We then calculate the FOM for each crystal by again making 50 keVee bins in the 1D PSD spectrum (*y*-projection of Fig. 2). The PSD profiles indicate that separation of >97% is achievable in all crystals below 150 keVee, and in some crystals as low as 100 keVee.

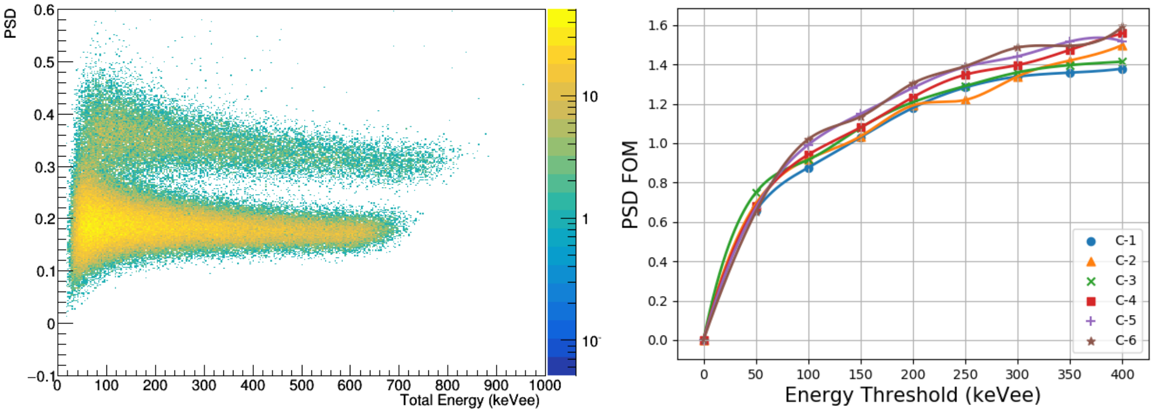

Fig. 2. (left) A typical 2D PSD spectrum. The PSD vs total energy shows the energy dependence of the PSD. The spectrum shown is from one of the central two crystals in the pseudo-bar C-3 which has the worst PSD of the few crystals. The top band corresponds to neutrons while the bottom band is γ-ray detections. (right) The PSD FOM profiles for each crystal.

With the energy dependence understood, we can look at the position discriminating parameter with the PSD parameter. Shown in Fig. 3 is the PSD vs position parameter. Here, a cut is made at 300 keVee as prescribed by the position FOM profiles in Fig. 1. There is clear position and n/γ discrimination for each crystal.

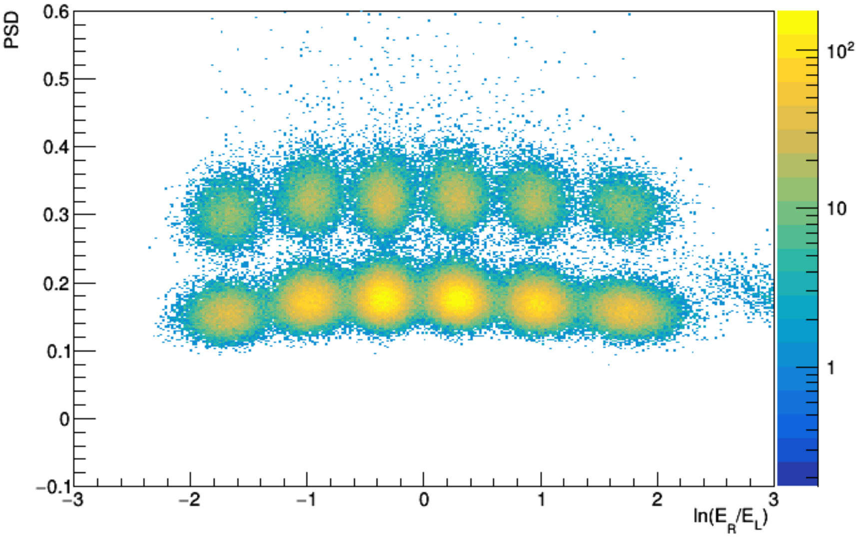

Fig. 3. Shown together is the PSD vs the position separation parameter. Here, a cut is made to exclude events at 300 keVee or less. The top band again corresponds to neutrons while the lower band corresponds to γ-ray detections.

To conclude, a neutron detector module has developed which can be used for the detection of fast neutrons with good spatial resolution and n/γ PSD below 300 keVee. We are currently working to measure the timing resolution of a module. We are continuing with the construction of a prototype array consisting of ~40 pseudo-bars due for commissioning in 2020, followed by addition of more modules to a full scale detector consisting of 128 pseudo-bars.

[1] D.P. Scriven *et al.*, *Progress in Research*, Cyclotron Institute, Texas A&M University (2018-2019), p. IV-55.

[2] C.E. Parker *et al.*, *Progress in Research*, Cyclotron Institute, Texas A&M University (2018-2019), p. IV-52.

Commissioning of Texas CsI Array for Astrophysical Measurements (TexCAAM)

E. Aboud,[1,2] L. Jeffery,[1,2] E. Koshchiy,[1] M. Barbui,[1] C. Hunt,[1,2] G.V. Rogachev,[1,2] S. Ahn,[1]
C.E. Parker,[1] J. Bishop,[1] S. Upadhyayula,[1,2] M. Roosa,[1,2] D.P. Scriven,[1,2] and A. Bosh[1,2]
[1]*Cyclotron Institute, Texas A&M University, College Station, Texas 77843*
[2]*Department of Physics and Astronomy, Texas A&M University, College Station, Texas 77843*

Texas **C**sI **A**rray for **A**strophysical **M**easurements (TexCAAM) detector system was built to perform alpha-transfer reactions at sub- and near- Coulomb energies with rare isotope beams to establish the alpha ANCs of astrophysicaly important sub-threshold states. The development of the TexCAAM was discussed in Ref. [1]. The detector apparatus consists of 32 Scionix CsI(Tl) (5cmx5cmx4cm) detectors that surround a target that is backed by a single Micron MSD026 Si detector and an array of plastics scintillators coupled to an array of Si photomultipliers (Fig. 1). The target assembly suspends the target and the Si detector inside of the beam pipe and is conveniently connected via a single flange such that the whole assembly can be removed and targets can quickly be changed (Fig. 2). The target consists of a rolled metal, such as ^{6}Li, that is designed to be thick enough to stop the incoming beam.

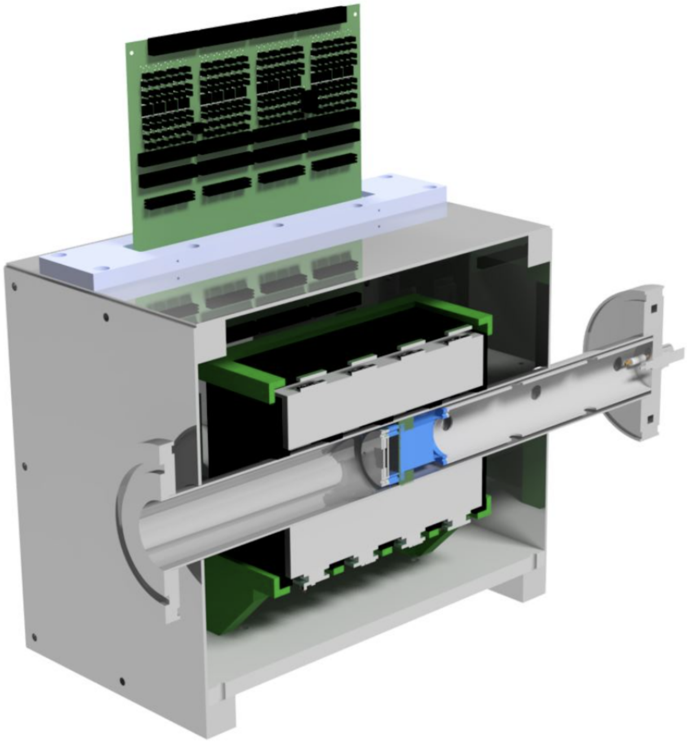

Fig. 1. Cutaway CAD drawing of TexCAAM. The target is inserted so that it is directly half way into the CsI array. The array of CsI is designed to maximize the solid angle covered while allowing the beampipe to go through the array. The black and green parts are a 3D printed skeleton that holds the CsI in place around the beampipe.

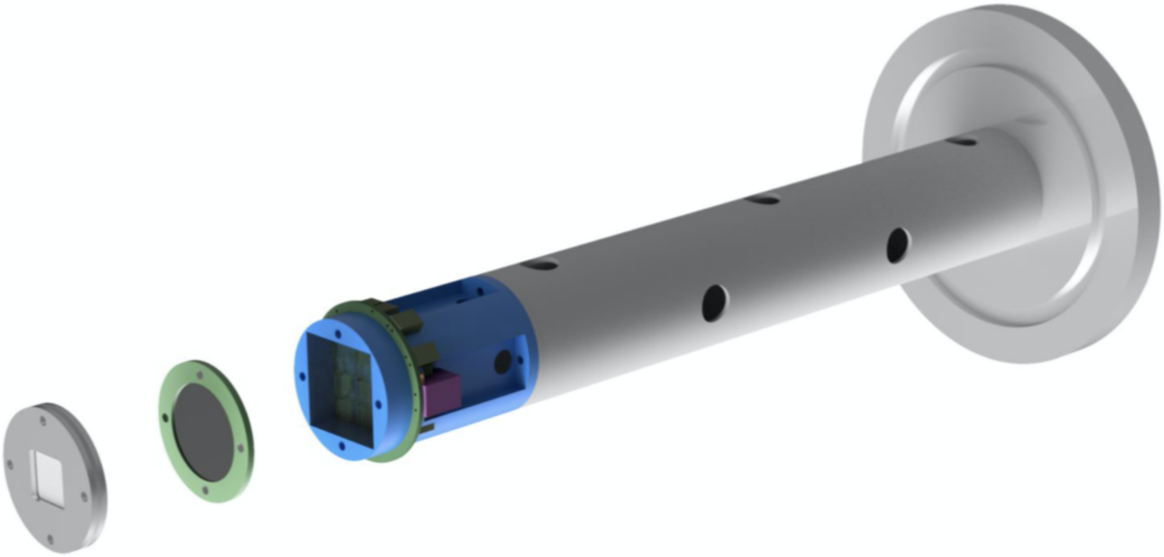

Fig. 2. CAD drawing of the target assembly where the right most object is a cutaway of the beampipe. The target assembly is blown out for ease of viewing and will slide into the beampipe being fixed via the flange. The frontmost component of the target assembly is the rolled target which is then backed by the Si detector and both are mounted to an array of plastic scintillators couple to an array of Si photomultipliers.

The production of a ^{6}Li target was a major hurdle to overcome. For the reaction of interest, a 50 um (2.67 mg/cm^{2}) thick ^{6}Li target was required. Since lithium oxidizes rapidly, target production had to be done carefully and procedurally. The lithium must be rolled in an inert gas environment while also being covered in diffusion oils. The lithium is pressed between two layers of thin, dense metals. The target must be frequently removed from the metal sandwich and the oils must be reapplied. If the lithium is left without checking, the lithium will stick to the metal and will be impossible to remove in a single piece. When ready for installation, the oils covering the lithium are removed using petroleum ether.

A commissioning run was performed using stable ^{12}C beam, but TexCAAM was attached to MARS rare isotope beamline, simulating an experiment with radioactive beam. The goal of the test run was to observe the ^{12}C(^{6}Li,dγ)^{16}O reaction by measuring deuterons and γ-rays in coincidence. We test the fundamental operations of TexCAAM. The main result of the commissioning run was an observation that TexCAAM performed as expected and that the γ background in coincidence with light charged particle is low. Given a data collection time of about 40 hours, we observed a background rate of 3-5 events per hour per MeV at all energies (see Fig. 3). Calculations for the ^{7}Be(^{6}Li,dγ)^{11}C reaction, the first one that will be performed using TexCAAM with radioactive beam, suggest a detection rate of ~10 events per hour for the state of interest, which surpasses the observed background rate. Various proof of principle conclusions were also made with this test run. For instance, confirmation of Si-γ coincidences, gating on events with light particles entering the Si detector, were used to remove significant noise from the γ-ray spectrum. The commissioning run provided the opportunity for troubleshooting of TexCAAM which was critical in order to move forward towards future experiments. We have not observed any γ-rays from ^{16}O in coincidence with deuterons. This is because the intensity of ^{12}C was limited due to pin-holes in the

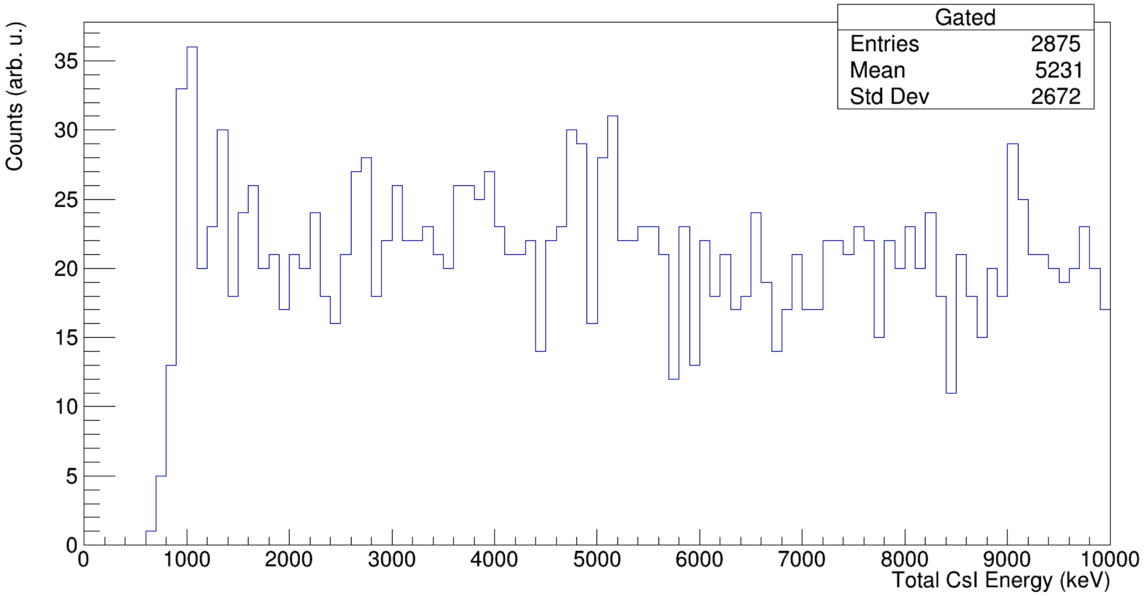

Fig. 3. Background measurement for the test run. This is a cumulative spectrum of the CsI detectors spanning over 40 hours. No statistically significant deviations from the background were observed.

lithium target and direct ^{12}C beam was overloading the detector. This issue will be fixed for the future runs. The TexCAAM setup was commissioned and is now ready for the first experiments.

[1] E. Aboud *et al.*, *Progress in Research*, Cyclotron Institute, Texas A&M University (2018-2019), p. IV-33.

Status of Texas Birmingham Active Target (TeBAT) development

S. Ahn,[1] G.V. Rogachev,[1,2] T. Kokalova,[3] L. Pollacco,[4] M. Barbui,[1] J. Bishop,[1,2] J. Elson,[5]
M. Griffiths,[3] A. Hollands,[3] C. Hunt,[1,2] E. Koshchiy,[1] C.E. Parker,[1] S. Pirrie,[3] M. Roosa,[1,2]
L. Sobotka,[5] C. Wheldon,[3] and J.C. Zamora[6]
[1]*Cyclotron Institute, Texas A&M University, College Station, Texas*
[2]*Department of Physics and Astronomy, Texas A&M University, College Station, Texas*
[3]*School of Physics and Astronomy, University of Birmingham, Birmingham, United Kingdom*
[4]*IRFU, CEA, Saclay, Gif-Sur-Ivette, France*
[5]*Department of Chemistry, Washington University, St. Louis, MO 63130*
[6]*Instituto de Fisica, Universidade de Sao Paulo, SP 05508-090, Brazil*

In order to measure nuclear reactions with exotic beams to elucidate the nature of nuclear force and to understand the origin of elements, we are developing a state-of-the-art detector system to achieve unprecedented precision of charged particle tracks and vertex position. This new device, Texas Birmingham Active Target (TeBAT), is the active target time projection chamber and it will allow studies for benchmarking predictions of contemporary microscopic models of atomic nuclei that start from QCD and nucleon-nucleon interactions. While the TeBAT is similar to the existing TexAT detector [1] in terms of geometry, the major difference will be a new Micro-MEsh Gaseous detector (micromegas) design that is a crucial part of the time projection chamber. The TeBAT will consist of a micromegas, a Silicon detector array and a CsI(Tl) detector array as shown in Fig. 1._It will provide a 3D particle track of a charge particle and measure its total energy deposition in Si and CsI(Tl), if the particle has enough energy escaping the active TPC volume and hitting the Si detector.

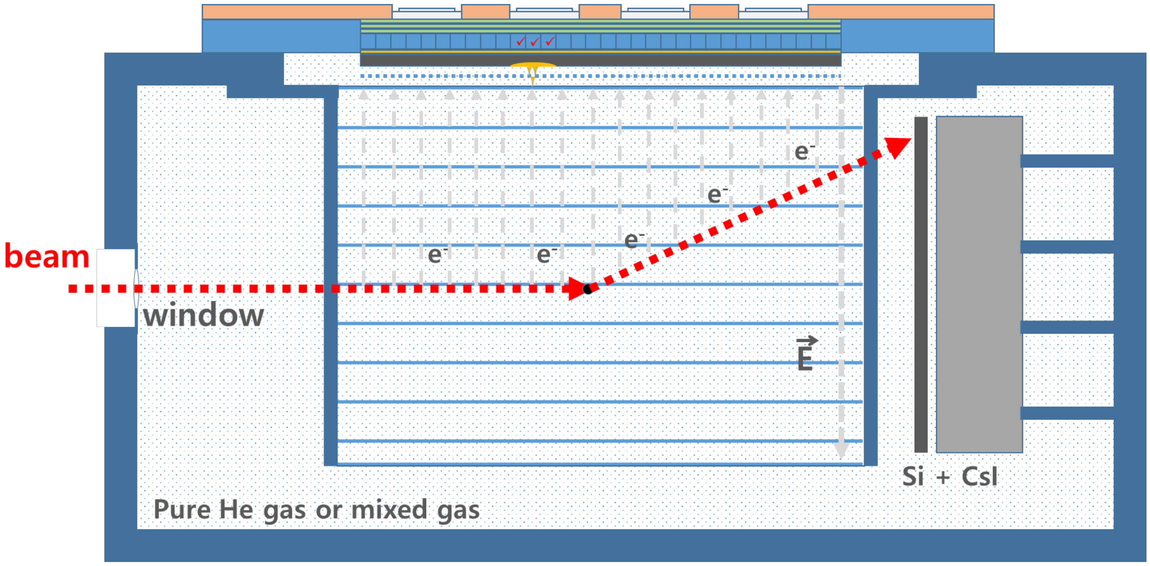

Fig. 1. A conceptual design of TeBAT detector. The Micromegas PCB board is sitting on top of the scattering chamber and the active area is placed on top of the field cage. The Silicon detector array is surrounding the field cage to detect particles escaping the field cage and the CsI(Tl) detectors are placed at the back of the Silicon detector array to detect silicon-punch-through particles.

The TeBAT will utilize a new technology on the micromegas, resistive layer, which will allow for position resolution as good as 200 microns. This will result in unprecedented angular resolution on the order of 0.1 degrees, which is critical for many nuclear reaction studies. Ionized electrons produced by particles will be drifted to the micromegas and amplified by the electron avalanche process. Then, the amplified electrons arriving at the resistive layer will induce signals on readout pads as demonstrated in Fig. 1. Depending on the surface resistivity and the distance between the resistive layer and the readout pad, the shape of the induced signal and the number of pad spread are significantly changed due to its RC constant. In order to collect spread induced signals and to reach a good position resolution, 7056 (84x84) readout pixels of 3x3 mm^2 are made on the board.

The size of the micromegas PCB board will be 400x400 mm^2 and its active area will be 252x252 mm^2. We use an “open” design. The micromegas detector will be attached to the scattering chamber directly and will also serve as a top flange. To accommodate this arrangement we will use a 1/2 inch thick stainless steel stiffener plate glued onto the micromegas board to prevent a deformation of the micromegas by the differential pressure between one atmosphere of air outside the chamber and vacuum or low pressure inside the chamber. To provide a different gain between heavy particles (beams and recoils) and light particles due to different energy loss in the gas, an additional detector, Gaseous Electron

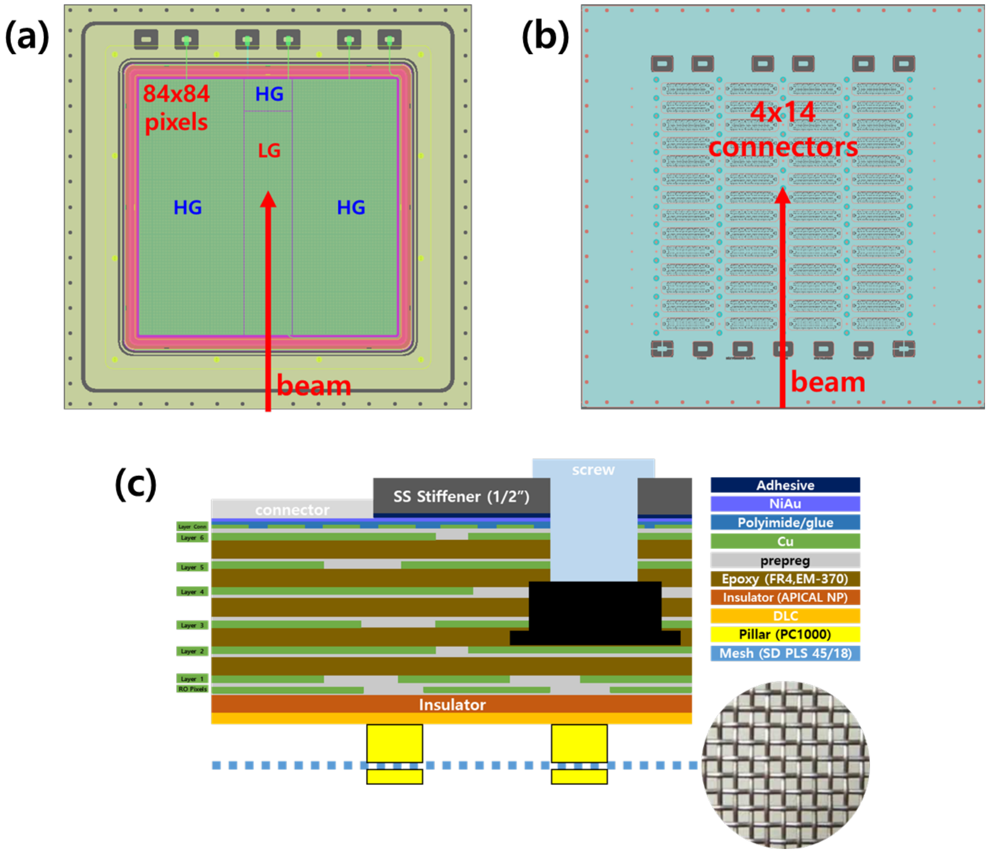

Fig. 2. (a) A micromegas design from the view of the resistive layer. 4 different gains of the GEM are also shown on top of the active area. (b) a micromegas design from the view of the connector side. (c) a conceptual drawing of micromegas layers colored by materials. The layer thickness in the drawing is not scaled. The microscopic image of the Mesh is shown next to the mesh layer. The screw will support the attachment between the PCB board and the stiffener.

Multiplier (GEM), will be used. It will be divided into 4 areas which can have independent gain, separately. Detailed PCB layout is shown in Fig. 2.

The flexible printed circuits (FPC) cable design is also under progress in order to carry signals from a large number of channels without any cross talks among channels. The readout of signals will be processed by the General Electronics for TPC (GET) [2]. The GET electronics for the TeBAT detector will consist of 1 microTCA crate, 1 Mutant trigger module, 8 CoBo communication modules and 28 AsAd motherboards. Detailed description of the GET electronics is explained in Ref. [1] and [2]. Digitized waveforms of signals are transferred from the AsAd boards to a computer storage by Ganil Data Acquisition System (Ganil DAQ) [3]. In order to analyze the recorded data efficiently, we decided to develop a shared library, TeBATlib, focused on the TPC data analysis. The following libraries are being built:

1. TeBATSim: a simulation tool of the TeBAT detector configuration using GEANT4 libraries,
2. TeBATResponse: an experimental data emulator using the output of the TeBATSim,
3. TeBATAnalysis: an offline data analysis tool and data viewer,
4. TeBATLive: an online data analysis tool.

The TeBAT Analysis Software Package project is divided into sub-groups by each software to concentrate on each task, while libraries made by one group will be shared by others.

In order to simulate the detector response and to model the induced signals produced by the resistive layer, the electric field maps of the mesh and micromegas are under calculation by outsourcing company, Radiation Detection and Imaging (RDI). The field map will be used as an input for the GARFIELD simulation to reproduce the charge distribution on readout pads.

In summary, our new state-of-the-art detector, TeBAT, is under development and this device will provide a position resolution of 200 micron. A new technique, resistive layer, has been applied to the micromegas. The active area of the detector will be 252x252 mm^2 and the GEM will be used to provide different gains for 4 sections. The final determination of DLC properties, layer stack of the FPC cable will be made soon in order to submit a production of the device. Also, the TeBAT analysis software package will be developed as well before the completion of the micromegas board.

[1] E. Koshchiy *et al.*, Nucl. Instrum. Methods Phys. Res. **A957**, 163398 (2020).
[2] E.C. Pollacco *et al.*, Nucl. Instrum. Methods Phys. Res. **A887**, 81 (2018).
[3] A. Boujrad and F. Saillant, 2000 IEEE Nuclear Science Symposium, Conference Record (Cat. No.00CH37149), Lyon, 2000, pp. 12/192-12/193 vol.2.

Toward the development of a next generation fast neutron portal monitor

E. Aboud,[1,2] G.V. Rogachev,[1,2] E. Koshchiy,[1] S. Ahn,[1,2] C.E. Parker,[1] J. Bishop,[1] D.P. Scriven,[1,2]
G. Christian,[1,2] and V. Johnson[3]
[1]*Cyclotron Institute, Texas A&M University, College Station, Texas*
[2]*Department of Physics and Astronomy, Texas A&M University, College Station, Texas*
[3]*Departments Statistics, Texas A&M University, College Station, Texas*

The non-proliferation of fissile materials is one of the most important fields in global security. Current generation neutron portal monitors mainly use a thermalization process that thermalizes the fast neutrons and counts them in a ^{3}He detector. A shortage of ^{3}He has made it increasingly rare and expensive. Special nuclear materials (SNMs), such as weapons-grade plutonium (WGPu) and high-enriched uranium (HEU), are dominated by non-spontaneous fissioning partners. This results in a spontaneous fission rate of 130 n/s/g for WGPu and a rate for HEU that is about four times lower than that of WGPu. As a comparison, ^{252}Cf, a common test source, has an emission rate of 2.1x10^3 n/s/ng. A method of detecting these materials is to induce fission via a thermal neutron generator, which is referred to as active interrogation. Using an active interrogation technique, it is difficult or impossible to detect these SNMs using a thermal neutron detector. Taking inspiration from the Gamma-Ray Burst Monitor [1], we are developing a fast neutron detector that will surpass these limitations. By utilizing a large array of small (2x2x2 cm^3) para-terphenyl scintillators we can distinguish ambient background neutrons from source neutrons and we can also localize a fissile source. This method preserves directional information while also minimizing the sensitivity limitations from the ambient neutron background.

The uniformly most powerful Bayesian tests (UMPBT) [3] statistical model was used to determine the sensitivity limitations of our detector based off of Monte Carlo N Particle (MCNP6)

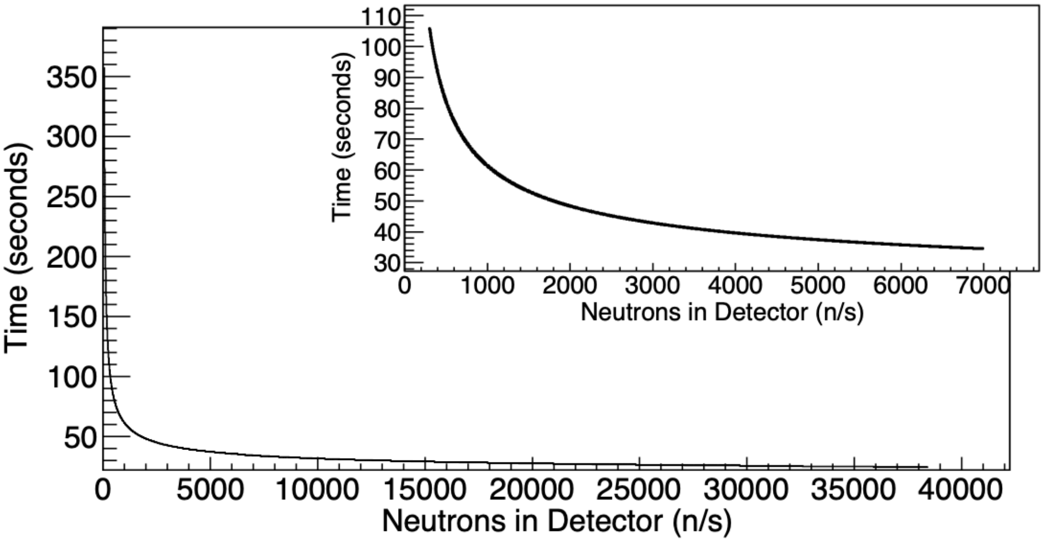

Fig. 1. Time vs source-neutron intensity entering the detector. The overlayed plot is a zoomed-in portion of the main plot to highlight the low-intensity region.

simulations that were conducted. The simulations were done using a ^{235}U+n Watt fission source and a measured ambient neutron background from New Orleans, Louisiana. A trend describing the time it takes for positive identification (with the confidence level of 1:1E6) with respect to the rate of neutrons being detected was formed with the model (Fig. 1).

Direct comparisons to current neutron portal monitors were done. The detector that was used as a comparison was the ^{3}He detector described in ref. [4]. An identical simulation was performed for both the ^{3}He detector and the proposed detector using passive interrogation of a ^{252}Cf source. For each of the simulations the efficiency of the detectors was calculated in terms of cps/ng. Table I shows the comparison of the efficiencies of the proposed detector and an assortment of current generation neutron portal monitors.

Table I. Comparison of neutron detection efficiency of the proposed detector and commercially-available detectors studied in Kouzes *et al.* [4]. The efficiencies labelled with a dagger were taken directly from ref. [4].

Detector Type	Efficiency (cps/ng)
Proposed Detector - Without UMPBT	12.0
^{3}He proportional detector (1 Tube)	$3.0(2)^{\dagger}$
BF_3 proportional detector (3 tubes)	$3.7(2)^{\dagger}$
Boron-lined proportional detector	$3.0(2)^{\dagger}$
Lithium-loaded glass fibers	$1.7(6)^{\dagger}$
Coated non-scintillating plastic fibers	$2.0(1)^{\dagger}$

A comparison of the proposed detector using the UMPBT model and the ^{3}He detector were done in terms of confidence levels. The confidence level was determined for various times of exposure to a ^{252}Cf source. For each of the times, a set of 50 MCNP6 simulations were conducted and the average number of detected neutrons from the source and background were calculated. Confidence levels for the ^{3}He detector were calculated based on the confidence intervals determined by the simulations. The simulation parameters were inputted into the UMPBT model to determine the confidence levels of the proposed detector. Fig. 2 shows the comparison of the confidence levels of both detectors for the times simulated.

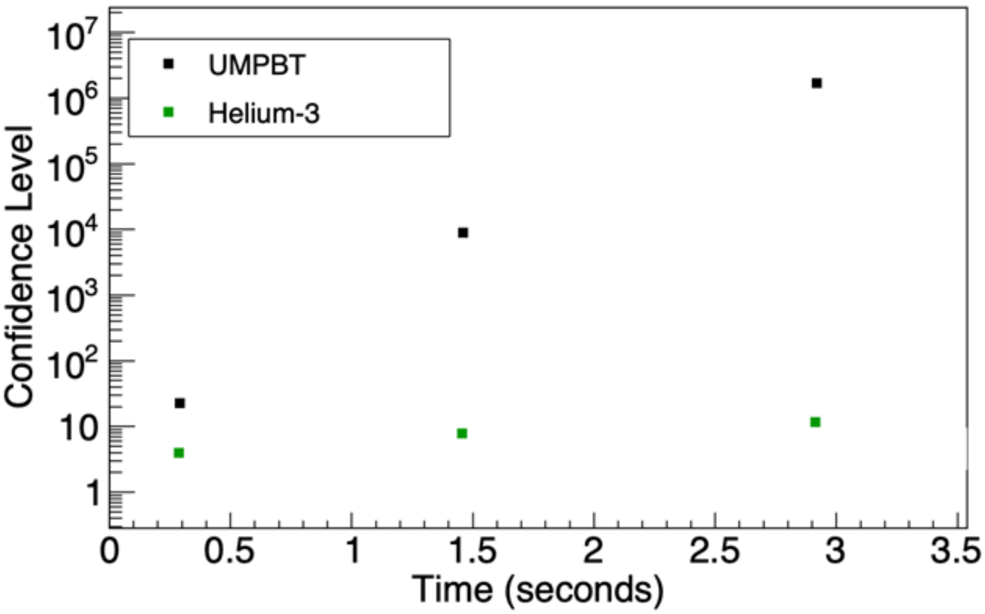

Fig. 2. Confidence levels in the form 1 in gamma, i.e. gamma = 10^6 corresponds to a confidence level of 1 in 10^6, which were calculated for a ^{3}He detector (green online) and the proposed detector using the UMPBT model (black). The confidence levels were derived from sets of 50 MCNP simulations with and without a source present. Comparison of the confidence levels shows a sensitivity comparison of the proposed detector to a standard ^{3}He detector.

[1] C. Meegan *et al.*, Astrophys. J. **702**, 791 (2009).

[2] T. Goorley *et al.*, Nucl. Technol. **180**, 298 (2012).

[3] V.E. Johnson, Ann. Stat. **41**, 1716 (2013), DOI: 10.1214/13-AOS1123

[4] R.T. Kouzes *et al.*, PNNL Technical Rep. PNNL-19311 (2010).

SECTION V

PUBLICATIONS

PAPERS PUBLISHED
April 1, 2019– March 31, 2020

First beams produced by the Texas A&M University radioactive-beam upgrade, D.P. May, F.P. Abegglen, J. Ärje, H. Clark, G. J. Kim, B.T. Roeder, A. Saastamoinen, and G. Tabacaru, Proc. of the 22nd International Conference on Cyclotrons and their Applications, Cape Town, South Africa, Sept. 2019.

Decay properties of ^{22}Ne+α resonances and their impact on ss-process nucleosynthesis, S. Ota, G. Christian, G. Lotay, W.N. Catford, E.A. Bennett, S. Dede, D.T. Doherty, S. Hallam, J. Hooker, C. Hunt, H. Jayatissa, A. Matta, M. Moukaddam, G.V. Rogachev, A. Saastamoinen, J.A. Tostevin, S. Upadhyayula, and R. Wilkinson, Phys. Lett. B **802**, 135256 (2020).

Constraining the ^{22}Ne(α,γ)^{26}Mg and ^{22}Ne(α,n)^{25}Mg reaction rates using sub-Coulomb αα-transfer reactions, H. Jayatissa, G.V. Rogachev, V.Z. Goldberg, E. Koshchiy, G. Christian, J. Hooker, S. Ota, B.T. Roeder, A. Saastamoinen, O. Trippella, S. Upadhyayula, and E. Uberseder, Phys. Lett. B **802**, 135267 (2020).

Alpha-capture reaction rate for ^{22}Ne(α, n) via sub-Coulomb α-transfer and its effect on final abundances of s-Process isotopes, H. Jayatissa, G.V. Rogachev, V.Z. Goldberg, E. Koshchiy, B.T. Roeder, O. Trippella, J. Hooker, S. Upadhyayula, E. Uberseder, A. Saastamoinen, and C. Hunt, Proc. XV Int. Symp. on Nuclei in the Cosmos, Lab.Naz.del Gran Sasso L'Aquilla, Assergi, Italy, June 24-29 2019, p.377 (2019).

High-resolution radioactive beam study of the ^{26}Al(d,p) reaction and measurements of single-particle spectroscopic factors, G. Lotay, P.J. Woods, M. Moukaddam, M. Aliotta, G. Christian, B. Davids, T. Davinson, D.T. Doherty, D. Howell, V. Margerin, and C. Ruiz, Eur. Phys. J. A **56**, 3 (2020).

Indium and thallium extraction into betainium bis(trifluoromethylsulfonyl)imide ionic liquid from aqueous hydrochloric acid media, M.F. Volia, E.E. Tereshatov, M. Boltoeva, and C.M. Folden III, J. Chem. **44**, 2527 (2020).

Hydrophobic polymerized ionic liquids for trace metal solid phase extraction: thallium transfer from hydrochloric acid media, E.E. Tereshatov, M. Boltoeva, V. Mazan, C. Baley, and C.M. Folden III, J. Chem. **43**, 8958 (2019).

Experimental validation of a nuclear forensics methodology for source reactor-type discrimination of chemically separated plutonium, J.M. Osborn, K.J. Glennon, E.D. Kitcher, J.D. Burns, C.M. Folden III, and S.S. Chirayath, Nucl. Eng. Tech. **51**, 384 (2019).

Measuring key Sm isotope ratios in irradiated UO22 for use in plutonium discrimination nuclear forensics, K.J. Glennon, J.M. Osborn, J.D. Burns, E.D. Kitcher, S.S. Chirayath, and C.M. Folden III, J. Radioanal. Nucl. Ch. **320**, 405 (2019).

New precise half-life measurement for the superallowed β+ emitter ^{34}Ar, V.E. Iacob, J.C. Hardy, H.I. Park, M. Bencomo, L. Chen, V. Horvat, N. Nica, B.T. Roeder, and A. Saastamoinen, Phys. Rev. C **101**, 015504 (2020).

Precise branching ratio measurement for the superallowed β+ decay of ^{26}Si: Completion of a second mirror pair, M. Bencomo, J.C. Hardy, V.E. Iacob, H.I. Park, L. Chen, V. Horvat, N. Nica, B.T. Roeder, A. Saastamoinen, and I.S. Towner, Phys. Rev. C **100**, 015503 (2019).

Improved limits on Fierz interference using asymmetry measurements from the Ultracold Neutron Asymmetry (UCNA) experiment, X. Sun, E. Adamek, B. Allgeier, Y. Bagdasarova, D.B. Berguno, M. Blatnik, T.J. Bowles, L.J. Broussard, M.A. Brown, R. Carr, S. Clayton, C. Cude-Woods, S. Currie, E.B. Dees, X. Ding, B.W. Filippone, A. García, P. Geltenbort, S. Hasan, K.P. Hickerson, J. Hoagland, R. Hong, A.T. Holley, T.M. Ito, A. Knecht, C. Liu, J. Liu, M. Makela, R. Mammei, J.W. Martin, D. Melconian, M.P. Mendenhall, S.D. Moore, C.L. Morris, S. Nepal, N. Nouri, R.W. Pattie, A. Pérez Galván, D.G. Phillips, R. Picker, M.L. Pitt, B. Plaster, D.J. Salvat, A. Saunders, E.I. Sharapov, S. Sjue, S. Slutsky, W. Sondheim, C. Swank, E. Tatar, R.B. Vogelaar, B. VornDick, Z. Wang, W. Wei, J.W. Wexler, T. Womack, C. Wrede, A.R. Young, and B.A. Zeck, Phys. Rev. C **101**, 035503 (2020).

Ion-trap application: Fundamental weak interaction studies using ion traps, P.D. Shidling, V.S. Kolhinen, B. Schroeder, M. Nasser, A. Ozmetin, and D. Melconian, AIP Conference Proceedings **2160**, 070011 (2019).

TAMUTRAP facility: Penning trap facility for weak interaction studies, P.D. Shidling, V.S. Kolhinen, B. Schroeder, M. Nasser, A. Ozmetin, and D. Melconian, Hyperfine Interactions **240**, 40 (2019).

Neutron-proton asymmetry dependence of nuclear temperature with intermediate mass fragments, X. Liu, H. Zheng, R. Wada, W. Lin, M. Huang, P. Ren, G. Qu, J. Han, M.R.D. Rodrigues, S. Kowalski, T. Keutgen, K. Hagel, M. Barbui, A. Bonasera, and J.B. Natowitz, Phys. Rev. C **100**, 064601 (2019).

Texas Active Target (TexAT) detector for experiments with rare isotope beams, E. Koshchiy, G.V. Rogachev, E. Pollacco, S. Ahn, E. Uberseder, J. Hooker, J. Bishop, E. Aboud, M. Barbui, V.Z. Goldberg, C. Hunt, H. Jayatissa, C. Magana, R. O'Dwyer, B.T. Roeder, A. Saastamoinen, and S. Upadhyayula, Nucl. Instrum. Methods Phys. Res. **A957**, 163398 (2020).

Search for the high-spin members of the α:2n:α band in ^{10}Be, S. Upadhyayula, G.V. Rogachev, J. Bishop, V.Z. Goldberg, J. Hooker, C. Hunt, H. Jayatissa, E. Koshchiy, E. Uberseder, A. Volya, B.T. Roeder, and A. Saastamoinen, Phys. Rev. C **101**, 034604 (2020).

Structure of ^{9}C through proton resonance scattering with the Texas Active Target detector, J. Hooker, G.V. Rogachev, E. Koshchiy, S. Ahn, M. Barbui, V.Z. Goldberg, C. Hunt, H. Jayatissa, E.C. Pollacco, B.T. Roeder, A. Saastamoinen, and S. Upadhyayula, Phys. Rev. C **100**, 054618 (2019).

Evidence for α-cluster structure in ^{21}Ne in the first measurement of resonant ^{17}O+α elastic scattering, A.K. Nurmukhanbetova, V.Z. Goldberg, D.K. Nauruzbayev, M.S. Golovkov, and A. Volya, Phys. Rev. C **100**, 062802 (2019).

State of the art measurements with TexAT, J. Bishop, G.V. Rogachev, E. Aboud, S. Ahn, M. Assunção, M. Barbui, A. Bosh, V. Guimaraes, J. Hooker, C. Hunt, H. Jayatissa, E. Koshchiy, S. Lukyanov, R. O'Dwyer, Y. Penionzhkevich, E. Pollacco, C. Pruitt, B.T. Roeder, A. Saastamoinen, L. Sobotka, E. Uberseder, S. Upadhyayula, and J. Zamora, J. Phys. Conf. Series **1308**, 012006 (2019).

Measurement of d+^{7}Be cross sections for big-bang nucleosynthesis, N. Rijal, I. Wiedenhöver, J.C. Blackmon, M. Anastasiou, L.T. Baby, D.D. Caussyn, P. Höflich, K.W. Kemper, E. Koshchiy, and G.V. Rogachev, Phys. Rev. Lett. **122**, 182701 (2019).

Studies of systematic effects of the AstroBox2 detector in online conditions, A. Saastamoinen, E. Pollacco, B.T. Roeder, R. Chyzh, L. Trache, and R.E. Tribble, Nucl. Instrum. Methods Phys. Res. **B463**, 251 (2020).

Isoscaling and nuclear reaction dynamics, A. Hannaman, A.B. McIntosh, A. Jedele, A. Abbott, J. Gauthier, K. Hagel, B. Harvey, Z. Kohley, Y. Lui, L.A. McIntosh, A.R. Manso, M. Sorensen, Z. Tobin, R. Wada, M. Youngs, and S.J. Yennello, Phys. Rev. C **101**, 034605 (2020).

Extending the dynamic range of electronics in a Time Projection Chamber, J. Estee, W.G. Lynch, J. Barney, G. Cerizza, G. Jhang, J.W. Lee, R. Wang, T. Isobe, M. Kaneko, M. Kurata-Nishimura, T. Murakami, R. Shane, S. Tangwancharoen, C.Y. Tsang, M.B. Tsang, B. Hong, P. Lasko, J. Łukasik, A.B. McIntosh, P. Pawłowski, K. Pelczar, H. Sakurai, C. Santamaria, D. Suzuki, S.J. Yennello, and Y. Zhang, Nucl. Instrum. Methods Phys. Res. **A944**, 162509 (2019).

Dynamical ternary decays of excited projectile-like fragments, A.R. Manso, A.B. McIntosh, J. Gauthier, K. Hagel, L. Heilborn, A. Jedele, Z. Kohley, A. Wakhle, A. Zarrella, and S.J. Yennello, Phys. Rev. C **100**, 044612 (2019).

Interplay of neutron-proton equilibration and nuclear dynamics, A.B. McIntosh and S.J. Yennello, Prog. Part. Nucl. Phys. **108**, 103707 (2019).

Strongly resonating bosons in hot nuclei, S. Zhang, A. Bonasera, M. Huang, H. Zheng, D.X. Wang, J.C. Wang, L. Lu, G. Zhang, Z. Kohley, Y.G. Ma, and S.J. Yennello, Phys. Rev. C **99**, 044605 (2019).

Simulation of fusion and quasi-fission in nuclear reactions leading to production of superheavy elements using the Constrained Molecular Dynamics model, J. Klimo, M. Veselsky, G.A. Souliotis, and A. Bonasera, Nucl. Phys. **A992**, 121640 (2019).

Yield ratio of neutrons to protons in $^{12}C(d,n)^{13}N$ and $^{12}C(d,p)^{13}C$ from 0.6 to 3~MeV W. Li, Y. Ma, G. Zhang, X. Deng, M. Huang, A. Bonasera, D. Fang, J. Cao, Q. Deng, Y. Wang, and Q. Lei, Nucl. Sci. Tech. **30**, 180 (2019).

Fusion hindrance effects in laser-induced non-neutral plasmas, S.S. Perrotta and A. Bonasera, Nucl. Phys. **A989**, 168 (2019).

A novel approach to medical radioisotope production using inverse kinematics: A successful production test of the theranostic radionuclide ^{67}Cu, G.A. Souliotis, M.R.D. Rodrigues, K. Wang, V.E. Iacob, N. Nica, B. Roeder, G. Tabacaru, M. Yu, P. Zanotti-Fregonara, and A. Bonasera, Appl. Radiat. Isot. **149**, 89 (2019

Experimental liquid-gas phase transition signals and reaction dynamics, R. Wada, W. Lin, P. Ren, H. Zheng, X. Liu, M. Huang, K. Yang, and K. Hagel, Phys. Rev. C **99**, 024616 (2019).

Nuclear probes of an out-of-equilibrium plasma at the highest compression, G. Zhang, M. Huang, A. Bonasera, Y.G. Ma, B.F. Shen, H.W. Wang, W.P. Wang, J.C. Xu, G.T. Fan, H. Xu, H. Xue, H. Zheng, L.X. Liu, S. Zhang, W.J. Li, X.G. Cao, X.G. Deng, X.Y. Li, Y.C. Liu, Y. Yu, Y. Zhang, C.B. Fu, and X.P. Zhang, Phys. Lett. A **383**, 2285 (2019).

Nuclear Astrophysics with Lasers, M. Huang, H.J. Quevedo, G. Zhang and A. Bonasera, Nucl. Phys. News **29**, 9 (2019).

The role of the Heisenberg principle in constrained molecular dynamics model, K. Wang, A. Bonasera, H. Zheng, G. Zhang, Y.G. Ma and W.Q. Shen, ", Int. J. Mod. Phys E **28**, 1950039 (2019).

Status on $^{12}C+^{12}C$ fusion at deep subbarrier energies: impact of resonances on astrophysical S∗ factors, C. Beck, A.M. Mukhamedzhanov, and X. Tang, Eur. Phys. J. A **56**, 2 (2020).

New method of analytic continuation of elastic-scattering data to the negative-energy region, and asymptotic normalization coefficients for ^{17}O and ^{13}C, L.D. Blokhintsev, A.S. Kadyrov, A.M. Mukhamedzhanov, and D.A. Savin, Phys. Rev. C **100**, 024627 (2019).

Astrophysical factors of $^{12}C+^{12}C$ fusion extracted using the Trojan horse method, A.M. Mukhamedzhanov, D.Y. Pang, and A.S. Kadyrov, Phys. Rev. C **99**, 064618 (2019).

Proton-beam stopping in hydrogen, J.J. Bailey, I.B. Abdurakhmanov, A.S. Kadyrov, I. Bray, and A.M. Mukhamedzhanov, Phys. Rev. A **99**, 042701 (2019).

Theory of surrogate nuclear and atomic reactions with three charged particles in the final state proceeding through a resonance in the intermediate subsystem, A.M. Mukhamedzhanov and A.S. Kadyrov, Few-Body Syst. **60**, 9 (2019).

Isoscalar and isovector giant resonances in ^{92,94,96,98,100}Mo and ^{90,92,94}Zr, G. Bonasera, S. Shlomo, D.H. Youngblood, Y. Lui, Krishichayan, and J. Button, Nucl. Phys. **A992**, 121612 (2019).

Isoscalar E0, E1, and E2 strength in ^{54}Fe and ^{64,68}Zn, J. Button, Y.-W. Lui, D.H. Youngblood, X. Chen, G. Bonasera, and S. Shlomo, Phys. Rev. C **100**, 064318 (2019).

Giant resonances in ^{40,48}Ca, ^{68}Ni, ^{90}Zr, ^{116}Sn, ^{144}Sm and ^{208}Pb and properties of nuclear matter, S. Shlomo, G. Bonasera, and M.R. Anders, AIP Conference Proceedings **2150**, 030011 (2019).

Direct neutron capture cross section on 80Ge and probing shape coexistence in neutron-rich nuclei, S. Ahn, D.W. Bardayan, K.L. Jones, A.S. Adekola, G. Arbanas, J.C. Blackmon, K.Y. Chae, K.A. Chipps, J.A. Cizewski, S. Hardy, M.E. Howard, R.L. Kozub, B. Manning, M. Matos, C.D. Nesaraja, P.D. O'Malley, S.D. Pain, W.A. Peters, S.T. Pittman, B.C. Rasco, M.S. Smith, and I. Spassova, Phys. Rev. C **100**, 044613 (2019).

Constraining spectroscopic factors near the r-process path using combined measurements: ^{86}Kr(d,p)^{87}Kr, D. Walter, S.D. Pain, J.A. Cizewski, F.M. Nunes, S. Ahn, T. Baugher, D.W. Bardayan, T. Baumann, D. Bazin, S. Burcher, K.A. Chipps, G. Cerizza, K.L. Jones, R.L. Kozub, S.J. Lonsdale, B. Manning, F. Montes, P.D. O'Malley, S. Ota, J. Pereira, A. Ratkiewicz, P. Thompson, C. Thornsberry, and S. Williams, Phys. Rev. C **99**, 054625 (2019).

Informing direct neutron capture on tin isotopes near the N=82 shell closure, B. Manning, G. Arbanas, J.A. Cizewski, R.L. Kozub, S. Ahn, J.M. Allmond, D.W. Bardayan, K.Y. Chae, K.A. Chipps, M.E. Howard, K.L. Jones, J.F. Liang, M. Matos, C.D. Nesaraja, F.M. Nunes, P.D. O'Malley, S.D. Pain, W.A. Peters, S.T. Pittman, A. Ratkiewicz, K.T. Schmitt, D. Shapira, M.S. Smith, and L. Titus, Phys. Rev. C **99**, 041302 (2019).

^{12}C(^{15}N,^{14}C)^{13}N reaction at 81 MeV. Competition between one and two particle transfers, A.T. Rudchik, A.A. Rudchik, O.E. Kutsyk, K.W. Kemper, K. Rusek, E. Piasecki, A. Trzcińska, S. Kliczewski, E.I. Koshchy, V.M. Pirnak, O.A. Ponkratenko, I. Strojek, V.A. Plujko, S.B. Sakuta, R. Siudak, A.P. Ilyin, Y.M. Stepanenko, Y.O. Shyrma, and V.V. Uleshchenko, Nucl. Phys. **A992**, 121638 (2019).

Elastic and inelastic scattering of 15N ions by 12C at 81 MeV and the effect of transfer channels, A.T. Rudchik, A.A. Rudchik, O.E. Kutsyk, K.W. Kemper, S. Kliczewski, K. Rusek, E. Piasecki, A. Trzcińska, E.I. Koshchy, V.M. Pirnak, O.A. Ponkratenko, I. Strojek, V.A. Plujko, A. Stolarz, S.B. Sakuta, R. Siudak, O.V. Herashchenko, A.P. Ilyin, Y.M. Stepanenko, Y.O. Shyrma, and V.V. Uleshchenko, Acta Physica Polonica B **50**, 753 (2019).

Nuclear Data Sheets for A=155, N. Nica, Nucl. Data Sheets **160**, 1 (2019).

GADGET: a gaseous detector with Germanium tagging, M. Friedman, D. Pérez-Loureiro, T. Budner, E. Pollacco, C. Wrede, M. Cortesi, C. Fry, B. Glassman, M. Harris, J. Heideman, M. Janasik, B.T. Roeder, M. Roosa, A. Saastamoinen, J. Stomps, J. Surbrook, P. Tiwari and J. Yurkon, Nucl. Instrum. Methods Phys. Res. **A940**, 93 (2019).

Nuclear level densities and γ-ray strength functions in samarium isotopes, F. Naqvi, A. Simon, M. Guttormsen, R. Schwengner, S. Frauendorf, C.S. Reingold, J.T. Burke, N. Cooper, R.O. Hughes, S. Ota, and A. Saastamoinen, Phys. Rev. C **99**, 054331 (2019).

Expansion of the surrogate method to measure the prompt fission neutron multiplicity for ^{241}Pu, O.A. Akindele, B.S. Alan, J.T. Burke, R.J. Casperson, R.O. Hughes, J.D. Koglin, K. Kolos, E.B. Norman, S. Ota, and A. Saastamoinen, Phys. Rev. C **99**, 054601 (2019).

Doppler broadening in ^{20}Mg(βpγ)^{19}Ne decay, B.E. Glassman, D. Pérez-Loureiro, C. Wrede, J. Allen, D.W. Bardayan, M.B. Bennett, K.A. Chipps, M. Febbraro, M. Friedman, C. Fry, M.R. Hall, O. Hall, S.N. Liddick, P. O'Malley, W.J. Ong, S.D. Pain, S.B. Schwartz, P. Shidling, H. Sims, L.J. Sun, P. Thompson, and H. Zhang, Phys. Rev. C **99**, 065801 (2019).

γ -ray strength function for barium isotopes, H. Utsunomiya, T. Renstrøm, G.M. Tveten, S. Goriely, T. Ari-izumi, V.W. Ingeberg, B.V. Kheswa, Y.-W. Lui, S. Miyamoto, S. Hilaire, S. Péru, and A.J. Koning Phys. Rev. C **100**, 034605 (2019).

Erratum: Photoneutron cross-section measurements in the ^{209}Bi(γ,xn) reaction with a new method of direct neutron-multiplicity sorting, I. Gheorghe, H. Utsunomiya, S. Katayama, D. Filipescu, S. Belyshev, K. Stopani, V. Orlin, V. Varlamov, T. Shima, S. Amano, S. Miyamoto, Y.-W. Lui, T. Kawano, and S. Goriely, Phys. Rev. C **99**, 059901 (2019).

Fusion reaction ^{48}Ca+^{249}Bk leading to formation of the element Ts (Z=117), J. Khuyagbaatar, A. Yakushev, C.E. Düllmann, D. Ackermann, L. Andersson, M. Asai, M. Block, R.A. Boll, H. Brand, D.M. Cox, M. Dasgupta, X. Derkx, A. Di Nitto, K. Eberhardt, J. Even, M. Evers, C. Fahlander, U. Forsberg, J.M. Gates, N. Gharibyan, P. Golubev, K.E. Gregorich, J.H. Hamilton, W. Hartmann, R.-. Herzberg, F.P. Heßberger, D.J. Hinde, J. Hoffmann, R. Hollinger, A. Hübner, E. Jäger, B. Kindler, J.V. Kratz, J. Krier, N. Kurz, M. Laatiaoui, S. Lahiri, R. Lang, B. Lommel, M. Maiti, K. Miernik, S. Minami, A. Mistry, C. Mokry, H. Nitsche, J.P. Omtvedt, G.K. Pang, P. Papadakis, D. Renisch, J. Roberto, D. Rudolph, J. Runke, K.P. Rykaczewski, L.G. Sarmiento, M. Schädel, B. Schausten, A. Semchenkov, D.A. Shaughnessy, P. Steinegger, J. Steiner, E.E. Tereshatov, P. Thörle-Pospiech, K. Tinschert, T. Torres De Heidenreich, N. Trautmann, A. Türler, J. Uusitalo, D.E. Ward, M. Wegrzecki, N. Wiehl, S.M. Van Cleve, and V. Yakusheva, Phys. Rev. C **99**, 054306 (2019).

Measurement of leakage neutron spectra for zirconium with D-T neutrons and validation of evaluated nuclear data, S. Zhang, N. Song, J.C. Wang, Y. Nie, X. Ruan, J. Ren, D.X. Wang, M. Huang, L. Lu, Z. Chen, Y. Ding, K. Zhang, H. Chen, R. Wada, R. Han, and Q. Sun, Fusion Eng. Des. **149**, 111311 (2019).

Analyzing powers and the role of multistep processes in the ^{12}C(^{7}Li, t)^{16}O reaction, W.D. Weintraub, N. Keeley, K.W. Kemper, K. Kravvaris, F. Marechal, D. Robson, B.T. Roeder, K. Rusek, and A. Volya, Phys. Rev. C **100**, 024604 (2019).

Isotopic cross-sections in proton induced spallation reactions based on the Bayesian neural network method, C. Ma, D. Peng, H. Wei, Z. Niu, Y. Wang, and R. Wada, Chinese Phys. C **44**, 014104 (2019).

Solidarity of signal of measures for the liquid-gas phase transition in the statistical multifragmentation model, W. Lin, P. Ren, H. Zheng, X. Liu, M. Huang, K. Yang, G. Qu, and R. Wada, Phys. Rev. C **99**, 054616 (2019).

Inverse odd-even staggering in nuclear charge radii and possible octupole collectivity in ^{217,218,219}At revealed by in-source laser spectroscopy, A.E. Barzakh, J.G. Cubiss, A.N. Andreyev, M.D. Seliverstov, B. Andel, S. Antalic, P. Ascher, D. Atanasov, D. Beck, J. Bieroń, K. Blaum, C. Borgmann, M. Breitenfeldt, L. Capponi, T.E. Cocolios, T. Day Goodacre, X. Derkx, H. De Witte, J. Elseviers, D.V. Fedorov, V.N. Fedosseev, S. Fritzsche, L.P. Gaffney, S. George, L. Ghys, F.P. Heßberger, M. Huyse, N. Imai, Z. Kalaninová, D. Kisler, U. Köster, M. Kowalska, S. Kreim, J.F.W. Lane, V. Liberati, D. Lunney, K.M. Lynch, V. Manea, B.A. Marsh, S. Mitsuoka, P.L. Molkanov, Y. Nagame, D. Neidherr, K. Nishio, S. Ota, D. Pauwels, L. Popescu, D. Radulov, E. Rapisarda, J.P. Revill, M. Rosenbusch, R.E. Rossel, S. Rothe, K. Sandhu, L. Schweikhard, S. Sels, V.L. Truesdale, C. Van Beveren, P. Van den Bergh, P. Van Duppen, Y. Wakabayashi, K.D.A. Wendt, F. Wienholtz, B.W. Whitmore, G.L. Wilson, R.N. Wolf, and K. Zuber, Phys. Rev. C **99**, 054317 (2019).

Underlying event measurements in p+pp+p collisions at s√=200 GeVs=200 GeV at RHIC, J. Adam, D.M. Anderson, C.A. Gagliardi, A. Hamed, T. Lin, X. Liu, Y. Liu, S. Mioduszewski, N.R. Sahoo, and R.E. Tribble (STAR Collaboration), Phys. Rev. D **101**, 052004 (2020)

Measurement of the mass difference and the binding energy of hypertriton and antihypertriton, J. Adam, D.M. Anderson, C.A. Gagliardi, A.M. Hamed, T. Lin, X. Liu, Y. Liu, S. Mioduszewski, N.R. Sahoo, and R.E. Tribble (STAR Collaboration), Nature Phys. **16**, 409 (2020).

Bulk properties of the system formed in Au+Au collisions at $\sqrt{s_{NN}}$ = 14.5 GeV, J. Adam, D.M. Anderson, C.A. Gagliardi, A.M. Hamed, T. Lin, X. Liu, Y. Liu, S. Mioduszewski, N.R. Sahoo, and R.E. Tribble (STAR Collaboration), Phys. Rev. C **101**, 024905 (2020).

Beam-energy dependence of identified two-particle angular correlations in Au+Au collisions at RHIC, J. Adam, D.M. Anderson, C.A. Gagliardi, A.M. Hamed, T. Lin, X. Liu, Y. Liu, S. Mioduszewski, N.R. Sahoo, and R.E. Tribble (STAR Collaboration), Phys. Rev. C **101**, 014916 (2020).

Charge-dependent pair correlations relative to a third particle in *p*+Au and *d*+Au collisions at RHIC, J. Adam, D.M. Anderson, C.A. Gagliardi, A.M. Hamed, T. Lin, X. Liu, Y. Liu, S. Mioduszewski, N.R. Sahoo, and R.E. Tribble (STAR Collaboration), Phys. Lett. B **798**, 134975 (2019).

Longitudinal double-spin asymmetry for inclusive jet and dijet production in *pp* collisions at $\sqrt{s}$ = 510 GeV, J. Adam, D.M. Anderson, C.A. Gagliardi, A.M. Hamed, T. Lin, X. Liu, Y. Liu, S. Mioduszewski, N.R. Sahoo, and R.E. Tribble (STAR Collaboration), Phys. Rev. D **100**, 052005 (2019). (CAG and Zilong Chang, former graduate student, were two of four principal authors. Zilong Chang was also a member of the god-parent committee.)

Measurement of inclusive J/ψ suppression in Au+Au collisions at $\sqrt{s_{NN}}$ = 200 GeV through the dimuon channel at STAR, J. Adam, D.M. Anderson, C.A. Gagliardi, A.M. Hamed, T. Lin, X. Liu, Y. Liu, S. Mioduszewski, N.R. Sahoo, and R.E. Tribble (STAR Collaboration), Phys. Lett. B **797**, 134917 (2019).

Polarization of Λ (anti-Λ) Hyperons Along the Beam Direction in Au+Au Collisions at $\sqrt{s_{NN}}$ = 200 GeV, J. Adam, D.M. Anderson, C.A. Gagliardi, A.M. Hamed, T. Lin, X. Liu, Y. Liu, S. Mioduszewski, N.R. Sahoo, and R.E. Tribble (STAR Collaboration), Phys. Rev. Lett. **123**, 132301 (2019).

Measurements of the transverse-momentum-dependent cross sections of J/ψ production at mid-rapidity in proton+proton collisions at $\sqrt{s}$ = 510 and 500 GeV with the STAR detector, J. Adam, D.M. Anderson, C.A. Gagliardi, A.M. Hamed, T. Lin, X. Liu, Y. Liu, S. Mioduszewski, N.R. Sahoo, and R.E. Tribble (STAR Collaboration), Phys. Rev. D **100**, 052009 (2019).

First Observation of the directed flow of D^0 and anti-D^0 in Au+Au collisions at $\sqrt{s_{NN}}$ = 200 GeV, J. Adam, D.M. Anderson, C.A. Gagliardi, A.M. Hamed, T. Lin, X. Liu, Y. Liu, S. Mioduszewski, N.R. Sahoo, and R.E. Tribble (STAR Collaboration), Phys. Rev. Lett. **123**, 162301 (2019).

Observation of excess J/ψ yield at very low transverse momenta in Au+Au collisions at $\sqrt{s_{NN}}$ = 200 GeV and U+U collisions at $\sqrt{s_{NN}}$ = 193 GeV, J. Adam, D.M. Anderson, C.A. Gagliardi, A.M. Hamed, T. Lin, X. Liu, Y. Liu, S. Mioduszewski, N.R. Sahoo, and R.E. Tribble (STAR Collaboration), Phys. Rev. Lett. **123**, 132302 (2019).

Collision-energy dependence of second-order off-diagonal and diagonal cumulants of net-charge, net-proton and net-kaon multiplicity distributions in Au+Au collisions, J. Adam, D.M. Anderson, C.A. Gagliardi, A.M. Hamed, T. Lin, X. Liu, Y. Liu, S. Mioduszewski, N.R. Sahoo, and R.E. Tribble (STAR Collaboration), Phys. Rev. C **100**, 014902 (2019).

Beam energy dependence of (anti-)deuteron production in Au+Au collisions at the BNL Relativistic Heavy Ion Collider, J. Adam, D.M. Anderson, C.A. Gagliardi, A.M. Hamed, T. Lin, X. Liu, Y. Liu, S. Mioduszewski, N.R. Sahoo, and R.E. Tribble (STAR Collaboration), Phys. Rev. C **99**, 064905 (2019).

Azimuthal harmonics in small and large collision systems at RHIC top eneriges, J. Adam, D.M. Anderson, C.A. Gagliardi, A.M. Hamed, T. Lin, X. Liu, Y. Liu, S. Mioduszewski, N.R. Sahoo, and R.E. Tribble (STAR Collaboration), Phys. Rev. Lett. **122**, 172301 (2019).

Collision-energy dependence of p_t correlations in Au+Au collisions at energies available at the BNL Relativistic Heavy Ion Collider, J. Adam, D.M. Anderson, C.A. Gagliardi, A.M. Hamed, T. Lin, X. Liu, Y. Liu, S. Mioduszewski, N.R. Sahoo, and R.E. Tribble (STAR Collaboration), Phys. Rev. C **99**, 044918 (2019).

Comparison of heavy-ion transport simulations: Collision integral with pions and Δ resonances in a Box, A. Ono, J. Xu, M. Colonna, P. Danielewicz, C.M. Ko, M.B. Tsang, Y.J. Wang, H. Wolter, Y.X. Zhang, L.W. Chen, D. Cozma, H. Elfner, Z.Q. Feng, N. Ikeno, B.A. Li, S. Mallik, Y. Nara, T. Ogawa, A. Ohnishi, D. Oliinychenko, J. Su, T. Song, F.S. Zhang, and Z. Zhang, Phys. Rev. C **100**, 044617 (2019).

Nuclear matter properties at finite temperatures from effective interactions, J. Xu, A. Carbone, Z. Zhang, and C.M. Ko, Phys. Rev. C **100**, 024618 (2019).

Charmed hadron production in an improved quark coalescence model, S. T. Cho, K.J. Sun, C.M. Ko, S.H. Lee, and Y.S. Oh, Phys. Rev. C **101**, 024909 (2019).

Isospin splitting of pion elliptic flow in relativistic heavy-ion collisions, H. Liu, F.T. Wang, K.J. Sun, J. Xu, and C.M. Ko, Phys. Lett. B **798**, 135002 (2019).

Properties of strange quark stars with isovector interactions, H. Liu, J. Xu, and C.M. Ko, Phys. Lett. B **803**, 135343 (2020).

Probing QCD critical fluctuations from the yield ratio of strange hadrons in relativistic heavy-ion collisions, T.H. Shao, J.H. Chen, C.M. Ko, and K.J. Sun, Phys. Lett. B **801**, 135177 (2020).

Implementing chiral three-body forces in terms of medium-dependent two-body forces, Jeremy W. Holt, Mamiya Kawaguchi, and Norbert Kaiser, Front. Phys. **8**, 100 (2020).

Bayesian modeling of the nuclear equation of state for neutron star tidal deformabilities and GW170817, Y. Lim and J.W. Holt, Eur. Phys. J. A **55**, 209 (2019).

Proton elastic scattering on calcium isotopes from chiral nuclear optical potentials, T.R. Whitehead, Y. Lim, and J.W. Holt, Phys. Rev. C **100**, 014601 (2019).

Predicting the moment of inertia of pulsar J0737-3039A from Bayesian modeling of the nuclear equation of state, Yeunhwan Lim, Jeremy W. Holt, and Robert J. Stahulak, Phys. Rev. C **100**, 035802 (2019).

The Hoyle family: break-up measurements to probe α-condensation in light nuclei, R. Smith, J. Bishop, J. Hirst, T. Kokalova, and C. Wheldon, SciPost Phys. Proc. **3**, 30 (2020).

SECTION VI

APPENDIX

TALKS PRESENTED
April 1, 2019 – March 31, 2020

Probing the nuclear equation-of-state with heavy-ion collisions, **S.J. Yennello**, **Invited talk**, 58th International Winter Meeting on Nuclear Physics, Bormio, Italy (January 2020).

Studying the stars here on earth: How the equation of state of nuclear matter impacts the formation of the elements, **S.J. Yennello**, **Invited talk**, ACS-DNCT Summer School in Nuclear Chemistry, San Jose State University, San Jose, California (July 2019).

Studying the stars here on earth: Experimental investigations of the nuclear equation-of-state, **S.J. Yennello**, **Invited talk**, University of Virginia, Charlotseville, Virginia (November 2019).

Graduate studies in nuclear science: an exciting beginning to a great future, **S.J. Yennello**, **Invited talk**, University of Virginia, Charlottesville, Virginia (November 2019).

Center for excellence in nuclear training and university-based research, **S.J. Yennello**, **Invited talk**, 2020 SSAP symposium, Washington, DC (February 2020).

First beams produced by the Texas A&M University radioactive-beam upgrade, **D.P. May**, **Invited talk**, F.P. Abegglen, J. Ärje, H. Clark, G.J. Kim, B.T. Roeder, A. Saastamoinen, and G. Tabacaru, 22nd International Conference on Cyclotrons and their Applications, Cape Town, South Africa (September 2019).

Production and reacceleration of ^{112}In with the Texas A&M light ion guide and charge breeding ECR, **B.T. Roeder**, 2nd North American Charge-Breeding (NACB) workshop at TRIUMF, British Columbia, Canada (June 2019).

Direct injection of radioactive 1+ ions into an ECRIS via a sextupole ion-guide, **D.P. May**, **Invited talk**, G. Tabacaru, J. Arje, F.P. Abegglen, S. Molitor, and B.T. Roeder, 2nd North American Charge-Breeding Workshop, Vancouver, British Columbia, Canada (June 2019).

Measuring $|V_{ud}|$ and testing CKM unitarity: past, present & future, **J.C. Hardy**, **Invited talk**, Workshop on the Current and Future Status of the First-Row CKM Unitarity, Amherst Center for Fundamental Interactions, University of Massachusetts Amherst, Amherst, Massachusetts (May 2019).

*Outlook for the determination of V*ud, **D. Melconian**, **Invited talk**, Workshop on Precise beta decay calculations for searches for new physics, ECT*, Trento, Italy (April 2019).

*Outlook for the determination of V*ud, **D. Melconian**, **Invited talk**, Atomic nuclei as laboratories for BSM physics, ECT*, Trento, Italy (April 2019).

Angular correlation measurements at ISAC: using the atomic nucleus to search for BSM physics for 20 years, **D. Melconian**, **Invited talk**, ISAC 20 Symposium, TRIUMF, Vancouver, British Columbia, Canada (August 2019).

Status of the superallowed data set, **D. Melconian**, **Invited talk**, Fundamental Symmetries Research with Beta Decay, The Institute for Nuclear Theory, Seattle, Washington, (November 2019).

Polarized angular correlations in ^{37}K*: Recent results from TRINAT*, **D. Melconian**, **Invited talk**, APS Division of Nuclear Physics Meeting, Crystal City, Virginia (October 2019).

Automation and computation of TAMUTRAP, **M. Nasser**, CENTAUR SAC Meeting, Los Alamos National Laboratory, Los Alamos, New Mexico (August 2019).

Automation and computation of TAMUTRAP, **M. Nasser**, CENTAUR SAC Meeting, Los Alamos National Lab, Los Alamos, New Mexico (August 2019).

β decay simulations in TAMUTRAP, **B. Schroeder**, CENTAUR Scientific Advisory Conference, Los Alamos National Laboratory, Los Alamos, New Mexico (August 2019).

Automation and computation of TAMUTRAP, **M. Nasser**, Stewardship Science Academic Programs 2020, Washington, DC (February 2020).

Cyclotron radiation emission spectroscopy simulations with Kassiopeia, **D. McClain**, CENTAUR SAC Meeting, Los Alamos National Laboratory, Los Alamos, New Mexico (August 2019).

Cyclotron radiation emission spectroscopy in a Penning trap, **D. McClain**, Stewardship Science Academic Programs 2020, Washington DC (February 2020).

Prospects for discovery of the next superheavy element, **C.M. Folden III**, **Invited talk**, Southwest Regional Meeting and Rocky Mountain Regional Meeting of the American Chemical Society, El Paso, Texas (November 2019)..

Future of new, superheavy element discoveries, **C.M. Folden III**, **Invited talk**, Southeast Regional Meeting of the American Chemical Society, Savannah, Georgia (October 2019).

The next element: How chemists are expanding the periodic table, **C.M. Folden III**, **Invited talk**, Featured expert for the American Chemical Society's webinar, Webinar (May 2019).

A novel approach to medical radioisotope production using inverse kinematics, **A. Bonasera**, **Invited talk**, MD Anderson Research Center, Houston, Texas (June 2019).

Nuclear physics using lasers, **A. Bonasera**, **Invited talk**, 10th European Summer School on Experimental Astrophysics, Catania, Italy (June 2019).

Determining modern energy density functional for nuclear many-body systems, **S. Shlomo**, **Invited talk**, Institute of Nuclear Research Workshop on nuclear Physics, Institute of Nuclear Research, Ukraine Academy of Science Kiev, Kiev, Ukraine (April 2019).

Giant resonances in ^{40,48}*Ca,* ^{68}*Ni,* ^{90}*Zr,* ^{116}*Sn,* ^{144}*Sm and* ^{208}*Pb and Properties of Nuclear Matter*, **S. Shlomo**, **Invited talk**, LXIX International Conference NUCLEUS-2019 on Nuclear Spectroscopy and Structure, JINR, Dubna, Russia (July 2019).

Sensitivity of giant resonances energies of nuclei to properties of nuclear matter, **S. Shlomo**, **Invited talk**, ECT* Workshop on "Light clusters in nuclei and nuclear matter: Nuclear structure and decay, heavy-ion collisions, and astrophysics", ECT*, Trento, Italy (September 2019).

Sensitivity of giant resonances energies of nuclei to properties of nuclear matter, **S. Shlomo**, **Invited talk**, 21st Colloque GANIL, Strassbourg, France (September 2019).

Lecture series: Nuclear experimental techniques with rare isotope beams, **S. Ahn**, **Invited talk**, Exotic Beam Summer School 2019, Oak Ridge National Laboratory, Oak Ridge, Tennessee (June 2019).

HabaNERO: A new experimental tool for the study of (α, *xn*) *reaction rates in the weak r-process*, **S. Ahn**, Low Energy Community Meeting 2019, Duke University, Durham, North Carolina (August 2019).

TexAT activities and idea to combine with HRS, **S. Ahn**, **Invited talk**, Low Energy Community Meeting 2019, Duke University, Durham, North Carolina (August 2019).

Looking for states analogous to the ^{12}C *Hoyle state in heavier nuclei*, **M. Barbui**, **Invited talk**, Light clusters in nuclei and nuclear matter: Nuclear structure and decay, heavy ion collisions and astrophysics, ECT* European center for theoretical studies in nuclear physics and related areas, Trento, Italy (September 2019).

Advanced technique for investigation of the properties of Superheavy nuclei, **G. Chubaryan**, **Invited talk**, The present and the future of the Periodic Table of Chemical Elements, Flerov Laboratory of Nuclear Research, JINR, Dubna, Russia (May 2019).

New era of resonance reaction studies, **V.Z. Goldberg**, **Invited talk**, 69th International Conference Nucleus-2019 on Nuclear Spectroscopy and Nuclear Structure Fundamental Problems of Nuclear Physics, Nuclei at Borders of Nucleon Stability, Joint Institute for Nuclear Research, Dubna, Russia (July 2019).

A nucleation model analysis of neck emission yields in heavy ion reactions, **J. Gauthier**, Light clusters in nuclei and nuclear matter: Nuclear structure and decay, heavy ion collisions, and astrophysics (ECT Workshop 2019), ECT*, Trento, Italy (September 2019).

Investigation of the decomposition of dilute nuclear matter, **K. Hagel**, **Invited talk**, Challenges to Transport Theory for Heavy-Ion Collisions, ECT*, Trento, Italy (May 2019).

TexAT: Experiments with modified TPC detector, **Y. Koshchiy**, **Invited talk**, Brown-bag Lunch Series, Cyclotron Institute, Texas A&M University, College Station, Texas (June 2019).

Precise α_K *and* α_T *internal conversion coefficients measurements of 39.752(6)-keV E3 transition in* ^{103m}Rh*: Test of internal conversion theory*, **N. Nica**, **Invited talk**, “Horia Hulubei" National Institute of Physics and Nuclear Engineering, Bucharest, Romania (April 2019).

Progress report on nuclear structure and decay data activities at Texas A&M University, **N. Nica**, 23rd Technical Meeting of the Nuclear Structure and Decay Data Network, IAEA Vienna, Vienna, Austria (April 2019).

Code GABS:%Iγ calculation when Iγ normalization (NR) is known, **N. Nica**, 23rd Technical Meeting of the Nuclear Structure and Decay Data Network, IAEA Vienna, Vienna, Austria (April 2019).

Code PANDORA and ENSDF consistency checking:Modify to get both “γfrom level” and “γto level listings”, **N. Nica**, 23rd Technical Meeting of the Nuclear Structure and Decay Data Network, IAEA Vienna, Vienna, Austria (April 2019).

Precise α_K *and* α_T *internal conversion coefficients measurements of 39.752(6)-keV E3 transition in* ^{103m}Rh*: Test of internal conversion theory*, **N. Nica**, 23rd Technical Meeting of the Nuclear Structure and Decay Data Network, IAEA Vienna, Vienna, Austria (April 2019).

Precise α_K and α_T internal conversion coefficients measurements of 39.752(6)-keV E3 transition in ^{103m}Rh: Test of internal conversion theory, **N. Nica**, 2019 International Conference on Nuclear Data for Science and Technology, Beijing, China (May 2019).

Precise α_K internal conversion coefficients measurements of 30.77-keV M4 transition in ^{93m}Nb: Last test of internal conversion theory, **N. Nica**, US National Nuclear Data Week 2019, National Nuclear Data Center, Brookhaven National Laboratory, Upton, New York (November 2019).

Texas A&M University US nuclear data program TAMU NSDD CENTER Report 2019, **N. Nica**, US National Nuclear Data Week 2019, National Nuclear Data Center, Brookhaven National Laboratory, Upton, New York (November 2019).

Reaction experiments with exotic beams (lecture part 1), **A. Saastamoinen**, **Invited talk**, Exotic Beam Summer School 2019, Oak Ridge National Laboratory, Oak Ridge, Tennessee (June 2019).

Reaction experiments with exotic beams (lecture part 2), **A. Saastamoinen**, **Invited talk**, Exotic Beam Summer School 2019, Oak Ridge National Laboratory, Oak Ridge, Tennessee (June 2019).

Breakup of ^{9}C and ^{66}Se at RIKEN, **A. Saastamoinen**, **Invited talk**, Cyclotron Institute Brown Bag Lunch Series, Texas A&M University, Cyclotron Institute, College Station, Texas (April 2019).

Gas cell for TAMUTRAP: Texas A&M University Penning trap facility, **P. Shidling**, **Invited talk**, Brown-bag lunch series, Cyclotron Institute, Texas A&M University, College Station, Texas (May 2019).

Surface functionalization towards nihonium homologs adsorption study, **E. Tereshatov**, 6th International Conference on the Chemistry and Physics of the Transactinide Elements, Wilhelmshaven, Germany (August 2019).

Hydrophobic ionic liquids and eutectic mixtures in metals separation: behavior of medical indium and thallium radionuclides, **E. Tereshatov**, 4th International Conference on Ionic Liquids in Separation and Purification Technology, Sitges, Spain (September 2019).

Exploring multinucleon transfer for super-heavy element formation, **A. Hood**, Stewardship Science Academic Programs (SSAP) Symposium 2020, Washington D.C. (February 2020).

Upgrades to the radiation effects facility at the Texas A&M University Cyclotron Institute, **H.L. Clark**, **Invited talk**, SEE Symposium, La Jolla, California (May 2019).

Status of the radiation effects facility at the Texas A&M University Cyclotron Institute, **H.L. Clark**, **Invited talk**, SEE Symposium, La Jolla, California (May 2019).

STAR spin: Present and future, **C.A. Gagliardi**, **Invited talk**,Workshop QCD Phys. Study QCD Phase Diagram, Weihai, China (July 2019).

STAR status, plans, and upgrades, **C.A. Gagliardi** (for the STAR Collaboration), **Invited talk**, Ann. Meet. Nucl. Phys. Div. APS (DNP 2019), RHIC Town Meeting, Arlington, Virginia (October 2019).

Probing gluon polarization in the proton with jets at STAR, **C.A. Gagliardi** (for the STAR Collaboration), Ann. Meet. Nucl. Phys. Div. APS (DNP 2019), Arlington, Virginia (October 2019).

Azimuthal transverse single-spin asymmetries of charged pions within jets from polarized pp collisions at sqrt(s)=200 GeV, **T. Lin** (for the STAR Collaboration), Ann. Meet. Nucl. Phys. Div. APS (DNP 2019), Arlington, Virginia (October 2019).

Chiral kinetic study of chiral magnetic and vortical effects in HIC, **C.M. Ko**, **Invited talk**, The 5th Workshop on Chirality, Vorticity and Magnetic Field in Heavy Ion Collisions, Beijing, China (April 2019).

Recent measurements of heavy quarkonium production in p+Au and p+p collisions at STAR, **Y. Liu**, Quark Matter 2019 - the XXVIIIth International Conference on Ultra-relativistic Nucleus-Nucleus Collisions, Wuhan, China (May 2019).

Reconstruction of neutral-triggered charged recoil jets in sqrt(s)=200 GeV p+p collisions at the STAR experiment, **D. Anderson**, XLIX International Symposium on Multi-particle Dynamics, Santa Fe, New Mexico (September 2019).

Centrality determination for p+Au collisions at sqrt(s_{NN}) = 200 GeV at the STAR experiment, **Y. Liu**, XLIX International Symposium on Multiparticle Dynamics, Santa Fe, New Mexico (September 2019).

Chiral kinetic study of chiral magnetic and vortical effects in HIC, **C.M. Ko**, **Invited talk**, The 5th Workshop on Chirality, Vorticity and Magnetic Field in Heavy Ion Collisions, Beijing, China (April 2019).

Fifty years of scientific career and the history of AMPT, **C.M. Ko**, **Invited talk**, International Workshop on Partonic and Hadronic Transport Approaches for Relativistic Heavy Ion Collisions, Dalian, China (May 2019).

In-medium effects on pion production, **C.M. Ko**, **Invited talk**, Challenges to Transport Theory for Heavy-Ion Collisions, Trento, Italy (May 2019).

Effects of vorticity in relativistic heavy ion collisions, **C.M. Ko**, **Invited talk**, The 7th International Symposium on Non-equilibrium Dynamics, Castiglione della Pescaia, Grosseto, Italy (June 2019).

Transport model study of chiral magnetic effects, **C.M. Ko**, **Invited talk**, Workshop on the Study of QCD Phase Diagram and New-type Topologic Effect, Weihai, China (July 2019).

Light nuclei as a probe of the QCD phase diagram, **C.M. Ko**, **Invited talk**, Workshop on the Study of QCD Phase Diagram and New-type Topologic Effect, Weihai, China (July 2019).

Nuclear matter properties at finite temperature from effective interactions, **C.M. Ko**, **Invited talk**, The 9th International Symposium on Nuclear Symmetry Energy, Da Nang, Vietnam (September/October 2019).

Coalescence production of (anti-)(hyper-)nulcei in ultra-relativistic heavy-ion collisions, **C.M. Ko**, **Invited talk**, Third EMMI Workshop on Anti-Matter, Hyper-Matter and Exotic Production at the LHC, Wroclaw, Poland (December 2019).

The coalescence model for particle production, **C.M. Ko**, **Invited talk**, Central China Normal University, Wuhan, China (June 2019).

Light nuclei yield ratio and nucleon density fluctuations, **C.M. Ko**, **Invited talk**, Central China Normal University, Wuhan, China (June 2019).

Density fluctuation in baryon-rich quark matter, **C.M. Ko**, **Invited talk**, Central China Normal University, Wuhan, China (June 2019).

Light Nuclei Production in Relativistic Heavy Ion Collisions, **C.M. Ko**, **Invited talk**, Fudan University, Shanghai, China (July 2019).

Equation of state, single-particle potential and response of dense matter, **J.W. Holt**, **Invited talk**, INT-JINA workshop: Dense Matter and Neutron Star Mergers, Seattle, Washington (December 2019).

Nucleon-nucleus optical potentials from chiral nuclear forces, **J.W. Holt**, **Invited talk**, 4th International Workshop on Quasi-Free Scattering with Radioactive-Ion Beams, Maresias, Brazil (October 2019).

Nuclear many-body theory from microscopic chiral 2N and 3N forces, **J.W. Holt**, **Invited talk**, APCTP Focus Program in Nuclear Physics 2019 "Nuclear Many-Body Theories: Beyond the Mean Field Approaches", Pohang, South Korea (July 2019).

Vertex corrections to dynamical response functions of neutron matter, **J.W. Holt**, **Invited talk**, INT-JINA workshop on weak interactions for astrophysics, Seattle, Washington (June 2019).

Hot and dense matter in supernovae and neutron star mergers, **J.W. Holt**, **Invited seminar**, Nuclear science seminar, Michigan State University, East Lansing, Michigan (September 2019).

Microscopic optical potentials from chiral nuclear forces, **J.W. Holt**, **Invited seminar**, Nuclear theory seminar, Michigan State University, East Lansing, Michigan (September 2019).

Hadronization, **R.J. Fries**, **Invited talk**, EMMI Rapid Response Task Force: The Space-Time Structure of Jet Quenching, GSI, Darmstadt, Germany (August 2019).

Hadronization, **R.J. Fries**, **Invited talk**, *3rd International thing on QCD Challenges*, Lund University, Lund, Sweden (August 2019).

Hybrid hadronization, **R.J. Fries**, Quark Matter 2019, Wuhan, China (November 2019).

Shear viscosity of hot hadronic matter, **R.J. Fries**, APS DNP Fall Meeting, Arlington, Virginia (October 2019).

Heavy-flavor probes of hot QCD matter, **R. Rapp**, **Invited talk**, APS April Meeting, Denver, Colorado (April 2019).

Brownian motion of heavy quarks and the strongly coupled quark-gluon plasma, **R. Rapp**, **Invited talk**, Physics Colloquium, Technical University Darmstadt, Darmstadt, Germany (July 2019).

Open issues in open heavy-flavor physics in high-energy nuclear collisions, **R. Rapp**, **Invited talk**, Third International þing on QCD Challenges from pp to AA, Lund University, Lund, Sweden (August 2019).

Heavy flavor in nuclear collisions -- Part I: focus on open heavy favor , **R. Rapp**, **Invited talk**, Third International þing on QCD Challenges from pp to AA, Lund University, Lund, Sweden (August 2019).

Using machine learning to extract properties of systems of particles, **E. Gulian** (REU Student), APS DNP Fall Meeting, Arlington, Virginia (October 2019).

RESEARCH PERSONNEL AND ENGINEERING STAFF

April 1, 2019 - March 31, 2020

Faculty and Research Group Leaders

Bonasera, Aldo - Senior Scientist
Christian, Gregory - Assist. Prof. of Physics
Fries,Rainer - Assoc. Professor of Physics
Folden, III, Charles M. - Assoc.. Prof. of Nuclear Chemistry
Gagliardi, Carl A. - Professor of Physics
Hardy, John C. - Professor Emeritus
Holt, Jeremy - Assist. Professor of Physics
Ko, Che Ming – Professor of Physics
Melconian, Dan - Assoc. Professor of Physics
Mioduszewski, Saskia - Professor of Physics
Natowitz, J. B. - Professor Emeritus
Rapp, Ralf - Professor of Physics
Rogachev, Grigory - Professor of Physics and Head of Department of Physics and Astronomy
Shlomo, Shalom - Senior Scientist
Tribble, Robert E. – Professor of physics (20%)
Yennello, Sherry J. - Professor of Chemistry, Bright Chair, Director
Youngblood, Dave H. - Professor Emeritus
Zhanov, Akram M. - Senior Scientist

Research Staff

Ahn, Sunghoon – Assist. Research Scientist
Ärje, Juha – Research Scientist
Barbui, Marina - Assist. Research Scientist
Chubaryan, Grigor - Research Scientist
Gauthier, Jerome - Assist. Res. Scientist-From 6/2/19
Goldberg, Vladilen - Research Scientist, Retired
Hagel, John C. - Research Scientist
Heilborn, Lauren –Assist. Research Scientist
Horvat, Vladimir - Research Scientist (50%)
Iacob, Victor - Research Scientist
Koshchiy, Yevgen - Assist. Research Scientist
Lui, Yiu-Wing - Research Scientist
McIntosh, Alan - Assist. Res. Scientist
Nica, Ninel - Associate Research Scientist
Ota, Shuya - Assist. Research Scientist
Rodrigues, Marcia Dias - Assist. Res. Scientist
Saastamoinen, Antti (100%) – From 9/1/19
Shidling, Praveen - Assist. Research Scientist
Tereshatov, Evgeny - Assist. Research Scientist
Wada, Roichi (40%)

Accelerator Physics and Radiation Line Staff

Avila, Geoffrey – Research Assistant – From 11/1/2019
Brinkley, Joseph - Research Associate (28%)
Clark, Henry - Accelerator Physicist
Horvat, Vladimir - Research Scientist (50%)
Hyman, Bruce - Research Associate
Kim, George - Accelerator Physicist
May, Don – Senior Accelerator Physicist
Roeder, Brian - Accelerator Physicist
Park, Hyo-In - Accelerator
Saastamoinen, Antti (50%) – To 8/31/19
Tabacaru, Gabriel - Accelerator Physicist

Computer Systems Staff

Burch, Jr. Robert Lead Microcomputer/LAN Administrator
Gauthier, Jerome - Assist. Res. Scientist
Hagel, John C. Research Scientist
Lui, Yiu-Wing - Research Scientist

Engineering Staff

Olsen, Robert Senior Mechanical Engineer

Postdoctoral Research Associates

Bishop, Jack
Holhinen, Veli Sakari
Hood, Ashley - From 1/2/2020
Kirakosyan, Vahan– To 10/24/19
Kordell, Michael
Lim, Yeunhwan – To 5/31/19
Lin, Ting
Liu, Shuai – To 9/24/19
Ota, Shuya – To 7/31/18
Parker, Cody
Rodriguez Manos, Alis - To 1/5/20
Sun KaiJia
Wakhle, Aditya – To 8/15/19

STUDENTS

April 1, 2019 - March 31, 2020

Graduate Students and Research Assistants

Abbott, Austin
Aboona, Bassam
Aboud, Eric
Anderson, Derek
Atchison, Joseph
Balhoff, Mary Catherine – To 6/6/19
Bencomo, Miguel – To 5/6/19
Bennett, Eames
Bonasera, Giacomo – To 8/9/19
Bosh, Alexandra
Chyzh, Roman – To 8/31/19
Dede, Stefania
Du, Xiaojian – To 10/31/19
Edgecomb, Joseph
Garza, Fabian
Glennon, Kevin
Hannaman, Andy
Harris, Emily – From 8/12/2019
Henderson, Lawrence
Hooker, Josh – To 5/31/19
Hunt, Curtis
Hunt, Ethan – From 9/1/19
Jayatissa, Heshani – To 8/9/19
Jedele, Andrea
Kim, Byunggyu
Liu, Yanfang
McCain, David
Nasser, Morgan
Onyango, Thomas
Ozmetin, Asim
Ramiriez, Mariah
Robicheaux, Stephen
Roosa, Michael
Rose, Steven – To 12/31/19
Sarver, Issac
Schroeder, Benjamin
Scriven, Dustin
Sengupta, Arjun
Settlemyre, Thomas – From 8/6/19
Shin, Eunkyoung
Sorensen, Maxwell
Tang, Zhanduo
Tobin, Zachary
Upadhyayula, Sriteja – To 3/13/20
Volia, Merinda To 12/6/19
Wang, Kang – To 8/31/18
Wang, Shanshan – To 9/14/19
Wen, Pengshen – From 8/8/2019
Whitehead, Taylor
Xu, Zhaojie
Yang, Zidong – To 6/1/19
Zakusilova, Vera – From 9/26/19

Undergraduates and Student Technicians

Ascione, Alexander – From 1/20/2019
Forbes, Haley – To 5/13/19
Griffin, Morgan – From 6/26/2019
Iles, Haley – From 8/19/2019
Jeanis, Ian – To 6/28/19
Jeffery, Logan
Jeske, Colby
Kircher, Philip
Muzak, Mateo
O'Dwyer, Rory
Roa, Karthik
Salas, Elysia – To 5/24/19
Tamez, Celeste – To 12/31/18
Thomas, John
Tepe,Victoria – To 5/8/19

ORGANIZATIONAL CHART - CYCLOTRON INSTITUTE

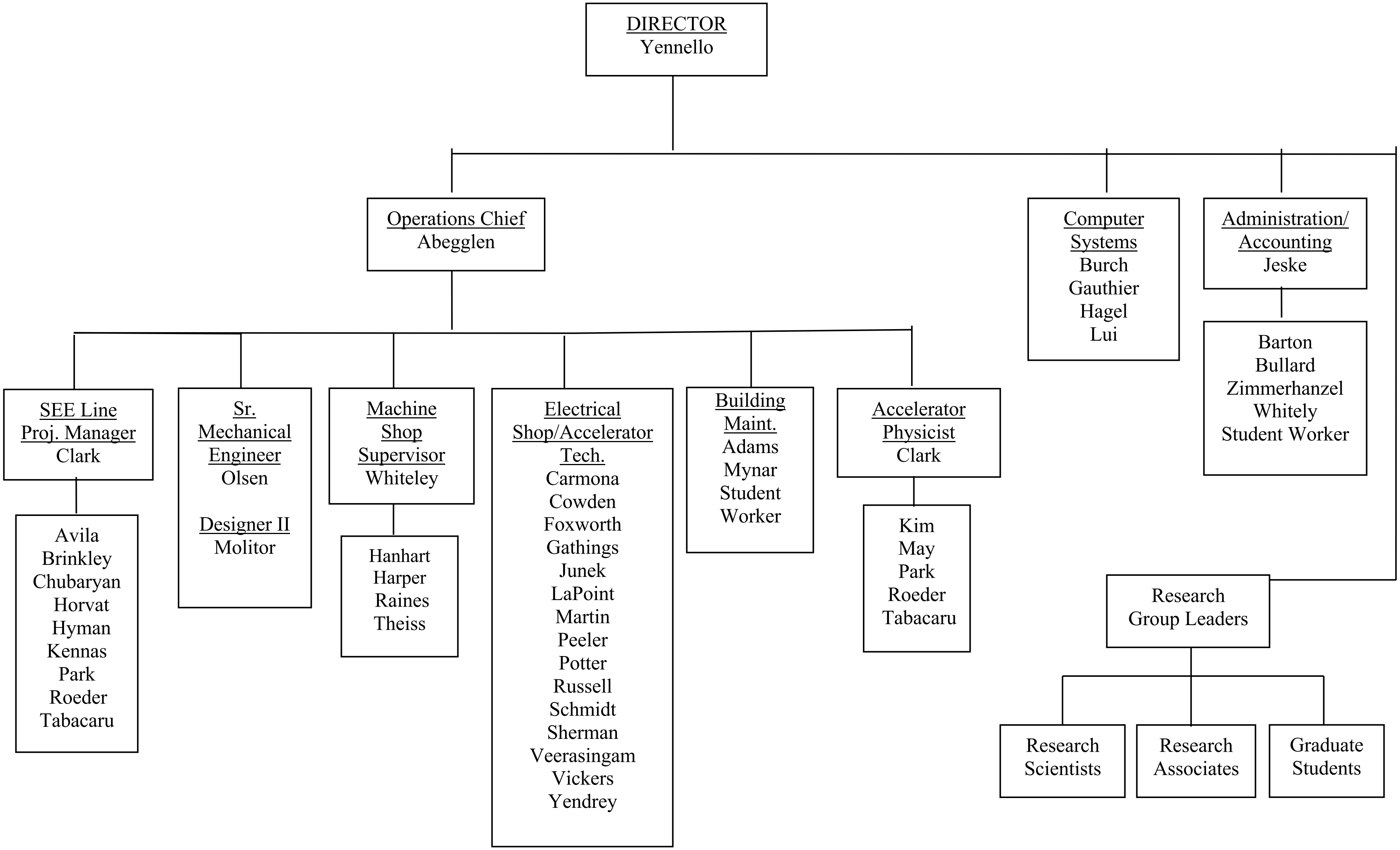

STUDENTS WHO RECEIVED GRADUATE DEGREES FROM THESIS WORK CONDUCTED AT THE CYCLOTRON INSTITUTE

April 1, 2019 – March 31, 2020

Name	Year	Thesis Title	Advisor	Present Position
Giacomo Bonasera	2019	*Mean-field investigation of strength functions of giant resonances compared with the unexpected experimental characteristics*	S. Shlomo	N/A
Roman Chyzh	2019	*Measurement of β-delayed protons from* ^{35}K *relevant to the* $^{34}Cl^{g,m}(p,\gamma)^{35}Ar$ *reaction*	R.E. Tribble	Post Doc., IRFU, CEA, Saclay, France
Heshani Jayatissa	2019	*α-capture reaction rate for* $^{22}Ne(\alpha,n)^{25}Mg$ *reaction via sub-Coulomb α-transfer and its effect on final abundances of s-process isotopes*	G. Rogachev	Post Doc. Argonne National Laboratory, Lemont, Illinois
Xiaojian Du	2019	*Quarkonium transport theory in ultra-relativistic heavy-ion collisions*	R. Rapp	Post Doc. Associate, Bielefeld University, Germany
Zhidong Yang	2019	*A self-consistent viscous blast wave model and its applications to high energy nuclear collision*	R.J. Fries	N/A
Merinda Volia	2019	*Liquid phase chemistry study of indium and thallium for a future investigation of nihonium chemistry*	C.M. Folden III	Staff, Indonesian Nuclear Energy Regulatory Agency, the directorate of regulation of radiation facility and radioactive material, Jakarta, Indonesia

INSTITUTE COLLOQUIA AND SEMINARS
April 1, 2019 - March 31, 2020

2019

April 9	Dr. Alex Gezerlis, Associate Professor, Physics Department, University of Guelph, Guelph, Ontario, Canada	*From Alpha Clustering to Homogeneous Matter*
May 7	Dr. Peter McIntyre, Professor, Department of Physics and Astronomy, Texas A&M University, College Station, Texas	*The Strong-Focusing Cyclotron: high-current 100MeV accelerator for protons and ions*
May 10	Dr. Teresa S. Bailey, Deterministic Transport Project Lead, Lawrence Livermore National Laboratory, Livermore, California	*Delivering a Nuclear Science Capability at Lawrence Livermore National Laboratory*
May 16	Dr. Iyabo Usman, Senior Lecturer, Physics Department, University of Witwatersrand, Johannesburg, South Africa	*Giant Resonances Experiments with the K600 Magnetic Spectrometer of iThemba Labs*
June 3	Dr. Nathan Nowlin, Manager, Advanced Microsystems Radiation Effects, Sandia National Laboratory, Albuquerque, New Mexico	*Recent Research on the Development of Radiation Hardened Technologies Manufactured at Sandia National Laboratory*
June 4	Dr. Shuya Ota, Postdoctoral Research Associate, Cyclotron Institute, Texas A&M University, College Station, Texas	*Neutron Production and Capture in s-Process Stars: Nuclear Physics with TIARA, STARLiTeR, and HYPERION*
June 11	Dr. Kathy Prestridge, Extreme Fluids Team Leader, Physics Division, Los Alamos National Laboratory, Los Alamos,New Mexico	*Mixing and Turbulence: Are We There Yet?*
June 13	Dr. Chad Forrest, Research Scientist, Laboratory for Laser Energetics, University of Rochester, Rochester, New York	*Nuclear Science Experiments at the University of Rochester's Omega Laser Facility*
July 27	Dr. Todd Bredeweg, Nuclear Chemistry Team Leader, Nuclear and Radiochemistry, Los Alamos National Laboratory, Los Alamos, New Mexico	*Fission Product Chain Yield Measurements*

August 6	Dr. Maximilian Hughes, Research Assistant, Michigan State University, East Lansing, Michigan	*Precision Measurements in* ^{20}*F Beta Decay*
September 10	Dr. C. Jeff Martoff, Professor of Physics, Temple University, Philadelphia, Pennsylvania	*The HUNTER Sterile Neutrino Search Experiment*
September 17	Dr. Joe Carlson, Nuclear, Particle, Astrophysics and Cosmology Group Leader, LANL Theoretical Division, Los Alamos National Laboratory, Los Alamos, New Mexico	*Nuclei, Neutrinos, and Neutron Stars*
September 24	Dr. Jonathan Barney, Graduate Assistant, Michigan State University, East Lansing, Michigan	*Measureing Charged Pion Emission from 112Sn+124Sn and 124Sn+112Sn Reactions with the SπRIT Time Projection Chamber*
October 8	Justin Estee, Research Assistant, Michigan State University, East Lansing, Michigan	*Studying the Nuclear Equation of State with Pions using the SπRIT Time Projection Chamber*
October 11	Dr. Romualdo deSouza, Provost Professor, Professor of Chemistry and Physics, Indiana University, Bloomington, Indiana	*The Science and Technology of Fusing Neutron-Rich Light Nuclei Near and Below the Barrier*
October 18	Dr. Oleksandr Koshchii, Postdoctoral Researcher, Johannes Gutenberg University Mainz, Mainz, Germany	*Parity Violation to Nuclear Structure and New Physics*
October 29	Dr. Nathan Holt, Assistant Professor, Piedmont College, Demorest, Georgia	*Toward the Omega Meson Contribution to the Muon Anomalous Magnetic Moment*
November 5	Dr. Jason Holt, Research Scientist, TRIUMF and The University of Brisish Columbia, Vancouver, Canada	*Ab Initio Nuclear Theory for Beyond Standard Model physics*
November 12	Dr. Guy Ron, Associate Professor, Hebrew University of Jerusalem, Jerusalem, Israel	*Tricks and traps: Low Energy Searches for High Energy Physics*
November 13	Professor Lee Sobotka, Department of Chemistry and Physics, Washington University, St. Louis, Missouri	^{11}*O and Other Invariant Mass Results At, Beyond or Isobarically Anchored to the Proton Drip Line*

2020

January 28	Kyle Godbey, Vanderbilt University, Nashville, Tennessee	*Microscopic Approaches to Understanding Multinucleon Transfer*
February 4	Dr. Andrew Steiner, Assistant Professor, University of Tennessee and Oak Ridge National Laboratory, Knoxville, Tennessee	*Determining the Properties of Dense Matter from Neutron Star Observations*
February 25	Professor Alexander Volya, Florida State University, Tallahassee, Florida	*Microscopic Studies of Alpha Clustering in Light Nuclei*